

**Electron Transfer and Electrocatalytic  
Studies on some Organic and Conducting  
Polymer Nanocomposite Thin Films**

*By*

**Rakesh Kumar Pandey**

*Thesis submitted to Jawaharlal Nehru University, New Delhi for the award of  
the degree of*

**Doctor of Philosophy**

**July 2010**



**Raman Research Institute  
Bangalore-560080**

# CERTIFICATE

This is to certify that the thesis entitled **“Electron transfer and electrocatalytic studies on some organic and conducting polymer nanocomposite thin films”** submitted by Mr. Rakesh Kumar Pandey, for the award of the degree of DOCTOR OF PHILOSOPHY of Jawaharlal Nehru University, New Delhi, is his original experimental investigation and conclusions. The subject matter of this thesis has not been previously published or submitted to any other university for the award of any other degree or diploma.

Prof. Ravi Subrahmanyam  
Director  
Raman Research Institute  
Bangalore –560080

Prof. V. Lakshminarayanan  
(Thesis Supervisor)

# DECLARATION

I hereby declare that the entire work embodied in this thesis is the result of the experimental investigation carried out by me independently at Raman Research Institute, Bangalore, under the guidance and supervision of Prof. V. Lakshminarayanan. The experimental work and conclusions presented in this thesis work have not been previously submitted and no part of this thesis work has formed the basis for the award of any other degree, diploma, fellowship or any other similar title.

Prof. V. Lakshminarayanan  
(Thesis Supervisor)  
Raman Research Institute  
Bangalore-560080

Rakesh Kumar Pandey

## Acknowledgements

*I wish to express profound sense of gratitude to my honored supervisor Prof. V. Lakshminarayanan who constantly inspired me at every stage of my research. Without his serious involvement, thoughtfulness and patience, it would have been difficult for me to complete this thesis in time. It was an invaluable experience to work with him and to learn so many things from him both as a scientist and as a human being. It has been a great pleasure and I really cherished working with him.*

*I must express my earnest gratitude to Prof. K. A. Suresh (Director, Center for Liquid Crystal Research, Bangalore) for his sound guidance during the initial period of my research and constant encouragement during the entire course of the present study.*

*I thank Prof. Sandeep Kumar, for many valuable discussions related to the organic chemistry. I also thank Dr. Reji Philip (light and matter physics group, RRI) for allowing me to carry out many optical experiments in his lab. I would not miss this opportunity to thank all the soft condensed matter staff members for their help in various ways.*

*I also thank Mr. N. Ravisankar for his invaluable help in the lab, Mr. Dhason for his help in AFM imaging and fabricating glass apparatus, Mr. Ram for preparing gold samples for electrochemical studies and Mr. Mani for his help in fabricating accessories for various experiments. I thank Mrs. Vasudha for her help in spectroscopic measurements. I also thank Mr. K. Radhakrishna for his valuable and timely help throughout my research work.*

*I thank my seniors in the lab Dr. Suresh, Dr. Ganesh, Dr. Kavitha and Mrs. Mohan Priya for their friendly support and valuable inputs regarding the research work. My sincere thank to my batch mate Mr. Nagaraju for many valuable conversations on academic and nonacademic matters.*

*I thank all my friends at soft condensed matter student's room Dr. Bharat, Mr. Satyam, Mr. Radhakrishnan, Mr. Bibhu, Ms. Tripta, Mr. Jayakumar, Mr. Madhukar, Ms. Alpana, Mrs. Radhika, Mr. Santosh, Mr. Shabeeb, Mr. Avinash, Mr. Swamy, Mr. Rajib, Mr. Debashish, Ms. Renu, Ms. Anagha, Ms. Antara, Mr. Arif, Mr. Venkat, Mr. Rao, Mr. Katti, Mr. Jetti, Mr. Srinivas and Mr. Shashi. I thank my seniors Dr. Amit, Dr. Arun, Dr. Pandey, Dr. Santanu, Dr. Brindaban, Dr. Hari and Dr. Sajal for many valuable discussions.*

*I thank my hostel friends and all my badminton friends Dr. Srikanth, Mr. Kanhaiya, Mr. Sandeep, Mr. Deepak, Mr. Chandrakant, Mr. Nishant, Mrs. Mamta, Mr. Yogesh, Mr. Kshitij, Mr. Wasim, Mrs. Ruta, Ms. Archana and Ms. Lee for providing hilarious and healthy time in the evening.*

*I also thank all my batch mates and friends at RRI and other institutions of Bangalore for their valuable inputs related to my work.*

*I thank Dr. William Grips (National Aerospace Laboratories, Bangalore) for his invaluable help in the characterization of many nanocomposite samples.*

*The library staffs of RRI have been outstanding during the course of my research work and it is a pleasure to thank all of them for their significant and timely help.*

*I would like to thank various other departments of RRI, Administration, Computer section, Accounts, Workshop, Transport, Canteen and Clinic for their constant support throughout my research work.*

*I am deeply indebted to Raman Research Institute for giving me the opportunity to carry out the research work in the friendliest surroundings. It is an immense pleasure to thank all the scientific as well as supporting staff of the institute for their cooperation.*

*Finally, I would like to thank my beloved parents for being a steady source of encouragement, support and help throughout my research work. It would be unfair if I don't mention my sincere thanks to my brother, sister and brother-in-law. I have been greatly benefited by their valuable suggestions and thought provoking advices.*

# Contents

<b>Abbreviations</b>	i
<b>Preface</b>	iv
<b>List of publications</b>	xiii
<b>Chapter 1: Introduction</b>	
1.1 Ultrathin films	3
1.1.1 Langmuir-Blodgett (LB) film	4
1.1.2 Self-assembled monolayers (SAMs)	5
1.1.3 Layer by layer (LbL) assembly	7
1.1.4 Electron transfer barrier properties of a thin film modified electrode	8
1.1.5 Applications of ultrathin films	9
1.2 Nanocomposites	10
1.2.1 Conjugated (conducting) polymers	11
1.2.2 Applications of conjugated polymers	13
1.2.3 Metal and conducting polymer nanocomposites	14
1.3 Electrocatalysis for fuel cells	15
1.3.1 Electrocatalysis of small organic molecules	19
1.3.2 Alkaline fuel cells (AFCs)	20
1.4 Aims and scope of the present thesis	22
Bibliography	24
<b>Chapter 2: Experimental Methods</b>	
2.1 Introduction	29

2.2 Electrochemical cell and electrodes	29
2.3 Electrochemical studies	30
2.4 Instrumentation	31
2.5 Electrochemical techniques	31
2.5.1 Cyclic voltammetry	31
2.5.2 Electrochemical impedance spectroscopy	35
2.5.3 Chronopotentiometry	41
2.5.4 Chronoamperometry	42
2.5.4.1 Tafel plot analysis	43
2.5.5 Anodic stripping voltammetry (ASV)	44
2.6 Imaging techniques	45
2.6.1 Scanning electron microscopy (SEM)	45
2.6.2 Scanning tunneling microscopy (STM)	48
2.6.3 Atomic force microscopy (AFM)	50
2.7 Spectroscopic techniques	52
2.7.1 Fourier transform infrared spectroscopy	52
2.7.2 Ultraviolet-visible (UV-vis) spectroscopy	54
2.7.3 Photoluminescence spectroscopy (PL spectroscopy)	54
2.7.4 X-ray photoelectron spectroscopy (XPS)	54
Bibliography	56
<b>Chapter 3: Formation and Electrochemical Studies of Nanosize Films of Organic Compounds on Gold Substrate</b>	
3.1 Introduction	58

3.2 Electron transfer studies on cholesterol LB films assembled on thiophenol and 2-naphthalenethiol SAMs	59
3.2.1 Methods and materials	61
3.2.1.1 Deposition of cholesterol on SAMs	61
3.2.1.2 Cyclic voltammetry	62
3.2.1.3 Electrochemical impedance analysis	64
3.2.1.4 Scanning probe and FTIR analysis of cholesterol monolayer on 2NT-SAM	72
3.3 Electrochemical characterization of LB films of a discotic liquid crystal molecule and its complex with DNA	75
3.3.1 Methods and materials	76
3.3.1.1 AFM studies	78
3.3.1.2 Electrochemical studies in aqueous system	80
3.3.1.3 Electrochemical studies in nonaqueous (ethanol) medium: Ferrocene redox reaction	83
3.4 Cyclodextrin inclusion complexes (ICs) with thiocholesterol and their self-assembly on gold: A combined electrochemical and lateral force microscopy (LFM) analysis	86
3.4.1 Methods and materials	88
3.4.1.1 Inclusion complex: Formation and self-assembly on gold	88
3.4.1.2 Electrochemical characterization	88
3.4.1.3 Lateral force microscopy studies and force-distance measurements on the different SAM systems	92
3.5 The layer-by-layer (LbL) assembly of oppositely charged polyelectrolytes morphological analysis and electron transfer studies	96

3.5.1 Methods and materials	97
3.5.1.1 Characterization of the LbL films	98
3.6 Conclusions	100
Bibliography	102
<b>Chapter 4: Formation of Nanostructures of Polyaniline (PANI) and Porphyrin Derivative, AFM Analysis, Optical Properties and Electrochemical Lead Sensing</b>	
4.1 Introduction	108
4.2 Methods and materials	110
4.2.1 Formation of the PTBA-PANI nanoparticles in the bulk and nonlinear optical properties	112
4.2.1.1 Characterization of the nanocomposite	112
4.2.1.2 Photoluminescence spectroscopy analysis	119
4.2.2 Formation of porphyrin/polyaniline nanostructures by layer-by-layer assembly and their application in ppb level lead sensing	120
4.2.2.1 Structural analysis	120
4.2.2.2 Lead detection	123
4.2.3 Formation of porphyrin nanofibers (J-aggregates) and their optical property	124
4.2.3.1 Synthesis and characterization of porphyrin nanofibers	125
4.2.3.2 Optical properties of the PTBA nanofibers (UV-vis and photoluminescence spectroscopy)	126
4.3 Conclusions	128
Bibliography	129

## **Chapter 5: Electrochemical Synthesis of Palladium and Conducting Polymer Nanocomposite films for Applications in Electrocatalysis**

5.1 Introduction	133
5.2 Methods and materials	134
5.2.1 Enhanced electrocatalytic activity of Pd dispersed PEDOT film in hydrogen evolution and ethanol electro-oxidation reactions	135
5.2.1.1 Synthesis of the Pd-PEDOT nanocomposite on gold substrate	135
5.2.1.2 Characterization of the Pd-PEDOT coated surface	137
5.2.1.3 Voltammetric response of the Pd-PEDOT coated electrode in acid medium, catalytic activity towards hydrogen evolution reaction (HER)	139
5.2.1.4 Catalytic activity of Pd-PEDOT coated electrode towards electro-oxidation of ethanol	143
5.2.1.5 Kinetics of ethanol electro-oxidation	147
5.2.2 Electro-oxidation of formic acid, methanol and ethanol on electrodeposited Pd-PANI nanofiber film in acidic and alkaline media	153
5.2.2.1 Synthesis of the Pd-PANI nanofiber film on gold substrate	153
5.2.2.2 SEM, EDAX, AFM and XRD studies on Pd-PANI nanofiber film	154
5.2.2.3 FTIR spectroscopy analysis	157
5.2.2.4 X-ray photoelectron spectroscopy (XPS) analysis	159
5.2.2.5 Cyclic voltammetry analysis and electrocatalytic activity of the Pd-PANI coated electrode	161
5.2.2.6 Kinetics of the formic acid oxidation	166

5.2.2.7 Catalytic activity of Pd-PANI surface towards electro-oxidation of ethanol and methanol	169
5.3 Conclusions	176
Bibliography	178
<b>Chapter 6: Electrochemical Synthesis of Nanocomposite Films of Gold with Different Conducting Polymers and Their Applications in Electrocatalysis</b>	
6.1 Introduction	183
6.2 Methods and materials	184
6.2.1 Synthesis of the Au-CP nanocomposites on gold substrate	185
6.2.2 Characterization of Au-PANI nanocomposites with SEM, EDAX, AFM and FTIR spectroscopy	186
6.2.2.1 SEM analysis	186
6.2.2.2 EDAX analysis	189
6.2.2.3 AFM analysis	190
6.2.2.4 FTIR spectroscopy analysis	191
6.2.3 Electrocatalytic activity of Au-CP nanocomposite films for ethanol oxidation	193
6.2.3.1 Mechanism of electro-oxidation	195
6.2.4 Kinetics of ethanol electro-oxidation	196
6.2.4.1 Activation energy ( $E_a$ ) determination	196
6.2.4.2 Tafel plot analysis for ethanol electro-oxidation	198
6.2.4.3 Reaction order calculation	202
6.3 Conclusions	203
Bibliography	205

<b>Chapter 7: Summary and Prospects for Future Works</b>	207
<b>Appendix</b>	214

## Abbreviations

<b>CV</b>	Cyclic voltammetry
<b>EIS</b>	Electrochemical impedance spectroscopy
<b>CE</b>	Chronopotentiometry
<b>CA</b>	Chronoamperometry
<b>ASV</b>	Anodic stripping voltammetry
<b>XRD</b>	X-ray diffraction
<b>STM</b>	Scanning tunneling microscopy
<b>AFM</b>	Atomic force microscopy
<b>LFM/FFM</b>	Lateral force microscopy/Friction force microscopy
<b>SEM</b>	Scanning electron microscopy
<b>FTIR</b>	Fourier transform infrared
<b>XPS</b>	X-ray photoelectron spectroscopy
<b>EDAX</b>	Energy dispersive X-ray analysis
<b>ICP-MS</b>	Inductively coupled plasma-mass spectroscopy
<b>SAM(s)</b>	Self-assembled monolayer(s)
<b>LB films</b>	Langmuir-Blodgett films
<b>LbL assembly</b>	Layer by layer assembly
<b><math>\nu</math></b>	Scan rate
<b><math>\epsilon</math></b>	Dielectric constant of the monolayer
<b><math>\epsilon_0</math></b>	Permittivity of free space or vacuum

<b>D</b>	Diffusion coefficient
<b>Z'</b>	Real part of impedance
<b>Z''</b>	Imaginary part of impedance
<b>Z'<sub>f</sub></b>	Real part of faradaic impedance
<b>Z''<sub>f</sub></b>	Imaginary part of faradaic impedance
<b>[Fe(CN)<sub>6</sub>]<sup>3-4-</sup></b>	Potassium ferrocyanide/ferri cyanide complex
<b>[Ru(NH<sub>3</sub>)<sub>6</sub>]<sup>2+3+</sup></b>	Hexaammineruthenium(III) chloride
<b>SDS</b>	Sodium dodecyl sulphate
<b>2NT</b>	2-Naphthalenethiol
<b>TP</b>	Thiophenol
<b>4-MPS</b>	4-Mercaptopropanesulfonate (sodium salt)
<b>Cys</b>	Cysteamine
<b>IC(s)</b>	Inclusion complex(s)
<b>R<sub>u</sub></b>	Solution resistance
<b>R<sub>ct</sub></b>	Charge transfer resistance
<b>W</b>	Warburg impedance
<b>Z<sub>f</sub></b>	Faradaic impedance
<b>Q/CPE</b>	Constant phase element
<b>C<sub>dl</sub></b>	Double layer capacitance
<b>η</b>	Overpotential
<b>ω</b>	Angular frequency

$\lambda$	Wavelength
<b>SCE</b>	Saturated calomel electrode
<b>HER</b>	Hydrogen evolution reaction
<b>HOPG</b>	Highly oriented pyrolytic graphite
<b>PTBA</b>	4,4',4'',4'''-(porphine-5,10,15,20- tetrayl) tetrakis (benzoic acid)
<b>PTBA-PANI</b>	PTBA and PANI nanocomposite
<b>CP(s)</b>	Conducting (conjugated) polymer(s)
<b>PANI</b>	Polyaniline
<b>PPY</b>	Polypyrrole
<b>PTP</b>	Polythiophene
<b>PEDOT</b>	Polyethylenedioxythiophene/Poly(3,4-ethylenedioxythiophene)
<b>EDOT</b>	3,4- ethylenedioxythiophene
<b>Pd-PANI</b>	Palladium and polyaniline nanocomposite
<b>Pd-PEDOT</b>	Palladium and polyethylenedioxythiophene nanocomposite
<b>Au-CP(s)</b>	Au and conducting polymer(s) nanocomposite
<b>Au-PANI</b>	Au and polyaniline nanocomposite
<b>Au-PPY</b>	Au and polypyrrole nanocomposite
<b>Au-PTP</b>	Au and polythiophene nanocomposite
<b>Au-PEDOT</b>	Au and polyethylenedioxythiophene nanocomposite

# Preface

## **Electron transfer and electrocatalytic studies on some organic and conducting polymer nanocomposite thin films**

The thesis describes the results of electron transfer and electrocatalytic studies carried out on some thin film modified electrodes. We have used different methods for ultrathin film formation namely, Langmuir-Blodgett (LB) techniques, self-assembled monolayers (SAMs) formation and layer by layer film formation (LbL). The main applications of these films include the use of coated film as modified substrates in molecular electronics, electrocatalysis, electron transfer studies and electroanalytical studies.

In LB method dilute solution of an amphiphilic compound is spread across an air-water water surface. The amphiphilic molecules form a single layer of molecules known as the Langmuir monolayer on water surface. This layer can be transferred onto a solid surface by dipping a solid substrate through the Langmuir layer into the solution. This is called the Langmuir-Blodgett (LB) technique. The necessary condition for the formation of LB film is that the compound should be amphiphilic in nature so that it can be spread on water surface.

SAMs are the molecular assemblies of organic films of a few nanometers thickness on certain metal surfaces. These films are formed by the spontaneous chemisorption of organic molecules on a substrate when it is immersed into a dilute solution containing organic molecules.

In contrast to the LB films, the bonding between the substrate and organic molecules is much stronger in SAMs due to the chemical adsorption process.

We have studied the LbL films of oppositely charged polyelectrolytes namely polystyrene sulfonate (PSS) and polyallylamine hydrochloride (PAH). The LbL deposition technique has become an efficient method for producing organized films of oppositely charged molecules due to its simplicity, versatility, low cost, and precise control of film thickness.

A major part of the thesis deals with the conducting polymers and their nanocomposites with different materials. The conductivity of a conducting polymer depends on both its ability to transport charge carriers along the polymer backbone and for the carriers to hop between polymer chains. Most conducting polymers do not have good electrical conductivity in their

native state and therefore they need to be doped with suitable dopant in order to achieve high conductivity.

For the formation of metal and conducting polymer films on conducting substrates we have used the electrodeposition method with the help of chronopotentiometry (CE). We have proposed a novel single step electrochemical method of synthesizing Pd-PEDOT and Pd-PANI nanocomposite films on gold surface by the galvanostatic dissolution of a Pd wire in the chloride containing acidic EDOT or aniline solution. A thin film of nanocomposite containing Pd nanoparticles embedded in the polymer matrix was formed on the surface. In a similar way gold and different conducting polymer nanocomposite films were prepared and characterized. All these nanocomposite films were found to be highly electrocatalytic towards the oxidation of small organic molecules. We have also studied the kinetics of the electro-oxidation by carrying out the Tafel slope analysis and activation energy calculation. For this the experiment was carried out at different temperatures. In the following paragraphs we will discuss in brief the synopsis of each chapter.

## **Chapter 1: Introduction**

This chapter conveys the importance of the studies carried out and the aims and scope of our research investigation. The chapter is divided into two parts, the first part contains the materials and methods used for the study, which includes the introduction to different types of ultrathin films (LB films, SAMs and LbL films), an introduction to nanocomposites and conducting polymers. This is followed by a discussion on electrocatalysis and fuel cells.

## **Chapter 2: Experimental techniques and chemicals**

In the second part of the chapter we discuss all the experimental techniques used in the thesis work, which includes electrochemical methods like cyclic voltammetry (CV), electrochemical impedance spectroscopy (EIS), chronopotentiometry (CE) and chronoamperometry (CA). We also discuss the imaging methods used in the work. These techniques are atomic force microscopy (AFM), scanning tunneling microscopy (STM), and scanning electron microscopy (SEM). At the end of the chapter we have discussed the spectroscopic techniques used for the analysis, such as UV-vis spectroscopy, photoluminescence spectroscopy, FTIR spectroscopy and X-ray photoelectron spectroscopy (XPS).

### **Chapter 3: Formation and electrochemical studies of nanosize films of organic compounds on gold substrate**

This chapter describes the formation and characterization of different types of nanosize films. The chapter is divided into four parts. The first part contains a study on the combination of SAM and LB techniques for fabricating monolayer and multilayer films of cholesterol. The composite film was used for studying the electron transfer properties of some redox active systems. The electron transfer and ion permeation properties were studied through the cholesterol monolayers and multilayer films formed on an Au substrate (modified with self-assembled monolayers of thiophenol (TP) and 2-naphthalenethiol (2NT)). For electrochemical measurements, cyclic voltammetry (CV) and electrochemical impedance spectroscopy (EIS) were used. Molecular films of cholesterol have also been characterized using STM, AFM and grazing angle FTIR studies. The STM and AFM studies of the cholesterol monolayer show that it is a good, compact and well-ordered film on 2-naphthalenethiol SAM. The STM studies were used to measure the area per molecule which is calculated to be  $0.64 \text{ nm}^2$  for a cholesterol molecule, with a tilt angle of about  $28.96^\circ$  from the surface normal as obtained from our STM studies.

The second part of the chapter describes the formation and electron transfer properties of the LB film of DNA and a pyridinium derivative of hexaalkoxytriphenylene (PyTp). PyTP is one among the discotic liquid-crystal molecules (discogens) which are of interest for their intriguing supramolecular architectures. The PyTp and PyTp-DNA complex films (Langmuir films) were first formed at an air-water interface and then transferred onto gold substrates by Langmuir-Blodgett technique. The electron transfer properties of films of PyTp and its complex with DNA (PyTp-DNA) were studied using electrochemical methods like cyclic voltammetry and electrochemical impedance spectroscopy. The studies were carried out on these LB films in different redox systems. AFM imaging was also carried out in order to know the topography of the modified surface. Our studies reveal that the electron transfer reaction of the ferrocene was allowed whereas the potassium ferrocyanide reaction was completely blocked. The bridge mediated electron transfer reaction is the possible mechanism for this interesting behavior.

An interesting SAM system composed of cyclodextrins and thiocholesterol inclusion complex was studied in the third part of this chapter. The SAM, which is composed of the host-guest inclusion complex (IC) of the  $\beta$ -cyclodextrin and thiocholesterol on gold was formed and

the electrochemical barrier properties of the SAM were analyzed in aqueous redox system. The above system was then compared with another system composed of methyl  $\beta$ -cyclodextrin and thiocholesterol inclusion complex. A high electron transfer blocking was observed in both the system and the blocking sequence was found to be thiocholesterol SAM <  $\beta$ -cyclodextrin-thiocholesterol SAM < methyl  $\beta$ -cyclodextrin-thiocholesterol SAM. Lateral force microscopy (LFM) and force-distance spectroscopy studies show the presence of regions of hydrophobic and hydrophilic nature.

In the fourth and the final part of the chapter the formation and characterization of LbL films of oppositely charged polyelectrolytes namely polystyrene sulfonate (PSS) and polyallylamine hydrochloride (PAH) were studied. The LbL deposition technique has become an efficient method for producing organized films of oppositely charged molecules. The multilayer films were analyzed with the help of AFM and cyclic voltammetry. AFM images of the LbL films show increase in the roughness and electron transfer barrier properties.

#### **Chapter 4: Formation of nanostructures from polyaniline (PANI) and porphyrin derivative, AFM analysis, optical properties and applications in lead Sensing**

In this chapter we show that the porphyrin derivative 4,4',4'',4'''-(porphine-5,10,15,20- tetrayl) tetrakis (benzoic acid) (PTBA) shown in Figure 1 forms uniformly distributed nanoparticles when mixed with the conducting polymer polyaniline (PANI) in a DMF/water mixture. The nanoparticles were characterized with the help of AFM as shown in Figure 2a.

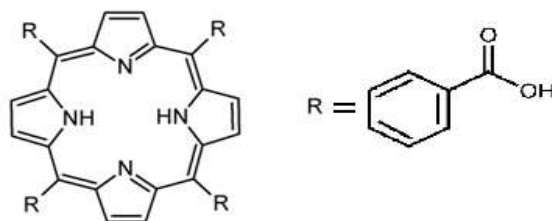


**Fig. 1** Porphyrin derivative 4,4',4'',4'''-(porphine-5,10,15,20- tetrayl) tetrakis (benzoic acid) (PTBA)

We have also synthesized porphyrin nanofibers which are essentially the J-aggregates of porphyrin and studied their structure with the help of AFM (Figure 2b). The optical properties (UV-vis and PL spectra) of the nanofibers were studied and it was observed that the nanofibers are highly emissive which stands quite in contrast to the behavior of usual dye aggregates. This behavior is called as the aggregation induced emission (AIE). In such a system the intramolecular motions (rotational and vibrational) serve as relaxation pathways to deactivate the excited state in solutions. The excitonic energy can be transferred to the solvent molecules during the collisions of the excited molecule with the surrounding solvent molecules in the form of heat and therefore the restriction of these motions will decrease the nonradiative recombination rate of the excited state and enhance the emission efficiency.

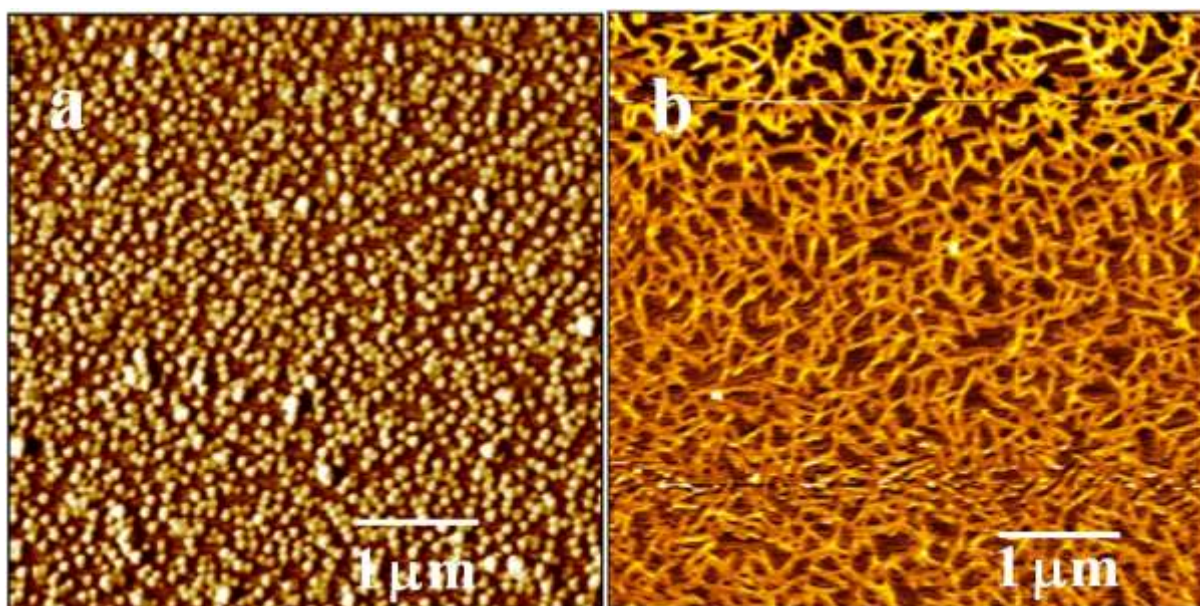


**Fig. 2** Nanoparticles of PTBA-PANI and nanofibers of PTBA

In the same chapter we also present a simple technique to build an assembly of PTBA-PANI nanostructures by LbL film formation method. These nanostructures are made of alternate layers of PTBA and PANI. Structural analysis was carried out using AFM. Deposition with 4 and 8 layers of was carried out on SAM modified gold. We have made use of the property of PTBA to chelate with heavy metal ions to study the lead sensing response of modified electrodes. The modified electrode was used for lead detection and it was observed that the electrode is capable of detecting down to 100 ppb with the help of anodic stripping voltammetry.

## Chapter 5: Electrochemical synthesis of palladium and conducting polymer nanocomposite films for applications in electrocatalysis

In this chapter we present a method to form Pd and conducting polymer nanocomposite films, which consists of *in-situ* electrochemical generation of Pd ions from a Pd wire anode at high current densities. The electrolyte contains the monomer (3,4-ethylenedioxythiophene or aniline) and dilute hydrochloric acid. The dissolved Pd ions immediately form chloropalladate complex with chloride ions present in the solution. The chloropalladate, which is an oxidizing agent can initiate the oxidative polymerization reaction of monomer and consecutively chloropalladate ions get reduced to Pd nanoparticles. These Pd nanoparticles electrophoretically deposit on gold and form a nanocomposite film with polymer (polyethylenedioxythiophene (PEDOT) or polyaniline (PANI)) on the electrode. Figure 3 shows the SEM images of Pd-PEDOT and Pd-PANI nanocomposite films.

The chapter is divided into two parts. The first part deals with the synthesis and characterization of Pd-PEDOT nanocomposite film and then study the electrocatalytic response of the resulting film towards ethanol oxidation in an alkaline medium and hydrogen evolution reaction (HER) in acidic medium. The nanocomposite film modified gold surface was characterized using scanning electron microscopy (SEM), energy dispersive X-ray analysis (EDAX), inductively coupled plasma-mass spectroscopy (ICP-MS) and atomic force microscopy (AFM).

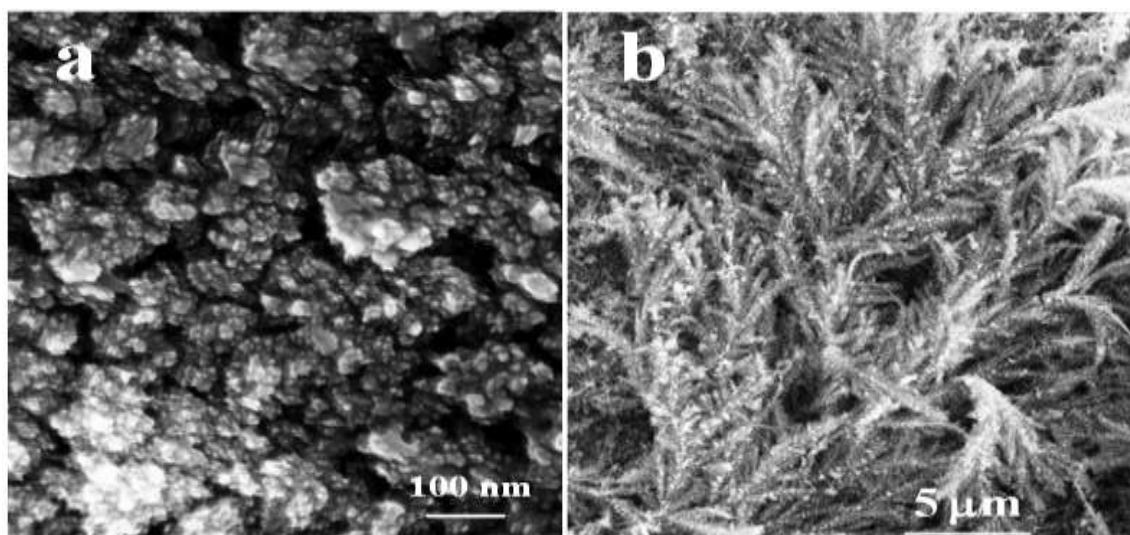


**Fig. 3** SEM image of (a) Pd-PEDOT and (b) Pd-PANI nanocomposite modified gold surface

The second part describes the synthesis and characterization of Pd-PANI nanofiber film by using the same method described above. The electrocatalytic response of the nanofiber film towards formic acid oxidation in acidic medium and alcohols (ethanol and methanol) oxidation in alkaline medium was studied. We have characterized the surface film with SEM, EDAX, XPS, AFM, XRD and FTIR spectroscopy.

In both the cases i.e. Pd-PEDOT nanocomposite and Pd-PANI nanofiber film, the electrocatalytic studies were also carried out at different temperatures to obtain activation energy values at different overpotentials. In addition, the study of reaction order and the Tafel slope analysis has provided information on the kinetics of the electrocatalytic process.

## **Chapter 6: Electrochemical synthesis of nanocomposite films of gold with different conducting polymers and their applications in electrocatalysis**

In chapter 5 we further extend our method of metal conducting polymer film deposition to produce gold and conducting polymer nanocomposite films on the conducting surfaces. We have used four of the most commonly used conducting polymers (CPs) namely, polyaniline (PANI), polypyrrole (PPY), polythiophene (PTP) and polyethylenedioxythiophene (PEDOT) in this work. The method involves the *in-situ* polymerization of the monomer to yield the polymer nanocomposite with gold. The polymer and gold nanocomposites (Au-CPs) were formed *in-situ* during the galvanostatic deposition process in the presence of their respective monomers in HCl with Au wire as the anode and another gold electrode as the cathode. The present method is of particular significance because it is a single step electrochemical method which avoids the extra steps of the preparation of CPs separately and subsequent mixing of polymer and gold. The prepared nanocomposite film can be directly used for further studying its properties such as electrocatalytic activity. Figure 4 shows the cyclic voltammograms for the electro-oxidation of ethanol on different Au-CPs modified electrodes.

The surface of the film was examined with various imaging techniques such as SEM and AFM, spectroscopic techniques such as EDAX and FTIR spectroscopy.

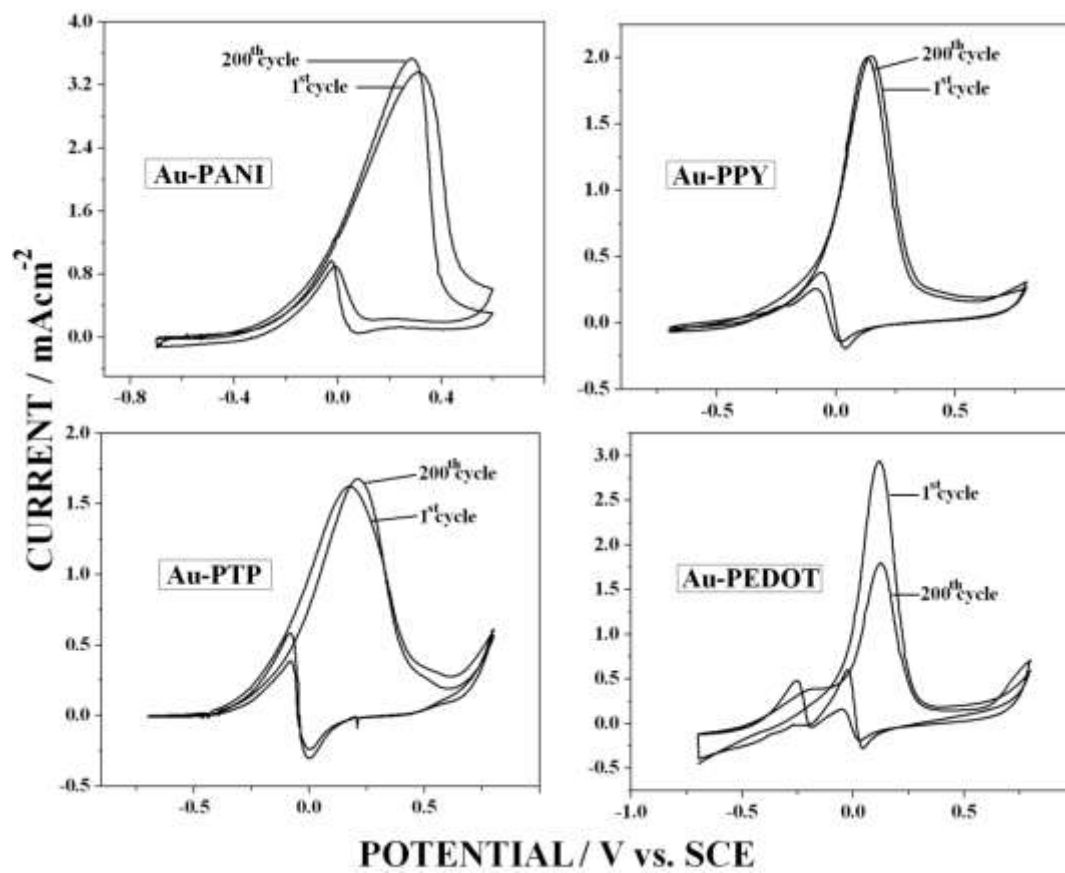


**Fig. 4** Cyclic voltammograms of Different Au-CPs nanocomposite modified gold surface

The nanocomposite films of Au and CPs were found to be highly porous and sustain a high rate of electro-oxidation of ethanol in the alkaline media as observed for nanocomposite modified electrodes. Although fuel cells based on acidic electrolytes are more popular than alkaline electrolytes, yet there is plenty of room for alkaline electrolytes based fuel cells because fuel cells based on acidic electrolytes function mainly with Pt based catalysts. This dependency makes them more expensive. However the alkaline fuel cells can function with cheaper metals such as Au, Ag and Ni too. The electrocatalytic activity of all the nanocomposite films towards ethanol electro-oxidation was studied in the alkaline medium and their electrocatalytic response was compared.

Electrocatalysis studies were also carried out at different temperatures to calculate the activation energies. Reaction order and Tafel slope measurements at different temperatures yield useful kinetic data for electrocatalysis. Based on these results, we have concluded that Au-PANI

nanocomposite is the best electrocatalyst material among all the Au-CP nanocomposites studied in this work in terms of the activation energy and electro-oxidation current.

## **Chapter 7: Summary and Prospect for Future Works**

In this chapter we summarize the results and conclusions of the work presented in the preceding chapters. We have also suggested the potential applications and future scope of our work.

## List of publications

(1) Electron transfer studies on cholesterol LB films assembled on thiophenol and 2-naphthalenethiol self-assembled monolayers.

*J. Coll. Inter. Sci.*, 315 (2007) 528.

**Rakesh K. Pandey**, K. A. Suresh and V. Lakshminarayanan

(2) Electrocatalytic studies of cytochrome c functionalized single walled carbon nanotubes on self-assembled monolayer of 4-ATP on gold.

*J. Electroanal. Chem.*, 627 (2009) 63.

D.H. Nagaraju, **Rakesh K. Pandey** and V. Lakshminarayanan

(3) Enhanced optical nonlinearity of polyaniline-porphyrin nanocomposite.

*J. Phys. Chem. C*, 113 (2009) 8630.

**Rakesh K. Pandey**, C. S. Suchand Sandeep, Reji Philip and V. Lakshminarayanan

(4) Electro-oxidation of formic Acid, methanol, and ethanol on electrodeposited Pd-polyaniline nanofiber films in acidic and alkaline medium.

*J. Phys. Chem. C*, 113 (2009) 21596.

**Rakesh K. Pandey** and V. Lakshminarayanan

(5) Formation of porphyrin /polyaniline nanostructured thin film by layer by layer assembly and application in ppb level lead sensing.

*Proceedings of Sensors-15 (15th national seminar on physics and technology of sensors)*

**Rakesh K Pandey**, Avinash B.S. and V. Lakshminarayanan

(6) Enhanced electrocatalytic activity of Pd-dispersed 3,4-polyethylenedioxythiophene film in hydrogen evolution and ethanol electro-oxidation reactions.

*J. Phys. Chem. C*, 114 (2010) 8507.

**Rakesh K. Pandey** and V. Lakshminarayanan

(7) Nanocomposite films of gold and conducting polymers synthesized by electrochemical method for applications in ethanol electrocatalysis.

*Manuscript under preparation*

**Rakesh K. Pandey** and V. Lakshminarayanan

(8) Cyclodextrin inclusion complexes (IC) with thiocholesterol and their self-assembly on gold: A combined electrochemical and lateral force microscopy (LFM) study.

*Manuscript under preparation*

**Rakesh K. Pandey** and V. Lakshminarayanan

(9) Electrocatalytic activity of Pd-dispersed PANI film on graphite electrode in methanol and ethanol electro-oxidation reactions.

*Manuscript under preparation*

**Rakesh K. Pandey**, Sandeep Patnaik and V. Lakshminarayanan

(10) Synthesis of nanofibrous porphyrin J-aggregates and their enhanced emission property.

*Manuscript under preparation*

**Rakesh K. Pandey**, Upendra Chitgupi and V. Lakshminarayanan

*“In arranging the bodies in order of their electrical nature, there is formed an electro-chemical system which, in my opinion, is more fit than any other to give an idea of chemistry”.*

*Jöns Jacob Berzelius*

# Chapter 1

## Introduction

The work described in this thesis deals with the study of thin films formed by four different techniques namely; Langmuir-Blodgett method, self-assembled monolayer formation, layer-by-layer assembly and electrochemical formation of metal-conducting polymer nanocomposite films. The main focus of the study is on the nature of these films with special emphasis on the electron transfer and electrocatalytic properties.

The thesis consists of three major parts; the first part deals with the synthesis and characterization of ultrathin films prepared by using different methods namely, Langmuir-Blodgett (LB) method, self-assembled monolayer (SAM) and layer-by-layer assembly (LbL). The LB approach of film formation relies on the physical adsorption, which is weaker in terms of adhesion to the substrate but possesses the advantage of the possibility of multilayers formation. In this work we have analyzed the LB films of cholesterol on two different SAM systems.

The SAM formation, on the other hand is a typical example of chemisorption which is essentially a strong adsorption but limited to the single layer of the molecules. In the present work we have studied a composite film system composed of cyclodextrin and thiocholesterol that shows a high electron transfer blocking property towards the redox couples in aqueous medium. The film exhibits regions of hydrophilic and hydrophobic properties on the modified surface, which was imaged using lateral force microscopy (LFM).

The LbL film formation is quite different from both the above mentioned methods. In this case the adhesion of material to the substrate is relatively stronger than the LB method. It is possible to form multilayer films using LbL method, where the stability of the layers is essentially due to the electrostatic interactions. Therefore the LbL method possesses the virtues of both LB and SAM methods. In this work we describe the LbL film formed by two oppositely charged polyelectrolytes namely; polystyrenesulfonate (PSS) and polyallylamine hydrochloride (PAH).

The second part of the thesis deals with the synthesis of conducting polymer polyaniline (PANI) by using electrochemical technique and the formation of nanocomposites from PANI and a porphyrin derivative. These nanocomposites are essentially the J-aggregates of porphyrin and

they form diverse nanostructures ranging from disc like nanostructures to nanofibers. We have shown that these nanostructures find useful applications in sensors and exhibit interesting linear and nonlinear optical properties.

The third part of the thesis deals with the synthesis, characterization and the study of the electrocatalytic property of conducting polymer and metal nanocomposites. We have proposed a new and simple one step electrochemical method for the synthesis of metal and conducting polymer nanocomposite films. We have studied four conducting polymers namely; polyaniline (PANI), polypyrrole (PPY), polythiophene (PTP) and polyethylenedioxythiophene (PEDOT). Noble metals gold and palladium were used to form nanocomposites with these conducting polymers. The nanocomposite films were characterized systematically by using various electrochemical, spectroscopic and microscopic techniques, which include cyclic voltammetry (CV), electrochemical impedance spectroscopy (EIS), FTIR spectroscopy, atomic force microscopy (AFM), scanning electron microscopy (SEM), X-ray photoelectron spectroscopy (XPS) and energy dispersive X-ray analysis (EDAX) among many others.

These nanocomposite films find useful applications as an electrocatalyst material for the electro-oxidation of small organic molecules such as methanol, ethanol and formic acid. This makes the present study useful for direct fuel cells (DFCs).

The present chapter provides a concise description of the methods and materials used in the thesis work.

## **1.1 Ultrathin films**

The LB films, SAMs and LbL films are three major types of the ultrathin films of organic compounds which can be formed on variety of substrates. In the following section we will discuss all the above three films in some detail. Nanoscale films produced with the above techniques have opened up interesting possibilities in organic electronics, electrocatalysis, bioelectrochemistry and electroanalysis. In addition to the fabrication of nanomaterials and uses in the molecular electronics, fundamental processes such as charge transfer mechanisms involving biomolecules can be investigated at the molecular level. In our work we have focused mainly on how a thin film modified surface affect the electron transfer process in some of the common redox systems and also how this behavior varies in different types of films.

### 1.1.1 Langmuir-Blodgett (LB) film

A single layer of amphiphilic molecules spread at air-water interface is termed as the Langmuir monolayer. The necessary condition for the formation of Langmuir film is that the compound should be amphiphilic in nature so that it can be spread on water surface [1,2]. An amphiphilic compound or amphiphile is the one which has both hydrophilic and hydrophobic groups. Figure 1.1 shows a typical amphiphilic molecule and its Langmuir film at air-water interface. The Langmuir monolayer can be transferred onto a solid surface by LB technique. In Figure 1.1 the polar part may refer to any functional group which has affinity towards water, which is also called the hydrophilic part. Some such groups are  $-\text{COOH}$ ,  $-\text{OH}$ ,  $-\text{CONH}_2$  etc. Nonpolar parts typically contain a hydrophobic group like a hydrocarbon chain. These molecules form a single molecule thick assembly on the water surface. The overall effect of a Langmuir film on water surface is the reduction in the surface energy or the surface tension of water.

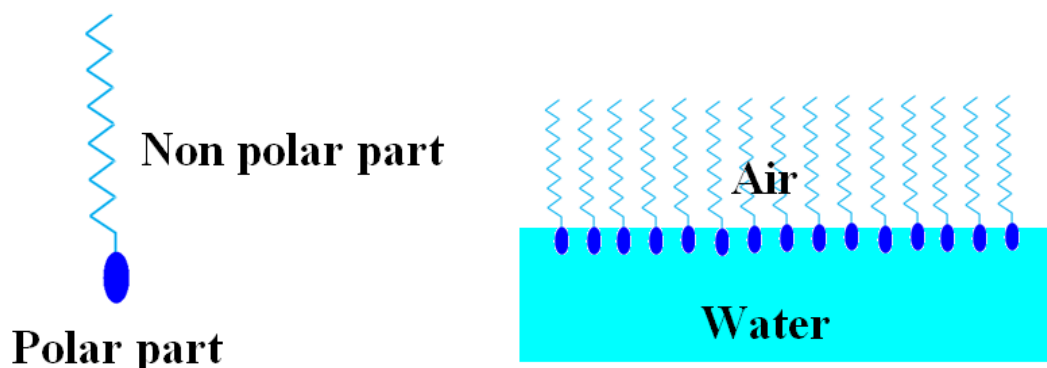


**Fig. 1.1** Schematic representation of the amphiphilic molecule and Langmuir monolayer at air-water interface

The LB film can be formed on a solid surface when a solid substrate is dipped upwards and downwards through the Langmuir monolayer at air-water interface. The polar parts of the molecules adsorb on the substrate during the upward motion and hydrophobic parts of the molecules adsorb on the substrate during the downward motion. The process is shown in Figure 1.2. Depending on the nature of the substrate *i.e.* hydrophilic or hydrophobic, different kinds of LB films are possible, which are named as X-type, Y-type and Z-Type as shown in Figure 1.2. The first layer of the molecules can only be deposited on hydrophilic substrates during up stroke whereas on hydrophobic substrates the initial layer can be deposited during the down stroke. However the monolayer formation can take place during both up and down stroke (Y-type

deposition). Deposition can also occur during only down stroke (X-type deposition) or only up stroke (Z-type deposition). During the LB film formation the surface area of the Langmuir monolayer decreases due to the continuous removal of the molecules from the surface onto the solid substrate. A parameter called the transfer ratio ( $\tau$ ) is defined as the ratio of the decrease in the Langmuir monolayer area to the total surface area of the substrate to be coated. A unit value of the transfer ratio reflects the ideal LB deposition.

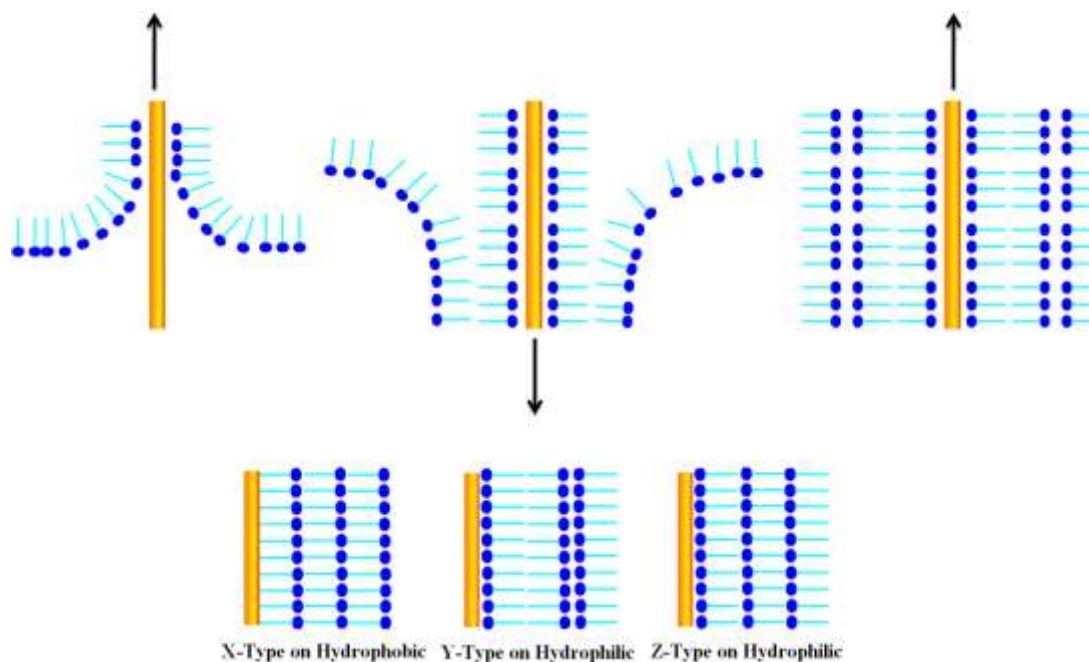


*Fig. 1.2 Schematic representation of the LB deposition process during the upward and downward motions and different types of LB deposition on different substrates*

### 1.1.2 Self-assembled monolayers (SAMs)

Self-assembled monolayers (SAMs) are the molecular assemblies of organic films of a few nanometers thickness. These films are formed by the spontaneous chemisorption of organic molecules on a substrate when it is immersed into a dilute solution containing organic molecules. In contrast to the LB films the bonding between the substrate and organic molecules is much stronger in SAMs due to the chemical adsorption process.

The self-assembly phenomenon is known for the past many years, yet the significant progress in the field has emerged only in recent times. A variety of studies can be carried out with the help of SAMs such as studying electron transfer reactions, single molecule electron tunneling, sensors and molecular electronics etc. There are many examples of SAM formation

with different organic molecules and substrate combinations. Alkanethiols and dithiols on gold [3,4], silver [5] and copper [6], dialkyl sulphides and disulphides on gold [7], alcohols and amines on platinum [8] and carboxylic acids on aluminum oxides [9] and silver [10] are the main examples of SAM. The process of self-assembly is mainly divided into three steps as shown in Figure 1.3, the first step is the chemisorption of the head group onto the substrate, which is an exothermic process.

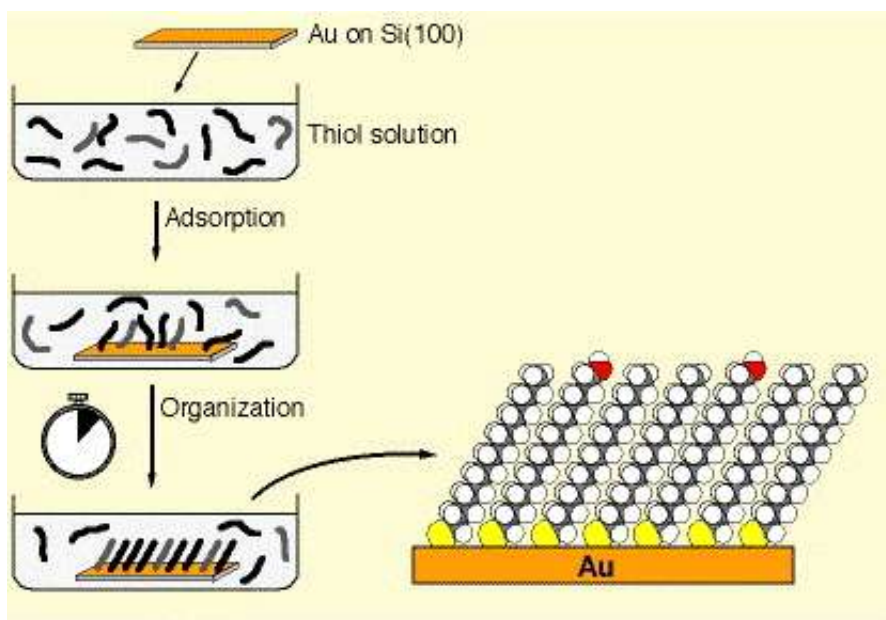
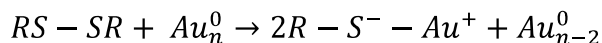


**Fig. 1.3** Schematic representation of the self-assembled monolayer formation process on gold substrates

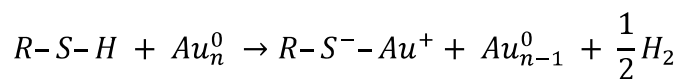
The very strong molecule-substrate interactions result in the pinning of the head group to a specific site on the surface through a chemical bond. The bonding can be covalent but slightly polar for alkanethiol monolayers on gold or ionic bond for carboxylic acids on AgO/Ag. The energy associated with the adsorption of carboxylic acid on Ag/AgO is of the order of tens of kcal/mol [11,12] and in the case of thiolate on gold it is 40-50 kcal/mol. As a result of the exothermic process during the first step, organic molecules try to occupy every available bonding site on the surface and in this process they compete with the molecules that have been already adsorbed. The second step is the inter chain van der Waals interactions among the alkyl groups. The energy associated with this process is only a few kcal/mol. The third and final step is the reorientation of the terminal groups. In the case of simple alkanethiol, methyl group is the terminal group. The thermal disorder at room temperature of the surface groups is evident from

the helium diffraction [13] and FTIR studies on monolayers [14]. The energy associated with this process is of the order of a few  $k_B T$ .

Both the alkanethiols and disulphides adsorb onto gold substrate to form the same thiolate ( $RS^-$ ) species. The reaction of dialkyl disulphides with gold is an oxidative addition reaction as shown below.



In the case of alkanethiol, the reaction may be considered as an oxidative addition of the thiol (S-H) bond to the gold surface, followed by a reductive elimination of hydrogen. When a clean gold surface is used for the monolayer preparation, the protons may probably end as  $H_2$  molecule. The chemical reaction occurs in this case can be expressed as below:



The combination of hydrogen atoms at the gold surface to form  $H_2$  molecule is an important exothermic step in the process of self-assembly. During the chemisorption process, the thiolate species has been formed, as can be seen from the equation represented above, which is verified by XPS [4,15,16], FTIR spectroscopy [17], FT-mass spectrometry [18], electrochemistry [19] and Raman spectroscopy [20].

### 1.1.3 Layer-by-layer (LbL) assembly

Figure 1.4 shows the schematic diagram of the typical LbL assembly process with two oppositely charged polyelectrolytes namely; polystyrenesulfonate (PSS) and polyallylamine hydrochloride (PAH). In the beginning of the LbL film formation, we need a charged substrate which, in the case of metals can be achieved by forming a charged SAM on metals such as a SAM of 4-mercaptopropane sulfonate (negative charge) or cysteamine (positive charge). The simplest mechanism of LbL adsorption can be described as a sequential adsorption of oppositely charged species by dipping the substrate into the respective solutions alternatively. Recent results show that the film formation takes place due to the charge overcompensation and this can only take place till a threshold value of surface charge density beyond which film formation will no longer take place [21-24].

Over the past few years the LbL deposition technique has become an efficient method for producing organized films of oppositely charged molecules. There are several advantages

associated with the LbL method such as simplicity, versatility, low cost, and precise control of film thickness. In addition LbL film formation has the advantage of multilayer film formation with variety of materials. The nanostructured films prepared by the use of LbL method have tremendous advantages especially to fabricate new devices whose properties can be tuned by carefully choosing the desired polyelectrolytes. These films find several applications in the field of electrochromism, bioelectrocatalysis, electroanalysis and electrocatalysis.

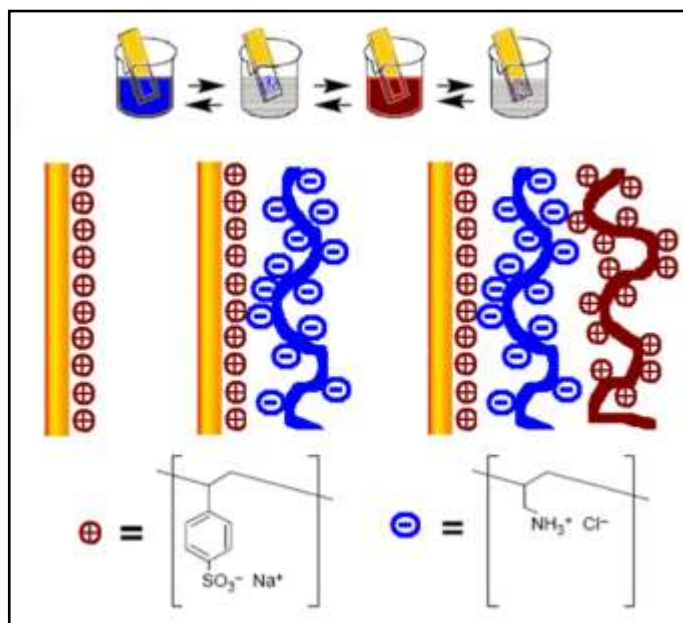


**Fig. 1.4** Schematic representation of the layer-by-layer film formation process on solid substrates

The alternate dipping of such charged surface into a solution of oppositely charged polyelectrolyte yield a film of that polyelectrolyte on the surface which after cleaning in Millipore water can be immersed into the solution of another polyelectrolyte to form a bilayer of polyelectrolyte. This process can be repeated many times to obtain required thickness of the film until a threshold value of surface charge density comes into the picture.

### 1.1.4 Electron transfer barrier properties of a thin film modified electrode

In the literature there has been a detailed and comprehensive study on the structure and properties of aliphatic thiols on gold surface [3,4,19]. The ultimate aim in the area of SAM is to obtain a completely blocking and almost defect free structure of the monolayer.

Main effect of the blocking SAMs is the suppression of simple redox reactions across metal-solution interface by acting as a dielectric spacer. This phenomenon is due to the blocking of redox ions due to the presence of a close packed domain of hydrocarbon chains. Several factors such as the heterogeneous rate constant for the electron transfer reaction, the size and charge of the redox species, mechanism of electron transfer (inner-sphere or outer-sphere) affect the apparent blocking properties of the SAMs. These factors complicate the interpretation of suppressed faradaic current in terms of pinholes, defects and electron tunneling across the monolayer. The electron transfer blocking properties of a thin film modified electrode can easily be studied with the help of cyclic voltammetry (CV) and electrochemical impedance spectroscopy (EIS). The current due to faradaic reactions at pinholes is limited by mass transfer at relatively low overpotentials compared to kinetically controlled currents due to tunneling. Hence the factors that affect the mass transfer should affect the observed currents if they are dominated by pinhole currents. This point of mass transfer controlled or kinetically controlled process for the electron transfer reactions can be resolved by using electrochemical impedance spectroscopic studies.

### **1.1.5 Applications of ultrathin films**

Ultrathin film modified substrates find a variety of applications in several fields such as in corrosion protection, molecular electronics, memory storage, supercapacitors, sensors, photolithography, wetting behavior and surface patterning for various uses. Apart from this the thin film modified electrodes also act as an electron transfer barrier for several redox species between the metal surface and the solution. These films act as an insulating layer between the metal and the electrolyte and obstruct the further reaction, which can find potential applications in corrosion inhibition. Ultrathin films have also been used for the studies of single molecular electronic properties using either scanning tunneling microscopy or scanning tunneling spectroscopy. With the help of these two methods, a single molecule can be addressed on the surface and the electronic properties of the molecule can be studied. Using the SAM of dithiols, two metal surfaces can be interconnected resulting in a molecular wire between two electrodes. It has been shown that the wetting properties of the surface can be tuned by using molecules that have different terminal functional groups. For example, carboxyl terminal group provides a

hydrophilic film surface while methyl group in the terminal position results in highly hydrophobic surface.

These films also influence the orientation of the water molecules at the film/water interface and it has been shown that the long chain alkanethiol SAMs form a hydrophobic gap at the interface [25,26]. This hydrophobic gap reduces the interfacial capacitance in alkanethiol SAMs to a large extent, while for SAMs with polar functional groups the capacitance decreases only to a small extent. Ultrathin films have been widely used for the synthesis of monolayer protected nanoparticles especially gold nanoparticles [27]. The functionalization of the nanoparticles yields a highly stable coating on them which prevents the agglomeration of nanoparticles and such nanoparticles have good solution processability for further studies.

One of the main advantages of the SAMs is the possibility for further functionalization of the surface through terminal functional groups like carboxyl, amino or other derivative groups at the terminal positions. Such groups can be easily attached with different organic molecules, redox probes, enzymes, proteins or other biomaterials [28-30]. Such biofunctionalized monolayers have been widely used for the sensor applications [31-33]. One of the recent advancement in the ultrathin film study is the lithography, where different patterns can be formed on the metal surface using the different organic molecules [34,35]. In this thesis, we have focused our studies on the electron transfer barrier properties of different types of ultrathin films. We have used electrochemical, FTIR and scanning probe techniques for the characterization of these monolayers.

## **1.2 Nanocomposites**

Nanocomposites, by plain definition are the materials having more than one phase and at least one of the phases should have one dimension less than 100 nanometers [36]. Of late the definition of nanocomposite materials has become wider notably to include a large range of systems for example one, two and three-dimensional materials, made of distinctly dissimilar components and mixed at the nanometer scale. In the broad sense this definition includes mesoporous materials, colloids, copolymers, organic-inorganic hybrid materials and multiphase nanostructures etc. The physical and chemical properties for example the electronic, mechanical, thermal, optical, electrochemical, catalytic properties of the nanocomposite are strikingly different from that of the component materials.

From ancient prehistoric times the human kind has been associated with nanostructures or nanocomposites either in the natural form like bones or the fascinating artificial ones like the Maya Blue. Ancient Romans had used colloidal gold (gold nanoparticles) to color glass with shades of violet or red. A fascinating class of hybrid materials can now be prepared by the mixing of different organic and inorganic materials. For last few years a rapid growth is noticed in the understanding and controlling of the chemistry of these nanocomposite materials to design and shape them for various applications.

In the present thesis, we have studied the electrochemical synthesis of organic-inorganic hybrid nanocomposite of conducting polymers and noble metals as a porous film on conducting substrates and their intriguing catalytic activity.

### **1.2.1 Conjugated (conducting) polymers**

The plastics which we use daily are essentially the polymers, which are large molecules with a repeating structural unit. In fact the electrical wires are coated with plastics (polymers) as insulating material to protect them from short-circuits. The polymers are known to be insulators. A.J. Heeger, A.G. MacDiarmid and H. Shirakawa have discovered a new class of polymers which are electrically conducting almost like a metal. They were awarded the Noble prize in chemistry in the year 2000 for their discovery.

Polyacetylene was the first polymer in which the electrical conductivity was first detected. This polymer was already known as a black powder since 1974. Polyacetylene was prepared by Shirakawa and co-workers from acetylene, using a Ziegler-Natta catalyst. Despite its metallic appearance it was not known to be a conductor until 1977 when Shirakawa, MacDiarmid and Heeger discovered that the polyacetylene can be made  $10^9$  times more conductive by oxidation with chlorine, bromine or iodine vapors. The oxidation by halogens is called the doping of the polymer.

The doped form of the polyacetylene has the conductivity about  $10^4$  to  $10^5$   $\text{S m}^{-1}$ , which can be compared with the conductivity of metals ( $10^8$   $\text{S m}^{-1}$ ). Figure 1.5 shows the conductivity chart of different materials, the conducting polymers are somewhere in between semiconducting to conducting zone. The conductivity in conducting polymers arises due to the presence of highly conjugated structure (the presence of alternate double bonds). It is known that conjugated double

bonds show entirely different behavior than isolated double bonds. These conjugated double bonds act in a group, as if they know that the next-nearest bond is also double.

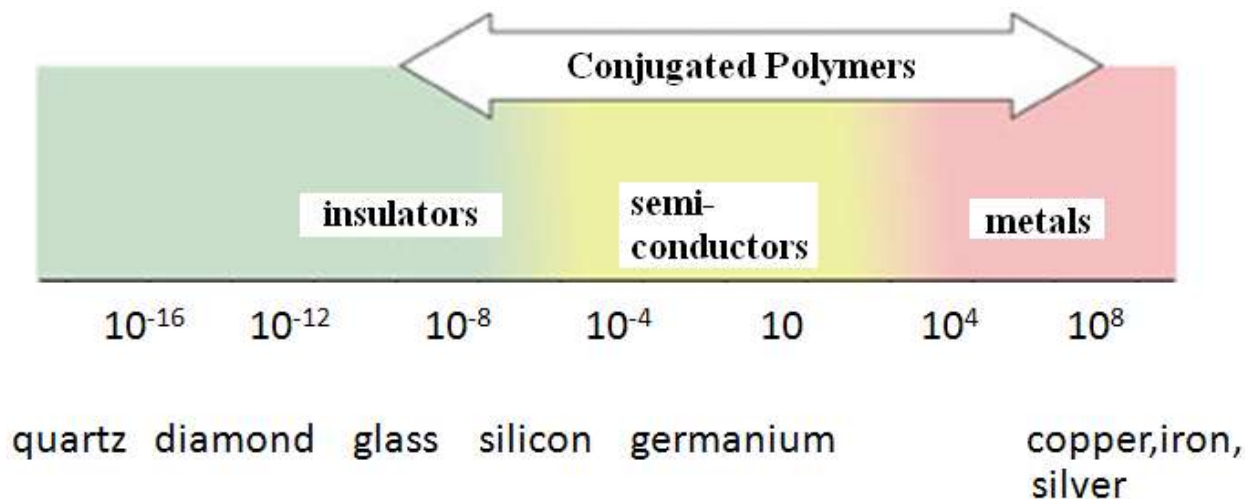


**Fig. 1.5** Conductivity chart showing different materials including the conducting polymers

Huckel's theory for aromaticity predicts that  $\pi$  electrons are delocalized over the entire length of the molecule, which makes the band gap very small especially for a long chain *i.e.* in the case of a polymer. The conductivity of a conducting polymer depends on both its ability to transport charge carriers along the polymer backbone and for the carriers to hop between polymer chains. Most of the conducting polymers do not have good electrical conductivity in their native state and therefore they need to be doped with suitable dopant in order to achieve high conductivity [37].

The high sensitivity of polyacetylene to air and insolubility in many of the solvents impose a barrier on the use and processability of polyacetylene. This has led researchers to look for another class of conjugated polymers. Polyaniline (PANI), polypyrrole (PPY), polythiophene (PTP) and polyethylenedioxythiophene (PEDOT) are the four most commonly used conducting polymers. These polymers can be prepared either by a chemical method or an electrochemical method. A chemical synthesis approach involves the addition of an oxidant such as ammonium peroxydisulfate (APS) into the solution of the monomer (aniline in case of polyaniline). The oxidizing agent initiates the polymerization reaction to yield the polymer. On the other hand in the case of electrochemical method, mineral acids such as sulfuric acid, hydrochloric acid and other strong acids are commonly used for the synthesis of conducting polymers. Table 1.1 shows some of the important conducting polymers and their conductivities.

Polymer	Conductivity ( $\text{S m}^{-1}$ )
Polyacetylene	$10^3$ to $10^5$
Polyphenylene	1000
Poly( <i>p</i> -phenylene sulfide)	100
Poly( <i>p</i> -phenylene vinylene)	1000
Polypyrroles	100
Polythiophenes	100
Polyaniline	10

*Table 1.1 Some of the important conducting polymers and their conductivities*

## 1.2.2 Applications of conjugated polymers

A large volume of research is being carried out worldwide on structural modifications and functionalization for making conducting polymers potentially attractive materials for device applications. Since, conducting polymers with proper functionality respond to gaseous vapors at room temperature itself and can be deposited on a wide variety of substrates ranging from metallic to polymeric, they can find applications that prove to be difficult for conventional gas sensors which often require high-temperature operation. For this purpose one can take advantage of the conductivity of these polymers which includes the fascinating ability of these polymers to undergo a transition from insulating to conducting form.

The conducting polymers are easy to be prepared in nanostructured form such as nanorods, nanofibers etc. An improvement in the sensing ability was observed in the case of nanofibers of PANI than the conventional PANI [38]. Most of the polymers are insulators, a small addition of conducting polymer increases the conductivity and eliminates electrostatic charge. Conducting polymers can also be used as antistatic devices, using them as electricity dissipative additives. In contrast to carbon and inorganic metals, conducting polymers can preserve transparency and homogeneity when mixed with other polymers. The antistatic properties of conducting polymers prevent possible explosions during the movement of combustible fuels through polymeric transport lines. The static dissipation also eliminates data loss or device malfunction caused by sparks in electronic equipment. Conducting polymers also find important applications in modern optical devices such as organic light emitting diodes

(OLEDs) [37]. There are many advantages of conducting polymers based OLEDs *i.e.* wide angle of visibility, reduced power consumption, high image quality, low operational temperatures and smaller size. Conducting polymer electrodes can also be used for electromechanical actuators that allow the transformation of the electrical signal into the mechanical movement [37]. The idea of artificial muscles can be realized using PANI, PPY and other conducting polymers. Electromechanical actuators have numerous applications, for example, a device may control small orifice in a drug delivery reservoir implanted in human body. Conducting polymers can also be applied for electromagnetic shielding in the microwave frequency range. This application requires highly conducting conjugated polymers [37].

### 1.2.3 Metal and conducting polymer nanocomposites

PANI is a conducting polymer with multiple, switchable inherent oxidation states (Figure 1.6). There are several reports in the literature about conducting polymers based inorganic–organic nanocomposites because the inclusion of inorganic materials into the polymer matrix can introduce entirely new properties to the polymer. This can lead to new functional materials with the advantages of both the inorganic and the organic components. For example, metal-PANI [37,39-42] and inorganic-PANI [37,43-46] nanocomposites have been found to be useful for sensors, catalysts, photovoltaic devices, and magnetic materials.

Different metal particles e.g., Au [47,48], Ag [49,50], Pt [41,50] and Pd [49,50] can be directly deposited on the polymer by direct chemical or electrochemical redox reactions between polymer and metal cations.

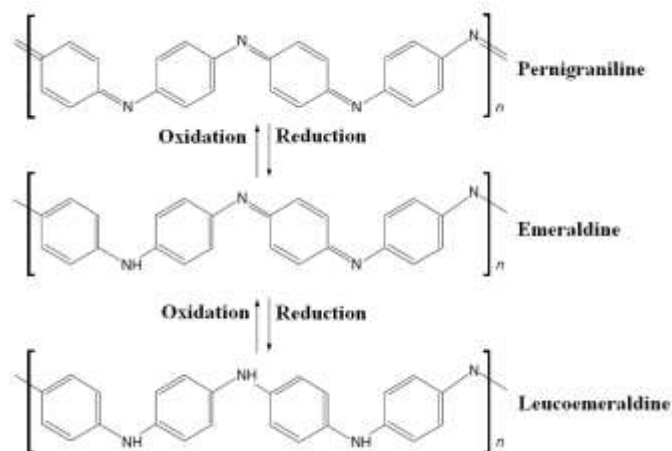


**Fig. 1.6** Different oxidation states of polyaniline

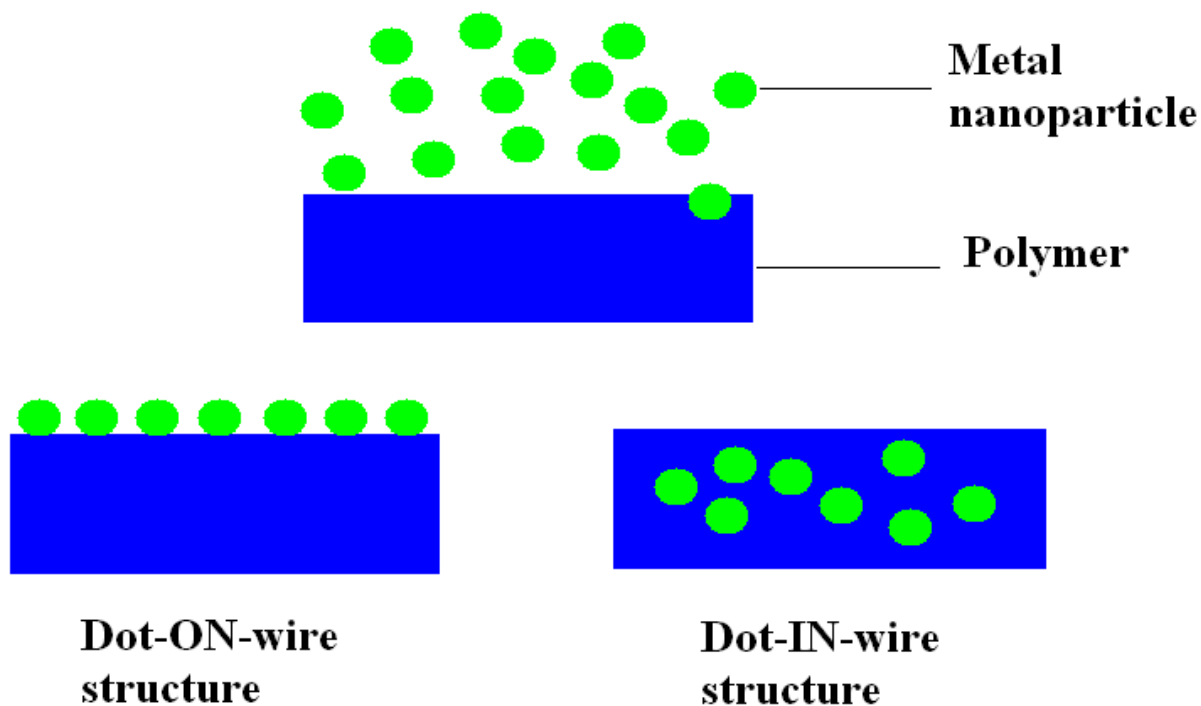


*Fig. 1.7 Two different structures for a metal and conducting polymers nanocomposites*

As shown in Figure 1.7, two types of structures are most commonly proposed in the literature for metal-conducting polymer nanocomposites [37], the first one is the dot-ON-wire structure and second one is the dot-IN-wire structure. In the former structure the metal nanoparticles are adsorbed (physical or chemical) or attached by a chemical bond on the surface of the polymer while in the latter the metal particles are impinged into the matrix of the polymer.

In this work we have synthesized metal-conducting polymer nanocomposites by using a novel electrochemical method. Palladium and gold were the metals used in this study. The nanocomposites were formed as a thin film on conducting substrates. We have studied the electrocatalytic activity of these nanocomposite films for electro-oxidation of small organic molecules such as ethanol, methanol and formic acid and also for hydrogen evolution reaction (HER). Such a study is useful in the development of fuel cell technology to meet the next generation energy demands.

### 1.3 Electrocatalysis for fuel cells

Electrocatalysis plays an important role in the context of energy conversion and storage. The electrocatalysis of fuel-cell reactions is a prominent area of research for both academics and in

industries. A simple definition of electrocatalysis, could be that “*It expresses the enhancement of electrochemical reaction rates by surface modifications of various kinds at the electrochemical active surface*”. An electrocatalyst is basically a catalyst, which participates in an electrochemical reaction and modifies or increases the rate of chemical reactions without being consumed in the process. In other words electrocatalyst in the context of the electrode process reduces the overpotential for the electrochemical reaction, bringing it closer to the thermodynamic equilibrium potential.

For any electrochemical reactions, the voltage applied across an electrolytic cell ( $\Delta V$ ) can be written as the following:

$$\Delta V = \Delta E + \eta + \Delta \Omega,$$

where  $\Delta E$  is the thermodynamic cell voltage depending on the electrode characteristics.  $\eta$  is the total overpotential which represents the additional energy required to carry out the reaction at practical rate and  $\Delta \Omega$  is the ohmic drop in the cell circuit. An electrocatalyst works in a way to bring down the overpotential ( $\eta$ ) required for the reaction. An increase in the rate of the reaction brought about by just enhancing the surface area is not the true electrocatalytic effect unless there is a modification of the nature of the surface active sites.

There are two basic parameters which determine the rate of an electrochemical reaction, for a given electrocatalyst. These parameters are linked with the geometric and electronic structure of the electrocatalyst. The geometrical effects determine how the geometrical structure of the catalyst material is responsible in bringing out the catalytic activity of the material. For example, the atoms on the primary surfaces of palladium metal  $\langle 100 \rangle$ ,  $\langle 110 \rangle$ , and  $\langle 111 \rangle$  are different, which causes an entirely different kind of interaction with reactant molecules at each plane [51].

As shown in Figure 1.8 (Source: Osada *et al.* reference 51) there is huge variation in the electrocatalytic activity on different planes of Pd for formic acid electro-oxidation. This can be understood because the bonding energy of reactant will be different in a molecule and on the metal surface atoms depending on the exposed metal surface geometry. In addition, if a metal is used in conjunction with another metal there will be a change in the surface structure and the catalytic activity will be affected.

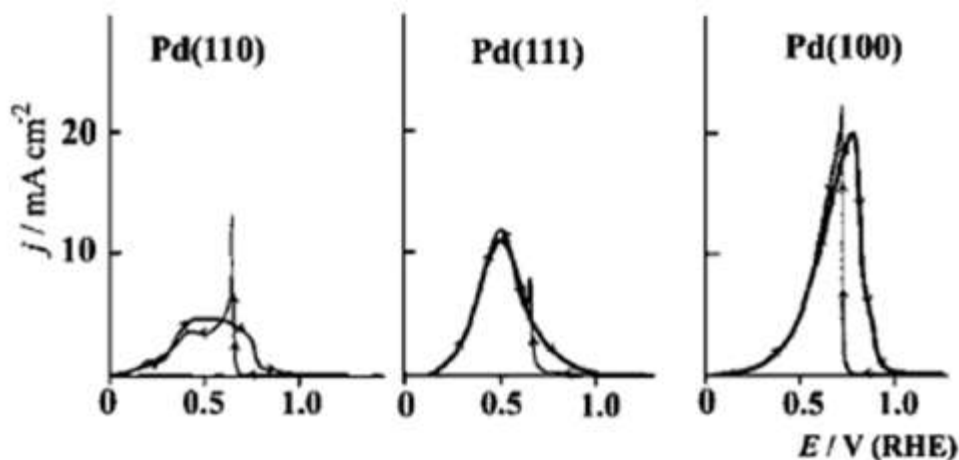


**Fig. 1.8** CV for the electro-oxidation of formic acid on low index planes of Pd in  $\text{HClO}_4$  (Source: Osada et al.[51])

Another noteworthy parameter that plays a crucial role in electrocatalysis is the electronic structure of the catalyst material. The electronic structure is described by the electronic orbitals of the catalyst atoms, especially the outer or valence electrons, which influence the catalytic properties most on the interaction with neighboring atoms. A majority of the electrocatalytic materials utilized for fuel cells are metals or more specifically the noble metals. These catalysts include platinum, iridium, ruthenium, palladium, gold and silver. Few of the non-noble elements have also demonstrated catalytic activity, often in combination with the noble elements, and they include nickel, iron, cobalt, chromium, vanadium, molybdenum, tin, tungsten and others. The most common electrocatalytic material is platinum metal because of its ability to function close to the thermodynamic potential.

There is huge interest in identifying the new catalytic materials which are cheaper and relatively more abundant. Volcano plots have been studied in the literature in order to understand the properties of any catalytic material. These are plots which show the maximum in the activity of a series of catalytic materials for a given value of the any property for example the heat of adsorption of the intermediate on the electrode surface with a linear decrease in either side of the plots. Figure 1.9 shows a typical volcano plot of electrocatalysis of hydrogen reaction. The property studied here is the enthalpy of hydrogen adsorption. From the figure we can see that Pt group metals have intermediate value of enthalpy of hydrogen adsorption and a high activity. This suggests that an intermediate value of enthalpy of hydrogen adsorption is required for

achieving high catalytic activity [52-54]. On Pt group metals, the chemisorption of hydrogen on the metal surface can easily remove the adsorbed oxygen with the formation of water.

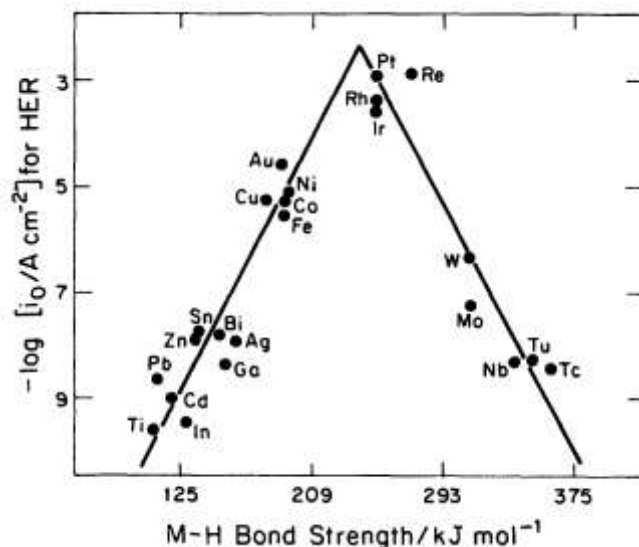


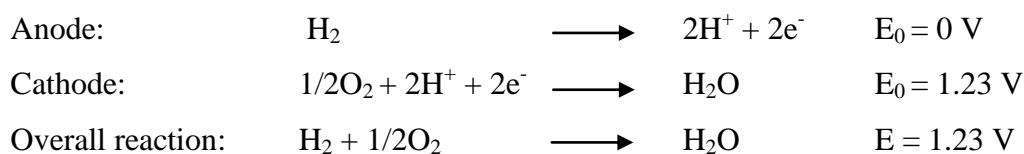
**Fig. 1.9** Volcano plot for the hydrogen evolution reaction (HER) for various pure metals (Source: Conway et al.[53])

Nanomaterials offer unique properties either used as electrodes or electrolytes in fuel cell devices. In the case of nanomaterials, which have very high surface area with small particle size the electronic structure of the surface atoms changes drastically and the catalytic properties improve. Nanomaterials of Pd, Au in combinations with other low cost materials have the potential to emerge as a substitute for Pt.

Fuel cell is basically an electrochemical device that converts chemical energy to electrical energy. In principle fuel cells operate in a way different from a battery in the sense that it does not run down or require recharging after use. However it produces electrical energy as long as the fuel is supplied. In a fuel cell, the fuel constantly flows into the cell so the cell never seizes, as long as the flow of fuel is maintained into the cell the electricity flows. A typical fuel cell consists of an electrolyte medium sandwiched between two electrodes. The first electrode or the anode is the place where electrochemical oxidation of fuel occurs while at other electrode or the cathode electrochemical reduction of oxidant takes place. Ionic species generated after the oxidation of the fuel are transported from anode to cathode through the ionically conducting but electronically insulating electrolyte membrane. This membrane also acts as a barrier between the fuel and oxidant. Electrons generated at the anode during oxidation have to pass through the

external circuit on their way to the cathode, where the reduction reaction occurs. This movement of electrons essentially creates the current. Since the fuel and oxidant do not mix at any point and no combustion takes place, the fuel cells are not limited by the Carnot efficiency and theoretically can yield 100% efficiency. However there are certain other issues which determine the efficiency of a fuel cell. Fuel cells are primarily classified according to the electrolyte material used. The choice of electrolyte material also governs the operating temperature of the fuel cell.

The most common type of a fuel cell is hydrogen-oxygen fuel cell. The chemical reaction in hydrogen oxygen fuel cell involves the following half-cell reaction schemes with the production of water.

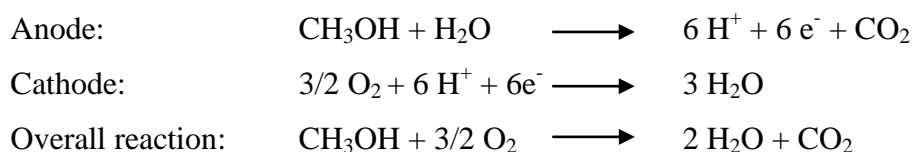


Even though the efficiency of a fuel cell is not limited by the Carnot efficiency, the operating efficiencies of the fuel cells are always lower than the theoretical values due to the overpotentials caused by activation, ohmic, and mass transport phenomena. All the available energy from the above reaction can be converted to electrical energy in an ideal process.

### 1.3.1 Electrocatalysis of small organic molecules

Due to the problems related to the processability, transmission and storage small chain alcohols such as methanol and ethanol, which are liquid at normal temperatures, have been used as the alternatives to hydrogen in fuel cells. The fuel cell devices that use these alcohols as fuel are called direct alcohols fuel cells (DAFCs). Direct methanol fuel cell (DMFCs) is the most common among the DAFCs. Methanol remains in liquid form from  $-97.0^\circ\text{C}$  to  $64.7^\circ\text{C}$  at atmospheric pressure, which is good enough to be used under all conditions. With higher energy density than hydrogen, methanol has become the most attractive fuel for fuel cell technology.

The half cell reactions in DMFC are following:



A great amount of work can be found on metal based catalytic materials for electrocatalysis [55-77]. For example the combination of different metal catalyst for methanol electrocatalysis have been studied [55-59]. Methanol oxidation reaction always yields carbon monoxide (CO), which strongly adsorbs on the platinum catalyst and reduces the catalytic surface area, which eventually deteriorates the performance of the cell. The addition of another metal for example ruthenium or gold is always useful in order to achieve CO tolerant catalytic material. According to the well known theory these metals produce hydroxyl ions which get adsorb on the catalyst and react with CO to form CO<sub>2</sub> [55-57]. Shukla *et al.* have studied the effect of tungsten on the electrocatalytic activity of Pt towards methanol electro-oxidation [58]. Interestingly in a recent report it was observed that Pt in combination with Ti and W is an excellent CO tolerant material [59].

Ross *et al.* have studied the effect of alloy on the electro-oxidation of methanol [60-62] in particular tin modified Pt electrode [61]. The effect of temperature on the activity of the Pt-Ru alloy was also studied [62]. Different aspects of the electrocatalysis were also studied by many researchers especially the poisoning of the electrode [63,64] and the synergistic effect in the electrocatalysis of methanol on Pt-Pd electrode [65].

In addition there are reports on the use of conjugated polymers and metal combinations for methanol electro-oxidation [66-71]. One of the early reports on the use of conjugated polymers appeared in a classic work by Kost *et al.* [69] wherein the Pt microparticles were dispersed in conducting polyaniline matrix and the modified electrode was found to be a good catalyst for hydrogen reduction and methanol electro-oxidation.

A majority of the electrocatalysis work is carried out with Pt as an electrocatalyst. However the high price of Pt has forced researchers to work on the alternate catalytic materials. In the present thesis we have studied the synthesis and applications of two different metals (Au and Pd) and conducting polymers combinations as the electrocatalyst materials for possible applications in fuel cell.

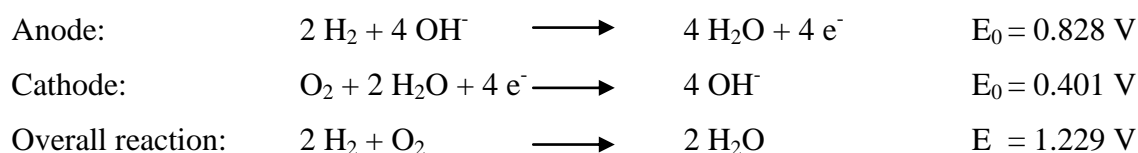
### **1.3.2 Alkaline fuel cells (AFCs)**

Alkaline fuel cells (AFCs) are fuel cells which use alkaline electrolytes separating the anode and cathode. Although fuel cells based on acidic electrolytes using Nafion, a perfluorinated polymer containing sulfonic acid side groups as a proton exchange membrane have received lot of

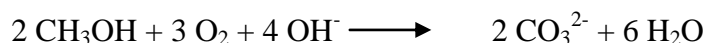
attention in the literature. However, alkaline electrolytes based fuel cells nevertheless have plenty of scope since fuel cells based on acidic electrolytes function mainly with Pt based catalysts and this dependency makes them more expensive [80-88]. However the AFCs can function with relatively less expensive metals such as Au, Ag and Ni too. In a report by Vercoe *et al.* it was observed that higher energy density fuel such as ethanol yields better results in AFCs than methanol [83,84]. There are many advantages associated with the AFCs which make them cost effective to manufacture than acidic electrolytes based fuel cells [81-84]. In AFCs a liquid alkaline electrolytes such as metal hydroxides e.g., potassium hydroxide is used, which reacts with CO<sub>2</sub> to form metal bicarbonates or carbonate salts. A sufficient amount of these salts can precipitate and irreversibly block the cathode thus acting as a poison and decreasing its electrolyte conductivity, which eventually results in a decline in the electrocatalytic performance. To avoid such problems, polymers with attached organic cations have been used as alkaline anion exchange membranes (AAEMs) because their cations can not aggregate with anions to form a crystal lattice [83,84]. This approach therefore is extremely useful for operation under alkaline conditions in the presence of CO<sub>2</sub>.

Figure 1.10 shows the schematic of an alkaline fuel cell where the charge carriers are hydroxyl ions which migrate from cathode to anode where the reaction with hydrogen produces water and electrons.

The reactions at both the electrodes can be written as following:



In the case of methanol as a fuel the reaction can be written as following:



It is clear from the reaction above that not only oxygen and methanol are consumed in the reaction but two hydroxyl ions are used per methanol molecule. This requires a procedure of electrolyte replenishment, which can be achieved by adding electrolyte with the consumption of the methanol [67].

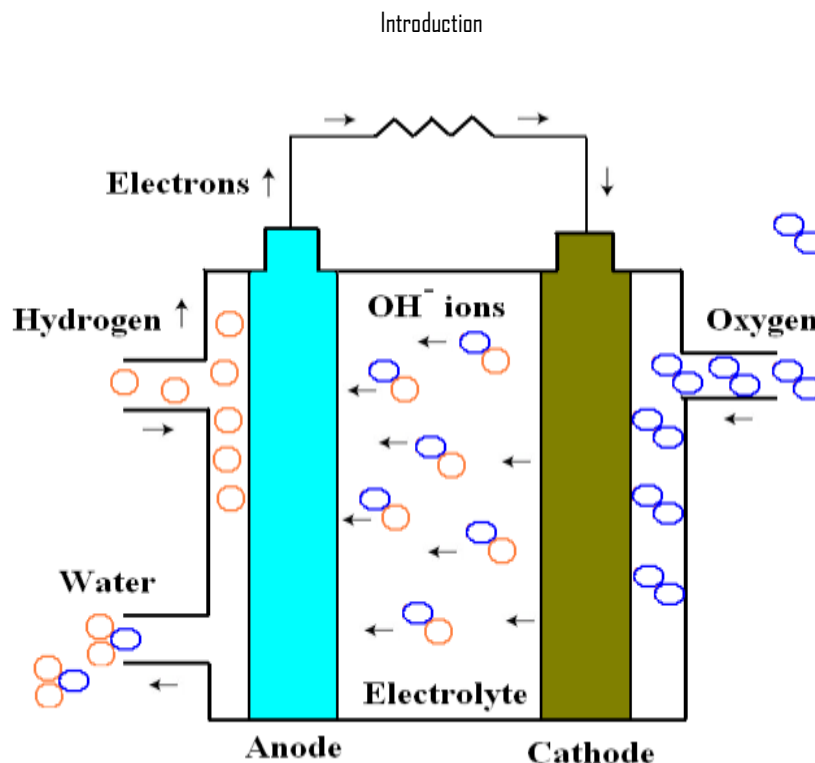


*Fig. 1.10 A schematic of an alkaline fuel cell.*

## 1.4 Aims and scope of the present thesis

The first part of the thesis deals with the electron transfer properties of ultrathin films formed by self-assembled monolayer, Langmuir-Blodgett films and layer-by-layer films. The thesis contains the study of the electron transfer properties of different composite films such as the LB film with a SAM or an LbL film in conjunction with SAM. We believe that the studies carried out during the course of this research investigation lead to a better understanding of the processes occurring during the electron transfer in different types of ultrathin films. The phenomenon of electron transport through composite thin films is very important not only from the commercial point of view but also in fundamental studies of electrochemical reactions especially in biological systems.

In the second part of the thesis we have explored electrocatalytic applications of the nanocomposite thin films of noble metals with conducting polymers. Different combinations of metals (gold and palladium) were studied with different conducting polymers. In the thesis work we have shown that the conducting polymers are a suitable matrix for the dispersion of the electrocatalyst material. The nanocomposites of metals and conducting polymers are shown as an efficient electrocatalyst material for oxidation of small organic molecules. The potential

application of the small organic molecules ranging from methanol and ethanol to formic acid as fuel in direct fuel cells have been explored and discussed in the thesis. We have focused more on the electrocatalysis in alkaline medium for potential applications in alkaline fuel cells. The alkaline fuel cells are relatively less explored by researchers but they have enormous applications as they can be used with relatively less expensive metal catalysis, which makes them cheaper to manufacture.

**Bibliography**

- [1] I. Langmuir, *J. Am. Chem. Soc.*, 39 (1917) 1848
- [2] G. Roberts, Langmuir-Blodgett Films, Plenum Press: New York, 1990.
- [3] C.D. Bain, E.B. Troughton, Y.T. Tao, J. Evall, G.M. Whitesides, R.G. Nuzzo, *J. Am. Chem. Soc.*, 111 (1989) 321.
- [4] M.D. Porter, T.B. Bright, D.L. Allara, C.E.D. Chidsey, *J. Am. Chem. Soc.*, 109 (1987) 3559.
- [5] A. Ulman, *J. Mat. Ed.*, 11 (1989) 205.
- [6] K.R. Stewart, G.M. Whitesides, H.P. Godfried, I.F. Silvera, *Surf. Sci.*, 57 (1986) 1381.
- [7] R.G. Nuzzo, D.L. Allara, *J. Am. Chem. Soc.*, 105 (1983) 4481.
- [8] E.B. Troughton, C.D. Bain, G.M. Whitesides, R.G. Nuzzo, D.L. Allara, M.D. Porter, *Langmuir*, 4 (1988) 365.
- [9] D.L. Allara, R.G. Nuzzo, *Langmuir*, 1 (1985) 45.
- [10] N.E. Schlotter, M.D. Porter, T.B. Bright, D.L. Allara, *Chem. Phys. Lett.*, 132 (1986) 93.
- [11] L.H. Dubois, B.R. Zegaski, R.G. Nuzzo, *Proc. Natl. Acad. Sci. U.S.A.*, 84 (1987) 4739.
- [12] L.H. Dubois, B.R. Zegarski, R.G. Nuzzo, *J. Am. Chem. Soc.*, 112 (1990) 570.
- [13] K.R. Stewart, G.M. Whitesides, H.P. Godfried, I.F. Silvera, *Surf. Sci.*, 57 (1986) 1381.
- [14] R.G. Nuzzo, E.M. Korenic, L.H. Dubois, *J. Chem. Phys.*, 93 (1990) 767.
- [15] M.M. Walczak, C. Chung, S.M. Stole, C.A. Widrig, M. D. Porter, *J. Am. Chem. Soc.*, 113 (1991) 2370.
- [16] R.G. Nuzzo, F.A. Fusco, D.L. Allara, *J. Am. Chem. Soc.*, 109 (1987) 2358.
- [17] R.G. Nuzzo, B.R. Zegarski, L.H. Dubois, *J. Am. Chem. Soc.*, 109 (1987) 733.
- [18] R.G. Nuzzo, L.H. Dobois, D.L. Allara, *J. Am. Chem. Soc.*, 112 (1990) 558.
- [19] Y. Li, J. Huang, R.T. McIver, J.C. Hemminger, *J. Am. Chem. Soc.*, 114 (1992) 2428.
- [20] C.A. Widrig, C. Chung, M.D. Porter, *J. Electroanal. Chem.*, 310 (1991) 335.
- [21] T.H. Silva, V. Garcia-Morales, C. Moura, J.A. Manzanares, F. Silva, *Langmuir*, 21 (2005), 7461.
- [22] S.V.P. Barreira, V. Garcia-Morales, C.M. Pereira, J.A. Manzanares, F. Silva, *J. Phys. Chem. B*, 108 (2004) 17973.
- [23] A. Liu , Jun-ichi Anzai, *Langmuir*, 19 (2003) 4043.
- [24] F.N. Crespilho, V. Zucolotto, O.N. Oliveira Jr. F.C. Nart, *Int. J. Electrochem. Sci.*, 1 (2006) 194.

- [25] U.K. Sur, V. Lakshminarayanan, *J. Coll. Interf. Sci.*, 254 (2002) 410.
- [26] V. Lakshminarayanan, U. K. Sur, *Pramana, J. Phys.*, 61 (2003) 361.
- [27] M. Brust, M. Walker, D. Bethell, D. J. Schriffin, R. Whyman, *J. Chem. Soc. Chem. Commun.*, 1994, 801.
- [28] W.H. Scouten, J.H.T. Luong, R.S. Brown, *Tr. Biotech.*, 13 (1995) 178.
- [29] M. Mrksich, G.M. Whitesides, *Annu. Rev. Biophys. Biomol. Struct.*, 25 (1996) 55.
- [30] J.J. Gooding, F. Mearns, W. Yang, J. Liu, *Electrocatalysis*, 15 (2003) 81.
- [31] T. Wink, S.J. van zuilen, A. Bult, W.P. Bennekom, *Analyst*, 122 (1997) 43R.
- [32] J.J. Gooding, D.B. Hibbert, *Tr., Anal. Chem.*, 18 (1999) 525.
- [33] N.K. Chaki, K. Vijayamohanan, *Biosensors and Bioelectronics*, 17 (2002) 1.
- [34] G.-Y. Liu, S. Xu, Y. Qian, *Acc. Chem. Res.*, 33 (2000) 457.
- [35] S. Kramer, R.R. Fuierer, C.B. Gorman, *Chem. Rev.*, 103 (2003) 4367.
- [36] P.M. Ajayan, L.S. Schadler, P.V. Braun, *Nanocomposite science and technology*, Wiley-VCH, 2003.
- [37] Kirchmeyer, S.; Reuter, K.; Simpson, J. C. in: T.A. Skotheim and J.R. Reynolds, (Eds) *Conjugated Polymers-Theory Synthesis Properties and Characterization* CRC Press Taylor & Francis Group Boca Raton, FL. 2007, 3rd Edition.
- [38] J.X. Huang, S. Virji, B.H. Weiller, R.B. Kaner, *J. Am. Chem. Soc.*, 125 (2003) 314.
- [39] P.R. Selvakannan, P.S. Kumar, A.S. More, R.D. Shingte, P.P. Wadgaonkar, M. Sastry, *Langmuir*, 20 (2004) 295.
- [40] J.A. Smith, M. Josowicz, J. Janata, *J. Electrochem. Soc.*, 150 (2003) E384.
- [41] J.G. Wang, K.G. Neoh, E.T. Kang, *J. Coll. Interf. Sci.*, 239 (2001) 78.
- [42] Y. Zhou, H. Itoh, T. Uemura, K. Naka, Y. Chujo, *Langmuir*, 18 (2002) 277.
- [43] S.N. Sawant, N. Bagkar, H. Subramanian, J.V. Yakhmi, *Philos. Mag.*, 84 (2004) 2127.
- [44] D.C. Schnitzler, M.S. Meruvia, I.A. Hummelgen, A.J.G. Zarbin, *Chem. Mater.*, 15 (2003) 4658.
- [45] D.C. Schnitzler, A.J.G. Zarbin, *J. Braz. Chem. Soc.*, 15 (2004) 378.
- [46] X.M. Sui, Y. Chu, S.X. Xing, C.Z. Liu, *Mater. Lett.*, 58 (2004) 1255.
- [47] T.K. Sarma, A. Chattopadhyay, *Langmuir*, 20 (2004) 4733.
- [48] T.K. Sarma, D. Chowdhury, A. Paul, A. Chattopadhyay, *Chem. Commun.*, 10 (2002) 1048.
- [49] J.X. Huang, S. Virji, B.H. Weiller, R.B. Kaner. *Chem. Eur. J.*, 10 (2004) 1314.

- [50] A.A. Antipov, G.B. Sukhorukov, Y.A. Fedutik, J. Hartmann, M. Giersig, H. Mohwald, *Langmuir*, 18 (2002) 6687.
- [51] N. Hoshi, K. Kida, M. Nakamura, M. Nakada, K. Osada, *J. Phys. Chem. B*, 110 (2006) 12480.
- [52] R. Parsons, *Trans. Faraday Soc.*, 34 (1958) 1053.
- [53] B. E. Conway, *Electrochemical Processes Involving H Adsorbed at Metal Electrode Surfaces Interfacial Electrochemistry: Theory, Experiment, and Applications* Ed: A. Wieckowski, M. Deccar Inc. New York.
- [54] S. Trasatti, *J. Electroanal Chem.*, 39 (1972) 163.
- [55] G. Selvarani, S. V. Selvaganesh, S. Krishnamurthy, G.V.M. Kiruthika, P. Sridhar, S. Pitchumani, A.K. Shukla *J. Phys. Chem. C*, 113 (2009) 7461.
- [56] J.B. Goodenough, R. Manoharan, A.K. Shukla, K.V. Ramesh, *Chem. Mater.*, 1 (1989) 391,
- [57] H.A. Gasteiger, N. Markovic, P.N. Ross Jr., E.J. Cairns, *J. Phys. Chem.*, 97 (1993) 12020.
- [58] A.K. Shukla, M.K. Ravikumar, S. Aricò, G. Candiano, V. Antonucci, N. Giordano, A. Hamnett, *J. Appl. Electrochem.*, 25 (1995) 528.
- [59] D. Wang, C. V. Subban, H. Wang, E. Rus, F. J. DiSalvo, H. D. Abruna *J. Am. Chem. Soc.*, 10.1021/ja102931d.
- [60] P.N. Ross, *Electrochim. Acta*, 36 (1991) 2053.
- [61] A.N. Haner, P.N. Ross, *J. Phys. Chem.*, 95 (1991) 3740.
- [62] H.A. Gasteiger, N. Markovic, P.N. Ross Jr., E.J. Cairns, *J. Electrochem. Soc.*, 141 (1994) 1795.
- [63] A. Hamnett, S.A. Weeks, B.J. Kennedy, G. Troughton, P.A. Christensen, *Phys. Chem. Chem. Phys.*, 94 (1990) 1014.
- [64] S.G. Sun, J. Clavilier, *J. Electroanal. Chem.*, 236 (1987) 95.
- [65] F. Kadirgan, B. Beden, J.M. Leger, C. Lamy, *J. Electroanal. Chem.*, 125 (1981) 89.
- [66] B. Rajesh, T.K. Ravindranathan, J.-M. Bonard, N. Xanthopoulos, H.J. Mathieu, B. Viswanathan, *Electrochemical and Solid-State Letters*, 5 (2002) E71.
- [67] B. Rajesh, T.K. Ravindranathan, J.-M. Bonard, H.J. Mathieu, N. Xanthopoulos, B. Viswanathan, *Chem. Commun.*, 9 (2003) 2022.
- [68] C.T. Hable, M.S. Wrighton, *Langmuir*, 7 (1991) 1305.
- [69] K.M. Kost, D.E. Bartak, B. Kazee, T. Kuwana, *Anal. Chem.*, 60 (1988) 2379.

- [70] K.R. Prasad, N. Munichandraiah, *J. Power Sources*, 103 (2002) 300.
- [71] S. Patra, N. Munichandraiah, *Langmuir*, 25 (2009) 1732.
- [72] S. Gilman, *J. Phys. Chem.* 68 (1964) 70.
- [73] O.A. Petry, B.I. Podlovchenko, A.N. Frumkin, H. Lal, *J. Electroanal. Chem.* 10 (1965) 253.
- [74] V.S. Bagotzky, Yu.B. Vassilyev, *Electrochim. Acta*, 12 (1967) 1323.
- [75] M. Watanabe, S. Motoo, *J. Electroanal. Chem.*, 60 (1975) 267.
- [76] A. Wieckowski, J. Sobkowski, *J. Electroanal. Chem.*, 63 (1975) 365.
- [77] M.M.P. Janssen, J. Moolhuysen, *Electrochim. Acta*, 21 (1976) 869.
- [78] B.D. McNicol, R.T. Short, *J. Electroanal. Chem.*, 81 (1977) 249.
- [79] P.A. Attwood, B.D. McNicol, R.T. Short, *J. App. Electrochem.*, 10 (1980) 213.
- [80] B. Beden, F. Kadirgan, C. Lamy, J.M. Leger, *J. Electroanal. Chem.*, 142 (1982) 171.
- [81] S. Lu, J. Pan, A. Huang, L. Zhuang, J. Lu, *Proc. Nat. Ac. Sci.*, 105 (2008) 20611.
- [82] N.J. Robertson, H.A. Kostalik, T.J. Clark, Paul F. Mutolo, H.D. Abruna, G.W. Coates *J. Am. Chem. Soc.*, 132 (2010) 3400.
- [83] J.R. Varcoe, R.C.T. Slade, E. L.H. Yee, S.D. Poynton, D.J. Driscoll, D.C. Apperley, *Chem. Mater.*, 19 (2007) 2686.
- [84] J.R. Varcoe, R.C.T. Slade, G.L. Wright, Y. Chen, *J. Phys. Chem. B*, 110 (2006) 21041.
- [85] M.R. Hibbs, M.A. Hickner, T.M. Alam, S.K. McIntyre, C.H. Fujimoto, C.J. Cornelius, *Chem. Mater.*, 20 (2008) 2566.
- [86] E. Agel, J. Bouet, J.F. Fauvarque, *J. Power Sources*, 101 (2001) 267.
- [87] G.F. McLean, T. Niet, S. Prince-Richard, N. Djilali. *International Journal of Hydrogen Energy*, 27 (2002) 507.
- [88] C. Bianchini, P.K. Shen, *Chem. Rev.*, 109 (2009) 4183.

## Chapter 2

### Experimental Methods

*This chapter deals with the description, instrumentation and basic principles of several experimental techniques that have been used during the thesis work. This chapter also gives the details of all the chemicals used in the thesis work. The experimental techniques are broadly classified into three types as electrochemical, imaging and spectroscopic techniques. Among the electrochemical techniques, we have extensively used DC techniques like cyclic voltammetry (CV), chronoamperometry (CA) and chronopotentiometry (CE), and ac technique like electrochemical impedance spectroscopy (EIS). For the topographical information of the surfaces, scanning tunneling microscopy (STM) and atomic force microscopy (AFM) were used. Scanning electron microscopy (SEM) was also used for imaging the nanocomposite films. Grazing angle Fourier transform infrared spectroscopy, UV-visible spectroscopy, photoluminescence spectroscopy and X-ray photoelectron spectroscopy (XPS) were used to characterize some of the materials and thin film coatings.*

## 2.1 Introduction

This chapter describes the experimental techniques used in this work. While mentioning the specific instruments used and the configuration employed for different studies, the chapter also deals with the principles as well as the salient features of the techniques and their potential utility in the studies of this nature.

## 2.2 Electrochemical cell and electrodes

A conventional three-electrode electrochemical cell was used for performing the electrochemical experiments. The cell is made up of glass with a Teflon lid machined to fit with the B-55 size neck. The lid was made to accommodate the working, counter and reference electrodes. In addition it also has the provision of inlet and outlet to allow the flow of inert gas to deaerate the cell containing the electrolytic solution. All the electrodes were fitted with a ground joint of size B-14 to use in the cell arrangement. The counter electrode is a platinum foil of large surface area, which was sealed to a glass tube. The reference electrode is a saturated calomel electrode (SCE), which was kept very close to the working electrode to minimize the ohmic drop. The working electrode was held by an electrode holder, which is a long gold plated brass rod with a slot at one end where the working electrode was held using screws. This sample holder was fixed to a Teflon B-14 cone that was fixed to the socket of the central ground joint.

In our study, either the evaporated gold sample with predominantly Au (111) orientation or a polycrystalline gold (disc) electrode was used as a working electrode. A platinum foil of large surface area was used as a counter electrode. A saturated calomel electrode (SCE) was used as a reference electrode in the aqueous medium whereas a silver rod was used as a quasi-reference electrode in the experiments involving non-aqueous solvents. This electrode has a stable potential and is also free from any liquid junction potential.

All the working electrodes used for the experimental studies were designed and fabricated in our laboratory. The gold disk electrode was fabricated by sealing of a 99.99% pure gold wire (obtained from Arora Mathey, Kolkata, India) of 0.5 mm diameter with the soda lime glass having the thermal expansion coefficient close to that of gold. Prior to use, the gold disc electrode was polished with emery paper, followed by polishing in aqueous slurries of progressively finer alumina of sizes ranging from 1.0 to 0.3 to 0.05  $\mu\text{m}$  on a microcloth

Gold (~100nm thickness) on glass with chromium underlayers (2-5) nm was used as the substrate for SAM, LB, LbL and other nanocomposite films formation and characterization. The substrate was heated to 350°C during gold evaporation under a vacuum pressure of  $2 \times 10^{-5}$  mbar, a process that normally yields a deposit with predominantly Au (111) orientation. The evaporated gold samples with well defined area (about 0.2 cm<sup>2</sup>) were used as an electrode for electrochemical studies. A conventional three-electrode electrochemical cell was used for electrochemical studies. A platinum foil of large surface area as the counter electrode and a saturated calomel electrode (SCE) as a reference electrode were used. The cell was cleaned thoroughly before each experiment and kept in a hot air oven at 100°C for at least 1 hour for drying before the start of the experiment. Evaporated Au strips or gold disc electrodes were used for SAM formation and were pretreated with “piranha” solution (3:1 conc. H<sub>2</sub>SO<sub>4</sub>:H<sub>2</sub>O<sub>2</sub>). SAMs were prepared by immersing the gold substrate in thiol solution in ethanol 12 hours. After the adsorption of thiol, the substrates were rinsed with ethanol, distilled water and finally with Millipore water and used for the further experiments.

### 2.3 Electrochemical studies

Electrochemical studies were carried out by cyclic voltammetry (CV) and electrochemical impedance spectroscopy (EIS). The barrier properties of the thin films modified electrodes in aqueous system have been evaluated by studying the electron transfer reaction using the potassium ferrocyanide/potassium ferricyanide couple ( $[\text{Fe}(\text{CN})_6]^{3-/4-}$ ) and *hexaammineruthenium (III) chloride* as redox probes.

CV was performed in redox probes along with 1 M NaF as a supporting electrolyte. The EIS measurements were carried out by applying an ac voltage of 10 mV amplitude at the formal potential of the redox couple in a solution containing equal concentrations of both the oxidized and reduced forms of the redox couples, for example 1 mM potassium ferrocyanide and 1mM potassium ferricyanide in 1 M NaF. A frequency range of 100 kHz to 100 mHz was used for impedance measurements. The interfacial capacitance measurements were carried out in a pure supporting electrolyte of 1.0 M NaF without any redox species. All the electrochemical studies were performed at 25<sup>0</sup> C. For electrochemical studies in nonaqueous system, 1 mM ferrocene solution was used in ethanol with 0.1 M LiClO<sub>4</sub> as a supporting electrolyte.

## 2.4 Instrumentation

CV was carried out using an EG&G potentiostat (model 263A) interfaced to a PC through a GPIB card. The potential ranges and scan rates used are shown in the respective diagrams. For EIS studies, the potentiostat was used along with an EG&G 5210 lock in amplifier controlled by the Power Sine software.

AFM and STM images were obtained at 25 °C in air. We have used a Pico plus (Agilent) AFM in tapping mode with a silicon tip. STM studies were carried out using a homemade STM in ultra low noise mode [1]. The STM was operated in constant current mode of 0.5 nA at a bias voltage of +100 mV. An electrochemically etched tungsten tip was used as the probe.

The images shown here are plane corrected and optimally Fourier filtered using scanning probe image processor (SPIP) software (Image Metrology, Denmark). To ensure that the images shown are representative of the monolayer morphology, multiple images were taken at different locations and scan ranges.

The FTIR spectra were obtained using an FTIR 8400 model (SHIMADZU) with a fixed 85° grazing angle attachment (FT-85; Thermo Spectra-Tech). SEM and EDAX studies were carried out using FESEM (Zeiss). In the case of Pd-PANI film for XPS studies, MULTILAB 2000 (THERMO SCIENTIFIC, UK) with Mg K alpha source at a pass energy of 10 eV was employed.

## 2.5 Electrochemical techniques

### 2.5.1 Cyclic voltammetry

Cyclic voltammetry, also known as CV, is one of the most extensively used electrochemical potential sweep techniques. The simplest of potential sweep techniques is linear sweep voltammetry (LSV), which involves sweeping the electrode potential between the limits  $V_1$  and  $V_2$  at a known sweep rate ( $v$ ) and measuring the current flow through the electrochemical system. In the case of CV the initial potential sweep is similar to that in LSV, but after reaching the potential  $V_2$  instead of terminating the scan, the sweep is reversed at the same scan rate as the forward sweep. A typical potential-time profile used in CV is shown in the Figure 2.1. In CV, the potential of the working electrode sweeps between the initial,  $V_1$  and final  $V_2$  values in the forward and reverse direction, and the corresponding current at the working electrode is

measured. Hence CV represents the current vs. potential profile in the electrochemical cell. The current arises due to two reasons, first is faradaic current resulting from various electrochemical processes like redox reactions, adsorption etc and second is due to the double layer charging of the electrode-electrolyte interface leading to the capacitance current [2,3].

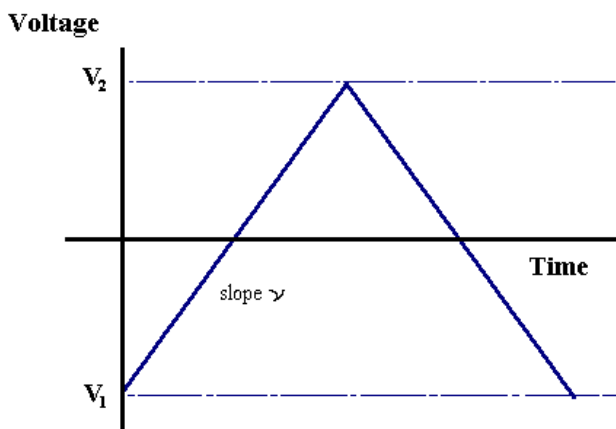


**Fig. 2.1** A typical potential vs. time curve used in case of cyclic voltammetry

A plot of measured current as a function of applied potential is known as cyclic voltammogram from which the potential corresponding to different processes can be obtained. From the dependence of peak current on the sweep rate, information regarding coupled homogeneous reactions, adsorption, kinetic parameters and the mechanism of different heterogeneous reactions occurring on the electrode surface can be obtained. The shape of the cyclic voltammogram depends on the type of redox reactions. Figure 2.2 shows a typical cyclic voltammogram for a reversible one-electron transfer process.

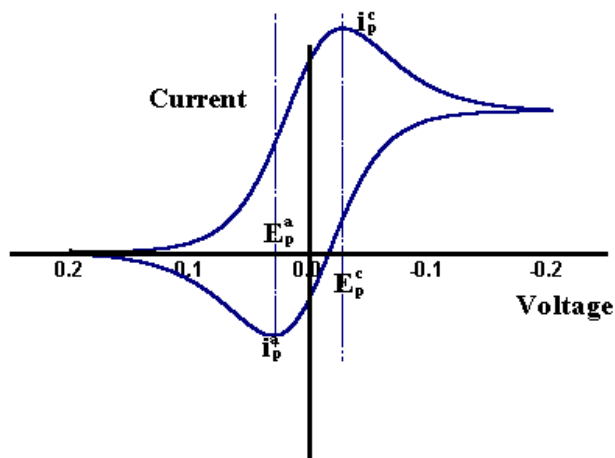
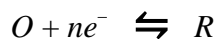


**Fig. 2.2** A typical current vs. voltage curve obtained for cyclic voltammetry

For a typical reversible one-electron redox reaction of the type;



where O is the oxidised species and R is the reduced species, the rate of charge transfer is always greater than the rate of mass transfer at all potentials which means that the redox reaction is under diffusion control. The ratio of concentrations of oxidant and reductant species of a reversible reaction is given by the Nernst equation and a concentration gradient exists within the region near the electrode surface known as Nernst diffusion layer, where the concentration gradient of the electroactive species is linear. The Nernstian equilibrium is always maintained at the electrode surface and at all the potentials. Based on this, the shape of current-potential profile for a one-electron reversible redox reaction, as shown in Figure 2.2, can be explained as follows. When the potential of the electrode is made more negative, at a characteristic potential for the redox species, the surface concentration of the reactant O decreases progressively due to reduction, thereby increasing the concentration gradient which leads to an increase in the current. Therefore the surface concentration of O decreases from its bulk value in order to satisfy the Nernst equation and a concentration gradient is setup. As a result, there is a flow of current proportional to this concentration gradient at the electrode. Due to diffusion of ions, the concentration gradient does not remain constant and it starts to decrease. At the same time, the electrode potential is also continuously changing leading to a further decrease of surface concentration of O until it effectively reaches zero. Once the concentration of O reaches zero, the gradient decreases due to the accumulation of reduced species R, in the vicinity of the electrode surface (relaxation effect) and hence the current flow also decreases. Overall, this behaviour gives rise to a peak shaped current potential profile as shown in Figure 2.2. Using similar arguments used for the forward sweep, it can be shown that the current change on reverse sweep also exhibit a peak shaped response but with an opposite sign. On increasing the sweep rate, the concentration gradient as well as the current resulting from it also increases due to the shorter time scale of the experiment leading to less relaxation effect. The peak current density  $I_p$  of the cyclic voltammogram is related to various parameters by the following relationship:

$$I_p = -0.4463 nF \left[ \frac{nF}{RT} \right]^{1/2} C_o^\infty D^{1/2} \nu^{1/2}$$

where,  $I_p$  is the peak current density in  $A/cm^2$   
 $n$  is the number of electrons involved in the redox reaction

F is Faraday constant

R is gas constant

T is the absolute temperature

$C_o$  is the concentration of reactant O in mol/cm<sup>3</sup>

D is the diffusion coefficient in cm<sup>2</sup>/s

$\nu$  is the sweep rate in Vs<sup>-1</sup>

This equation is known as the Randles-Sevcik equation and at a temperature of 25<sup>0</sup>C this equation reduces to the form given as follows,

$$I_p = -(2.69 \times 10^5)n^{3/2}C_o^\infty D^{1/2}\nu^{1/2}$$

From the above equation, it can be noted that the peak current density ( $I_p$ ) of the reversible reaction is directly proportional to the concentration of the electroactive species, square root of the diffusion coefficient and also to the square root of the scan rate. The sign of the current is negative because it is the current for cathodic reaction (as denoted by the convention followed).

A test of reversibility of the electrochemical system is to check whether a plot of  $I_p$  as a function of  $\nu^{1/2}$  is both linear and passes through the origin or alternatively ( $I_p / \nu^{1/2}$ ) is constant. If this is found to be true then further diagnostic tests, which are given below can be applied to verify the reversible nature of the given electrochemical system. For a reversible system the following are the diagnostic tests [3].

1.  $\Delta E_p = |E_p^A - E_p^C| = 59/n$  mV ( $E_p^A$  and  $E_p^C$  are the peak potentials of anodic and cathodic reactions respectively)
2.  $|E_p - E_{p/2}| = 59/n$  mV
3.  $|I_p^A / I_p^C| = 1$  ( $I_p^A$  and  $I_p^C$  are the peak currents of anodic and cathodic reactions respectively)
4.  $I_p \propto \nu^{1/2}$
5.  $E_p$  is independent of  $\nu$

Apart from the reversible system the CV can also be used to find out the quasi-reversible and irreversible nature of the electrochemical system. There are also diagnostic tests for these systems to verify the quasi-reversibility and irreversibility of the given system.

We have extensively used CV in the present study especially in order to check the electron transfer blocking behaviour of the different thin film modified electrodes in aqueous and non-aqueous systems.

## 2.5.2 Electrochemical impedance spectroscopy

Electrochemical impedance spectroscopy (EIS) is basically an ac technique for the electrochemical studies. In contrast to other electrochemical techniques such as CV, the EIS measurements involve essentially a small perturbation of the electrode potential from the equilibrium potential or desired dc potential by the application of a sinusoidal signal of 5-10 mV peak-to-peak amplitude in a range of frequencies and measuring the response of the electrochemical system. Usually, the response in terms of current to the perturbation, differs in phase and amplitude from the applied voltage signal. Figure 2.3 shows the sinusoidal signal of perturbation and response of the electrochemical system. The measurement of phase difference and amplitude of the response signal compared to the applied signal over a wide frequency range can be used for the analysis of different electrode processes like double layer charging, kinetics of redox reactions, diffusion of the redox probes, homogeneous and heterogeneous electron transfer reactions and coupled chemical and redox reactions. The impedance spectroscopy has been extensively used in the study of corrosion, battery, membranes, ionic solids, solid electrolytes, chemically modified electrodes and template deposited porous electrodes. In many of the measurements involving the fast electron transfer reactions, the information has to be obtained at very short times, otherwise diffusion rather than the kinetics becomes the rate determining process. In such a case, the ac techniques are widely used to determine the rate constant for the fast redox reactions.

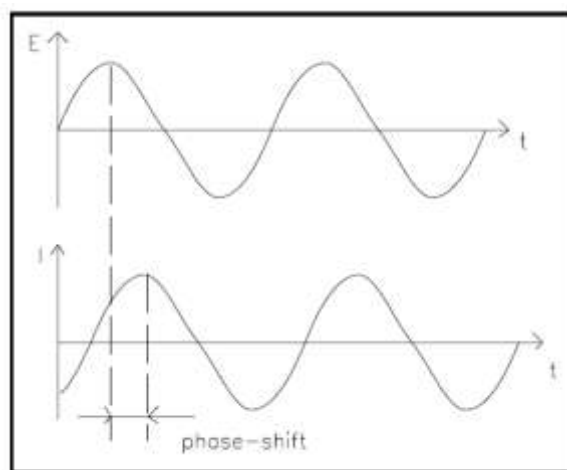


**Fig. 2.3** Schematic representation of a sinusoidal applied perturbation ( $E$ ) and corresponding current response ( $I$ )

Due to the small perturbation, the system is in the linear regime and the advantage lies in the ability to treat the response theoretically using the linear current-potential characteristics. Since, the working region in this method is very close to the equilibrium, the detailed knowledge about the behaviour of the current-voltage response over a large range of overpotential is not required. This simplifies the treatment of kinetics and diffusion equations. Using this method, the high precision measurements can be made because the response is indefinitely steady and therefore can be averaged over a long period. Usually, a comparison is made between the electrochemical cell and an equivalent circuit, which contains a combination of resistors and capacitors that are assumed to behave like an electrochemical cell under consideration. The aim of the impedance measurements is to interpret these equivalent circuits and the values determined using these circuits, in terms of the interfacial phenomena occurring at the electrode-solution interface. The impedance spectroscopy is frequently used for the evaluation of heterogeneous charge transfer parameters and to study the double layer structure.

The electrochemical response of a cell to an ac perturbation can be analysed by the knowledge of fundamental principles of ac circuits. If a sinusoidal signal of voltage  $V = V_0 \sin(\omega t)$  is applied to an electrical circuit that contains a combination of resistors and capacitors, the response is a current, which is given by,  $I = I_0 \sin(\omega t + \phi)$ , where  $V_0$  is the maximum amplitude,  $I_0$  is the maximum current,  $\omega$  is the angular frequency and  $\phi$  is the phase angle between the perturbation and response. The proportionality factor between  $V$  and  $I$  is known as the impedance  $Z$ . In phasor terms the rotating vectors are separated in the polar diagram by the angle. In the case of a pure resistor,  $R$ , the phase angle  $\phi$  is zero. According to Ohm's law,  $V = IR$ , which leads to  $I = V_0 \sin \omega t / R$ . There is no phase difference between the applied potential and the response current. For a pure capacitor,  $C$ , the current  $I$  is given by,  $I = C dV / dt$ .

On substituting the value of  $V$  as  $V_0 \sin(\omega t)$  and differentiating, the equations become;

$$I = \omega C V_0 \sin(\omega t + \pi/2)$$

$$I = V_0 \sin(\omega t + \pi/2) / X_C$$

where  $X_C = (\omega C)^{-1}$  is known as the capacitive reactance. Here we find that the phase angle is  $\pi/2$ , implying that the current leads the potential by  $90^\circ$  or  $\pi/2$  in the case of a pure capacitor. Similarly, for a circuit element containing a pure inductance, the potential leads the current by  $90^\circ$  or  $\pi/2$ . In general, an electrode-solution interface can be considered as an impedance to a

small sinusoidal excitation. The impedance of such kind of electrochemical interface is a complex function,  $Z(\omega)$  that can be expressed either in polar coordinates or in Cartesian coordinates, as shown below:

$$Z(\omega) = |Z|e^{j\phi}$$

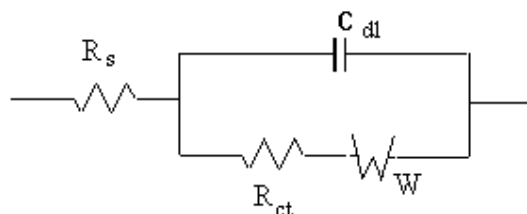


**Fig. 2.4** A simple Randle's equivalent circuit for a diffusion controlled reaction

$$Z(\omega) = Z'(\omega) + j Z''(\omega)$$

$$|Z|^2 = |Z'_{re}|^2 + |Z''_{im}|^2$$

where  $Z'_{re}$  and  $Z''_{im}$  are the real and imaginary components of the impedance.

The phase angle  $\phi$  can be expressed as,

$$\phi = \text{Arctan} [Z''_{im}/Z'_{re}] = \text{Arctan} [Z''(\omega)/Z'(\omega)] \text{ and}$$

$$Z_{re} \text{ or } Z'(\omega) = |Z| \cos \phi$$

$$Z_{im} \text{ or } Z''(\omega) = |Z| \sin \phi$$

Hence the electrode-electrolyte interface of the electrochemical cell can be represented by a suitable equivalent circuit consists of resistors and capacitors that pass current with the same amplitude and the same phase angle under a given excitation. In Figure 2.4 an equivalent circuit popularly known as Randle's equivalent circuit for a diffusion controlled electron transfer reaction is shown which contains the solution resistance,  $R_s$ , the double layer capacitance  $C_{dl}$ , the charge transfer resistance,  $R_{ct}$  and the Warburg impedance  $W$ , which is related to the diffusion of the redox probe.

The total current on the working electrode is obtained by the sum of distinct contributions from the faradaic current  $I_f$  and the double layer charging current  $I_c$ . The double layer capacitance arises from the charges stored at the electrode-electrolyte interface. This double layer structure closely resembles a pure capacitor and hence it is represented by the element  $C_{dl}$  in the equivalent circuit. The faradaic impedance  $Z_f$  can be separated into two components namely, the charge transfer resistance,  $R_{ct}$  and the Warburg impedance,  $W$ . The charge transfer

resistance,  $R_{ct}$  denotes a resistance offered to the electron transfer process and  $W$  represents resistance to the mass transfer process or diffusion.  $W$  depends on the frequency of the perturbation.

At high frequencies, the Warburg impedance is small because the reactants do not have to diffuse very far. In contrast, at low frequencies, the diffusing reactants have to move very far, thereby increasing the Warburg impedance. The uncompensated solution resistance denoted by  $R_s$  exists between the working electrode and the reference electrode. In the equivalent circuit representation, the uncompensated solution resistance,  $R_s$  is inserted as a series element since all the current has to pass through this element.

For a planar diffusion, the value of  $R_{ct}$  can be expressed as;

$$R_{ct} = RT/nFI_0$$

where  $I_0$  is the exchange current density. The solution resistance  $R_s$  is given by the following expression;

$$R_s = x/\kappa A$$

where  $x$  is the distance of the capillary tip from the electrode,  $\kappa$  is the conductivity of the solution and  $A$  is the area of the electrode. The values of  $R_{ct}$  and  $W$  indicate whether a redox reaction is charge-transfer controlled or diffusion controlled reaction. For reactions with large  $I_0$  value,  $R_{ct}$  will be proportionately less and dominated by  $W$  leading to a diffusion controlled reaction. On the other hand, for very small  $I_0$  value, where the kinetics of the reaction is very less,  $R_{ct}$  will be very high, that results in a kinetically controlled reaction. The total analysis of the impedance is known as complex plane impedance analysis. Randle's equivalent circuits are used for the representation of the elements involved in the circuits which are series and parallel combination of the different elements like capacitors and resistors. This has two limiting cases. At low frequencies, as  $\omega \rightarrow 0$ , the real and imaginary parts of impedance are given by,

$$Z' = R_s + R_{ct} + \sigma \omega^{-1/2}$$

$$Z'' = \sigma \omega^{-1/2} + 2\sigma^2 C_{dl}$$

where

$$\sigma = \left( \frac{RT}{\sqrt{2}n^2F^2AD^{1/2}} \right) \left( \frac{1}{C_o^\infty} + \frac{1}{C_R^\infty} \right)$$

in which,  $D$  is the diffusion coefficient of the species in solution,  $A$  is the area of the electrode,  $C_0$  and  $C_R$  are the bulk concentrations of the oxidised and reduced species. On rearranging these equations, we get,

$$Z'' = Z' - R_s - R_{ct} + 2\sigma^2 C_{dl}$$

This is the equation of a straight line of unit slope and with an intercept on the real  $Z'$  axis is given by,

$$R_s + R_{ct} - 2\sigma^2 C_{dl}$$

At high frequencies where the Warburg impedance is negligible in comparison to  $R_{ct}$ , the two components are represented by,

$$Z' = R_s + R_{ct} / (1 + \omega^2 R_{ct}^2 C_{dl}^2)$$

$$\text{and } Z'' = C_{dl} R_{ct}^2 \omega / (1 + \omega^2 R_{ct}^2 C_{dl}^2)$$

Eliminating  $\omega$  using these two equations gives,

$$(Z' - R_s - R_{ct}/2)^2 + (Z'')^2 = (R_{ct}/2)^2$$

which is the equation of a circle with center at  $Z' = R_s + R_{ct}/2$  and a radius of  $R_{ct}/2$ . A plot of the whole expression for  $Z'$  versus  $Z''$ , which is known as Cole-Cole plot or Nyquist plot, for a kinetically controlled and a diffusion controlled reactions are shown in Figure 2.5.

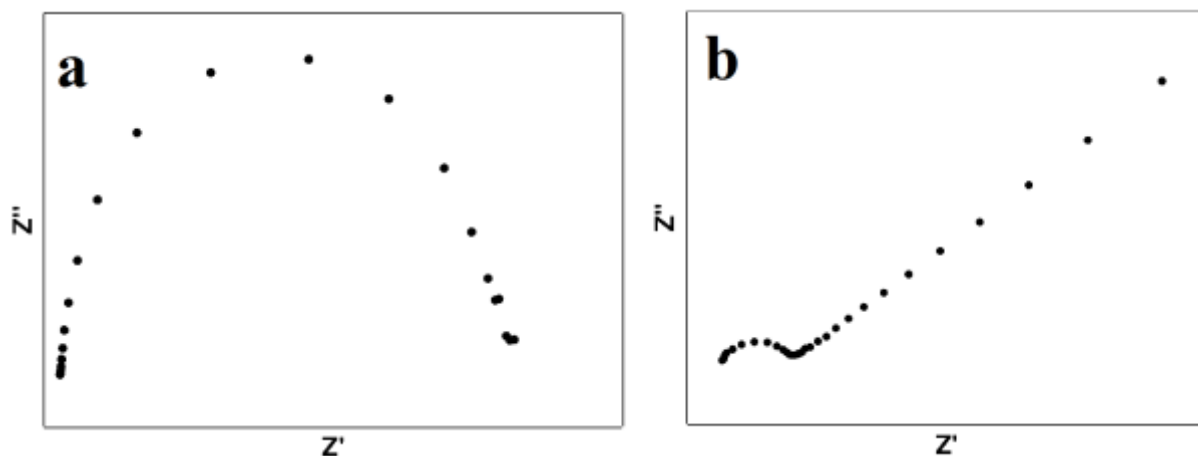


**Fig. 2.5** Nyquist plot for (a) kinetically controlled reaction and (b) diffusion controlled reaction

The Cole-Cole plot of a charge transfer controlled reaction shows a semicircle and it is obtained by plotting the values of  $Z'$  and  $Z''$  at different frequencies. It is also known as the Nyquist plot. At infinite frequency,  $Z''$  approaches zero as the capacitance in the equivalent circuit offers a very little impedance. At low frequencies, the impedance is purely resistive,

because the reactance of C is very large. The solution resistance has the effect of translating the semicircle on the  $Z'$  axis.  $R_s$  can be determined by reading out the real axis value at the high frequency intercept.  $C_{dl}$  can be obtained from the maximum value of  $Z''$  in the semicircular region where  $\omega = 1/R_{ct}C_{dl}$ . The diameter of the semicircle provides the value of  $R_{ct}$ . For a diffusion-controlled reaction, Warburg impedance is an additional term. At low frequencies, it varies inversely with frequency and at very low frequencies, it increases and dominates, leading to a straight line with a phase angle of  $45^\circ$ . Another way of representing the impedance data is by the Bode plot, where both the logarithm of the modulus of impedance ( $\log |Z|$ ) and the phase angle are plotted in the y-axis against a common abscissa of frequency (in logarithmic scale). On such a plot a pure resistance is denoted by a horizontal line and a constant phase angle  $\phi$  of  $0^\circ$ , while a capacitor is a straight line of unit slope and a constant phase angle  $\phi$  of  $90^\circ$ . The impedance measurements must be made over a wide range of frequencies in order to attain the high frequency limit of the impedance, which is equal to the electrolyte resistance. At high frequencies, the capacitive effect is attributed to a pure double layer capacitance. The frequency range for the measurement may be from 100 mHz to 10 MHz, depending on the electrochemical system employed for the analysis.

There are different types of methods used to measure the impedance of an electrochemical system namely, Wheatstone bridge, analogue ac analyser, phase sensitive detection, sine wave correlation, frequency response analyser and Fourier transform methods [2,3]. In our work, we have carried out the impedance measurements using a Perkin Elmer Model 5210 lock-in amplifier controlled by Power Sine software. Phase sensitive detection method was employed for the measurement of the impedance of the electrochemical cell above 5 Hz using a single-sine technique that provides the highest accuracy. Below 5 Hz, the measurement of impedance was performed using a fast Fourier transform technique based on multi sine experiments that avoids any drift or change in the impedance value of the electrochemical system. The potential of the working electrode is held at a desired DC potential of interest using a potentiostat. A small amplitude of sinusoidal ac voltage with 5-10 mV peak-to-peak is applied to the cell from a lock-in amplifier. The current output from the cell has a phase difference with respect to the input voltage. The lock-in amplifier measures this phase difference and amplitude of the current response, which can be converted to the real and imaginary part of the impedance.

### 2.5.3 Chronopotentiometry

This is another electrochemical technique wherein, the current flowing through the cell is instantaneously stepped from zero to some finite value and the potential of the working electrode is monitored as a function of time while the overall reaction rate is fixed. This technique comes under the galvanostatic (constant current) experiment. The plot of potential versus time is known as chronopotentiogram. Figure 2.6 shows a typical chronopotentiogram for a reversible system.

Consider a simple reaction,



as the current pulse is applied there is an initial fairly sharp decrease in the potential as the double layer capacitance is charged, until a potential at which the species O is reduced to R is reached. Then there is a slow decrease in the potential determined by the Nernst equation, until the surface concentration of O essentially reaches zero. The flux of O to the surface is then no longer sufficient to maintain the applied current and the electrode potential again falls sharply, until a further electrode process occurs.

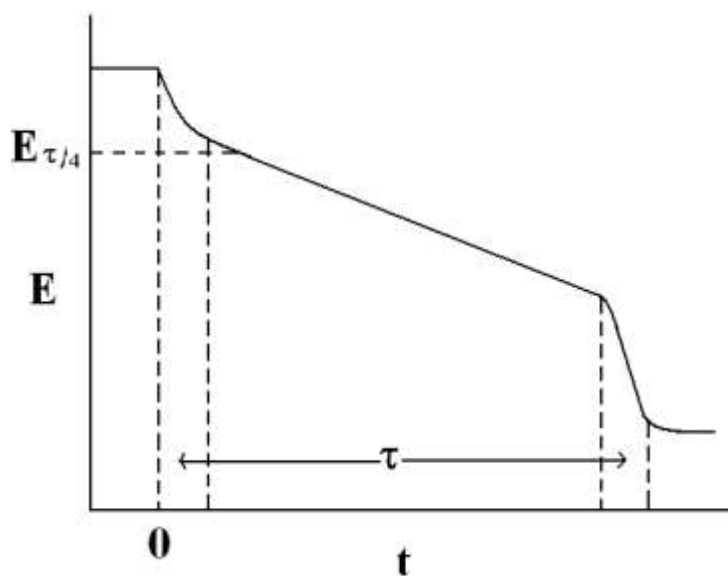


**Fig. 2.6** Schematic diagram of a chronopotentiogram for a reversible system

The dependence of current density on the transition time and the diffusion coefficient of the species in this case are given by Sand's equation, which is represented as follows:

$$|I\tau^{1/2}| = n F D_0^{1/2} \pi^{1/2} C_0^\infty / 2$$

where  $\tau$  is the transition time and  $D_0$  is the diffusion coefficient of the species. Thus the product of  $I\tau^{1/2}$  is independent of the applied current density and proportional to  $C_0^\infty$ . This is used as a diagnostic test for a diffusion controlled process. In the present thesis, we have used chronopotentiometry to deposit nanocomposite film of metal and conducting polymers on electrode.

### 2.5.4 Chronoamperometry

This method is essentially a potential step method, wherein the potential of the working electrode is changed instantaneously and the current-time response is recorded. The plot of change of current with time at a constant potential is obtained. Figure 2.7 shows the typical potential step applied to an electrochemical system and its response in terms of current that is being recorded as a function of time. In chronoamperometry Cottrell equation describes how the current,  $I$ , decays as a function of time.

$$I = nFAC_0D^{1/2}\pi^{-1/2}t^{-1/2}$$

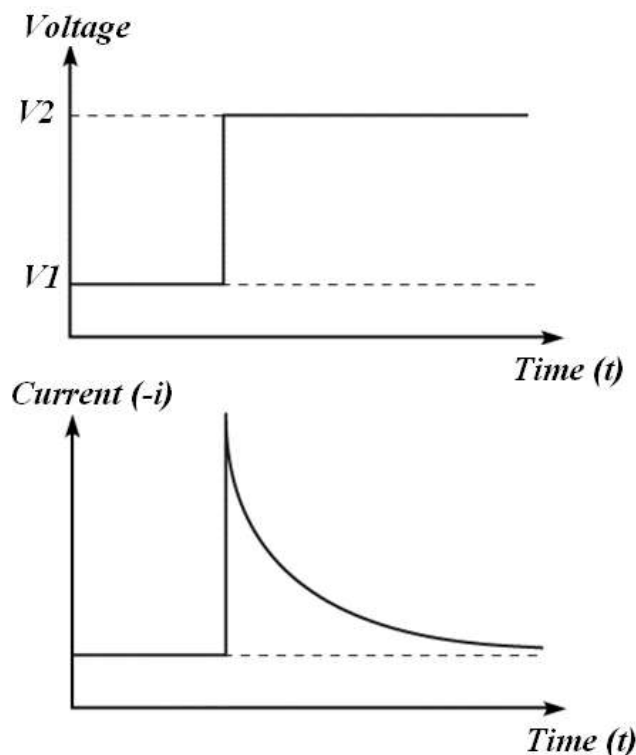


**Fig. 2.7** Schematic representation of potential step applied during chronoamperometric measurements and the response in terms of current as a function of time

We can see from the figure that as soon as the potential is applied to an electrochemical system, there is a large flow of current due to the reaction occurring at the electrode surface.

Initially the electrode surface is covered fully with the oxidant species and once the potential is applied to the electrode, it is being reduced, which leads to a large current flow. Further, this current decreases with time due to its dependence on concentration gradient. In the present thesis, we have used chronoamperometry to calculate currents at different overpotentials in order to calculate the Tafel slope for electrocatalysis experiments as explained in chapter 5 and 6.

### 2.5.4.1 Tafel plot analysis

The Tafel plot analysis is extensively used in the corrosion studies and catalysis especially for hydrogen evolving cathodes. In our work we have used Tafel plot analysis to study the electrocatalytic activity of the nanocomposite films towards the oxidation of small organic molecules (methanol and ethanol).

The general form of the Tafel equations, are given as follows:

For a cathodic reaction,

$$\log |I| = \log I_0 - \alpha_C n F \eta / 2.303 RT$$

while for an anodic reaction,

$$\log |I| = \log I_0 + \alpha_A n F \eta / 2.303 RT$$

where  $I$  is the total current density,  $I_0$  is the exchange current density,  $\alpha_C$  and  $\alpha_A$  are the respective cathodic and anodic Tafel slopes and  $\eta$  is the overpotential, which is defined as the deviation of applied potential from the equilibrium potential. The plot of  $\log |I|$  versus  $\eta$  is known as the Tafel plot, from which the values of  $\alpha_C$ ,  $\alpha_A$  and exchange current density ( $I_0$ ) can be determined from the slopes and intercept respectively.

### *Tafel slope in alcohol electro-oxidation*

The slopes of the overpotential-current plots, which are generally called Tafel slopes, have some special significance when they deviate from the ideal situation. The usage of the term Tafel slope in the context of alcohol oxidation research is based on the nature of the surface conditions such

as reaction intermediates, adsorption and surface poisoning etc., which affects the available surface sites for the reaction.

There is a view in the literature, which we subscribe, that the term “Tafel slope does not have its fundamental meaning in the electro-oxidation of small organic molecules, since the straight line between overpotential and  $\log I$  is not generally obtained.” The problem essentially arises due to the presence of adsorbed poisonous intermediates on the surface partially blocking the access to the electrode surface in varying extents at different potentials [4-6].

In most of the electrocatalysis experiments we have observed two slopes at low and high overpotentials. Always the slope at higher overpotentials is higher than the one at low overpotential. This aspect was also pointed out by Wieckowski *et al.*[4]. It is always desirable to have a low value of the Tafel slope to achieve high electrocatalysis currents at low overpotentials [6]. To achieve this, control on the rate determining step (rds) is required, which is not easy to accomplish. Even in the literature, the values of Tafel slope for a given catalyst do not always appear to be consistent. For instance, the different platinum based electrocatalysts show different Tafel slopes. However a prior potential pulse program is always helpful in removing the adsorbed intermediates [7]. The Tafel slopes measured and reported in this work provide some significant insights into the reaction process and the effect of the temperature on the electro-oxidation reaction. This aspect will be discussed in detail in chapter 5.

### **2.5.5 Anodic stripping voltammetry (ASV)**

Anodic stripping voltammetry (ASV) is essentially a linear sweep voltammetry (LSV) method, which is extremely useful and highly sensitive for the quantitative determination of trace amount of ionic species. In ASV the analyte of interest is deposited on the working electrode by applying a constant potential, before the potential sweeping. This is called the deposition step. During the potential sweeping the deposited material gets oxidized from the electrode, which is also called the stripping step. The current is measured during the stripping step. The oxidation of species can be seen as a peak in the current vs. potential curve. We have carried out ASV studies in order to check the lead sensing ability of the PTBA-PANI modified gold electrode. The lead sensing studies with the help of ASV are discussed in detail in chapter 4.

## 2.6 Imaging techniques

### 2.6.1 Scanning electron microscopy (SEM)

SEM is one among the electron microscopes, which were developed to overcome the limitations associated with the light microscopes such as the magnification and resolution. The electron microscopes are scientific instruments that use a beam of highly energetic electrons to image the specimen on a very fine scale and to gain information on its structure and composition. The images obtained from the SEM can provide information on the topography, morphology, composition and the crystallographic orientation of the sample. There are two kinds of electron microscope namely transmission electron microscope (TEM) and scanning electron microscope (SEM) that are commonly used in the surface science. In the present work, we have used SEM to characterize the surface morphology of the electrodeposited nanocomposite films.

SEM uses an electron beam rather than light to form an image. The electromagnets are used to bend the electron beam to produce the image on a screen. By using the electromagnets, we can have more control over the magnification and the use of electron beam provides clarity in the image produced. The SEM has a large depth of field, which allows a large amount of the sample to be in focus at one time. The SEM also produces images of high resolution, which means that closely spaced features can be examined at a very high magnification.

A beam of electrons is generated from the electron gun using tungsten tip located at the top of the column. The electron beam is attracted through the anode, condensed by a magnetic lens and focused as a very fine point on the sample by the objective lens. The scan coils are energized by varying the voltage produced by the scan generator and thus magnetic field is created, which deflects the beam back and forth in a controlled pattern. There are many things that occur when the beam hits the sample surface by the interaction of electron beam with the surface as shown in the Figure 2.8.

In case of SEM imaging when the electron beam hits the sample surface, the secondary electrons produced from the sample are collected by the secondary electron detector or the backscatter detector, which are then converted to a signal resulting in an image in the viewing screen. The image obtained corresponds to the surface topography of the sample. SEM is always used in the vacuum, which avoids the problem of interaction of electron beam with the other gaseous molecules, which would result in the lower contrast images.

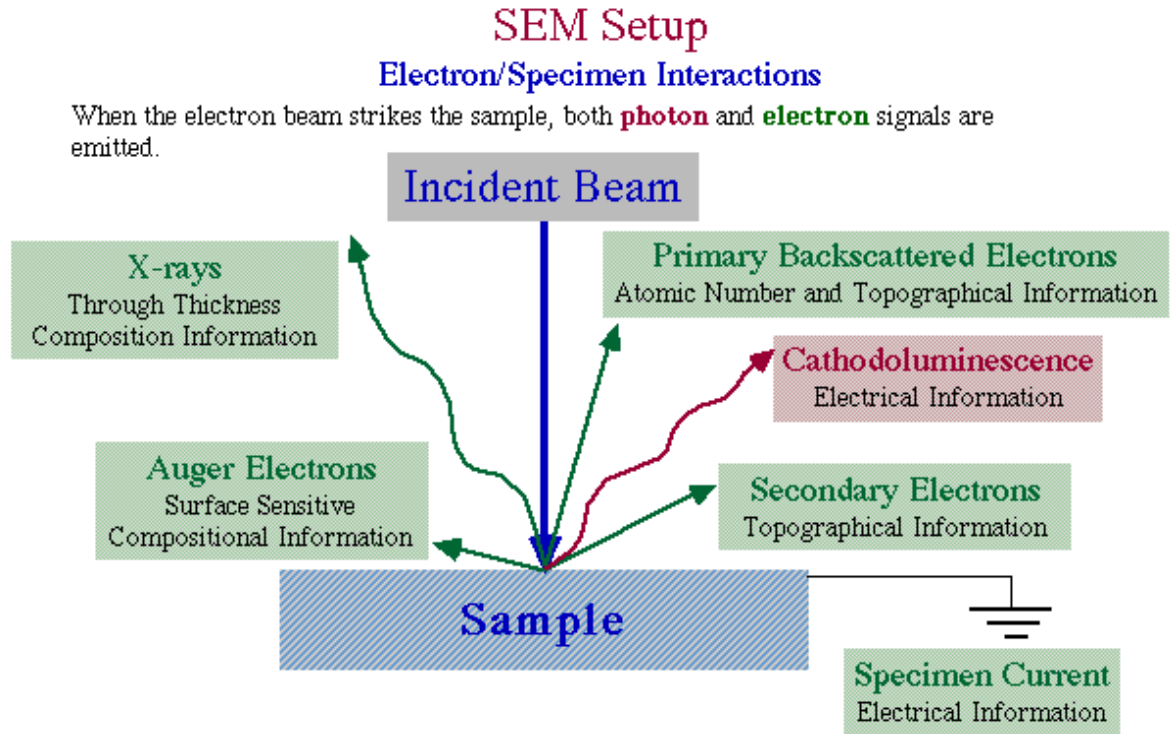


*Fig 2.8 Schematic representation of electron beam interactions with specimen*

An important criterion in the study of SEM is that the sample should be conducting and for this reason a thin film of gold is sometimes coated over the sample surface using sputtering technique before the process of imaging. The working principle of a scanning electron microscope is schematically shown in the following, Figure 2.9.

In addition to imaging an SEM imaging system can be used for energy dispersive X-ray spectroscopy (EDS or EDAX) which is an analytical technique used for the elemental analysis or chemical characterization of a sample. It relies on the investigation of a sample through interactions between electromagnetic radiation and matter, analyzing X-rays emitted by the matter in response to being hit with electron beams. The characterization is done using the fundamental principle that each element has a unique atomic structure allowing X-rays that are characteristic of an element's atomic structure to be identified uniquely from one another. EDAX analysis was used in our work to obtain the composition of the nanocomposites.

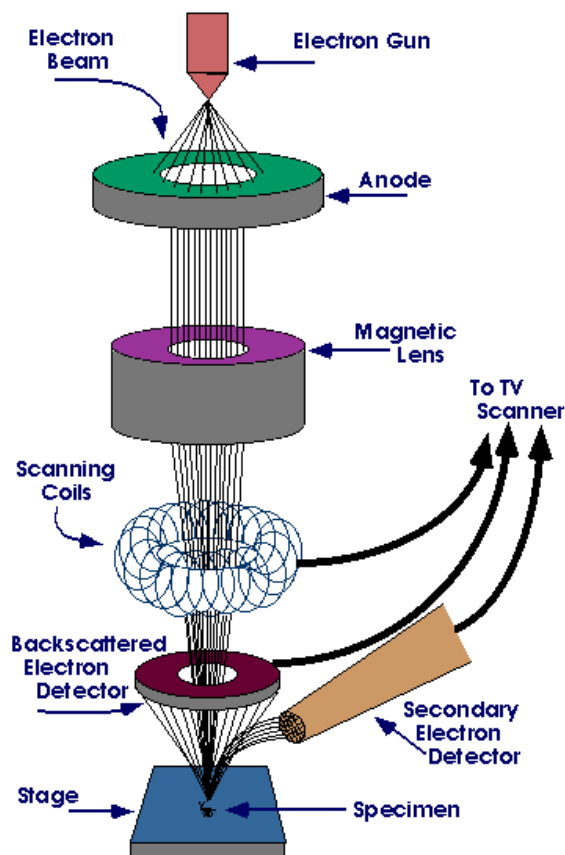


*Fig. 2.9 Schematic representation of an SEM*

Recently there is lot of interest in a new high resolution version of SEM known as “field emission scanning electron microscope” (FESEM). The emitter type is the main difference between the SEM and the FESEM. SEM uses thermionic emitters where electrical current is used to heat up a filament; the two most common materials used for filaments are tungsten (W) and lanthanum hexaboride (LaB<sub>6</sub>). When the heat is enough to overcome the work function of the filament material, the electrons can escape from the material. In conventional thermionic emitters evaporation of cathode material and thermal drift during operation are the major problems which cause less contrast in the images. In an FESEM a field emission source (FES) also called a cold cathode field emitter, is used which does not heat the filament. The emission is reached by placing the filament in a huge electrical potential gradient. The FES is usually a wire of tungsten wrought into a sharp point. The significance of the small tip radius is that an electric field can be concentrated to an extreme level, as a result the work function of the material is lowered and electrons can leave the cathode. FESEM produces a cleaner image with less

electrostatic distortions and better spatial resolution than SEM. In majority of our work, FESEM was used to study the structural morphology of the electrodeposited metal and conducting polymer nanocomposite films unless otherwise mentioned.

## 2.6.2 Scanning tunneling microscopy (STM)

STM is the precursor of all the surface probe microscopes [8]. It is a versatile tool in the area of surface science to obtain the topographic images of smooth conductive surfaces. The instrument scanning tunneling microscope was invented by Gerd Binnig and Heinrich Rohrer at the IBM research institute, Zurich in the year 1982 for that they were awarded the Nobel prize in 1985. It can be used in the investigation of very small areas of surfaces in the order of nanometers with extremely high level of precision. It also has the advantage of studying atomically smooth conducting surfaces in a variety of environments like ultra high vacuum (UHV), air, electrolytic media etc. In a typical STM experiment an atomically sharp metallic tip made up of either Pt/Ir, Pt/Rh, Pt or W is brought very close to the surface with the separation of the order of few angstroms between them. The movement of the tip in all the three directions is carried out with the help of piezoelectric crystals. Application of a small potential difference ( $\sim 0.1\text{V}$ ) between the sample surface and the tip leads to the flow of tunneling current in the order of pA to nA. This electron tunneling is due to the fact that the electron wave functions of the tip and the sample overlap. The tunneling current is of the form  $I_t \approx V e^{-kd}$  where  $I_t$  is the tunneling current,  $V$  is the bias voltage,  $k$  is a constant that includes the work function of the material and  $d$  is the spacing between the lowest atom on the tip and the highest atom on the sample. The strong exponential dependence of the tunneling current on the tip-to-sample spacing makes it possible to use this current in a feedback loop to control the motion of the tip precisely using a device known as the piezoelectric scanner. In response to an applied voltage, the scanner moves the tip over an area of the sample in a raster pattern and the feedback loop causes the tip to track the sample surface with sub-angstrom precision. The coordinates of the tip's path can then be transformed into a map of the surface topography. In fact, the STM image at atomic resolution corresponds to a contour map of the local density of states (LDOS) of atoms on a conducting sample. The tunneling current is very much sensitive to the distance between the tip and sample. This current decreases about one order of magnitude per  $1 \text{ \AA}$  of the electrical gap width, which results in an accuracy of the order of  $0.1 \text{ \AA}$  that can be achieved using STM. This extreme sensitivity of the

STM means that the features, which are of atomic dimensions, can be imaged precisely provided the distance between the tip and the sample is accurately controlled.

The STM can be operated in two ways namely, the constant current mode and the constant height mode. In the constant current mode of operation, the tip is moved slowly in the x-y plane, which is parallel to the sample surface and simultaneously the distance z from the sample surface (height) is adjusted in such a way that the current will remain constant by the application of a feedback voltage to the tip. The image is obtained as a map of this feedback voltage versus the lateral x and y coordinates resulting in the topographic image of the surface. In this way the structure of single crystal surfaces, the occurrence of steps, kinks and defects can be realized. In the constant height mode, the tip is moved at a constant height z from the sample to image the surface. As a result, the tunneling current will change as a change of tip-sample separation. In this case, the current is recorded as a function of lateral coordinates to obtain the topographic image of the sample. This technique is only used on atomically smooth conducting surfaces, since on rougher surfaces the tip may hit a protrusion leading to tip crash that may result in blurred images. In our work, we have carried out STM studies on different modified surfaces using a home built instrument [9,10]. Figure 2.10 shows the schematic of the operation of an STM and a representative highly oriented pyrolytic graphite (HOPG) STM image.

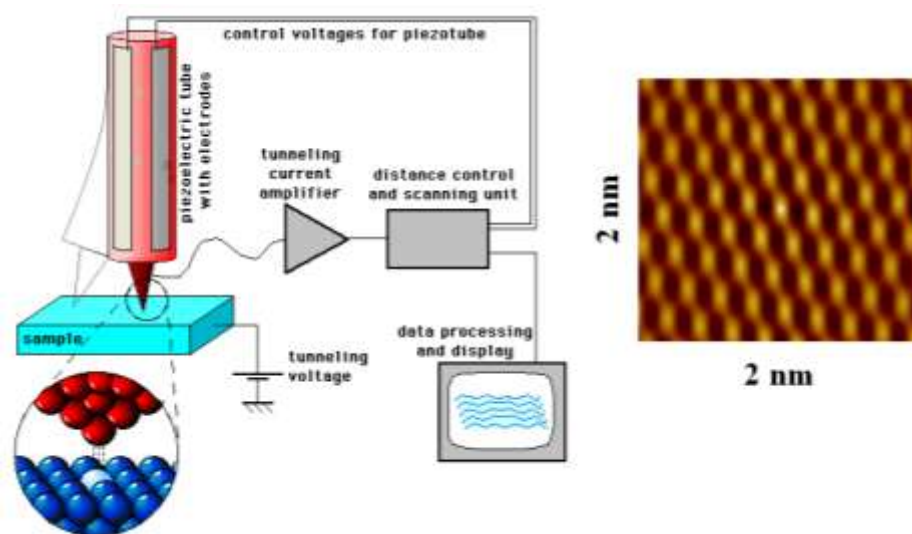


**Fig 2.10** Schematic representation of the working principle of an STM and 2x2 nm STM image of HOPG surface

### 2.6.3 Atomic force microscopy (AFM)

AFM provides a number of advantages over conventional microscopy techniques and also over other scanning probe microscopes. AFM probes the sample and makes measurements in three directions, x, y, and z, thus enabling the presentation of three-dimensional images of a sample surface. This presents a great advantage over any microscope available with good resolution in the x-y plane ranging from 0.1 to 1.0 nm and in the z direction is 0.01 nm (atomic resolution). AFMs require neither a vacuum environment nor any special sample preparation, and they can be used in either an ambient or liquid environment. With these advantages AFM has significantly become a leader in the imaging of materials in the fields of materials science, chemistry, biology and physics.

The AFM probes the surface of a sample with a sharp tip, a couple of microns long and often less than 100Å in diameter. The tip is located at the free end of a cantilever that is 100 to 200 μm long. Forces between the tip and the sample surface cause the cantilever to bend, or deflect. A detector measures the cantilever deflection as the tip is scanned over the sample.

There are basically three modes of imaging in AFM.

1. Contact mode
2. Non-contact mode
3. Tapping mode or intermittent contact mode

#### ***Contact mode***

In contact AFM mode, also known as repulsive mode, an AFM tip makes soft "physical contact" with the sample. The tip is attached to the end of a cantilever with a low spring constant, lower than the effective spring constant holding the atoms of the sample together. As the scanner gently traces the tip across the sample (or the sample under the tip), the contact force causes the cantilever to bend to accommodate changes in topography. Once the AFM has detected the cantilever deflection, it can generate the topographic data set by operating in one of two modes, *constant-height* or *constant-force* mode. During this mode the height of the scanner is fixed. This is used in taking atomic scale images where the variations are small.

In constant-force mode, the deflection of the cantilever can be used as input to a feedback circuit that moves the scanner up and down in z direction, responding to the topography by

keeping the cantilever deflection constant. In this case, the image is generated from the scanner's motion. With the cantilever deflection held constant, the total force applied to the sample is constant.

### ***Non-contact mode***

Non-contact AFM is one of the vibrating cantilever techniques in which an AFM cantilever is vibrated near the surface of a sample. The spacing between the tip and the sample for non-contact AFM is of the order of tens to hundreds of angstroms. Non-contact AFM is desirable because it provides a means for measuring sample topography with little or no contact between the tip and the sample. Like contact AFM, non-contact AFM can be used to measure the topography of insulators and semiconductors as well as electrical conductors. Cantilevers used for non-contact AFM must be stiffer than those used for contact AFM because soft cantilevers can be pulled into contact with the sample surface. Non-contact AFM does not suffer from the tip or sample degradation effects that are sometimes observed after taking numerous scans with contact AFM. An AFM operating in contact mode will penetrate the liquid layer to image the underlying surface, whereas in non-contact mode an AFM will image the surface of the liquid layer. Figure 2.11 shows the schematic representation of the AFM, working in contact and non-contact mode.

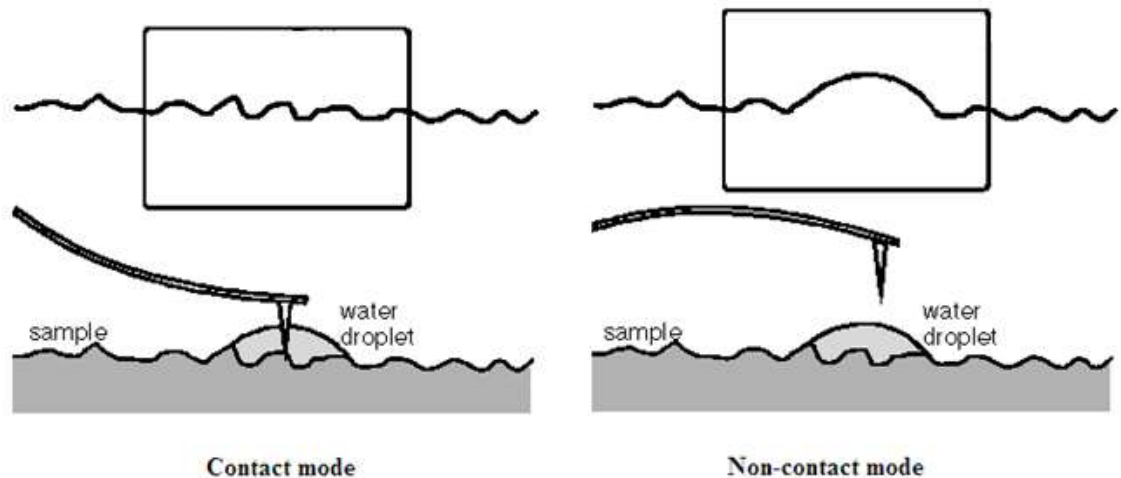


**Fig 2.11** Schematic representation of the working principle of an AFM in contact and non-contact mode

## ***Tapping mode***

To obtain quality images, in general, the AFM tip should not damage the surface while being able to obtain the high resolution images of the surface. This is possible in tapping mode, which is the most commonly used mode of imaging in AFM. In this mode the tip is just about to hit the sample or the tip taps on the surface of the sample. Therefore this mode is also called “Tapping mode”.

In this mode the cantilever oscillates and the tip makes repulsive contact with the surface of the sample at the lowest point of the oscillation. In other words the cantilever is oscillated at its resonant frequency and is positioned above the surface of the sample, so that it only taps the surface. This method has the advantage that the tip does not damage the sample being scanned, and there is also a large reduction in the lateral forces, since the proportion of time where the tip and sample are in contact is quite low. Also, the phase of the oscillation can give information about the sample properties, such as stiffness and mechanical information or adhesion. The resonant frequency of the cantilever depends on its mass and spring constant; normally, stiffer cantilevers have higher resonant frequencies. In this mode, the set point value is the amplitude of the oscillation, so a higher set point value means less damping by the sample and hence lower imaging forces. In our work, tapping mode of the AFM was used to image the nanocomposite film modified surfaces.

## **2.7 Spectroscopic techniques**

### **2.7.1 Fourier transform infrared spectroscopy**

Fourier transform infrared spectroscopy, also known as FTIR spectroscopy is mainly based on the interaction of infrared (IR) radiation with a sample (liquid or solid) and measuring the frequencies at which the sample absorbs the radiation. The FTIR spectrometer records the intensities of absorption over a range of frequency and represented as a plot called IR spectrum. The intensity is generally reported in terms of absorbance, the amount of light absorbed by a sample, or percentage of transmittance, the amount of light that passes through the sample. The frequency is expressed in terms of wave numbers. The chemical structure and the presence of various functional groups in the given sample can be identified from this spectrum, as the chemical functional groups absorb IR radiation only at certain fixed frequencies.

In addition to bulk samples, FTIR can be used to study ultra thin organic films on various metallic and non-metallic surfaces essentially to characterize the molecular packing and orientation on the surface [11,12]. The spectrum is obtained using either internal or external reflection modes of operation. The internal reflection mode is known as the (ATR) attenuated total reflection spectroscopy, whereas the external reflection mode is known as reflection-absorption or grazing angle spectroscopy. The beam is directed into an angled crystal and reflected within the crystal until it emerges from the other end where it has been collected. The number of reflections depends on the angle of incidence upon the crystal. The crystal is usually made of KRS-5, zinc selenide or germanium. Grazing angle reflection or external reflection technique provides a nondestructive method of measuring the surface coatings of thin films. External reflectance is a mirror like reflection from the surface of a sample. The infrared radiation is directed onto the surface of a sample at an angle of incidence  $\theta_I$ . For an external reflectance, the angle of reflection,  $\theta_R$ , is equal to the angle of incidence,  $\theta_I$ . The amount of radiation reflected from the sample depends on the angle of incidence, refractive index, surface roughness and the absorption properties of the sample. The angle of incidence is selected on basis of the thickness of coating, which is being used for the study. For very thin film coatings in the range of nanometer thickness like ultra thin organic films, an angle of incidence of  $85^\circ$ - $88^\circ$  is used for the characterization of modified surfaces. Reflectance measurements at this angle of incidence are often called as grazing angle measurements.

In our work, we have carried out the FTIR spectroscopy studies for the thin film modified surfaces using a FTIR 8400 model (SHIMADZU) with a fixed  $85^\circ$  grazing angle attachment (FT-85; Thermo Spectra-Tech). The unique design of the FT-85 also features the built-in polarizing elements. The silicon refracting elements are positioned at angles, which allow only the p-polarization light to pass through the sample. The samples are placed on the horizontal sampling surface of the accessory. Therefore, no clamps are necessary. The sample area is approximately 10 mm wide and 40-50 mm long. The FT-85 accessory is available for almost all the popular FTIR spectrometers and is easily installed with minimal alignment. In addition we have also used the FTIR spectra to analyze the different functional groups present in the metal conducting polymer nanocomposite film coating.

### **2.7.2 Ultraviolet-visible (UV-vis) spectroscopy**

Ultraviolet-visible (UV-vis) spectroscopy is a type of absorption spectroscopy in the ultraviolet and visible spectral region. This spectroscopy exploits light in the visible and adjacent *i.e.* near-UV and near-infrared (NIR) region of the electromagnetic spectrum. In this region of the electromagnetic spectrum, molecules typically undergo electronic transitions. This technique is complementary to the fluorescence spectroscopy, in a way that fluorescence deals with transitions from the excited state to the ground state, whereas absorption measures transitions from the ground state to the excited state. In the present work we have used this technique to characterize conducting polymers and porphyrins based nanocomposites. Porphyrins show their characteristic bands in the UV-vis spectra such as an intense Soret band at about 400 nm and Q bands at higher wavelengths.

### **2.7.3 Photoluminescence spectroscopy (PL spectroscopy)**

In photoluminescence spectroscopy light is directed onto a sample, where it is absorbed and passes on the excess energy into the material in a process called photo-excitation. This excess energy can be dissipated by the sample via the emission of light, or luminescence. In the case of photo-excitation, the generated luminescence is called photoluminescence. The intensity and spectral content of this photoluminescence is a direct measure of various important material properties. Photo-excitation causes electrons in the material to move into permissible excited states. When these electrons return to their equilibrium states, the excess energy is released and may include the emission of light in a radiative process or may not emit (a nonradiative process). The energy of the emitted light which is called the photoluminescence relates to the difference in energy levels between the two electronic states involved in the transition. The quantity of the emitted light is related to the relative contribution of the radiative process. We have used PL spectroscopy to measure the emission characteristics of the porphyrin aggregates.

### **2.7.4 X-ray photoelectron spectroscopy (XPS)**

X-ray photoelectron spectroscopy (XPS) provides valuable information on the density of occupied electronic states for a surface. The X-ray beam penetrates the material and ejects electrons from the valence or core levels yielding information about the atomic composition and

the oxidation states of the atom in the material [13]. With the help of XPS we can measure the elemental composition, empirical formula, chemical state and electronic state of the elements that exist within a material. XPS spectra are typically obtained by irradiating a material with a beam of X-rays and simultaneously measuring the kinetic energy and number of electrons that escape from the top few nanometers of the material. The technique requires ultra high vacuum (UHV) conditions.

Because the energy of a particular X-ray wavelength is known, the electron binding energy of each of the emitted electrons can be determined by using an equation that is based on the formula:

$$E_{\text{binding}} = E_{\text{photon}} - (E_{\text{kinetic}} + \phi)$$

where  $E_{\text{binding}}$  is the binding energy (BE) of the electron,  $E_{\text{photon}}$  is the energy of the X-ray photons being used,  $E_{\text{kinetic}}$  is the kinetic energy of the electron as measured by the instrument and  $\phi$  is the work function of the spectrometer. With the help of XPS many inorganic compounds, metal alloys, semiconductors, polymers, pure elements, ceramics, paints, papers, inks, woods, plant parts, teeth, bones, human implants and biomaterials etc. can be scanned. In our work we have used XPS to characterize the palladium and polyaniline (Pd-PANI) nanocomposite film.

## Bibliography

- [1] M. Jayadevaiah, V. Lakshminarayanan, *Meas. Sci. Technol.*, 15 (2004) N35.
- [2] A.J. Bard, L.R. Faulkner, *Electrochemical Methods Fundamentals and Applications*, John Wiley and Sons, Noida, 2<sup>nd</sup> edn., 2004.
- [3] R. Greef, R. Peat, L.M. Peter, D. Pletcher, J. Robinson, *Instrumental Methods in Electrochemistry*, Ellis Horwood Ltd., Chichester, Great Britain, 1990.
- [4] W. Chrzanowski, A. Wieckowski, *Langmuir*, 14 (1998) 1967.
- [5] Z.X. Liang, T.S. Zhao, J.B. Xu, L.D. Zhu, *Electrochim. Acta*, 54 (2009) 2203.
- [6] J.O'M. Bockris, *J. Serb. Chem. Soc.* 70 (2005) 475.
- [7] E. Herrero, K. Franaszczuk, A. Wieckowski, *J. Phys. Chem.*, 98 (1994) 5074.
- [8] *Introduction to Scanning Tunneling Microscope*, by C. Julian Chen, Oxford University Press, New York, 1993.
- [9] V. Lakshminarayanan, *Curr. Sci.*, 74 (1998) 413.
- [10] M. Jayadevaiah, V. Lakshminarayanan, *Meas. Sci. Technol.*, 15 (2004) N35.
- [11] M.D. Porter, T.B. Bright, D.L. Allara, C.E.D. Chidsey, *J. Am. Chem. Soc.*, 109, (1987), 3559.
- [12] C.E.D. Chidsey, D.N. Loiacono, *Langmuir*, 6, (1990), 682.
- [13] J. Chastain, *Handbook of XPS*, Perkin Elmer: Minneapolis, MN, 1992.

## Chapter 3

### Formation and Electrochemical Studies of Organic Thin Films on Gold Substrate

*Nanosize thin films are basically the layers of a material coated on any substrate with size ranging from a nanometer to few micrometers in thickness. These films find useful applications in many device applications depending on the properties of the material used in the fabrications of these films. The Langmuir-Blodgett (LB) films, self-assembled monolayers (SAM) and layer-by-layer (LbL) assembly are the three main methods of the preparation of thin films. The present chapter describes our experimental results of electron transfer reactions on thin film modified electrodes by using a variety of redox probes in aqueous and non-aqueous systems. Cyclic voltammetry (CV) and electrochemical impedance spectroscopy (EIS) techniques have been used to evaluate the electrochemical parameters i.e. the charge transfer resistance ( $R_{ct}$ ) and double layer capacitance ( $C_{dl}$ ). Essentially the studies are a useful comparison of the electron transfer barrier property in these three different kind of films. The study tells us that how the electron transfer process in the common redox systems is affected by the presence of a thin film, as a barrier on the electrode.*

### 3.1 Introduction

The Self-assembled monolayers (SAMs), Langmuir-Blodgett (LB) films, and layer-by-layer (LbL) film assembly are three major techniques for the formation of thin films of organic compounds. The ultrathin films of organic molecules are intensively studied for their potential applications in organic LEDs, TFTs, solar cells and other molecular electronics studies. In addition, they provide excellent model systems for fundamental studies in biology, study of molecular recognition, single molecular spectroscopy and molecular transport phenomenon.

The SAM is essentially a single monolayer thick film of chemically adsorbed organic molecules on solid surfaces mainly noble metals. SAMs exhibit a high degree of orientation, molecular ordering and packing density [1,2]. Among several compounds that can form SAM, the chemisorptions of thiols and disulphides on gold have attracted a great deal of attention especially due to the simplicity and the ease of formation. They also find potential application in a variety of fields such as sensors [3-7], photolithography [7-9], nonlinear optical materials [10], high-density memory storage devices [11] and corrosion protection [12,13].

A single layer of amphiphilic molecules spread at air-water interface is termed as the Langmuir monolayer. This layer can be transferred onto a solid surface by LB technique. The necessary condition for the formation of LB film is that the compound should be amphiphilic in nature so that it can be spread on water surface [2].

This chapter is divided into four parts. In the first part, we have described a method of fabricating monolayer and multilayers films of cholesterol by a combination of SAM and LB technique. The composite film was used for the study of electron transfer properties of some redox active systems. Our intention was to study the properties of the composite self-assembled and LB films, as such systems are not much explored in the literature. We have studied the electron transfer and ion permeation properties through the cholesterol monolayers and multilayer films formed on Au substrate modified with SAMs of thiophenol (TP) and 2-naphthalenethiol (2NT). Molecular films of cholesterol have also been characterized using STM, AFM and grazing angle FTIR studies.

The second part of the chapter deals with the formation and electron transfer properties of the LB film of DNA and a pyridinium derivative of hexaalkoxytriphenylene (PyTp). The PyTp and PyTp-DNA complex films were first formed at an air-water interface and then transferred

onto gold substrates by LB technique. Electrochemical measurements viz. CV and EIS studies were carried out on these LB films in different redox systems. AFM studies were also carried out in order to know the topography of the modified surface.

Third part of the chapter contains the formation and characterization of an interesting SAM film composed of cyclodextrins and thiocholesterol host-guest inclusion complex on gold. The electrochemical barrier properties of the SAMs were analyzed in aqueous redox system. Lateral force microscopy (LFM) and force-distance spectroscopy studies show the definite demarcations of the regions of hydrophobic and hydrophilic nature. The above system was then compared with another one composed of methyl  $\beta$ -cyclodextrin and thiocholesterol inclusion complex.

In the fourth and the final part of this chapter we have described the formation and characterization of LbL films of oppositely charged polyelectrolytes namely polystyrene sulfonate (PSS) and polyallylamine hydrochloride (PAH). Over the past few years the LbL deposition technique has become an efficient method for producing organized films of oppositely charged molecules. There are several advantages of the LbL method such as simplicity, versatility, low cost, and precise control of film thickness.

### **3.2 Electron transfer studies on cholesterol LB films assembled on thiophenol and 2-naphthalenethiol SAMs**

Cholesterol, a sterol and an amphiphilic molecule, is an essential component of cell membranes and some of the hormones and is known to alter several properties of lipid bilayers as it influences the permeability and fluidity of membranes [14-18]. In this work we propose a novel method of fabricating monolayer and multilayers films of cholesterol by a combination of SAM and LB technique and the use of the composite SAM/LB film for the study of electron transfer properties. The particularly striking feature of the SAMs on a surface such as gold for the electrochemical studies is their remarkable stability over a wide potential window in aqueous medium.

There are very few reports in the literature on the studies of the composite SAM and LB films. Recently Ashwell *et al.* have studied the rectification behavior in hybrid Au/SAM/LB device [19]. Yu *et al.* have studied the different bridges for interfacial electron transfer in azobenzene LB/SAM composite bilayers [20]. While cholesterol and its derivatives are known

to form Langmuir monolayers at air-water interface [21-24] and LB films on substrates coated with hexamethyldisilazane [25], there are very few studies of these films by using electrochemical and surface probe techniques. Bin *et al.* have carried out the PM-IRRAS studies on the effect of cholesterol on the DMPC bilayer supported at Au electrode [26,27]. Yang *et al.* have reported the electrochemical and IRAS characterization of thiocholesterol SAM [28] and thiocholesterol, fatty acids mixed SAM [29]. To the best of our knowledge, there is no report in the literature on the study of electron transfer properties through the cholesterol monolayers and multilayer films formed on aromatic SAMs. Such a study has the potential to improve our understanding of the biological processes across the cell membranes. The composite SAM and LB film can mimic the behavior of the soft membranes to provide a powerful model system for the study of transport of biomaterials across cell membranes.

Ganesh *et al.* have reported the formation and characterization of the SAM of 2NT using electrochemical techniques, STM and FTIR [30]. Due to its highly ordered structure, rich  $\pi$  electrons density and hydrophobic nature, this aromatic thiol monolayer can act as a suitable substrate for the LB film formation and for electron transfer studies. It is known that the cholesterol molecules prefer hydrophobic surfaces rather than hydrophilic surfaces to form LB films [25]. The 2-naphthalenethiol SAM, with the hydrophobic aromatic group pointing upwards, therefore lends itself as an ideal platform for the deposition of cholesterol LB films to form the composite SAM/LB film. The aromatic thiol monolayer also facilitates electron transfer across the film, a useful property in the present study involving composite films. For comparison, we have also formed the LB film of cholesterol on thiophenol (TP) SAM surface and characterized it in a similar manner.

In this part of the chapter we report the results of electron transfer and ion permeation studies on the cholesterol monolayers and multilayers LB films on SAMs of 2NT and TP on the Au (111) surface. We have used the redox system of  $[\text{Fe}(\text{CN})_6]^{3-/4-}$  as a probe to evaluate the barrier properties towards the electron transfer of the system using electrochemical techniques such as CV and EIS. The films have been characterized using STM [31], AFM and FTIR techniques.

### 3.2.1 Methods and materials

#### 3.2.1.1 Deposition of cholesterol on SAMs

Cholesterol solution of the concentration of 0.64 mg/ml was prepared in chloroform. The freshly prepared solution was spread using a micro syringe (Hamilton) on the Millipore water in an LB trough (NIMA 611M). The solvent was allowed to evaporate for 15 minutes before starting the compression. The experiments were carried out at room temperature (25°C). The target surface pressure was kept at 30 mN/m, which is well within the regime of monolayer (Figure 3.1). After attaining the target pressure, a duration of 15 minutes was allowed for the monolayer to attain the equilibrium. The monolayer of cholesterol was obtained from a single cycle of deposition while for the formation of two, three and four layers, repeated cycles of the respective number were performed. The speed of dipper was maintained at 10 mm/min and 5 mm/min for the downward and upward motions. The electrochemical characterization of the cholesterol monolayer and multilayer films was carried out using CV and EIS in order to understand the electron transfer properties of the redox species across the film and also the ionic permeation through the film.

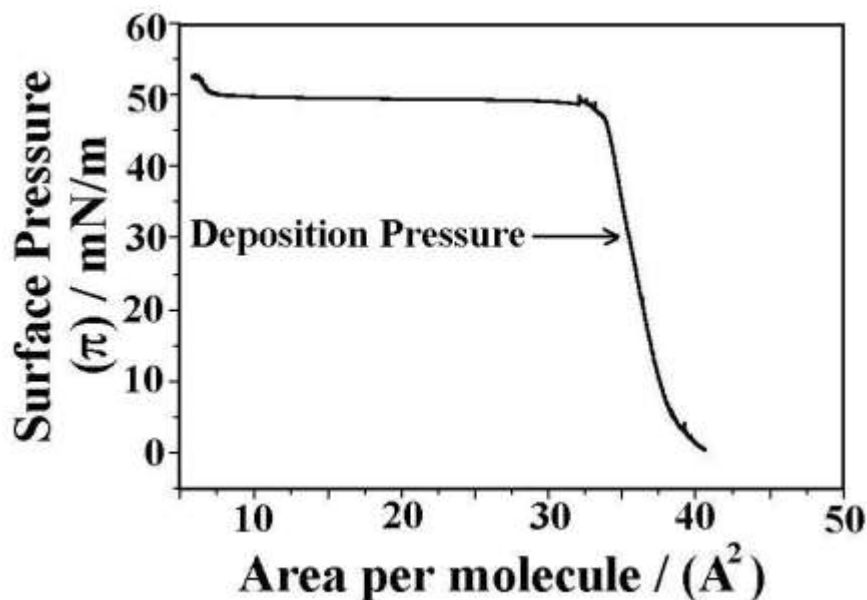


**Fig 3.1** Surface pressure-area isotherm of cholesterol at the air-water interface. The deposition was carried out at a surface pressure of 30 mN/m, as indicated by the arrow

### 3.2.1.2 Cyclic voltammetry

#### *2-naphthalenethiol (2NT) system*

Figure 3.2 shows the cyclic voltammograms of (a) bare gold electrode, (b) 2NT modified electrode, (c) monolayer of cholesterol modified SAM (denoted as Au/2NT-SAM/1-ch) and (d) bilayer of cholesterol modified SAM (Au/2NT-SAM/2-ch) in 1 mM potassium ferrocyanide with 1 M NaF as supporting electrolyte at potential scan rate of  $50 \text{ mVs}^{-1}$ . It can be seen that bare gold electrode shows the reversible peaks for the redox couple, characteristic of a diffusion controlled reaction. On the other hand, the SAM of 2NT modified electrode (Figure 3.2b) shows an irreversible behavior with a large peak separation and lower peak currents. This indicates that the SAM of 2NT considerably hinders the electron transfer process though not completely blocking it. This behavior is also typical of aromatic monolayer covered surfaces with poor blocking character towards the redox species [30]. It is generally known that aromatic thiols, due to their highly delocalized  $\pi$  electrons in the aromatic ring and extended conjugation of the molecules do not completely block the electron transfer reactions [32-38]. This property of the aromatic SAM is made use of in sensor and catalysis studies [35-37]. In contrast to 2NT-SAM on gold, the CV of the cholesterol monolayer on 2NT SAM (Figure 3.2c) shows almost complete blocking of the electron transfer reaction. This is due to the formation of well-organized and good blocking SAM-LB composite film on the surface of gold. The driving force for the organization of the cholesterol molecules on the surface of SAM is by hydrophobic interaction, which is very much stable and sustained in aqueous medium.

It has been shown earlier that cholesterol forms a well-organized LB monolayer only on a hydrophobic surface and not on a hydrophilic surface [25]. This observation is supported by the fact that our efforts to form a stable LB film of cholesterol on hydrophilic surfaces of bare gold and 4-aminothiophenol modified gold were not successful. Figure 3.2(d) shows cyclic voltammogram of the sample after the formation of two layers of cholesterol on the 2NT modified gold substrate. It can be seen that the cholesterol bilayer modified electrode shows an excellent blocking towards the redox reaction, which is even better than that of the monolayer modified SAM electrode. This confirms that a stable film with excellent barrier properties for electron transfer has been achieved by forming a bilayer of cholesterol on the 2NT-SAM.

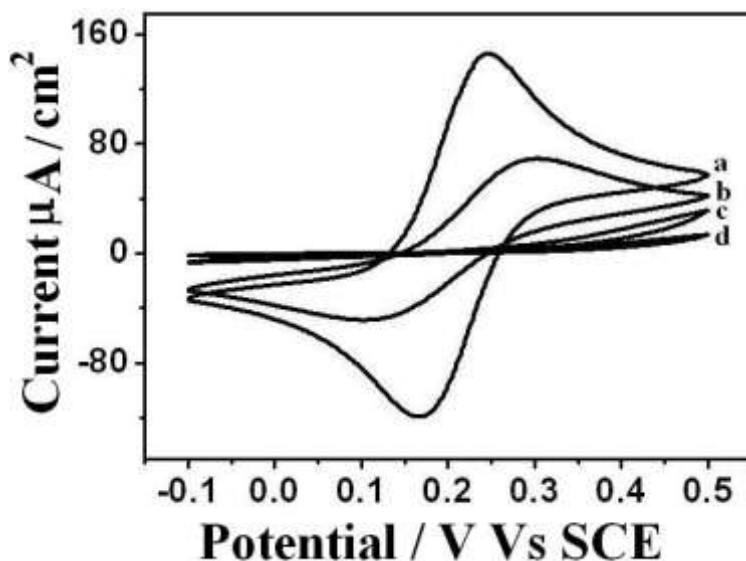


**Fig. 3.2** Cyclic voltammograms of (a) bare gold, (b) 2NT SAM, (c) 2NT SAM and cholesterol monolayer and (d) 2NT SAM and cholesterol bilayer in 1mM potassium ferrocyanide solution with 1M NaF as supporting electrolyte

### ***Thiophenol (TP) system***

Figure 3.3 shows the cyclic voltammograms for the (a) bare gold, (b) TP-SAM, (c) monolayer of cholesterol modified TP SAM (Au/TP-SAM/1-ch) and (d) bilayer of cholesterol modified SAM (Au/TP-SAM/2-ch). We find that the TP-SAM does not block the electron transfer process completely which is in agreement with the literature reports [39-42]. The composite film however, exhibits a remarkable improvement in the blocking property towards the  $[\text{Fe}(\text{CN})_6]^{3-/4-}$  redox couple. The order of the blocking ability is,  $\text{Au} < \text{Au/TP-SAM} < \text{Au/TP-SAM/1-ch} < \text{Au/TP-SAM/2-ch}$ . However, we find that the electron transfer blocking ability of the monolayer and bilayer of cholesterol on TP SAM is less effective than in the case of 2NT SAM.

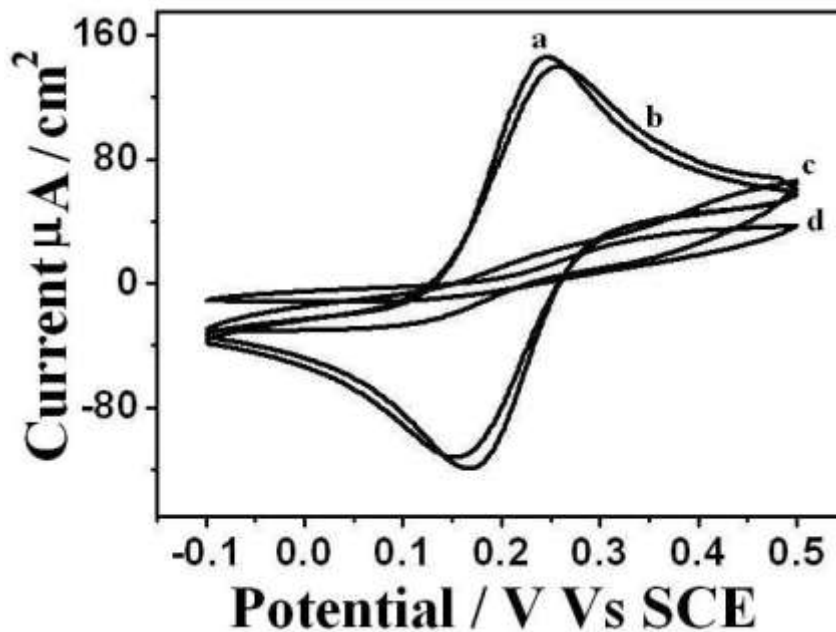


**Fig 3.3** Cyclic voltammogram of (a) bare gold, (b) TP SAM, (c) TP SAM and cholesterol monolayer and (d) TP SAM and cholesterol bilayer in 1mM potassium ferrocyanide solution with 1M NaF as supporting electrolyte

The CV studies discussed above are only qualitative indicator of the electron transfer process. In order to obtain quantitative information of the charge transfer resistance, we have carried out EIS studies.

### 3.2.1.3 Electrochemical impedance analysis

#### *2-naphthalenethiol (2NT) system*

Figure 3.4 shows the impedance plots of (a) Bare gold (b) SAM of 2NT, (c) Au/2NT-SAM/monolayer of cholesterol (1-ch) and (d) Au/2NT-SAM/bilayer of cholesterol (2-ch). The experiments were performed in equal concentrations of  $[\text{Fe}(\text{CN})_6]^{3-/4-}$  with 1 M NaF as the supporting electrolyte.

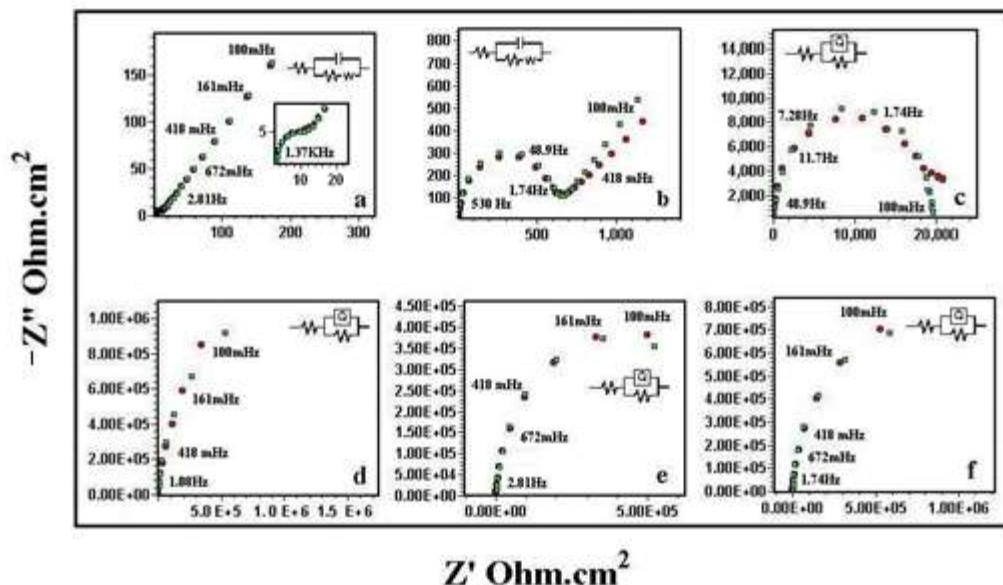


**Fig 3.4** Impedance Nyquist plots for (a) bare gold, (b) 2NT SAM, (c) 2NT SAM and cholesterol monolayer, (d) 2NT SAM and cholesterol bilayer, (e) 2NT SAM and cholesterol trilayer and (f) 2NT SAM and cholesterol tetralayer in 1mM potassium ferrocyanide/potassium ferricyanide solution with 1 M NaF as supporting electrolyte

It can be seen from Figure 3.4(a) and the inset that the impedance plot for the bare gold electrode shows a very small semicircle at high frequency range and a straight line over a wide frequency window signifying a process that is fully under diffusion control. Figure 3.4(b) shows the characteristic semicircle at higher frequencies representing the charge transfer process and a low frequency Warburg impedance for the 2NT-SAM modified gold electrode. The diameter of the semicircle increases for the cholesterol monolayer and bilayer deposited on the SAM (Figure 3.4(c) and (d)). The impedance plots were fitted to Randle's equivalent circuit and the values of  $R_{ct}$  for each system were calculated. The equivalent circuits used for fitting the measured data are also shown in the respective Figure (3.4 a-f). The typical Randle's equivalent circuit is composed of a series uncompensated resistance  $R_u$ , a series combination of charge transfer resistance  $R_{ct}$  and the Warburg impedance ( $W$ ), which are in parallel with the double layer capacitance  $C_{dl}$  or a constant phase element  $Q$ . The Warburg impedance,  $W$  is not considered wherever the low frequency Warburg region is absent in the impedance plot. The values obtained from fitting the impedance plots for various samples are shown in Table 3.1. There is a remarkable increase in

the  $R_{ct}$  value in Au/2NT-SAM/1-ch system as compared to that of SAM modified electrode by a factor of about 30.

Electrode Type	$R_{ct}/(\text{Ohm.cm}^2)$	$Q$ ( $\text{S.sec}^n.\text{cm}^{-2}$ )	$n$ ( $0 < n < 1$ )
Bare gold	7.60 [RC(RW)]	-	-
SAM of 2NT	592.1 [RC(RW)]	-	-
Cholesterol monolayer on 2NT SAM	19.57K [R(QR)]	$2.4 \times 10^{-6}$	0.97
Cholesterol bilayer on 2NT SAM	2.406M [R(QR)]	$1.27 \times 10^{-6}$	0.96
Cholesterol trilayer on 2NT SAM	786.0K [R(QR)]	$1.4 \times 10^{-6}$	0.97
Cholesterol tetralayer on 2NT SAM	1.47M [R(QR)]	$1.3 \times 10^{-6}$	0.97

**Table 3.1** Charge transfer resistance ( $R_{ct}$ ), constant phase element ( $Q$ ) and its exponent ( $n$ ) for ferrocyanide/ferricyanide redox reaction from the equivalent circuit fitting of electrochemical impedance spectroscopy data in 2NT system

We have calculated the surface coverage from the formula  $\theta = 1 - R_{ct}/R'_{ct}$  (by assuming that the current is due to the presence of pinholes and defects within the monolayer) where  $R_{ct}$  is the charge transfer resistance of bare gold electrode and  $R'_{ct}$  is the charge transfer resistance of the corresponding modified electrode. For the cholesterol monolayer the surface coverage is calculated to be 99.94%. The bilayer of cholesterol shows very high charge transfer resistance, which is more than two orders of magnitude higher compared to the Au/2NT-SAM/1-ch system. The surface coverage in this case is calculated to be 99.99%. This extremely high resistance is attributed to the hydrophobic cholesterol molecules that are exposed to the solution and inhibit the diffusion of ions through the film towards the electrode surface.

Cholesterol monolayer has the hydrophilic nature because of  $-\text{OH}$  group being in the upright direction, the bilayer system is hydrophobic which is formed by two cycles of deposition. We have extended the bilayer by two additional cholesterol layers in order to evaluate the integrity and stability of the films. We find that trilayer, which is formed by three cycles of

deposition interestingly shows less  $R_{ct}$  value than the Au/2NT-SAM/2-ch system (Figure 3.4 (e)). This is due to the fact that the trilayer has the hydrophilic surface since three cycles of deposition creates a surface with the –OH group of cholesterol exposed to the solution.

The hydrophilic character of the film helps the charged ions in solution to permeate the film. Moreover, the presence of multiple layers increases the defects in the film, which opens the path for the diffusing ions to permeate through the film. Interestingly, the deposition of fourth layer increases the resistance of the film, which is higher than Au/2NT-SAM/3-ch system (Figure 3.4(f)) though not so high as for the bilayer system. This is because, after the formation of fourth layer, the surface again acquires hydrophobic character, which makes it difficult for the ions to permeate through the film. However the value of  $R_{ct}$  is less than Au/2NT-SAM/2-ch system (Figure 3.4(b)). This implies that due to the weak adsorption, the formation of further layers above the bilayer introduces more voids and defects by disorienting the cholesterol molecules. This facilitates the permeability of ions from the solution and consequently decreases the  $R_{ct}$  compared to the more compact Au/2NT-SAM/2-ch system.

We have also carried out interfacial capacitance studies using EIS. The capacitance of the electrical double layer precisely describes the adsorption properties and is being used widely in the study of thin films on metal surfaces [43,44]. The interfacial capacitance can be precisely measured in pure supporting electrolyte and by carefully selecting the high frequency region of the impedance plot where the capacitance essentially remains constant [44]. The experiments were performed in 1 M NaF solution without any redox species. The capacitance values measured in this case are shown in Table 3.2. The values show that the additional layers beyond the bilayer do not change the measured capacitance values significantly. This shows that the small sodium and fluoride ions can penetrate through the cholesterol film of third and fourth layers comparatively easily thereby effectively restricting the dielectric thickness to the bilayer over SAM.

Table 3.2 shows that the measured capacitance value for 2NT-SAM as  $2.6 \mu\text{Fcm}^{-2}$ , which corresponds to the expected value of the thickness based on the height of 2NT (0.8 nm) molecules. This indicates that a compact film of 2NT is formed on the surface of gold. The measured capacitance value of  $1.76 \mu\text{Fcm}^{-2}$  for the cholesterol monolayer on 2NT-SAM is higher than the expected value of  $0.92 \mu\text{Fcm}^{-2}$  by assuming the total thickness of the composite film to be 2.4 nm and dielectric constant  $\epsilon = 2.5$  and by using the formula:

$$C = \epsilon \epsilon_0 / d$$

where  $\epsilon_0$  is the permittivity of the space and  $d$  is the distance between the two plates of the parallel plate capacitor or height of the SAM in our case.

Electrode type	Measured capacitance ( $\mu\text{Fcm}^{-2}$ )	Calculated capacitance ( $\mu\text{Fcm}^{-2}$ )
SAM of 2NT	2.60	2.55
Cholesterol monolayer on 2NT SAM	1.76	0.92
Cholesterol bilayer on 2NT SAM	1.10	0.55
Cholesterol trilayer on 2NT SAM	1.13	0.40
Cholesterol tetralayer on 2NT SAM	1.14	0.31

**Table 3.2** Capacitance values obtained from electrochemical impedance spectroscopy in supporting electrolyte in 2NT system (1 M NaF aqueous solution)

Since the cholesterol film acts as a dielectric film over the 2NT SAM, the total measured capacitance of  $1.76 \mu\text{Fcm}^{-2}$  is the effective series capacitance of both the layers. From this value, the cholesterol film capacitance alone can be calculated to be  $5.5 \mu\text{Fcm}^{-2}$ . This value is rather large when compared to the theoretically expected capacitance value of  $1.38 \mu\text{Fcm}^{-2}$  for a compact film. This suggests that the cholesterol layer over 2NT SAM has several defects through which the ions can quite easily access the electrode surface. However, the  $R_{ct}$  value for the  $[\text{Fe}(\text{CN})_6]^{3-/4-}$  has increased considerably for this system when compared to 2NT SAM. This implies that in spite of the large number of defects, the redox reaction is considerably inhibited. Based on this observation, we propose that the defect sites in the 2NT SAM have been filled by cholesterol, which therefore effectively blocks the electron transfer reaction. The cholesterol molecules, which fill the defect sites, may also be anchored by the hydrophobic interaction with neighboring 2NT molecules. Besides, there can be a tilt of the cholesterol molecules over the surface of the SAM, which can decrease the thickness and increase the capacitance. This model is schematically depicted in Figure 3.5.

The addition of a second cholesterol layer on top of the first one further lowers the interfacial capacitance to  $1.10 \mu\text{Fcm}^{-2}$ . The value of  $R_{\text{ct}}$  has considerably increased to  $2.4 \text{ M}\Omega\cdot\text{cm}^2$  which confirms the formation of a compact bilayer of cholesterol on the 2NT SAM on gold.

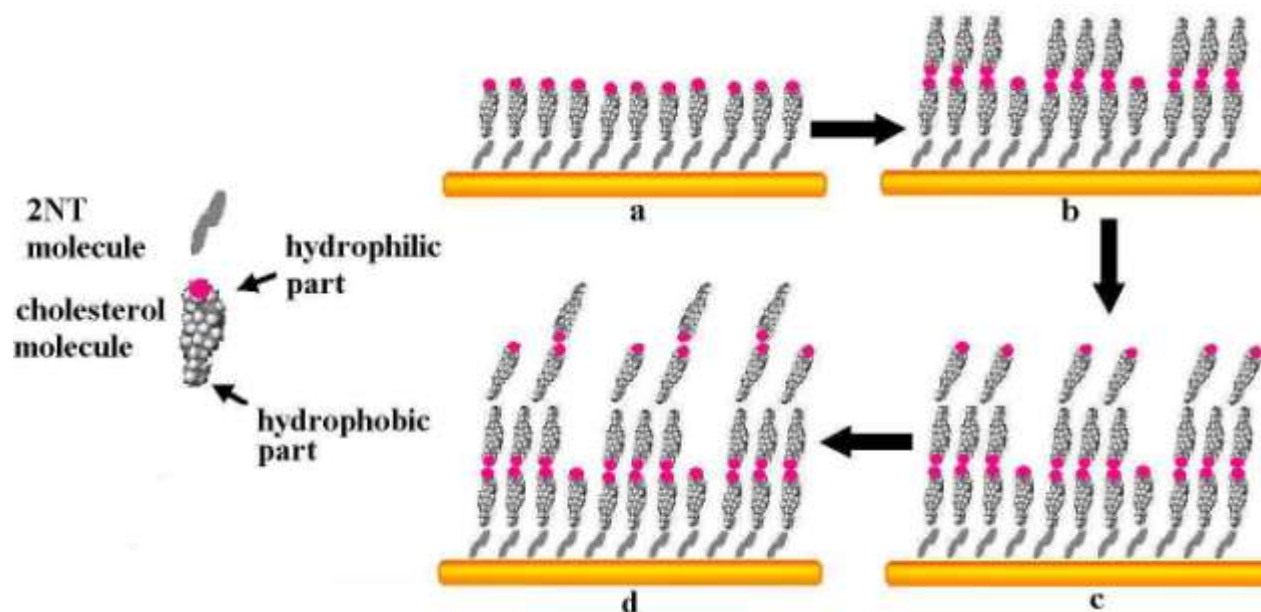


**Fig 3.5** Schematic representation of different layers of cholesterol on 2NT SAM (a) monolayer of cholesterol, (b) bilayer of cholesterol, (c) trilayer of cholesterol and (d) tetralayer of cholesterol. Cholesterol molecule is depicted showing the hydrophobic and hydrophilic ends in the figure

There is however, little variation in capacitance beyond the bilayer. It is therefore concluded that the size and number of the defects increase in the higher layers, which facilitate the permeation of ions closer to the surface till up to a certain distance.

### ***Thiophenol (TP) system***

The comparison between the electron transfer properties of 2NT system with that of TP system was carried out. Figure 3.6 shows the impedance curves for TP system. Table 3.3 shows that the  $R_{\text{ct}}$  values for the TP system increasing systematically from SAM of TP right up to the four layers of cholesterol. However, the measured  $R_{\text{ct}}$  values are less than the corresponding values of 2NT system. We also find that the interfacial capacitance values for Au/TP-SAM/1-ch, Au/TP-

SAM/3-ch and Au/TP-SAM/4-ch are almost the same. The TP SAM shows a capacitance value of  $3.96 \mu\text{Fcm}^{-2}$  which is quite higher than the theoretically expected value of  $2.5 \mu\text{Fcm}^{-2}$ . This may indicate a large tilt in the molecules forming the monolayer as has been suggested earlier by Sabatani *et al.* [39]. In this system, the capacitance of the cholesterol monolayer alone on TP SAM is calculated to be  $2.00 \mu\text{Fcm}^{-2}$ . This value of capacitance is somewhat larger when compared to the theoretically calculated capacitance of  $1.38 \mu\text{Fcm}^{-2}$  by assuming a vertical orientation of the cholesterol molecules. The reason for this increase could be due to the presence of defects as well the tilt in the cholesterol arrangement on the surface of TP-SAM.

Significantly, the  $R_{ct}$  value for the  $[\text{Fe}(\text{CN})_6]^{3-/4-}$  redox system is not quite large as it is in the case of cholesterol layer on 2NT. The rather low value of  $R_{ct}$  is also consistent with the CV results, which shows very poor blocking of the redox reaction both for the TP SAM and the cholesterol on TP SAM.

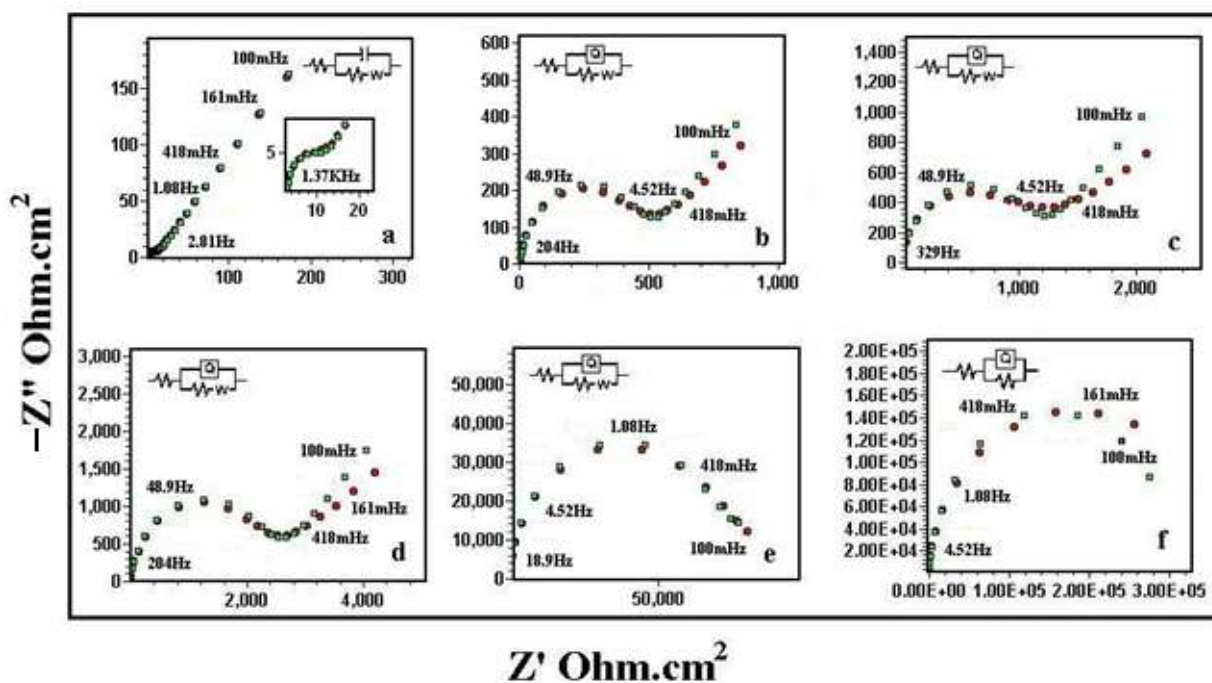


**Fig 3.6** Impedance Nyquist plots for (a) bare gold, (b) TP SAM, (c) TP SAM and cholesterol monolayer, (d) TP SAM and cholesterol bilayer, (e) TP SAM and cholesterol trilayer and (f) TP SAM and cholesterol tetralayer in  $1 \text{ mM } [\text{Fe}(\text{CN})_6]^{3-/4-}$  solution with  $1 \text{ M NaF}$  as supporting electrolyte

Electrode Type	$R_{ct}$ (Ohm.cm <sup>2</sup> )	Q (S.sec <sup>n</sup> .cm <sup>-2</sup> )	n(0<n<1)
Bare gold	7.60 [RC(RW)]	-	-
SAM of TP	462.5 [RQ(RW)]	$1.6 \times 10^{-5}$	0.93
Cholesterol monolayer on TP SAM	1.1K [RQ(RW)]	$6.6 \times 10^{-6}$	0.92
Cholesterol bilayer on TP SAM	2.34K [RQ(RW)]	$2.8 \times 10^{-6}$	0.93
Cholesterol trilayer on TP SAM	76.0K [R(Q(RW))]	$1.5 \times 10^{-6}$	0.98
Cholesterol tetralayer on TP SAM	308.0K [R(QR)]	$1.6 \times 10^{-6}$	0.97

**Table 3.3** Charge transfer resistance calculation from the equivalent circuit fitting of electrochemical impedance spectroscopy data for ferrocyanide/ferricyanide redox reaction in TP system

There is however marked decrease in the capacitance of Au/TP-SAM/2-ch system from that of the Au/TP-SAM system. Table 3.4 shows the capacitance values for thiophenol-cholesterol system. The measured capacitance for the Au/TP-SAM/1-ch is smaller than that of the Au/2NT-SAM/1-ch, which indicates a greater thickness of the film formed by the former system. This is rather surprising since the TP is a shorter molecule and therefore the thickness of TP-SAM is expected to be shorter than 2NT-SAM.

Electrode type	Measured Capacitance ( $\mu\text{Fcm}^{-2}$ )	Calculated Capacitance ( $\mu\text{Fcm}^{-2}$ )
SAM of TP	3.96	2.50
Monolayer of cholesterol on TP SAM	1.33	1.10
Bilayer of cholesterol on TP SAM	0.93	0.62
Trilayer of cholesterol on TP SAM	1.27	0.43
Tetralayer of cholesterol on TP SAM	1.31	0.33

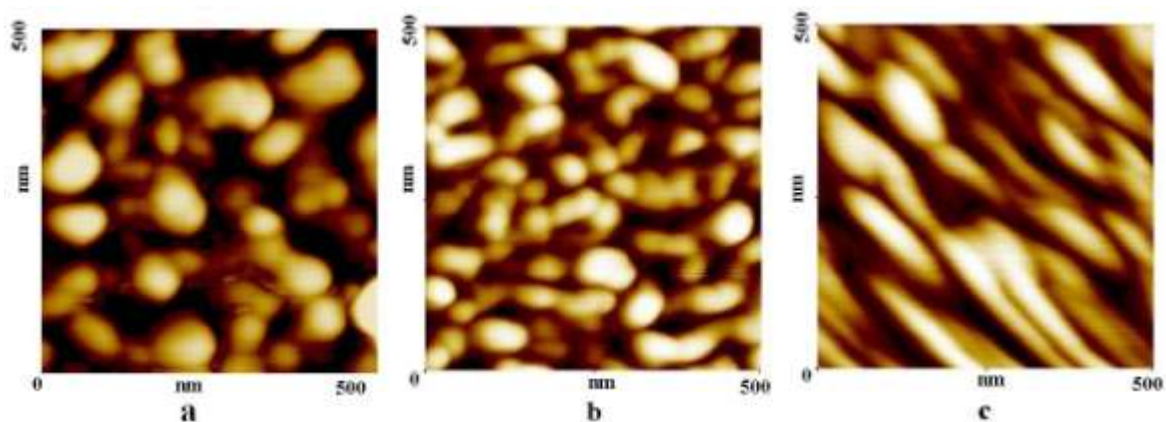
**Table 3.4** Calculated and measured capacitance values in TP system by electrochemical impedance spectroscopy in 1M NaF solution

The measured capacitance value in the case of Au/TP/1-ch is close to the expected value based on the thickness of the film (0.4 nm). There is no change in the capacitance beyond bilayer in the case of TP system. This indicates that after the formation of bilayer, the system becomes more permeable for sodium and fluoride ions. These ions approach closer to the surface, which decreases the effective separation between the electrode surface and the solution. In other words, the third and fourth layers of cholesterol molecules do not function as effective dielectric separators.

### 3.2.1.4 Scanning probe and FTIR analysis of cholesterol monolayer on 2NT-SAM

#### *AFM studies*

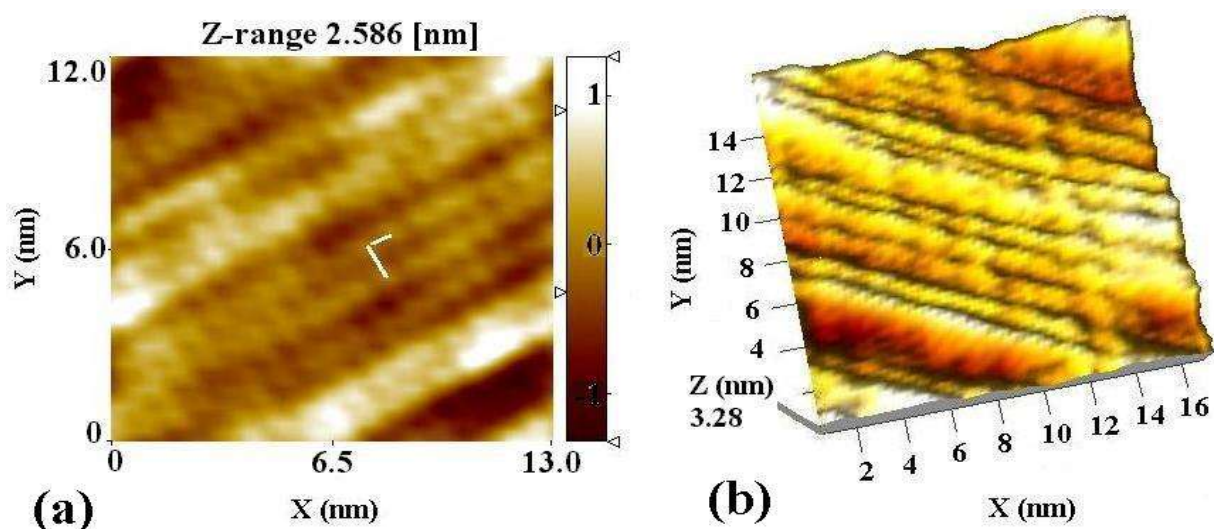
We have carried out tapping mode AFM studies on bare gold surface, 2NT-SAM and the cholesterol monolayer film over the SAM system (Figure 3.7). Figure 3.7a shows the bare gold substrate, which has crystalline domains typical of the vacuum, deposited and annealed surface at this scan range. The AFM image of 2NT-SAM on Au essentially follows the crystalline domains seen on the bare gold surface (Figure 3.7b). However, the AFM image of cholesterol monolayer formed on the 2NT-SAM (Figure 3.7c) shows several elongated domains, which were absent in 2NT-SAM on gold. The elongated features present in cholesterol LB film can be attributed to the formation of the cholesterol monolayer along the direction of dipping of the substrate in the LB trough [45,46].



**Fig 3.7** Tapping mode AFM images of (a) bare gold, (b) 2NT SAM on Au surface and (c) cholesterol monolayer on 2NT SAM /Au

### STM studies

STM imaging has been carried out in constant current mode using +100 mV sample bias voltage and 1 nA tunneling current to confirm the organization of cholesterol molecules and to obtain information on the structural and orientational aspects of the cholesterol molecules arranged on the 2NT-SAM. The structure of 2NT-SAM on Au (111) was already reported using STM [30]. It was shown to form a well aligned ( $\sqrt{3} \times 3$ ) R  $30^\circ$  over layer structure on Au (III) surface. Figure 3.8a shows the STM image of the monolayer of cholesterol molecules on the SAM of 2NT on evaporated gold surface. It can be seen that cholesterol molecules arrange themselves in rows forming a striped pattern.



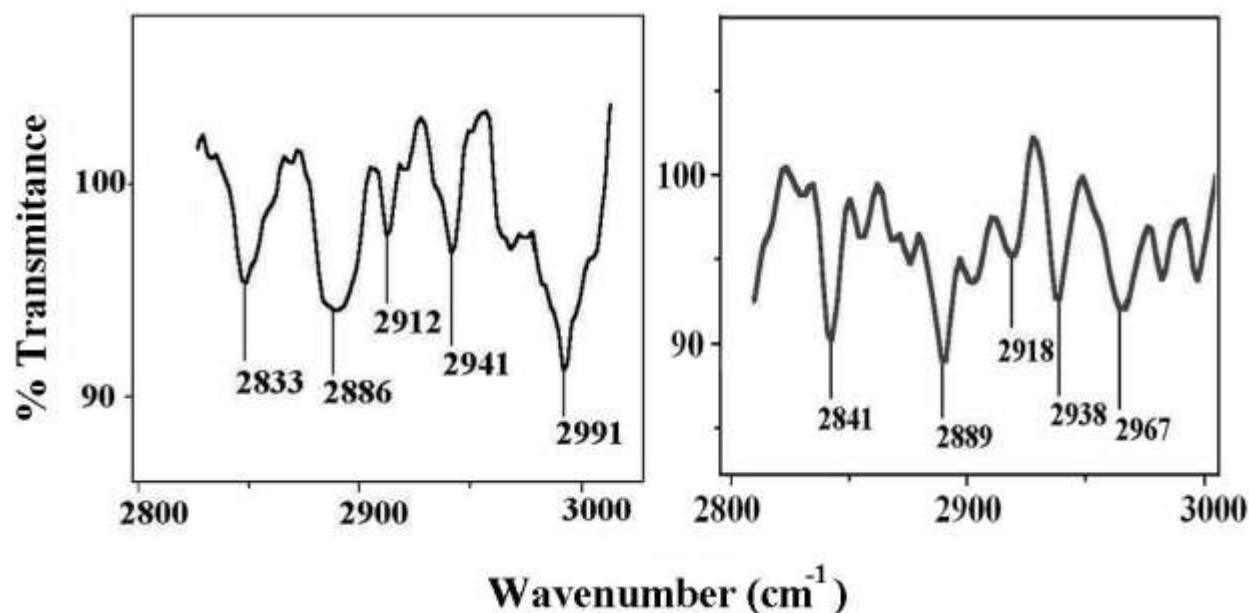
**Fig 3.8** Constant current STM images of (a) cholesterol monolayer on 2NT SAM showing individual cholesterol molecules arranged in rows (b) 3-d view of cholesterol monolayer on 2NT SAM showing individual cholesterol molecules. The lines drawn on the image show 0.5 nm along the rows and 1 nm along the columns. Tunneling current = 1nA; Bias voltage = +100 mV (substrate)

Figure 3.8b shows several bright features in the image. The bright features can be attributed to higher electron density polar  $-\text{OH}$  groups oriented in the upright direction. The calculated area occupied by individual cholesterol molecule from STM images is  $0.64 \text{ nm}^2$ . The tilt angle can be measured from the *arcos* function of the ratio of the true area of the molecule and area per molecule from STM image. This is calculated to be  $28.96^\circ$  from the surface normal.

The STM studies confirm the formation of a well-aligned compact monolayer of cholesterol molecules on 2NT-SAM. This is also in accordance with our electrochemical and AFM results.

### *Grazing angle FTIR analysis*

We have carried out grazing angle FTIR spectroscopy on the Au/2NT-SAM/LB system to confirm the organization of cholesterol on SAMs. Figure 3.9a and 3.9b are the FTIR spectra of the Au/2NT/cholesterol and Au/TP/cholesterol respectively.



**Fig. 3.9** Grazing angle FTIR spectra of (a) cholesterol film on 2NT SAM and (b) cholesterol film on TP SAM

We have observed the typical cholesterol peaks in both cases, which confirm the presence of cholesterol. The peaks are representative of the different modes of vibrations present in cholesterol. In 2NT system we have well defined peaks at 2833, 2886 and 2912  $\text{cm}^{-1}$  which correspond to the  $\text{CH}_2\text{C-H}$  symmetric stretch,  $\text{CH}_3\text{C-H}$  symmetric stretch and  $\text{CHC-H}$  asymmetric stretch respectively. Also we have peaks at 2941 and 2991  $\text{cm}^{-1}$  showing  $\text{CH}_2\text{C-H}$  asymmetric stretch and  $\text{CH}_3\text{C-H}$  asymmetric stretch respectively. The transmittance peaks are observed in case of TP system. Here the different peaks at 2841, 2889 and 2918  $\text{cm}^{-1}$  correspond to the  $\text{CH}_2\text{C-H}$  symmetric stretch,  $\text{CH}_3\text{C-H}$  symmetric stretch and  $\text{CHC-H}$  asymmetric stretch respectively. The peaks at 2938 and 2967  $\text{cm}^{-1}$  correspond to  $\text{CH}_2\text{C-H}$  asymmetric stretch and

CH<sub>3</sub>C-H asymmetric stretch respectively. The grazing angle FTIR spectra confirm the presence of cholesterol monolayer on the 2NT-SAM.

### **3.3 Electrochemical characterization of LB films of a discotic liquid crystal molecule and its complex with DNA**

Discotic liquid-crystal molecules (discogens) are of interest for their intriguing supramolecular architectures [47]. Their unique molecular electronic properties, such as two-dimensional delocalization of electrons, make them potential candidates for applications in devices such as light emitting diodes, photovoltaic solar cells and field-effect transistors [48]. In addition, these molecules are biologically significant. There are some naturally occurring disk-shaped biomolecules such as vitamins, hemoglobin and chlorophyll. Inspired by the wide range of applications, researchers have designed and synthesized several types of discogens [47]. An interesting class of discogens is the ionic discogen, which can find application in designing anisotropic ion-conductive materials [49]. Moreover, the cationic discogen molecules can be complexed with negatively charged biological molecules like DNA. In literature, there are several reports on aliphatic lipid-DNA complexes, which are primarily stimulated by nonviral gene delivery [50,51]. However, the discogen-DNA complexes have been studied only recently and they are expected to have some novel properties [52].

The self-assembly of discogen-DNA complexes, prepared in the bulk, are reported to exhibit a double lamello-columnar structure [53]. The discogen-DNA complex monolayer, prepared at an air-water interface, exhibited increased stability and rigidity as compared to the pure discogen monolayer [54]. Further, the discogen-DNA complex formed stable multilayers with high efficiency (transfer ratio  $\sim 1$ ) by LB technique. All these indicate a good packing between discogen and DNA molecules. There is a unique matching between the structures of DNA and discogen molecules. In a double-stranded DNA, the distance separating adjacent planes of hydrogen-bonded base pairs is 0.34 nm, close to the  $\pi$ - $\pi$  stacking distance of about 0.34 nm in the discogen columns. This enables a good packing between DNA and discogen molecules by electrostatic attraction. Another important aspect of the system is that, both DNA and discogen have their own intrinsic electronic properties. Therefore, complexing DNA with discogen is a novel approach to develop functional materials for organic electronics. Hence, the study of the electronic properties of such systems becomes significant. Recently, nanoscale

conductivity of LB films of a discogen-DNA complex studied using current-sensing atomic force microscopy was reported by Nayak *et al.* [55].

In this work, we report the electrochemical studies on LB films of an ionic discogen, viz., pyridinium tethered with hexaalkoxytriphenylene with bromide counterion (PyTp) and its complex with DNA (PyTp-DNA). We have analyzed the electrochemical barrier property of the LB films of discogen and its complex with DNA towards different redox systems. Our studies show the electron transfer reaction of the ferrocene redox system was allowed whereas the potassium ferrocyanide reaction was completely blocked. A mechanism for this interesting behavior is proposed.

### 3.3.1 Methods and materials

The material hexaalkoxytriphenylene with bromide counterion (PyTp) was synthesized by Sandeep Kumar *et al.* of this institute [56]. It is a discotic mesogen exhibiting columnar mesophase with the phase sequence: Solid-columnar (Col); 83.7°C, Col-isotropic; 95°C. The monolayer film of PyTp was prepared at air-water interface in a Langmuir trough (NIMA, model: 611M). To obtain PyTp-DNA complex monolayer film at A-W interface, we formed a PyTp monolayer on aqueous subphase containing  $10^{-8}$  M concentration of DNA. We have used double stranded deoxyribonucleic acid sodium salt (SIGMA) with approximate molecular weight of  $1.3 \times 10^6$  (~2000 bp).

The PyTp monolayer and the PyTp-DNA complex monolayer films were transferred at a target surface pressure of 35 mN/m onto gold coated glass substrates by LB technique. We have used both hydrophilic and hydrophobic gold substrates for LB film deposition. Evaporated Au strips were used for SAM formation and were pretreated with “piranha” solution (3:1 conc.  $\text{H}_2\text{SO}_4$ :  $\text{H}_2\text{O}_2$ ). The treatment with piranha removes all organic contaminations and yields the hydrophilic gold substrate. For hydrophobic surfaces we have formed SAMs of TP on gold surface. All the films with odd number of layers were transferred onto hydrophilic gold substrates, and those with even number of layers were transferred onto hydrophobic gold substrates.

The surface pressure-area per molecule isotherms of the PyTp monolayer, and the PyTp-DNA complex monolayer formed with  $10^{-8}$  M concentration of DNA in the subphase, are shown in Figure 3.10. The chemical structure of the molecule PyTp is shown as an inset in Figure 3.10.

On spreading the PyTp molecules on the surface of water, the  $\text{Br}^-$  counterions dissolve into the subphase and a positively charged PyTp monolayer forms at the air-water interface [57]. When such a monolayer was formed on an aqueous subphase containing DNA, the negatively charged phosphate groups of DNA interacted electrostatically with the cationic pyridinium groups in the PyTp monolayer and formed a PyTp-DNA complex monolayer film at the air-water interface. The PyTp-DNA complex monolayer exhibited a collapse pressure 25 % higher than the pure PyTp monolayer indicating enhanced stability.

For electrochemical studies, the PyTp film and the PyTp-DNA complex film were transferred at a target surface pressure of 35 mN/m by LB technique. The transfer efficiencies of these films were found to be in the range of 70-90 %. In an earlier report, it was shown that the PyTp molecules exhibit an edge-on configuration at this surface pressure in both the films [54].

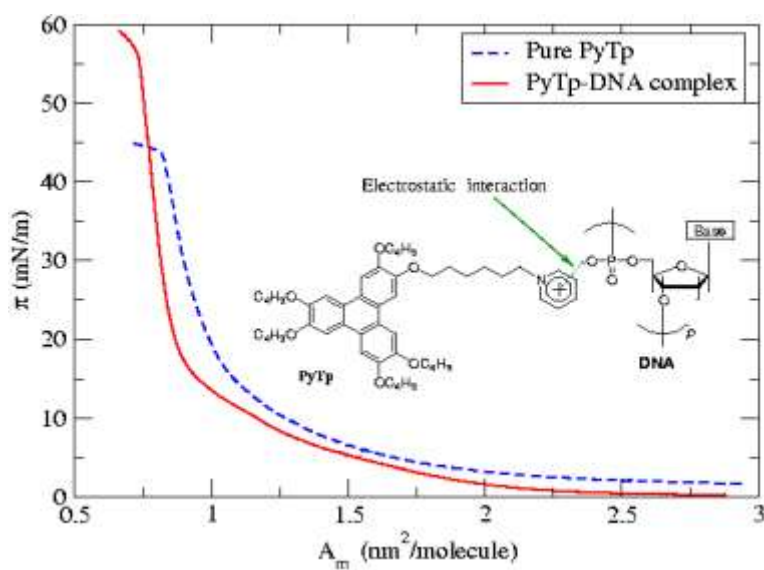


**Fig 3.10** Surface pressure ( $\pi$ )-area per molecule ( $A_m$ ) isotherms of pure PyTp monolayer (dashed line) and PyTp-DNA complex monolayer (continuous line). The complex monolayer was obtained with a subphase containing  $10^{-8}$  M concentration of DNA in ultra pure water. Inset shows the chemical structure of pyridinium tethered with hexaalkoxytriphenylene (PyTp) molecule with bromine as counterion (PyTp)

### 3.3.1.1 AFM studies

Figure 3.11 shows simultaneously acquired topography and phase images of the LB film of pure PyTp transferred onto gold coated glass substrates along with TP SAM modified gold substrate. The topography images (c.f. Figures 3.11a and c) could not reveal any significant differences in the morphology of the films because of the crystalline nature of the bare gold substrate. In this context, the respective phase images of these films provide very useful information (Figure 3.11b and d).

The phase imaging is known to be a powerful method for mapping the variations in composition, viscoelasticity, stiffness and adhesion of the sample surface at high spatial resolution [58,59]. The fact that the phase shift is sensitive to the material properties enabled us to distinguish between the LB films of pure PyTp and the PyTp-DNA complex [60].

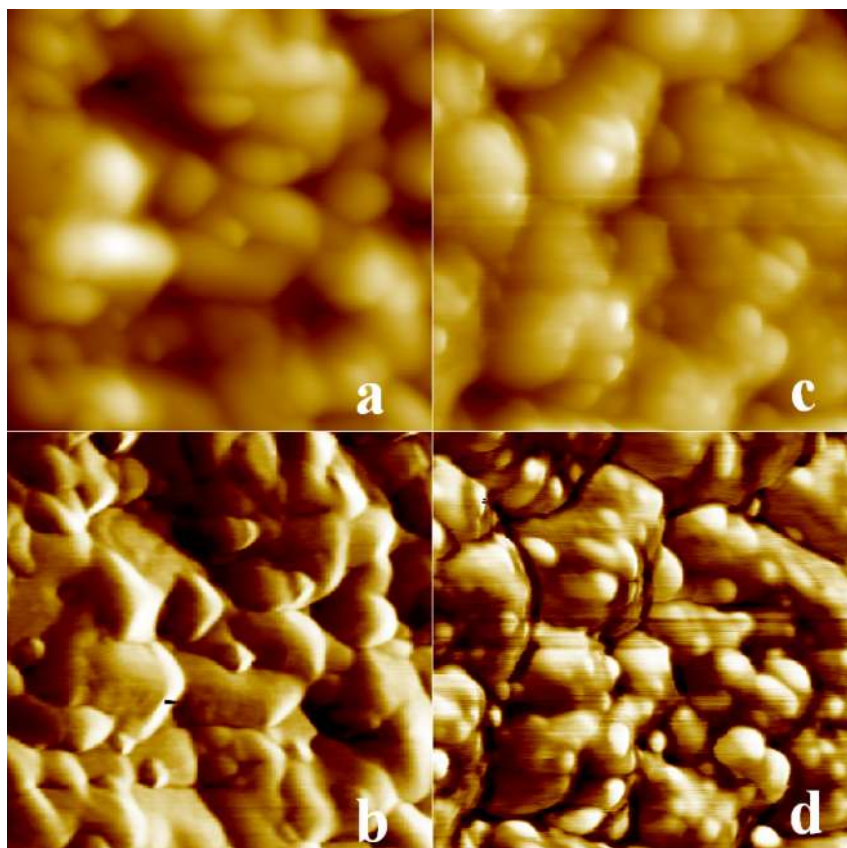


**Fig 3.11** AFM topography and phase images of the (a, topography and b, phase) TP SAM on gold, (c, topography and d, phase) 1 layer of PyTp on TP SAM (all the images are  $1\mu\text{m} \times 1\mu\text{m}$ )

Figure 3.12 shows the AFM topographic and phase images of PyTp-DNA complex LB films. In contrast to the pure PyTp film (Figure 3.11d), the phase images of the PyTp-DNA complex LB films with 2, 4 and 8 layers (Figure 3.12b, d and f) exhibit dark patches which can be attributed to DNA bundles present in the film. The PyTp-DNA complex LB film with 2 layers also exhibits fine thread-like features in the phase image (Figure 3.12b) indicating the presence of DNA [54]. These observations confirm the transfer of DNA from air-water interface to the air-solid interface during the LB process. In the following sections, we have presented the electrochemical studies performed on these films which revealed significant differences in the charge transfer properties of pure PyTp films and the PyTp-DNA complex films.

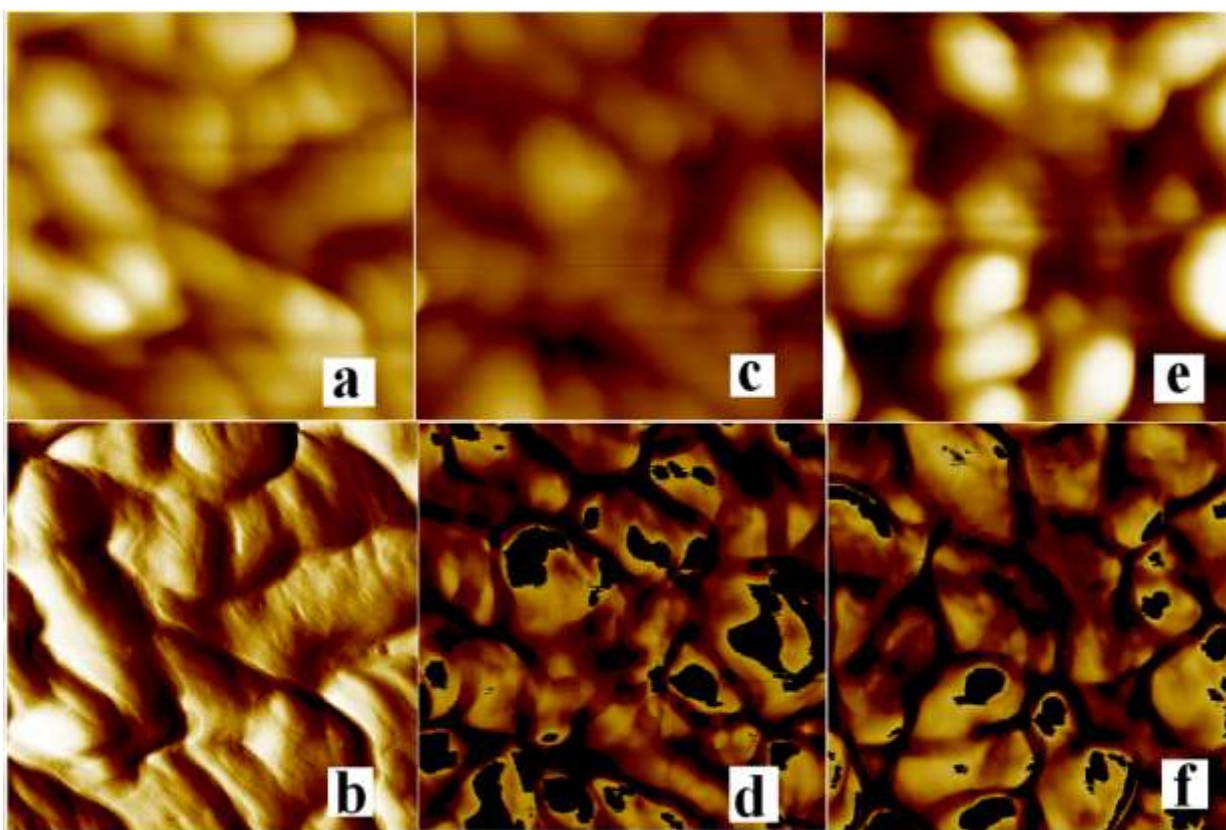


**Fig 3.12** AFM topography and phase images of the (a, topography and b, phase) 2 layers of DNA-PyTp complex on TP SAM, (c, topography and d, phase) 4 layers of DNA-PyTp complex on TP SAM and (e, topography, f phase) 8 layers of DNA-PyTp complex on TP SAM (all the images are  $1\mu\text{m} \times 1\mu\text{m}$ )

### 3.3.1.2 Electrochemical studies in aqueous system

We have deposited PyTp on both unmodified gold and TP SAM modified gold. It was shown that the TP SAM surface was an ideal platform for the deposition of the LB film [61]. The CV and EIS studies show that the LB film of PyTp on unmodified gold does not show any blocking towards the electron transfer reaction of  $[\text{Fe}(\text{CN})_6]^{3-/4-}$  (Figure 3.13a, 3.14a). This behavior shows that PyTp does not form stable film on unmodified gold and the monolayer film detaches away in the aqueous solution.

The LB deposition of PyTp was also carried out on TP SAM, it forms 2 layers on TP SAM during upward and downward dipping. The superior LB deposition on TP SAM is because of the hydrophobic nature of the TP SAM which is a suitable platform for the deposition of the hydrophobic PyTp. TP SAM is useful in the electrochemical point of view also because it does not show any electron transfer blocking of  $[\text{Fe}(\text{CN})_6]^{3-/4-}$  redox reaction and it is possible to study the electron transfer barrier property of the subsequently deposited films on TP SAM [61].

The CV in 1 mM potassium ferrocyanide + 1 M NaF does not show any peak current for Py-Tp on TP modified surface which indicates the complete blocking of the electron transfer reaction (Figure 3.13b). EIS quantifies the blocking ability of the system in terms of charge transfer resistance ( $R_{ct}$ ) for the electron transfer reaction. The  $R_{ct}$  value in the case of PyTp LB film on unmodified gold is  $5.17 \Omega \cdot \text{cm}^2$  (Figure 3.14a) whereas the  $R_{ct}$  value for LB film of PyTp on TP SAM is  $9.93 \text{ K}\Omega \cdot \text{cm}^2$  (Figure 3.14b). The more than three orders of magnitude change in  $R_{ct}$  shows the formation of better organized film with very few pin holes and defect sites. The above EIS results endorse the behavior of the two systems in CV experiment.

Measurement of interfacial capacitance is very important to study the ionic permeation through a thin film. The capacitance of the electrical double layer precisely describes the adsorption properties and is being used widely in the study of thin films on metal surfaces [61-63]. We have earlier shown that the interfacial capacitance can be precisely measured in pure supporting electrolyte and by carefully selecting the high frequency region of the impedance plot where the capacitance essentially remains constant [61,63]. The capacitance measurements were carried out in 1 M NaF solution without any redox species.

The interfacial capacitance value for the 2 layers LB film of PyTp on TP SAM is found to be  $1.45 \mu\text{Fcm}^{-2}$ . From this value, the calculated dielectric constant is 0.77 which is smaller

than the observed dielectric constant value of triphenylene (2.5). The probable reason for this is the ionic permeation through the pin holes and defects present in the LB film which causes the electrolyte ions to reach near the electrode surface. Thus the decrease in the effective distance increases the capacitance which otherwise would be  $0.4 \mu\text{Fcm}^{-2}$  for a fully compact and impermeable film.

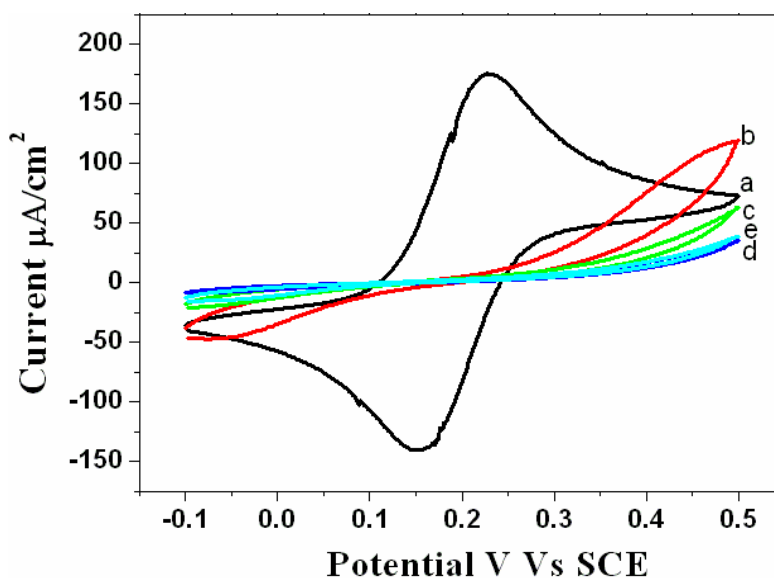


**Fig 3.13** Cyclic voltammogram of (a) LB film of PyTp on unmodified gold, (b) PyTp 2 layers on TP SAM modified gold, (c) LB bilayer of DNA-PyTp on TP SAM modified gold (d) 4 layers of DNA-PyTp complex on TP SAM modified gold and (e) 8 layers of DNA-PyTp complex on TP SAM modified gold in 1mM potassium ferrocyanide solution with 1M NaF as supporting electrolyte

DNA is found to form complex with PyTp at air-water interface and the complex is quite stable under ambient conditions. We have deposited different number of layers of the complex on the unmodified and TP SAM modified gold. The CV results show that the complex deposited on gold does not show any blocking behavior towards the redox reaction of  $[\text{Fe}(\text{CN})_6]^{3-/4-}$ . Thus we can conclude that the LB deposition of DNA-PyTp on unmodified gold is poor. The LB bilayer of DNA-PyTp on TP modified gold shows enhanced barrier properties towards the same redox system. The cyclic voltammogram shows complete blocking of the electron transfer reaction (Figure 3.13c). The blocking in case of DNA-PyTp bilayer is even better than the PyTp bilayer.

The observation is further confirmed by EIS studies where the DNA-PyTp bilayer system shows very high  $R_{ct}$  value, 21.4  $K\Omega.cm^2$  (Figure 3.14c). Hence we conclude that the DNA-PyTp system has fewer pin holes and defects than the PyTp bilayer. The interfacial capacitance analysis gives a capacitance value  $1.24 \mu Fcm^{-2}$ . This again shows that this system is less permeable for ions.

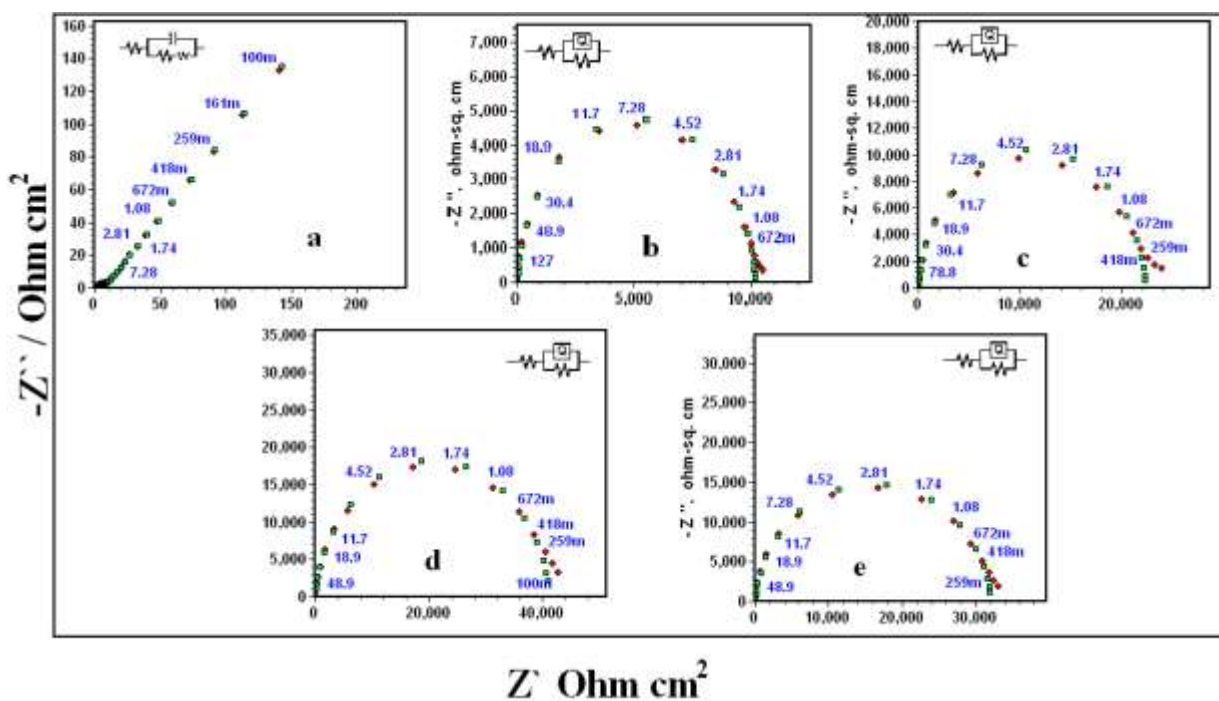


**Fig. 3.14** Nyquist plots for electrochemical impedance spectroscopy for (a) LB film of PyTp on unmodified gold, (b) PyTp 2 layers on TP SAM modified gold, (c) LB bilayer of DNA-PyTp on TP SAM modified gold (d) 4 layers of DNA-PyTp complex on TP SAM modified gold and (e) 8 layers of DNA-PyTp complex on TP SAM modified gold in 1mM potassium ferrocyanide and 1mM potassium ferricyanide solution with 1M NaF as supporting electrolyte

We have further deposited 4 layers of DNA-PyTp complex on TP modified gold. We found that 4 layers system still enhances the electron transfer barrier properties towards the redox reaction. Cyclic voltammogram shows the decrease in the current (Figure 3.13d) and the observed  $R_{ct}$  value in this case is 41.2  $K\Omega.cm^2$  (Figure 3.14d). Interfacial capacitance value also decreases in this system and it measured to be  $0.91 \mu Fcm^{-2}$ . Deposition of further layers does not improve the barrier property but it is rather stable. 8 layers LB film of DNA-PyTp complex shows an  $R_{ct}$  value 32  $K\Omega.cm^2$  and capacitance value  $1.2 \mu Fcm^{-2}$  (Figure 3.13e, 3.14e). The

charge transfer resistance and interfacial capacitance values for all the systems are summarized in Table 3.5.

Electrode type	$R_{ct}$ (K $\Omega$ .cm <sup>2</sup> )	$C_{dl}$ ( $\mu$ Fcm <sup>-2</sup> )
SAM of TP	0.46	3.96
2 layers of PyTP on TP SAM	9.93	1.45
2 layers of DNA-PyTP on TP SAM	21.4	1.24
4 layers of DNA-PyTP on TP SAM	41.2	0.91
8 layers of DNA-PyTP on TP SAM	32.0	1.20

**Table 3.5** charge transfer resistance ( $R_{ct}$ ) in  $[Fe(CN)_6]^{3-/4-}$  and interfacial capacitance ( $C_{dl}$ ) in pure supporting electrolyte, NaF for different LB films on TP SAM

### 3.3.1.3 Electrochemical studies in nonaqueous (ethanol) medium: Ferrocene redox reaction

We have carried out electrochemical studies on the LB films of discotic liquid crystal and DNA-discotic liquid crystal complex in ethanol for ferrocene redox system. 1 mM ferrocene solution was prepared in ethanol with 0.1 M LiClO<sub>4</sub> as a supporting electrolyte. Figure 3.15 shows the behavior of different layer systems in ferrocene. The electrochemical results show that the redox reaction in the ferrocene is not hindered in any of the LB film system composed of discotic liquid crystal and DNA-discotic liquid crystal complex.

Although there is slight asymmetry observed in the cyclic voltammograms which may be due to the different number of LB layers on the electrode, nevertheless the anodic and cathodic peak separation is close to 70 mV in all the cases. This shows the facile nature of the ferrocene charge transfer process even in the presence of LB film of DNA-discotic complex. The EIS results are shown in Figure 3.16. This shows that the process is fully under diffusion controlled. This behavior is different from the  $[Fe(CN)_6]^{3-/4-}$  redox reaction. Normally such anomaly may be attributed to the disorganization of the film in the non-aqueous solvent such as ethanol. To check this, we again carried out CV experiment in  $[Fe(CN)_6]^{3-/4-}$  soon after doing the experiment in the ferrocene medium. Surprisingly we found that electron transfer reaction is not allowed in  $[Fe(CN)_6]^{3-/4-}$  (Figure 3.17(a-d)). This confirms that the LB film has not been detached by the nonaqueous electrolytic system.

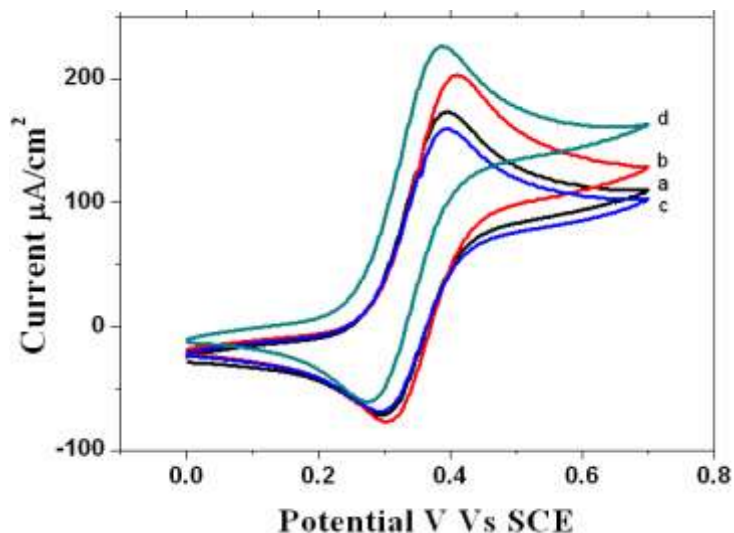


**Fig 3.15** Cyclic voltammogram of (a) PyTp on TP SAM, (b) 2 layers of DNA-PyTp on TP SAM, (c) 4 layers of DNA-PyTp on TP SAM and (d) 8 layers of DNA-PyTp on TP SAM in 1mM ferrocene in ethanol with 0.1 M LiClO<sub>4</sub> as supporting electrolyte

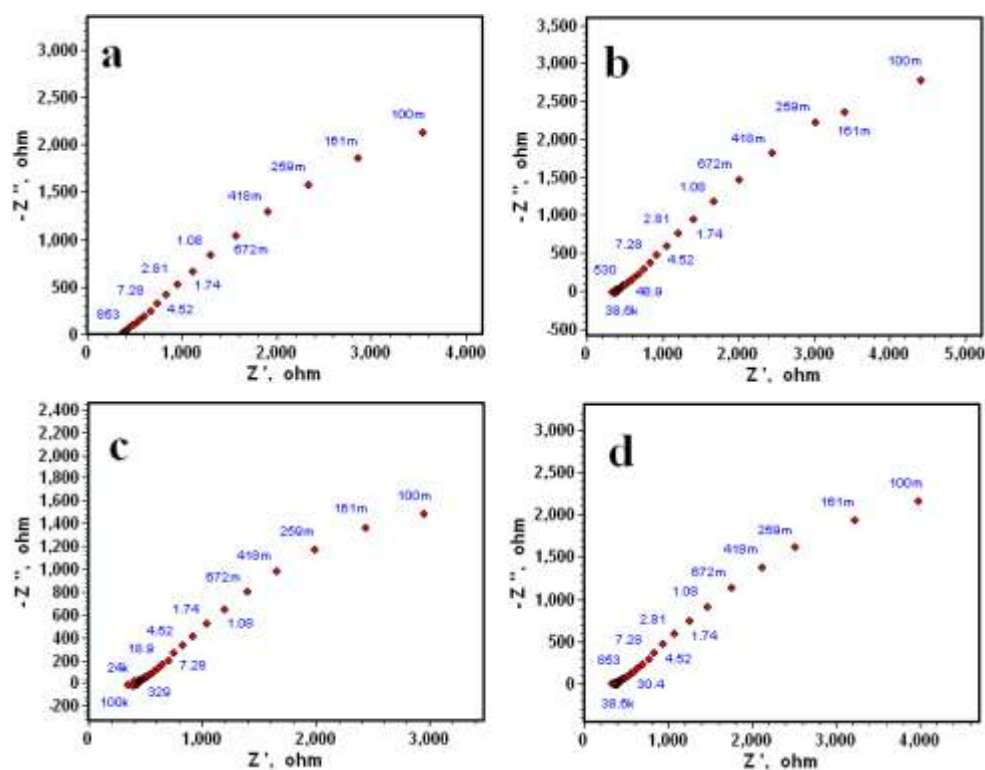


**Fig 3.16** EIS results for (a) PyTp on TP SAM, (b) 2 layers of DNA-PyTp on TP SAM, (c) 4 layers of DNA-PyTp on TP SAM and (d) 8 layers of DNA-PyTp on TP SAM in 1mM ferrocene in ethanol with 0.1 M LiClO<sub>4</sub> as supporting electrolyte

Moreover the potential range for the CV in ferrocene is also similar to what we employed in  $[\text{Fe}(\text{CN})_6]^{3-/4-}$  system therefore the question of the potential induced disturbance in the film is ruled out.

We propose the probable cause for the ferrocene redox reaction as due to the bridge mediated electron transfer [64] where the electron transfer takes place through the medium between the electrode and the redox molecule. The medium could be a nanosize organic film. It is well known that ferrocene undergoes an outer-sphere electron-transfer reaction in which the redox species come close to the SAM-modified electrode surface and electron transfer takes place with the metal at some distance. Also ferrocene has  $\pi$ -electrons which can also interact with the  $\pi$ -electrons of the DNA-PyTp film.

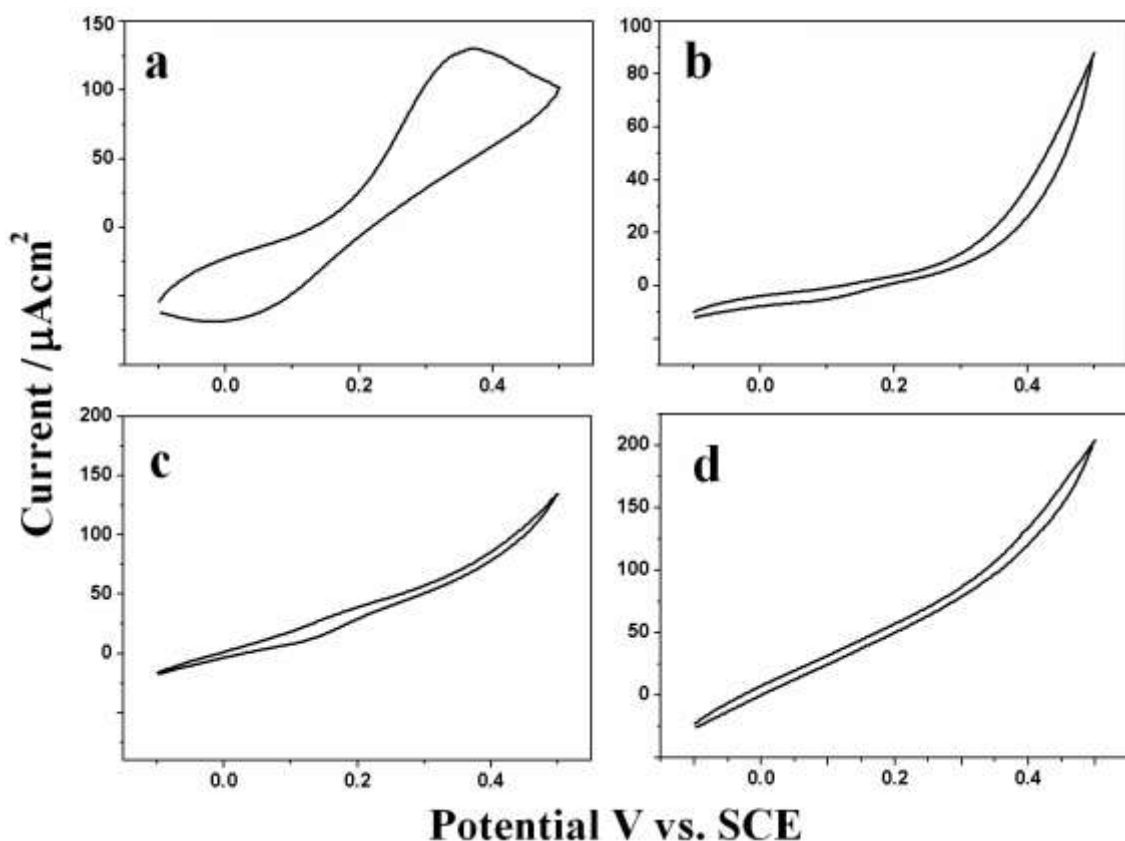


**Fig. 3.17** Cyclic voltammograms recorded in potassium ferrocyanide solution with 1.0 M NaF as supporting electrolyte soon after the electrochemical experiment in ferrocene (a) PyTp on TP SAM, (b) 2 layers of DNA-PyTp complex on TP SAM, (c) 4 layers of DNA-PyTp complex on TP SAM and (d) 8 layers of DNA-PyTp complex on TP SAM

This is in contrast to that of the redox reaction of the  $[\text{Fe}(\text{CN})_6]^{3-/4-}$  system, which involves the formation of reaction intermediates that get adsorbed on the electrode surface. But in the present case of DNA-PyTp film the negative charge of the LB film will repel the negatively charged  $[\text{Fe}(\text{CN})_6]^{3-/4-}$ . That is also the reason of the high charge transfer resistance shown in  $[\text{Fe}(\text{CN})_6]^{3-/4-}$  case.

Discotic molecule PyTp and DNA-PyTp complex are rich in  $\pi$ -electrons. Furthermore DNA has been shown to act as a bridge for electron conduction as well [65,66]. The presence of  $\pi$ -electron rich discotic molecules between the electrode and redox species which is an LB film in the present case, tends to promote the electron transfer process. The  $\pi$ -electrons of ferrocene molecule will interact with the  $\pi$ -electrons of the LB film.

The bridge mediated electron transfer actually assists in the electron transfer process. However, the electron transfer by tunneling depends upon the distance between the donor and acceptor sites. When the redox species are somewhat far away from the surface, the electron transfer would be slow whereas if the redox species are near to the electrode surface electron transfer will be fast. In the case of distant-dependent electron transfer for a bridge mediated system, the current (I) is exponentially related to the distance (x) between the donor and acceptors by the relationship  $I \propto e^{-\beta x}$ , where  $\beta$  is the inverse decay length. The value of  $\beta$  also depends on the nature and structure of the film.  $\beta$  is observed to be smaller for the system with  $\pi$ -electrons compare to the saturated system without  $\pi$ -electrons like alkanethiols SAM [67-69]. This is attributed to the delocalization of donor and acceptor states on the bridge.

### **3.4 Cyclodextrin inclusion complexes (ICs) with thiocholesterol and their self-assembly on gold: A combined electrochemical and lateral force microscopy (LFM) analysis**

Different approaches are being used for building the architecture for molecular electronics. Self-assembly of certain organic thiol molecules on surfaces is of significant interest and it has been widely perceived to find applications in molecular electronics [70-73], and fundamental studies of creating hydrophobic and hydrophilic surfaces [74,75]. Cyclodextrins are the cyclic oligosaccharides of glucose having different number of glucose units in them. For example  $\alpha$ ,  $\beta$  and  $\gamma$  cyclodextrins have 6, 7 and 8 glucose units respectively. Owing to their hydrophobic cavity they are known to form inclusion complexes (ICs) with various hydrophobic compounds

[76-80]. The main advantage of the inclusion complex (IC) is the increased solubility of the guest in water. Also since cyclodextrins are nontoxic they find useful applications in drug, food, agricultural and environmental related industries.  $\beta$ -cyclodextrin and methyl  $\beta$ -cyclodextrin are extensively used to remove cholesterol from cultured cell [81-83]. There are several reports on the formation of IC between cyclodextrins and cholesterol. Thiocholesterol is the thiol analogues of the cholesterol and it forms SAM on gold. Yang *et al.* have studied the behavior of thiocholesterol SAM by electrochemical methods and IRAS spectroscopy [84,85]. Thiocholesterol forms a defect rich monolayer (65% coverage) on gold surface. These defects arise because the molecular packing in SAM is not compact because of its structure. There are a few literature reports on the formation of the inclusion complexes and the self-assembly of the inclusion complexes onto gold. Yan *et al.* have made the SAM of IC of alkanethiols [80] and viologens [78] with  $\alpha$ -cyclodextrin and  $\beta$ -cyclodextrin. The resulting SAM shows better electron transfer blocking properties than corresponding alkanethiol. Samitsu *et al.* have immobilized the molecular tubes made up of cyclodextrin on gold surface using self-assembly process [77].

In this work we report the self-assembly of the host-guest inclusion complex (IC) made up of  $\beta$ -cyclodextrin and thiocholesterol. We have characterized the SAM of IC by electrochemical methods such as CV and EIS. Electrochemical characterization is very useful in order to get the information about the ionic permeability of the SAM which is determined by the compactness of the film. We have used the redox system of  $[\text{Fe}(\text{CN})_6]^{3-/4-}$  as probe to evaluate the barrier properties of the system.

We have also carried out LFM, also known as friction force microscopy, studies on the film. The LFM technique is known to reveal the presence of materials with different chemical characteristics on surface [86-88]. It can give important information about the hydrophilic and hydrophobic regions present on the surface. That arises because of the different kind of interactions observed by the tip while scanning different regions on the substrate. Combined with the topographical analysis by AFM and force distance curve, LFM is a compelling technique for surface characterization. So far there is no study in the literature about the friction imaging of the surface coated with the self assembled monolayer of IC and the measurements of the interaction force by force-distance spectroscopy. In this work we have also studied the SAM composed of IC of methyl  $\beta$ -cyclodextrin and thiocholesterol.

### 3.4.1 Methods and materials

#### 3.4.1.1 Inclusion complex: Formation and self-assembly on gold

Thiocholesterol solution was prepared in isopropanol/chloroform (2:1) in a beaker and 8 mg of thiocholesterol was dissolved into 5 ml of that solution. 330 mg of  $\beta$ -cyclodextrin was dissolved in 5 ml of the phosphate buffer solution of pH = 7. The  $\beta$ -cyclodextrin solution was kept for heating at around 70°C and thiocholesterol solution was added slowly into the  $\beta$ -cyclodextrin solution with continuous stirring. Initially there was a formation of turbid colored solution which turned into a clean solution on further addition. This is the indication of the formation of the inclusion complex. The IC was found to be very stable at room temperature for several days. We have used the above IC solution directly as the loading solution for the SAM formation. The similar procedure was followed in the case of methyl  $\beta$ -cyclodextrin too. For comparison we have also formed the SAM of thiocholesterol. We have used 0.3 mM thiocholesterol solution in ethanol as a loading solution for the SAM. Au strips were used for SAM formation and were pretreated with “piranha” solution (3:1 conc. H<sub>2</sub>SO<sub>4</sub> : H<sub>2</sub>O<sub>2</sub>). SAMs were prepared by immersing the gold substrate in the aqueous solution of IC for 24 hours. After the adsorption of IC, the substrates were thoroughly rinsed with distilled water and finally with Millipore water and used for the electrochemical and AFM analysis.

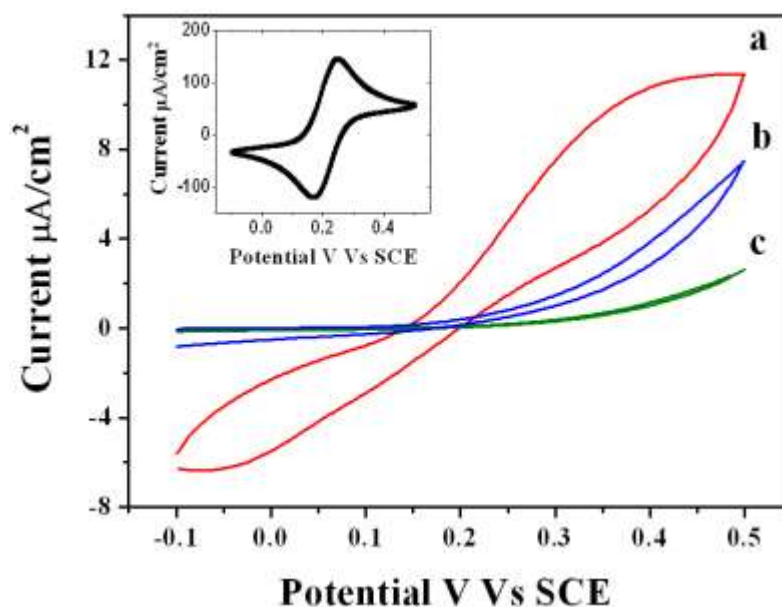
#### 3.4.1.2 Electrochemical characterization

#### **$\beta$ -cyclodextrin-thiocholesterol and methyl $\beta$ -cyclodextrin-thiocholesterol inclusion complex SAM in [Fe(CN)<sub>6</sub>]<sup>3-/4-</sup> solution**

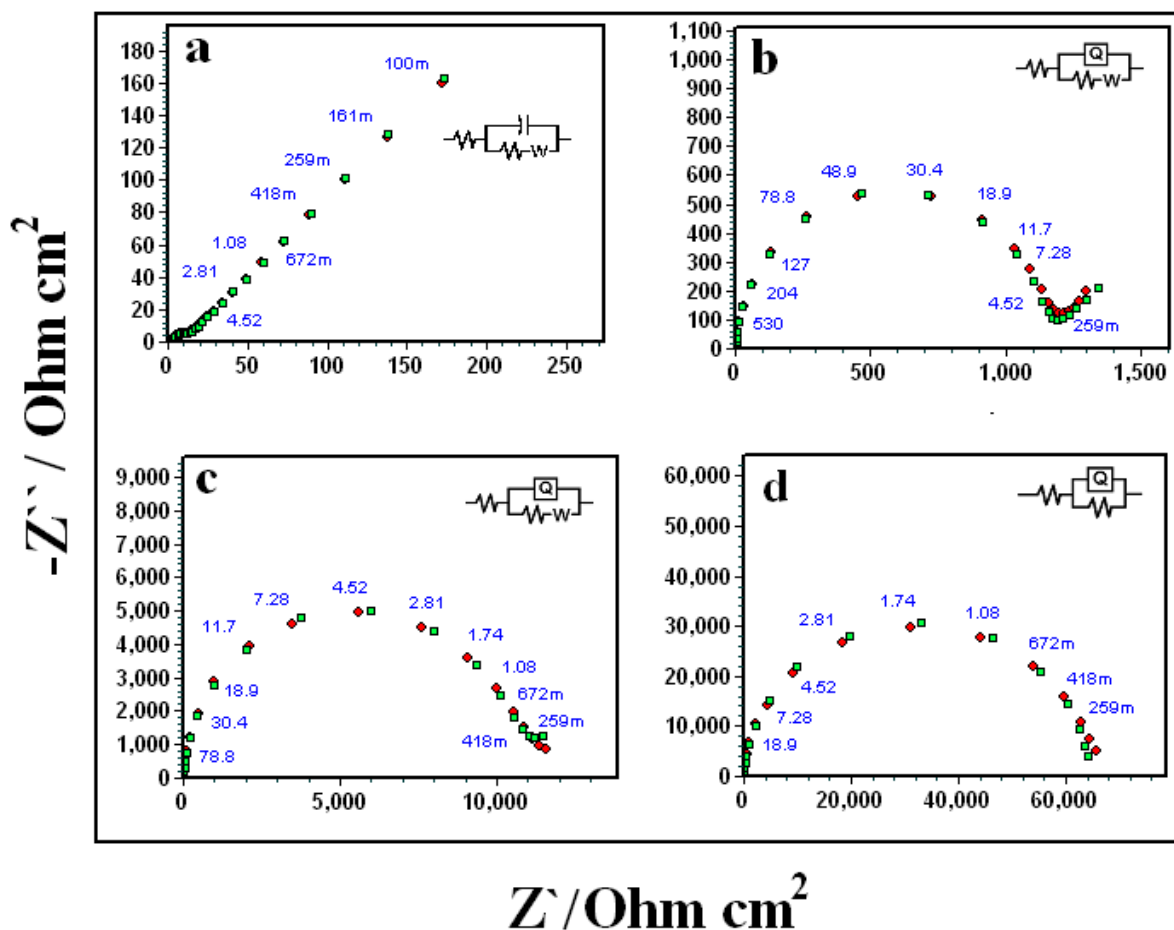
The electrochemical characterization of the SAM was carried out using CV and EIS in order to understand the electron transfer properties of the different redox species across the film and also the ionic permeation through the film.

Figure 3.18 shows the cyclic voltammograms in the [Fe(CN)<sub>6</sub>]<sup>3-/4-</sup> for the (a) Thiocholesterol SAM on gold surface, (b)  $\beta$ -cyclodextrin-thiocholesterol IC SAM on gold, (c) methyl  $\beta$ -cyclodextrin-thiocholesterol IC SAM on gold and inset shows the response of gold electrode. The relatively large current in the case of Figure 3.18(a) for the thiocholesterol SAM can be attributed to the noncompact film formed in this case. The cyclic voltammogram for

thiocholesterol shows very little peak current that confirms that the SAM does not block the electron transfer reaction completely. However  $\beta$ -cyclodextrin-thiocholesterol IC SAM on gold shows improved blocking behavior over the thiocholesterol SAM. The cyclic voltammogram shows no peaks. It confirms that the electron transfer is blocked significantly that can happen when cyclodextrin molecules form a rigid network on the electrode surface which does not allow ions from solution to permeate the monolayer.  $\beta$ -Cyclodextrin has hydrophilic outer core due to the presence of hydroxyl groups. These -OH groups are responsible for the high water solubility of the cyclodextrin. Also the secondary hydroxyl groups located on the cyclodextrin can stabilize the SAM by forming the intermolecular hydrogen bonds among themselves [80,89]. This kind of network will be very stable compared to the thiocholesterol SAM. Figure 3.18(c) is the cyclic voltammogram for methyl  $\beta$ -cyclodextrin-thiocholesterol IC SAM on gold which shows excellent electron transfer blocking. Methyl  $\beta$ -cyclodextrin is known to form inclusion complex with cholesterol and we find that it is more efficient than the  $\beta$ -cyclodextrin [83]. The reason for the higher electron transfer blocking property arises due to the large number of ICs, forming a more compact film which is better than the  $\beta$ -cyclodextrin-thiocholesterol IC SAM.



**Fig. 3.18** Cyclic voltammograms in the  $[Fe(CN)_6]^{3-/4-}$  for the (a) thiocholesterol SAM on gold surface, (b)  $\beta$ -cyclodextrin-thiocholesterol IC SAM on gold, (c) methyl  $\beta$ -cyclodextrin-thiocholesterol IC SAM on gold and inset shows the CV for bare gold electrode



**Fig. 3.19** The electrochemical impedance spectroscopy results in the potassium ferrocyanide/ferricyanide for the (a) bare gold electrode (b) thiocholesterol SAM on gold surface, (c)  $\beta$ -cyclodextrin-thiocholesterol IC SAM on gold and (d) methyl  $\beta$ -cyclodextrin-thiocholesterol IC SAM on gold

Figure 3.19 shows the EIS results in the  $[\text{Fe}(\text{CN})_6]^{3-/4-}$  for (a) bare gold electrode (b) thiocholesterol SAM on gold surface, (c)  $\beta$ -cyclodextrin-thiocholesterol IC SAM on gold, (d) methyl  $\beta$ -cyclodextrin-thiocholesterol IC SAM on gold.

It can be seen from Figure 3.19(a) that the impedance plot for the bare gold electrode shows a very small semicircle at high frequency range and a straight line over a wide frequency window signifying a process that is fully under diffusion control. Figure 3.19(b) shows the EIS plot for the thiocholesterol SAM with the large semicircle showing the reaction is under charge transfer control. The  $R_{ct}$  value was found to be 1.1  $\text{K}\Omega \cdot \text{cm}^2$ . Figure 3.19(c) shows an increase in the diameter of the semicircle, the  $R_{ct}$  value for this SAM is observed to be 10.5  $\text{K}\Omega \cdot \text{cm}^2$ . There

is an increase in the  $R_{ct}$  by ten times in this case. Figure 3.19(d) shows the impedance plot for the methyl  $\beta$ -cyclodextrin-thiocholesterol SAM which shows a large  $R_{ct}$  value  $64.6 \text{ K}\Omega\cdot\text{cm}^2$ . These results are in accordance with the CV results. Thus in summary the electron transfer blocking sequence was found to be thiocholesterol SAM <  $\beta$ -cyclodextrin-thiocholesterol SAM < methyl  $\beta$ -cyclodextrin-thiocholesterol SAM. The  $R_{ct}$  values are shown in Table 3.6.

We have also carried out interfacial capacitance studies using EIS. We have earlier shown that the interfacial capacitance can be precisely measured in pure supporting electrolyte and by carefully selecting the high frequency region of the impedance plot where the capacitance essentially remains constant [61]. The experiments were performed in 1 M NaF solution without any redox species. Table 3.6 shows the values of interfacial capacitance in different electrode systems.

We have observed a capacitance value of  $3.5 \mu\text{Fcm}^{-2}$  for thiocholesterol SAM. This value is larger than the value expected from a compact SAM and this shows the porous nature of the thiocholesterol SAM that is permeable for the ions in electrolyte solution. However the  $\beta$ -cyclodextrin-thiocholesterol SAM shows capacitance values of  $3.0 \mu\text{Fcm}^{-2}$ .

Electrode Type	Capacitance ( $\mu\text{Fcm}^{-2}$ )	$R_{ct}$ ( $\text{K}\Omega\cdot\text{cm}^2$ )
Thiocholesterol SAM	3.5	1.1
$\beta$ -cyclodextrin-thiocholesterol IC SAM	3.0	10.5
Methyl $\beta$ -cyclodextrin-thiocholesterol IC SAM	1.3	64.6

**Table 3.6** Interfacial capacitance in pure supporting electrolyte (NaF) and charge transfer resistance values for different systems in  $[\text{Fe}(\text{CN})_6]^{3-/4-}$  redox system

Methyl  $\beta$ -cyclodextrin-thiocholesterol SAM shows a further decrease in the capacitance which is  $1.3\mu\text{Fcm}^{-2}$ . The rather low capacitance value may arise due to the less hydrophilic nature of the methyl  $\beta$ -cyclodextrin-thiocholesterol SAM than the  $\beta$ -cyclodextrin-thiocholesterol SAM. Methyl  $\beta$ -cyclodextrin-thiocholesterol SAM as we have already discussed shows high  $R_{ct}$  value. It is known that Methyl  $\beta$ -cyclodextrin forms complex with cholesterol more efficiently than  $\beta$ -cyclodextrin [83]. The high  $R_{ct}$  reflects a more ordered film. This also leads to lower value of the capacitance as the ions are prevented from penetrating the film.

### 3.4.1.3 Lateral force microscopy studies and force-distance measurements on the different SAM systems

#### *LFM imaging*

Lateral force microscopy provides an excellent method to probe the lateral or the friction forces present between the probe tip and the substrate. LFM studies are valuable for imaging the variations in surface friction while scanning by an AFM in contact mode. Friction forces can arise from inhomogeneity in surface properties for example the presence of the hydrophobic and hydrophilic films on any surface, which can yield different values of friction force and this can be easily probed with LFM. An LFM is a very sensitive tool to detect the changes in material property when no accompanying changes in morphology occur [86-88].

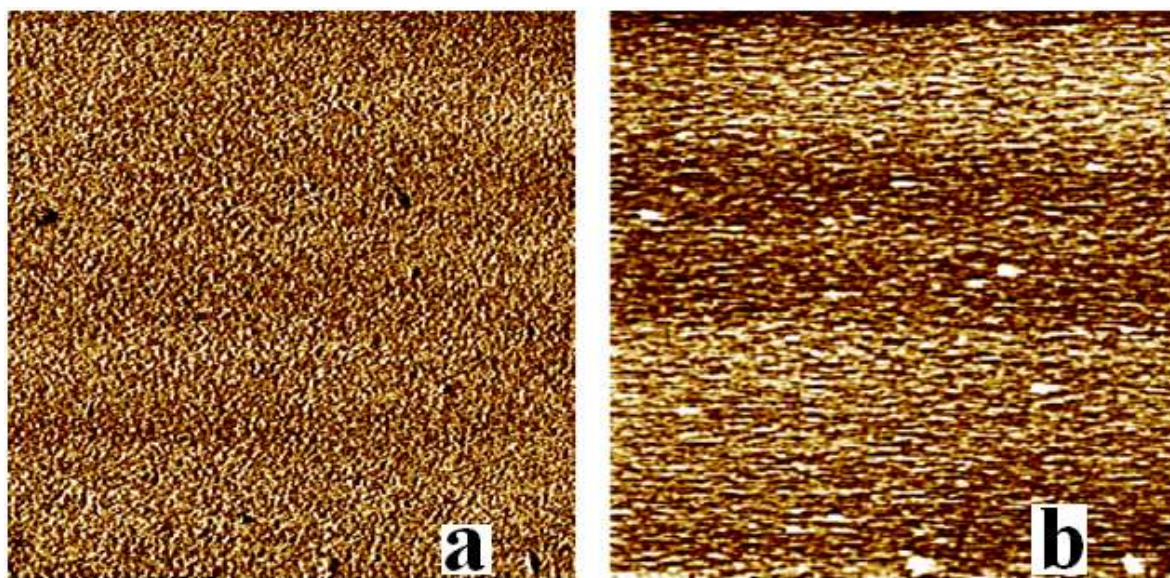


**Fig. 3.20**  $10\ \mu\text{m} \times 10\ \mu\text{m}$  LFM image (a) and corresponding topographic image (b) for bare gold

Therefore it is suitable technique for imaging the SAM surface composed of  $\beta$ -cyclodextrin-thiocholesterol IC SAM and methyl  $\beta$ -cyclodextrin-thiocholesterol IC SAM. Figures 3.20, 3.21, 3.22 and 3.23 show the different LFM images and their corresponding topographic images.

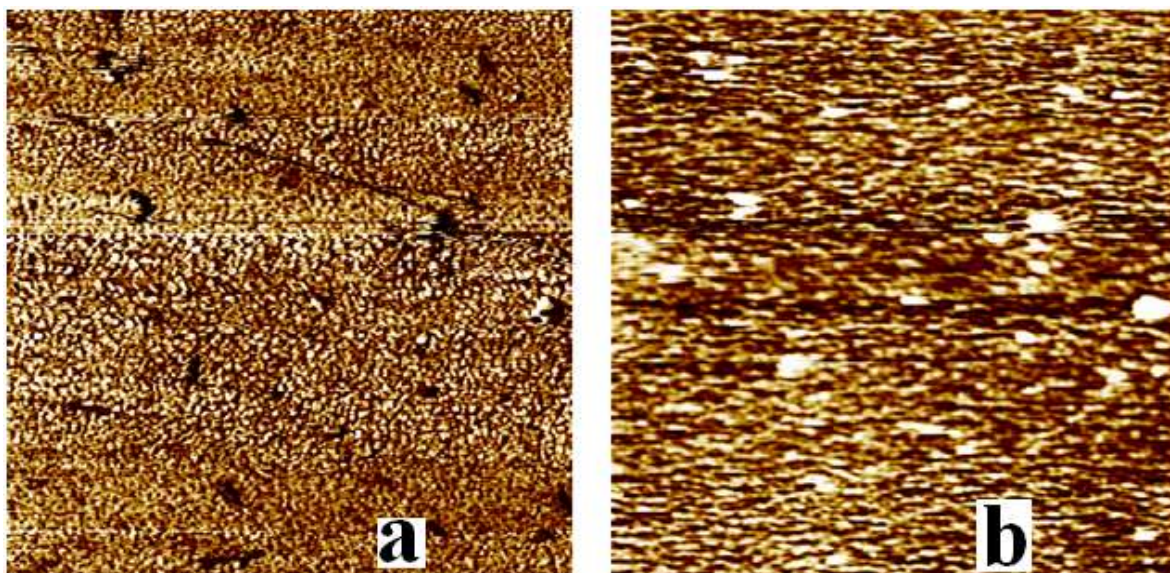


*Fig. 3.21 10  $\mu\text{m}$  x 10  $\mu\text{m}$  LFM image (a) and corresponding topographic image (b) for thiocholesterol SAM*

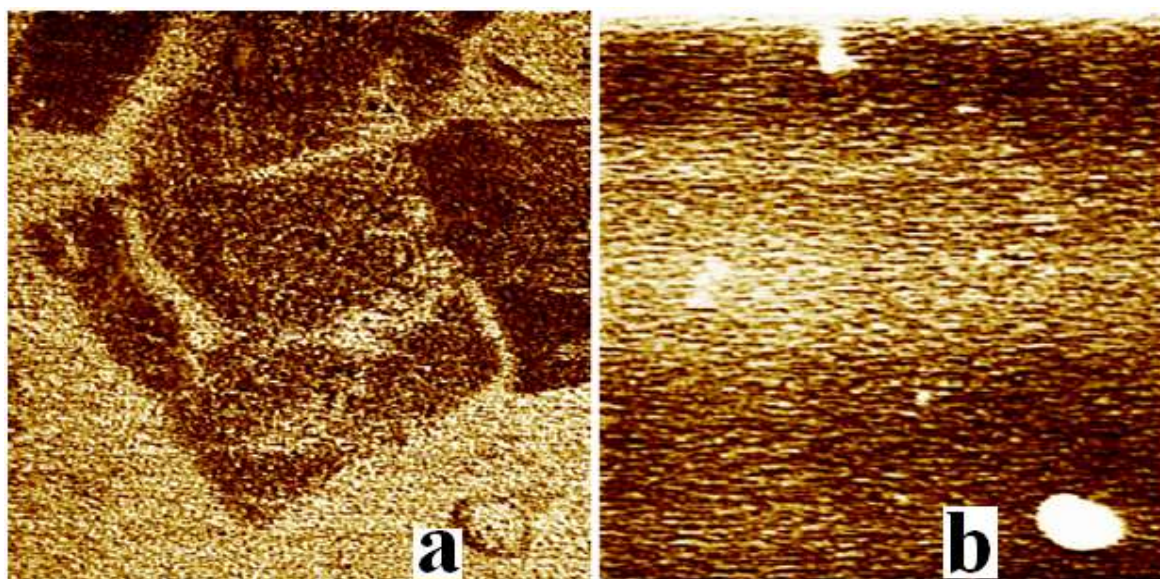


*Fig. 3.22 10  $\mu\text{m}$  x 10  $\mu\text{m}$  LFM image (a) and corresponding topographic image (b) of  $\beta$ -cyclodextrin-thiocholesterol SAM*

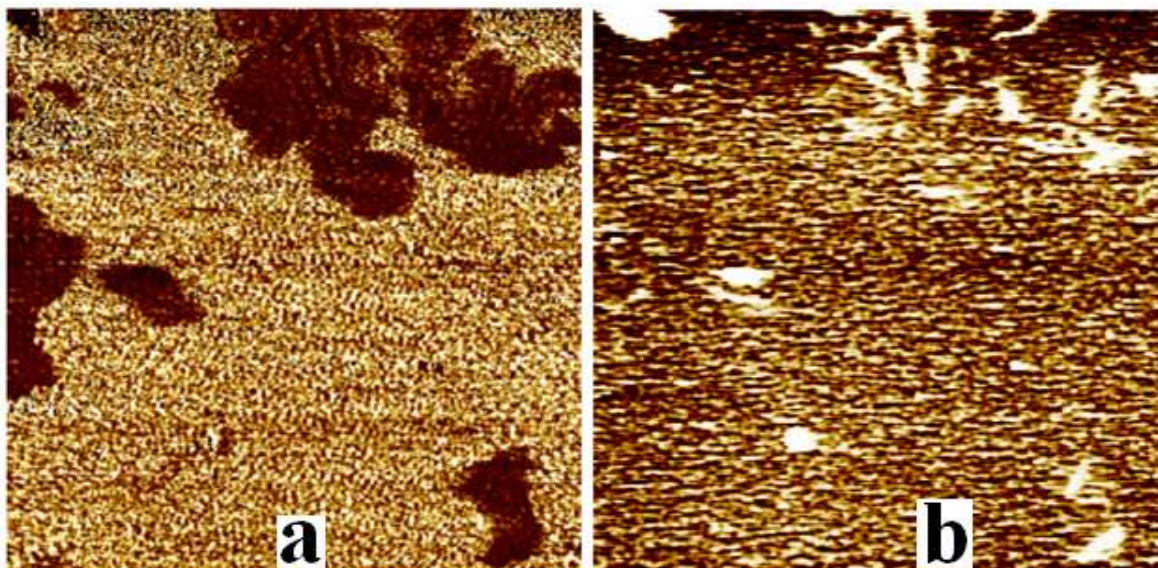


**Fig. 3.23**  $10\ \mu\text{m} \times 10\ \mu\text{m}$  LFM image (a) and corresponding topographic image (b) of methyl  $\beta$ -cyclodextrin-thiocholesterol SAM

We have used hydrophilic silicon tip in all the AFM/LFM measurements. In case of bare gold the LFM image Figure 3.20(a) and topographic image Figure 3.20(b) are almost identical and this shows that the surface is uniformly made up of a single phase, in other words the force of friction is almost uniform in bare gold surface. Figure 3.21 (a) and (b) are the LFM and corresponding topographic images of the thiocholesterol SAM. In this case also the almost identical images show that thiocholesterol monolayer is uniformly deposited and the surface property is homogeneous.

Figure 3.22 (a, b) are the LFM and corresponding topographic images of the SAM composed of  $\beta$ -cyclodextrin-thiocholesterol SAM. One can see that LFM image shows two distinct phases which indicates different magnitude of friction. This shows that the SAM system in case of  $\beta$ -cyclodextrin-thiocholesterol IC has two components where one component is the  $\beta$ -cyclodextrin-thiocholesterol IC and the other component is thiocholesterol alone. This is likely to be possible since there might be some uncomplexed thiocholesterol which does not form IC with  $\beta$ -cyclodextrin. The bright regions present in the LFM image are attributed to the hydrophilic region which is composed of  $\beta$ -cyclodextrin-thiocholesterol IC and the dark regions are because of the presence of thiocholesterol molecules. Hence the system is like a mixed SAM with clear phase separation between the two components which is revealed by our LFM imaging. While the

topographic image does not show any phase separation it does indicate that the SAM surface is quite uniform and does not have multilayer kind of structure.

Figure 3.23 (a, b) are the LFM and corresponding topographic images of the SAM composed of methyl  $\beta$ -cyclodextrin-thiocholesterol SAM. LFM image shows two distinct phases that arise because of the different magnitude of friction observed by the tip. The bright regions present in the LFM image are attributed to the hydrophilic methyl  $\beta$ -cyclodextrin-thiocholesterol IC SAM and the dark regions are made up of thiocholesterol SAM.

We know from the literature that methyl  $\beta$ -cyclodextrin forms inclusion complex with cholesterol more efficiently than  $\beta$ -cyclodextrin [83]. The reason for the more bright regions in the LFM images is attributed to the more number of ICs present on the surface. This property of methyl  $\beta$ -cyclodextrin is probably due the somewhat more hydrophobic outer surface of the molecule, which is helpful in the inclusion complex formation. This was also reflected in the electron transfer blocking property towards  $[\text{Fe}(\text{CN})_6]^{3-14-}$  redox system, which is better than the  $\beta$ -cyclodextrin-thiocholesterol IC SAM.

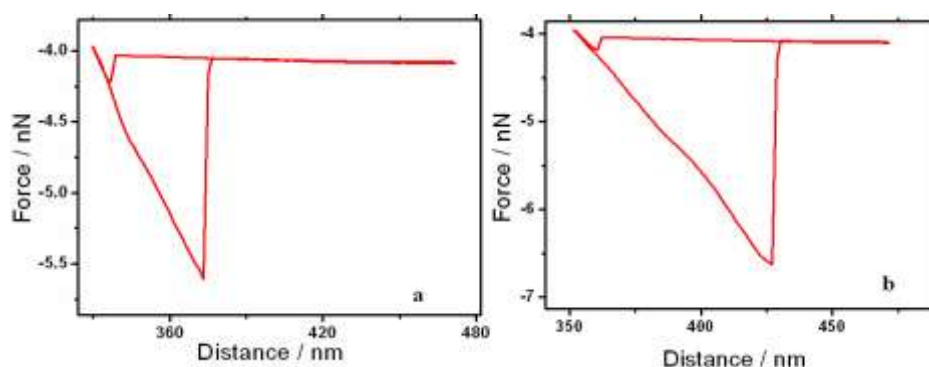
### ***Force-distance measurements***

We have also performed the force-distance spectroscopy on the SAM to measure the interaction between the tip and sample, for which we have selectively chosen the bright and the dark region on the LFM image and brought the tip near the different regions to measure the friction force. In each case 50 force-distance curves were obtained, the plots shown are the average of all the curves.

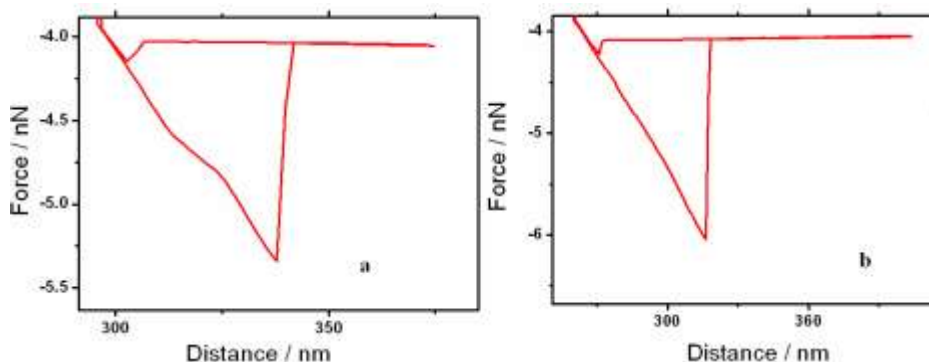
Figure 3.24 (a) and (b) are the force-distance curves taken at the dark (hydrophobic) region and bright (hydrophilic) regions of the  $\beta$ -cyclodextrin-thiocholesterol IC SAM respectively. From the figures it is clear that the calculated friction force is more in case of the bright regions (2.6 nN) compared to the dark regions (1.5 nN) which can be due to the presence of attractive hydrophilic-hydrophilic forces between tip and the hydrophilic IC SAM. On the other hand the darker regions, due to their hydrophobic character, show less friction force. This shows that bright regions in the LFM images are hydrophilic and dark regions are hydrophobic.

Figure 3.25 (a) and (b) are the force-distance curves taken at the dark (hydrophobic) region and bright (hydrophilic) region of the methyl  $\beta$ -cyclodextrin-thiocholesterol IC SAM respectively. The friction force in bright regions (2.1 nN) is more compared to the dark regions

(1.4 nN) and this is again because of the presence of attractive hydrophilic-hydrophilic forces between tip and the hydrophilic IC SAM. The friction force observed for the brighter region in this case is lesser than the force observed in previous case of  $\beta$ -cyclodextrin-thiocholesterol IC SAM. The reason for this may be the less hydrophilic character of the methyl  $\beta$ -cyclodextrin molecule than  $\beta$ -cyclodextrin molecule which causes a less tip surface interaction.



**Fig. 3.24** The force-distance curves taken at the dark (hydrophobic) region (a) and bright (hydrophilic) region (b) of the  $\beta$ -cyclodextrin-thiocholesterol IC SAM respectively



**Fig. 3.25** The force-distance curves taken at the dark (hydrophobic) region (a) and bright (hydrophilic) region (b) of the methyl  $\beta$ -cyclodextrin-thiocholesterol IC SAM respectively

### 3.5 The layer-by-layer (LbL) assembly of oppositely charged polyelectrolytes: Morphological analysis and electron transfer studies

The nanostructured films prepared by the use of LbL assembly have tremendous advantages especially to fabricate new devices whose properties can be tuned by carefully choosing the desired polyelectrolytes. These films find several applications in the field of electrochromism,

bioelectrocatalysis, electroanalysis and electrocatalysis. The simplest mechanism of LbL adsorption can be described as a sequential adsorption of oppositely charged species by dipping the substrate into the solutions alternatively. Recent results show that the film formation takes place due to the charge overcompensation and this can only take place till a threshold value of surface charge density beyond which film formation will no longer take place [90-93]. In the present work we have prepared an LbL film of opposite charged polyelectrolyte namely polystyrenesulfonate (PSS) and polyallylamine hydrochloride (PAH) (Figure 3.26).

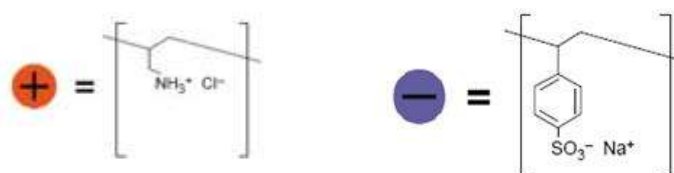


**Fig. 3.26** Poly allylaminehydrochloride (PAH) and Polystyrene sulfoante (PSS)

These polyelectrolytes are widely used as a model system in LbL. In the present work, we have utilized their opposite charges and prepared different number of layers of these polyelectrolytes (4, 8, 12 and 16 bilayers). Here the term bilayer refers to a layer of PSS and PAH. The deposition was carried out on gold electrode modified with a charged self-assembled monolayer. The morphological characterization was carried out with the help of an AFM and electrochemical studies *i.e.* CV and EIS were carried out in the presence of  $[\text{Fe}(\text{CN})_6]^{3-/4-}$  redox couple to measure the electron transfer properties of the different number of PSS and PAH layer systems.

### 3.5.1 Methods and materials

Prior to the LbL deposition the gold substrate was modified with SAM of 4-mercaptopropanesulfonate (4-MPS) to get a negatively charged surface. The SAM of 4-MPS provides a negatively charged gold surface and does not block the electron transfer reaction of  $[\text{Fe}(\text{CN})_6]^{3-/4-}$  redox couple. For SAM preparation 10 mM 4-MPS was prepared in 10 ml ethanol and a cleaned gold electrode was immersed into the solution for 12 hours. The SAM modified gold surface was then immersed into the 1 mg/ml solution of PAH for 10 minutes followed by cleaning in Millipore water to remove weakly adsorbed polyelectrolytes and again immersed in 1 mg/ml solution of PSS. This one cycle of deposition yields us a single bilayer of

polyelectrolytes. For more number of bilayers formation that many cycles of deposition were performed. Figure 3.27 shows the schematic representation of the LbL process.

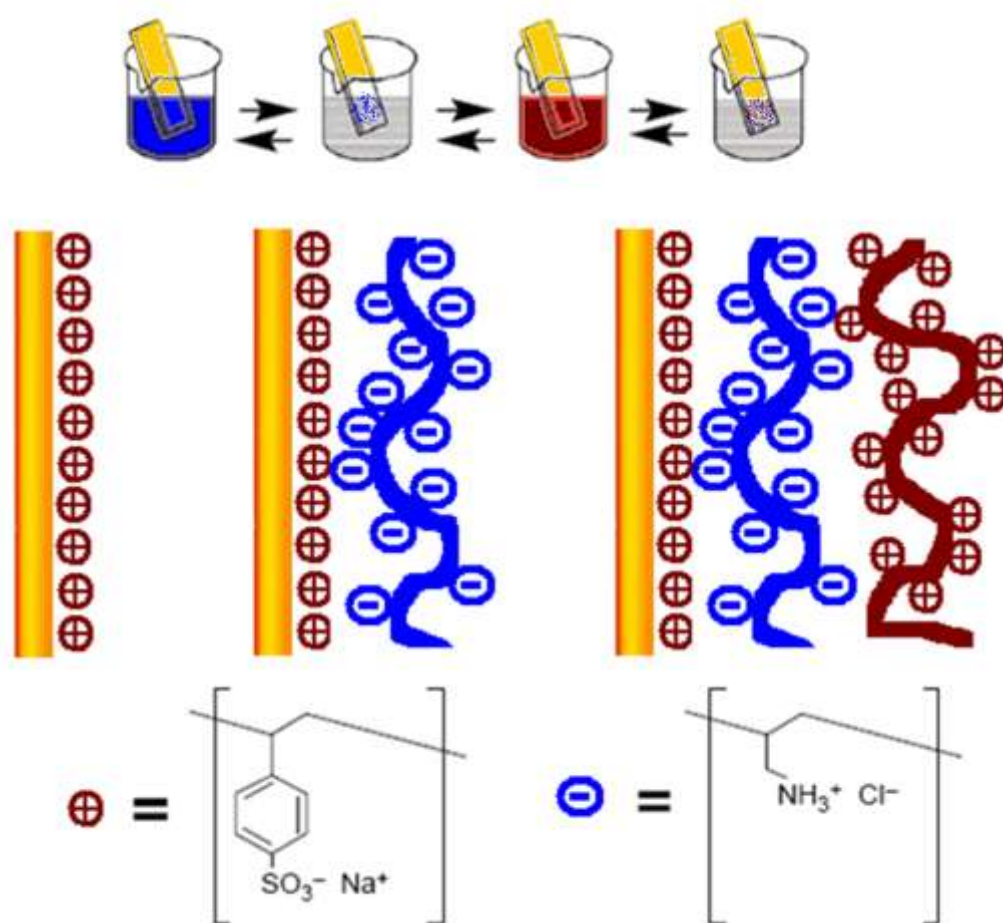


**Fig. 3.27** Schematic representation of the layer-by-layer assembly of polyallylaminehydrochloride (PAH) and polystyrene sulfoante (PSS)

### 3.5.1.1 Characterization of the LbL films

Figure 3.28 a-d shows the AFM topographic images of different number of bilayer coated gold surface. All the images are  $10\mu\text{m} \times 10\mu\text{m}$  scale. One can clearly see the difference in the roughness as the number of bilayers increases. The inset in Figure 3.28 (a) shows the relatively smooth unmodified gold surface. The AFM study confirm the adsorption of polyelectrolytes (PSS and PAH) on gold surface.

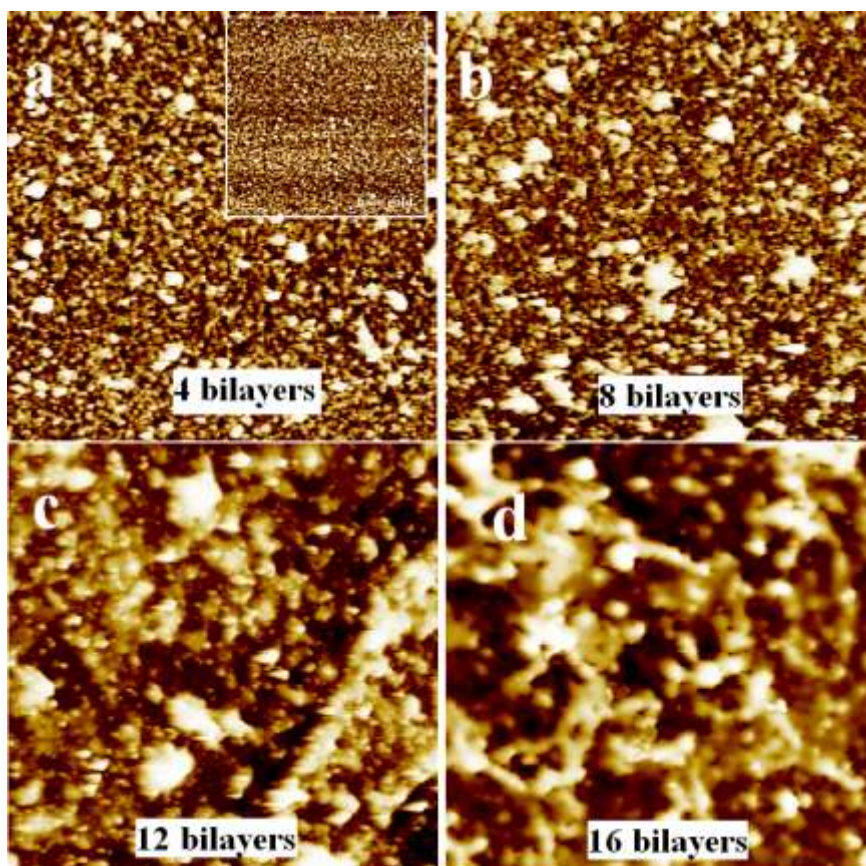


**Fig. 3.28** AFM topographic images of the layer-by-layer assembly of polyallylaminehydrochloride (PAH) and polystyrene sulfoante (PSS). (a) 4 bilayers, (b) 8 bilayers, (c) 12 bilayers and (d) 16 bilayers. Inset in (a) shows the unmodified gold surface all images are  $10\ \mu\text{m} \times 10\ \mu\text{m}$

We have also carried out CV experiment in order to check the electron transfer barrier property of the films towards  $[\text{Fe}(\text{CN})_6]^{3-/4-}$  redox couple. Figure 3.29 shows the CV results for the different number of bilayer modified gold electrode. One can see from the figure that bare gold electrode shows no blocking of electron transfer reaction of  $[\text{Fe}(\text{CN})_6]^{3-/4-}$ . But 2 bilayers system is capable of blocking the electron transfer reaction. The extent of blocking increases for more number of bilayers modified electrode. We also observe that there is not much change in the electron transfer blocking properties after 8 bilayers. It was observed that 12 and 16 bilayers systems have same extent of blocking. The similar electron transfer blocking character after 8 bilayers could be due to the porous network of the polyelectrolyte layers where electrolyte ions

can penetrate the layers. This also manifests that a threshold value of surface charge density exists beyond which film formation no longer takes place [90-93].

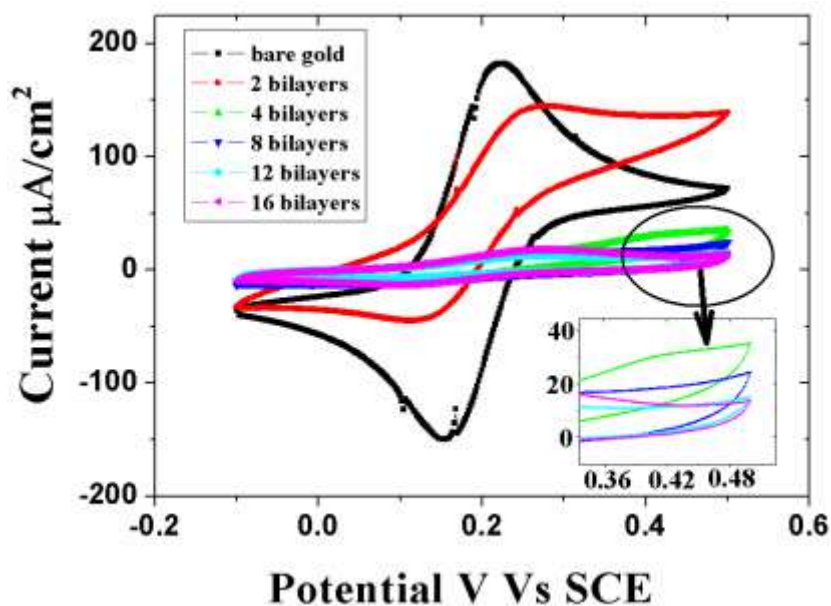


**Fig. 3.29** Cyclic voltammetry results for the different number of layer-by-layer assembly of polyallylaminehydrochloride (PAH) and polystyrene sulfoante (PSS).

### 3.6 Conclusions

This chapter deals with the preparation and electrochemical characterization of the ultrathin molecular thin films on gold substrate. In the first part of the chapter, we have studied the electron transfer and ion permeation properties through the cholesterol monolayers and multilayer films formed on SAMs of TP and 2NT on Au substrate. The molecular films of cholesterol have also been characterized using STM, AFM and grazing angle FTIR studies. We find that the charge transfer resistance ( $R_{ct}$ ) value for the  $[\text{Fe}(\text{CN})_6]^{3-/4-}$  redox system has increased remarkably by the deposition of cholesterol layers on the SAM. The  $R_{ct}$  and interfacial capacitance values depend upon the exposed part of the cholesterol molecules towards electrolyte and also the structure of the monolayer. The modified electrodes show almost complete blocking of the electron transfer reaction. Interfacial capacitance studies with EIS confirm the formation of LB films onto the SAM. The STM and AFM studies of the cholesterol monolayer show that it forms a good, compact and well-ordered film on 2-naphthalenethiol SAM.

The area per molecule is measured to be  $0.64 \text{ nm}^2$  for cholesterol molecule with a tilt angle of about  $28.96^\circ$  from the surface normal as obtained from STM studies.

In the second part of the chapter the electrochemical barrier properties of the discotic liquid crystal and its complex with DNA were studied with three different redox probes namely potassium ferrocyanide, ferrocene. The study shows that the bridge-mediated electron transfer mechanism in the case of ferrocene redox system is responsible for the very low  $R_{ct}$  values whereas the high  $R_{ct}$  values obtained in the case of potassium ferrocyanide system are due to the fact that the LB film of DNA-Discogen is impermeable for the ferrocyanide ions. The study of these biologically important DNA complex films is helpful in the understanding of the conducting nature of these films and in designing the anisotropic ion conducting materials for various applications.

In the third part we have analyzed the self-assembly of the inclusion complexes formed between  $\beta$ -cyclodextrin and thiocholesterol and also between methyl  $\beta$ -cyclodextrin and thiocholesterol. Electrochemical tools and AFM were used for the characterization of the SAM. The solution formed contains the IC as well as free thiocholesterol. This was confirmed by our lateral force microscopy analysis combined with the force measurements between the AFM tip and the sample. AFM topographical images show that the system does not have multilayered structure and it is quite uniform. Friction images were analyzed to understand the dissimilar chemical nature of both the regions. Two distinct regions were found in each of the cases having hydrophilic and hydrophobic nature. Hydrophilic region was made up of cyclodextrin IC whereas the hydrophobic region was composed of only thiocholesterol molecules. Force-distance spectroscopy reveals the greater tip-surface interaction in bright (hydrophilic) regions than the dark (hydrophobic) regions. Electrochemical studies such as CV and EIS were also carried out in aqueous medium to obtain the further insight to the IC SAM.

The fourth part of the chapter is about the LbL films of oppositely charged polyelectrolytes namely PSS and PAH. We have analyzed the polyelectrolyte films with the help of AFM and CV. AFM images of the LbL films shows increase in the roughness and electron transfer barrier properties.

## Bibliography

- [1] H.O. Finklea, Self-assembled monolayers on Electrodes in Encyclopedia of Analytical Chemistry, R.A. Meyers, (Ed.), John Wiley & Sons Ltd, Chichester, U.K.
- [2] A. Ulman, An Introduction to Ultrathin organic films from Langmuir-Blodgett to self-assembly, Academic Press, San Diego, CA, (1991).
- [3] J.J. Hickman, D. Ofer, P.E. Laibinis, G.M. Whitesides, *Science*, 252 (1991) 688.
- [4] C.A. Mirkin, M.A. Ratner, *Annu. Rev. Phys. Chem.*, 43 (1992) 719.
- [5] C.J. Zhong, M.D. Porter, *Anal. Chem.*, 67 (1995) 709A.
- [6] B.A. Cornell, V.L.B. Braach-Maksvytis, L.G. King, P.D.J. Osman, B. Raguse, L. Wieczorek, R.J. Pace, *Nature*, 387 (1997) 580.
- [7] M.J. Tariov, D.R.F. Burgess, G. Gillen, *J. Am. Chem. Soc.*, 115 (1993) 5305.
- [8] J. Huang, D.A. Dahlgren, J.C. Hemminger, *Langmuir*, 10 (1994) 626.
- [9] E.W. Wollman, D. Kang, C.D. Frisbie, T.M. Larcovic, M.S. Wrighton, *J. Am. Chem. Soc.*, 116 (1994) 4395.
- [10] D. Li, M.A. Ratner, T.J. Marks, C.H. Zang, J. Yang, G.K. Wong, *J. Am. Chem. Soc.*, 112 (1990) 7389.
- [11] Y. Kawanishi, T. Tamaki, M. Sakuragi, T. Seki, Y. Swuzki, K. Ichimura, *Langmuir*, 8 (1992) 2601.
- [12] P.E. Laibinis, G.M. Whitesides, *J. Am. Chem. Soc.*, 114 (1992) 9022.
- [13] N. Ohno, J. Uehara, K. Aramaki, *J. Electrochem. Soc.*, 140 (1993) 2512.
- [14] M. Sugahara, M. Uragami, X. Yan, S. L. Regen, *J. Am. Chem. Soc.*, 123 (2001) 7939.
- [15] D. Needham, R. S. Nunn, *Biophys. J.*, 58 (1990) 997.
- [16] F. A. Nezil, M. Bloom, *Biophys. J.*, 61 (1992) 1176.
- [17] M. Doxastakis, A. K. Sum, J. J. De Pablo, *J. Phys. Chem. B*, 109 (2005) 24173.
- [18] K. Tu, M. L. Klein, D. J. Tobias, *Biophys. J.*, 75 (1998) 2147.
- [19] G. J. Ashwell, M. Sujka, A. Green, *Faraday Discuss.*, 131 (2006) 23.
- [20] H. Z. Yu, N. Xia, J. Zhang, Z. F. Liu, *J. Electroanal. Chem.*, 448 (1998) 119.
- [21] P. Viswanath, K. A. Suresh, *Phys. Rev. E*, 67 (2003) 061604.
- [22] P. Viswanath, K. A. Suresh, *J. Phys. Chem. B*, 108 (2004) 9198.
- [23] R. S. Abendan, J. A. Swift, *Langmuir*, 18 (2002) 4847.

- [24] S. Lafont, H. Rapaport, G. J. Somjen, A. Renault, P. B. Howes, K. Kjaer, J. Als-Nielsen, L. Leiserowitz, M. Lahav, *J. Phys. Chem. B* 102 (1998) 761.
- [25] R. K. Gupta, K. A. Suresh, *Eur. Phys. J. E*, 14 (2004) 35.
- [26] X. Bin, S. L. Horswell, J. Lipkowski, *Biophys. J.*, 89 (2005) 592.
- [27] X. Bin, J. Lipkowski, *J. Phys. Chem. B*, 110 (2006) 26430.
- [28] Z. P. Yang, I. Engquist, J. M. Kauffmann, B. Liedberg, *Langmuir*, 12 (1996) 1704.
- [29] Z. P. Yang, I. Engquist, B. Liedberg, J. M. Kauffmann, *J. Electroanal. Chem.*, 430 (1997) 189.
- [30] V. Ganesh, V. Lakshminarayanan, *J. Phys. Chem. B*, 109 (2005) 16372.
- [31] M. Jayadevaiah, V. Lakshminarayanan, *Meas. Sci. Technol.*, 15 (2004) N35.
- [32] N. Krings, H.-H. Strehblow, J. Kohnert, H.-D. Martin, *Electrochim. Acta*, 49 (2003) 167.
- [33] M. A. Rampi, G. M. Whitesides, *Chem. Phys.*, 281 (2002) 373.
- [34] Q. Jin, J. A. Rodriguez, C. Z. Li, Y. Darici, N. J. Tao, *Surf. Sci.*, 425 (1999) 101.
- [35] C. Retna Raj, Takeo Ohsaka, *J. Electroanal. Chem.*, 540 (2003) 69.
- [36] T. Sawaguchi, F. Mizutani, S. Yoshimoto, I. Taniguchi, *Electrochim. Acta*, 45 (2000) 2861.
- [37] Y. Yang, S. B. Khoo, *Sensors. Actuators. B*, 97 (2004) 221.
- [38] R. R. Kolega, J. B. Schlenoff, *Langmuir*, 14 (1998) 5469.
- [39] E. Sabatani, J. Boulakia-Cohen, M. Bruening, I. Rubinstein, *Langmuir*, 9 (1993) 2974.
- [40] T. Sawaguchi, F. Mizutani, S. Yoshimoto, I. Taniguchi, *Electrochim. Acta*, 45 (2000) 2861.
- [41] Y.-T. Tao, C.-C. Wu, J. Y. Eu, W. L. Lin, K.-C. Wu, C.-H. Chen, *Langmuir*, 13 (1997) 4018.
- [42] S. Frey, V. Stadler, K. Heister, W. Eck, M. Zharnikov, M. Grunze, B. Zeysing, A. Terfort, *Langmuir*, 17 (2001) 2408.
- [43] H. O. Finklea, in: *Electroanalytical Chemistry, A Series of Advances*, A. J. Bard, I. Rubinstein, (Eds), Marcel Dekker, New York, 1996, Vol. 19, p 166.
- [44] R. Subramanian, V. Lakshminarayanan, *Electrochim. Acta*, 45 (2000) 4501.
- [45] S. J. Tans, L. J. Geerligs, C. Dekker, J. Wu, G. Wegner, *J. Vac. Sci. Technol.*, B 15 (1997) 586.
- [46] W. Zhu, N. Minami, S. Kazaoui, Y. Kim, *J. Mater. Chem.*, 13 (2003) 2196.
- [47] S. Kumar. *Chem. Soc. Rev.*, 35 (2006) 83.
- [48] S. Sergeev, W. Pisula, Y.H. Geerts, *Chem. Soc. Rev.*, 36 (2007) 1902.

- [49] M. Yoshio, T. Mukai, H. Ohno, T. Kato, *J. Am. Chem. Soc.*, 126 (2004) 994.
- [50] J.O.Radler, I. Koltover, T. Salditt, C.R. Sanya, *Science*, 275 (1997) 810.
- [51] D. Putnam, *Nature Materials*, 5 (2006) 439.
- [52] L. Cui, J. Miao, L.Zhu, *Macromolecules*, 39 (2006) 2536.
- [53] L. Cui, L. Zhu, *Langmuir*, 22 (2006) 5982.
- [54] A. Nayak, K.A. Suresh, *J. Phys. Chem. B*, 112 (2008) 2930.
- [55] A. Nayak, K.A. Suresh, *Phys. Rev. E*, 78 (2008) 021606.
- [56] S. Kumar, S.K. Pal, *Tetrahedron Letters*, 46 (2005) 4127.
- [57] A. Nayak, K.A. Suresh, S. K. Pal, S. Kumar, *J. Phys. Chem., B* 111 (2007) 11157.
- [58] M. S. Marcus, R. W. Carpick, D. Y. Sasaki, M. A. Eriksson, *Phys. Rev. Lett.*, 88 (2002) 226103.
- [59] D. Raghavan, X. Gu, T. Nguyen, M. VanLandingham, and A. Karim, *Macromolecules*, 33 (2000) 2573
- [60] A. Nayak, K. A. Suresh, *J. Phys. Chem. B*, 113 (2009) 3669.
- [61] R.K. Pandey, K.A. Suresh, V. Lakshminarayanan, *J. Coll. Inter. Sci.*, 315 (2007) 528.
- [62] H.O. Finklea, in: A.J. Bard, I. Rubinstein (Eds.), *Electroanalytical Chemistry*, in: A Series of Advances, vol. 19, Dekker, New York, 1996, p. 166.
- [63] R. Subramanian, V. Lakshminarayanan, *Electrochim. Acta*, 45(2000) 4501.
- [64] V. Ganesh, V. Lakshminarayanan, *J. Phys. Chem. B*, 109 (2005) 16372.
- [65] F.D. Lewis, T. Wu, Y. Zhang, R. L. Letsinger, S. R. Greenfield, M. R. Wasielewski, *Science*, 277 (1997) 673.
- [66] D. Porath, A. Bezryadin, S.de Vries, C. Dekker, *Nature*, 403 (2000) 635.
- [67] W. Wang, T. Lee, M.A. Reed, *J. Phys. Chem. B*, 108 (2004) 18398.
- [68] W.B. Davis, W.A. Svec, M.A. Ratner, M.R. Wasieiewski, *Nature*, 396 (1998) 60.
- [69] F.D. Lewis, J. Liu, W. Weigel, W. Rettig, I.V. Kurnikov, D.N. Beratan, *Proc. Nat. Acad. Sci.*, 99 (2002) 12536.
- [70] A. Girlando, C. Sissa, F. Terenziani, A. Painelli, A. Chwialkowska, G.J. Ashwell, *ChemPhysChem*, 8 (2007) 2195.
- [71]. W. Chen, X.Y. Gao, D.C. Qi, S. Chen, Z.K. Chen, A.T.S. Wee, *Adv. Funct. Mater.*, 17 (2007) 1339.
- [72] S. Neppel, U. Bauer, D. Menzel, P. Feulner, A. Shaporenko, M. Zharnikov, P. Kao, D.L.

- Allara, *Chem. Phys. Lett.*, 447 (2007) 227.
- [73] H.B. Akkerman, R.C.G. Naber, B. Jongbloed, P.A. Van Hal, P.W.M. Blom, D.M. De Leeuw, B. De Boer, *Proc. Nat. Acad. Sci.*, 104 (2007) 11161.
- [74] R.L. Grimm, N.M. Barrentine, C.J.H. Knox, J.C. Hemminger, *J. Phys. Chem. C*, 112 (2008) 890.
- [75] A.K. Gnanappa, C. O'Murchu, O. Slattery, F. Peters, T. O'Hara, B. Aszalós-Kiss, S.A.M. Tofail, *J. Phys. Chem. C*, 112 (2008) 14934.
- [76] H. Shigekawa, K. Miyake, J. Sumaoka, A. Harada, M. Komiyama, *J. Am. Chem. Soc.*, 122 (2000) 5411.
- [77] S. Samitsu, T. Shimomura, K. Ito, M. Hara, *Appl. Phys. Lett.*, 85 (2004) 3875.
- [78] J. Yan, S. Dong, J. Li, W. Chen, *J. Electrochem. Soc.*, 144 (1997) 3858.
- [79] S. R. McAlpine, M. A. Garcia-Garibay, *J. Am. Chem. Soc.*, 118 (1996) 2750.
- [80] J. Yan, S. Dong, *Langmuir*, 13 (1997) 3251.
- [81] Y. Ohtani, T. Irie, K. Uekama, K. Fukunaga, J. Pitha, *Eur. J. Biochem.*, 186 (1989) 17.
- [82] E.P. Kilsdonk, P.G. Yancey, G.W. Stoudt, F.W. Bangerter, W.J. Johnson, M.C. Phillips, G.H. Rothblat, *J. Biol. Chem.*, 270 (1995) 17250.
- [83] U. Klein, G. Gimpl, F. Fahrenholz, *Biochem.*, 34 (1995) 13784.
- [84] Z. P. Yang, I. Engquist, J. M. Kauffmann, B. Liedberg, *Langmuir*, 12 (1996) 1704.
- [85] Z. P. Yang, I. Engquist, B. Liedberg, J. M. Kauffmann, *J. Electroanal. Chem.*, 430 (1997) 189.
- [86] A. Noy, D. V. Vezenov, C.M. Lieber, *Annu. Rev. Mater. Sci.*, 27 (1997) 381.
- [87] S. Peach, R. D. Polak, C. Franck, *Langmuir*, 12 (1996) 6053.
- [88] G. Bar, S. Rubin, A. N. Parikh, B. I. Swanson, T. A. Zawodzinski, Jr. M.-H. Whangbo, *Langmuir*, 13(1997) 373.
- [89] J.A. Hamolton, L.Y. Chen, *J. Am. Chem. Soc.*, 110 (1988) 4379.
- [90] T.H. Silva, V. Garcia-Morales, C. Moura, J.A. Manzanares, F. Silva, *Langmuir*, 21 (2005), 7461.
- [91] S.V.P. Barreira, V. Garcia-Morales, C.M. Pereira, J.A. Manzanares, F. Silva, *J. Phys. Chem. B*, 108 (2004) 17973.
- [92] A. Liu, Jun-ichi Anzai, *Langmuir*, 19 (2003) 4043.

- [93] F.N. Crespilho, V. Zucolotto, O.N. Oliveira Jr. F.C. Nart, *Int. J. Electrochem. Sci.*, 1 (2006) 194.

## Chapter 4

### **Formation of Nanostructures of Polyaniline (PANI) and Porphyrin Derivative, AFM Analysis, Optical Properties and Electrochemical Lead Sensing**

*In recent times nanostructures made from organic compounds have found vast interest in material science especially because these organic nanostructures can be tailored by means of chemical methods to achieve variety of applications. Porphyrins are the organic compounds which can be very useful for building organic nanostructures. Porphyrins derivatives can form interesting nanostructures of different shapes and sizes. These nanostructures form due to the ability of porphyrin derivatives to form J-aggregates. In the present chapter we show that the nanostructures prepared from conducting polymer, polyaniline and a porphyrin show interesting optical properties and their Lbl formed on gold substrate can be used for metal ions sensing.*

## 4.1 Introduction

Porphyrins are derived from four pyrroline subunits and are highly conjugated aromatic macrocycles. They are widely studied for their potential applications as molecular electronics materials in light harvesting devices [1,2], catalysts [3], sensors [4] and in supramolecular chemistry [5,6]. In recent times, there has been an immense interest in the formation and study of nanostructures of porphyrins, which show interesting chemical, physical and optoelectronic properties [7-11]. Just as in the case of metal nanoparticles, the challenge involved in the synthesis of porphyrin nanoparticles is to control the size and prevent their agglomeration. There have been reports on the use of polymers such as polyethylene glycol (PEG) as a stabilizer for the nanoparticles of porphyrin [7] and also counterion-dependent aggregates of porphyrin nanostructures in aqueous acidic solutions [8]. Rotomskis *et al.* have shown how the porphyrin molecules attain ring shape by what is known as J-aggregation, which is similar to the “spread deck of cards” like conformation. They hypothesized the formation of tubular structures from porphyrin J-aggregates which was also confirmed by AFM images on silicon substrate [12]. The ability of porphyrin derivatives to form interesting structures in the form of J and H-aggregates is the key to the formation of nanostructures. The J-aggregates form due to the interaction between the negatively charged functional groups attached to the porphyrin, and the positive charge at the centre of the adjacent porphyrin. The H-aggregates form when porphyrin molecules are stacked in a face-to-face configuration [7].

From the spectral shifts one can distinguish various aggregation patterns of the dyes in different media. For instance, the bathochromically shifted J-bands (J for Jelly, who was the first worker to investigate these shifts) and hypsochromically shifted H-bands (H for hypsochromic) of the aggregates have been explained in terms of molecular exciton coupling theory [7,8]. According to the simple definition, the J-aggregate is a one-dimensional molecular arrangement in which the transition dipole moments of individual monomers are aligned parallel to the line joining their centers (end-to-end arrangement). The H-aggregate is also a one-dimensional array of molecules in which the transition dipole moments of individual monomers are aligned parallel to each other but perpendicular to the line joining their centers (face-to-face arrangement).

An extensive study on aggregates has resulted in the proposal that these aggregates exist as a one-dimensional assembly in solution that could be in one of the following arrangement:

1. Ladder,
2. Staircase or
3. Brickwork type of arrangement.

The schematic of the assembly is shown in the Figure 4.1.

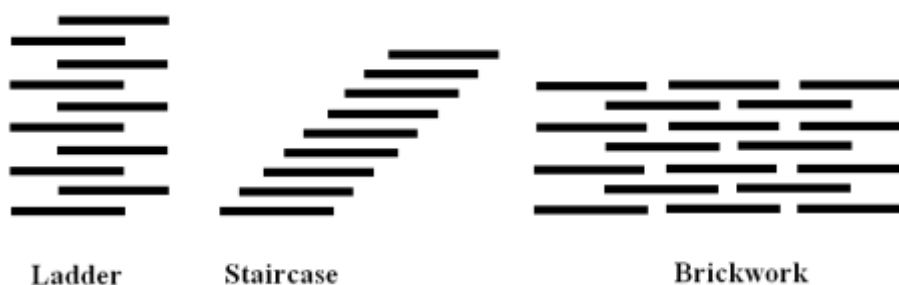


**Fig. 4.1** Different kind of aggregate structures

H and J-aggregates show many interesting properties for example linear and nonlinear optical (NLO) response, photoelectric, photorefractive, photochromism, superradiance, superfluorescence, electroluminescence, photoluminescence, attenuated total reflection (ATR) etc.

This chapter contains three parts, the first part describes the formation of porphyrin and PANI nanostructures in the bulk, their characterization by spectroscopic and scanning probe techniques and their optical properties. The second part includes the formation of these organic nanostructures as a thin film on self-assembled monolayer modified gold substrate, their characterization and application in lead sensing. In the last part we have discussed about the one pot synthesis of porphyrin nanofibers and their interesting optical properties, in particular the improved emission property.

A simple method of preparation of porphyrin nanoparticles and the study of their nonlinear optical properties is discussed in this work. We also show in the second part that a film of porphyrin nanoparticles with PANI can be used for electrochemical sensing of lead. 4,4',4'',4'''-(porphine-5,10,15,20-tetrayl)tetrakis(benzoic acid) (PTBA) is used as the precursor. The nanoparticles were prepared by mixing the PTBA solution with a dilute solution of PANI, which is a well known conducting polymer. These nanoparticles show long time stability. PANI

acts as an effective stabilizing agent which prevents further aggregation of the nanoparticles, which otherwise would result in precipitation.

Nonlinear optics (NLO) is the branch of optics, which expresses the behavior of light in non-linear media. Non-linear optical properties are very important in optics and they give rise to the many phenomenons which include second harmonic generation, third harmonic generation, sum frequency generation and optical rectification etc. Many organic compounds including porphyrins, phthalocyanines, conjugated polymers etc. show good non-linear optical properties. While the non-linear optical properties of porphyrins are well studied in literature [13-15], we show that the porphyrin-polyaniline nanocomposite described here exhibits an enhanced non-linear optical property compared to the parent compounds PTBA and PANI.

Since porphyrins are well known chelating agent they can be used to chelate poisonous heavy metals such as lead. [16] Prolong exposure of lead may cause neurological harm, kidney disease and also cardiovascular diseases [17,18]. In addition, lead interferes with a variety of body processes and is found to be highly toxic, predominantly to children. The major sources of lead are paints, pigments, cosmetics, and lead acid batteries which affect especially the workers in automobile service stations.

However, the foremost tool for the detection of lead is the measurement of the blood lead level, which can be achieved by a suitable lead sensor with very low detection limit. In the present work we have shown that PTBA-PANI nanostructures modified gold electrode has the potential to be used as lead sensor with the help of anodic stripping voltammetry.

## **4.2 Methods and materials**

PANI was prepared by electrochemical potential cycling in an electrolyte containing 0.1 M  $\text{H}_2\text{SO}_4$  and 0.5 M aniline at a potential range of -0.2 V to 1.0 V. An indium tin oxide (ITO) electrode was used for the deposition of the PANI film. It is known that PANI has a higher solubility in DMF when synthesized through electrochemical route than by chemical method [19]. Ultrasonication of the electropolymerized PANI film for 10 minutes in DMF/water mixture provides a good dispersion of PANI. To prepare the nanoparticles, a 12  $\mu\text{M}$  solution of PANI and a 0.25 mM solution of PTBA, both prepared in DMF/water (1:1), were used as the precursors. When these two solutions were mixed in a 1:1 proportion the PTBA-PANI nanocomposite was formed.

For layer-by-layer assembly we have used gold coated mica substrate obtained from the vacuum evaporation method. Prior to the deposition of PTBA and PANI, the gold substrate was modified with the self-assembled monolayer of 4-mercaptopropane sulfonate sodium salt (4-MPS) to create a negatively charged layer on gold substrate. Modified gold was dipped for 10 minutes in the solution of PANI and PTBA, alternately. The substrate was cleaned with Millipore water each time after the layer deposition to remove weakly adsorbed PANI or PTBA. We have performed 4 and 8 cycles of deposition of PTBA and PANI.

The UV-vis absorption spectra of PANI, PTBA and PTBA-PANI mixture were measured using a spectrophotometer (Perkin Elmer-Lambda 35). Photoluminescence measurements were carried out using a standard spectrofluorometer (Fluoromax 4, Horiba Jobin Yvon). Atomic force microscopy (AFM) was used for the characterization of the nanoparticles and film. A drop of the nanoparticle solution prepared in DMF/water system was deposited on mica substrate and the solvent was allowed to evaporate. For AFM studies, we have used a muscovite mica substrate, which was freshly cleaved by means of a Scotch tape. AFM studies were carried out using Pico plus (Molecular Imaging) AFM in AC (tapping) mode with a silicon tip. The images obtained were raw images, which were plane corrected using the scanning probe image processor (SPIP) software (Image Metrology, Denmark).

The nonlinear absorption measurements were conducted using pulse laser facility available at the Light and Matter Physics group of RRI. The experiments were carried out at the excitation wavelength of 532 nm, using laser pulses of 7 nanoseconds duration obtained from a Q-switched, frequency doubled Nd:YAG laser (Quanta Ray, Spectra Physics). The technique of open aperture Z-scan [20] was used for the measurements.

Anodic stripping voltammetry (ASV) experiment was carried out for checking the sensitivity of the modified electrode towards lead. Lead nitrate solution was prepared with 0.1 M NaF as the supporting electrolyte in Millipore water of resistivity 18 M $\Omega$ .cm. A conventional three-electrode electrochemical cell was used for ASV. A platinum foil of large surface area as the counter electrode and a saturated calomel electrode (SCE) as a reference electrode were used.

## 4.2.1 Formation of the PTBA-PANI nanoparticles in the bulk and nonlinear optical properties

### 4.2.1.1 Characterization of the nanocomposite

In porphyrins and phthalocyanines two kinds of bands are generally seen in the UV-vis spectra. First one is an intense band in the blue wavelength region of the visible spectrum which is called the Soret band and at higher wavelengths there are four Q bands. Any structural and functional changes associated with these molecules are normally reflected by the change in the intensity, shape and shifts of these bands. The samples and the UV-vis spectra of PTBA-PANI solution are shown in Figures 4.2a and 4.2b respectively. The spectra show a clear splitting in the Soret band. It is also seen that the Soret band is broadened and the Q bands are slightly shifted towards the longer wavelengths which indicates the formation of the porphyrin aggregates in the solution [7,21-26]. Usually the porphyrin aggregates fall into the two categories of H-type and J-type aggregates. In H-type aggregation porphyrin molecules are stacked in a sandwich-like manner which is also called the face-to-face configuration. In J-type aggregation the porphyrin molecules are stacked in a spread deck of cards like arrangement. The absorption spectrum of the PTBA-PANI mixture gives a clear indication of the formation of PTBA nanoparticles, which are essentially the PANI stabilized aggregates of PTBA.

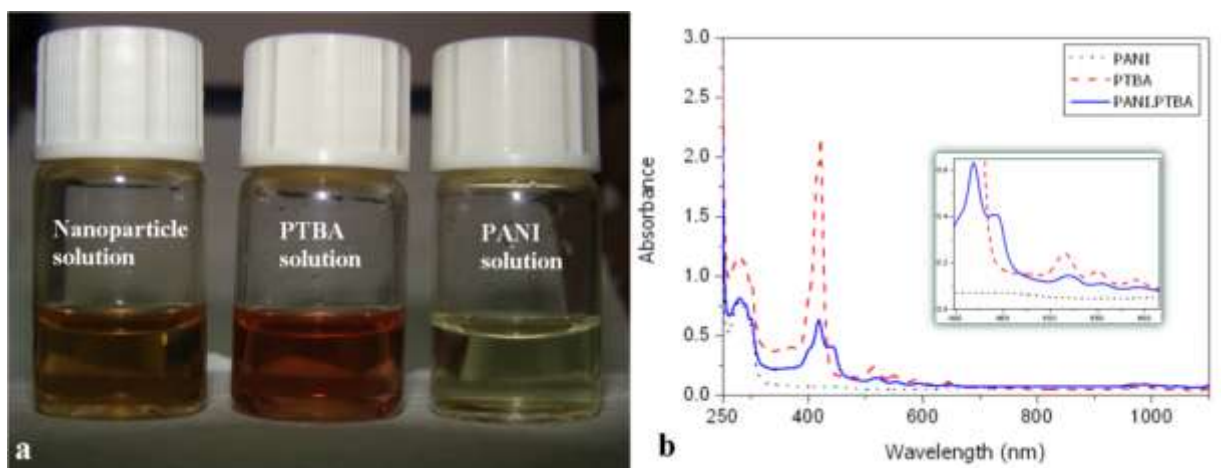


**Fig. 4.2** Photograph of the solutions of PANI, PTBA and PTBA nanoparticles (a), and UV-VIS absorption spectra of the samples showing the splitting in the Soret band (b). Inset shows the red shift in the Q bands

Figure 4.3 shows the tapping mode AFM topographic image of nanoparticles on the mica substrate. It shows a homogeneous distribution of nanoparticles on mica substrate. The typical particle size is found to be 80-100 nm and the z-height corresponding to the thickness of the nanocomposite is 3-4 nm. In addition, a few bigger clusters are also observed in the topographic image.

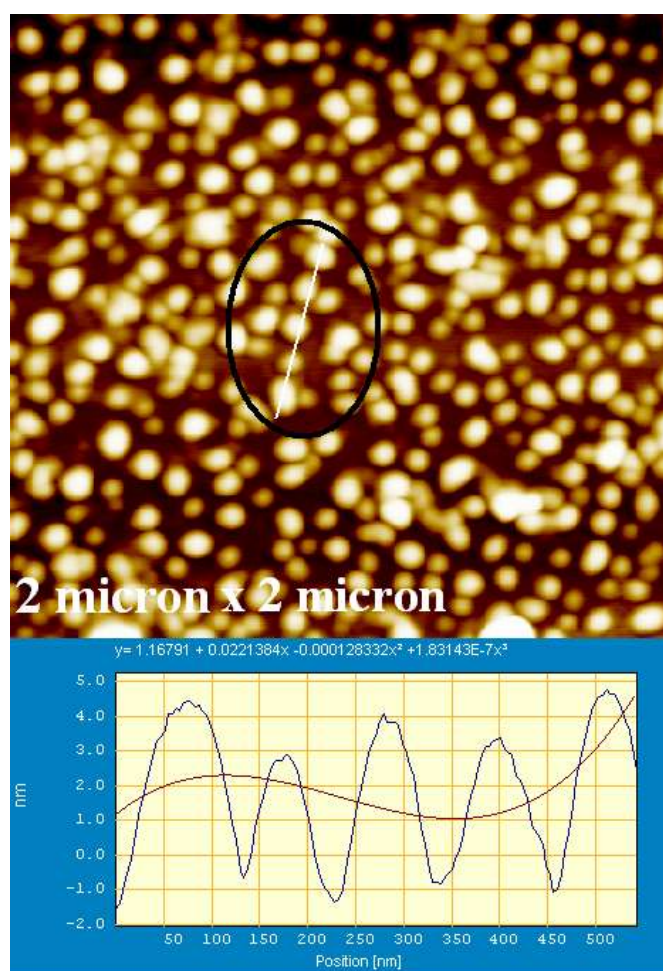


**Fig. 4.3**  $2\ \mu\text{m} \times 2\ \mu\text{m}$  AFM topographic image of porphyrin nanoparticles on mica substrate showing the height and size of the individual nanoparticle

AFM phase imaging was also carried out, as it is known to yield much sharper features than the topographic images. Figure 4.4 shows the  $10\ \mu\text{m} \times 10\ \mu\text{m}$  AFM phase image of the nanoparticles on mica. The inset in Figure 4.4a shows the zoomed image where the well-resolved individual nanoparticles can be clearly seen. The phase image confirms that most of the nanoparticles are of uniform size ranging from 80-100 nm. It can also be seen from the Figure

4.4(b) that the bigger clusters, which are found in the topographic image (Figure 4.4c), are actually made up of smaller sized nanoparticles.

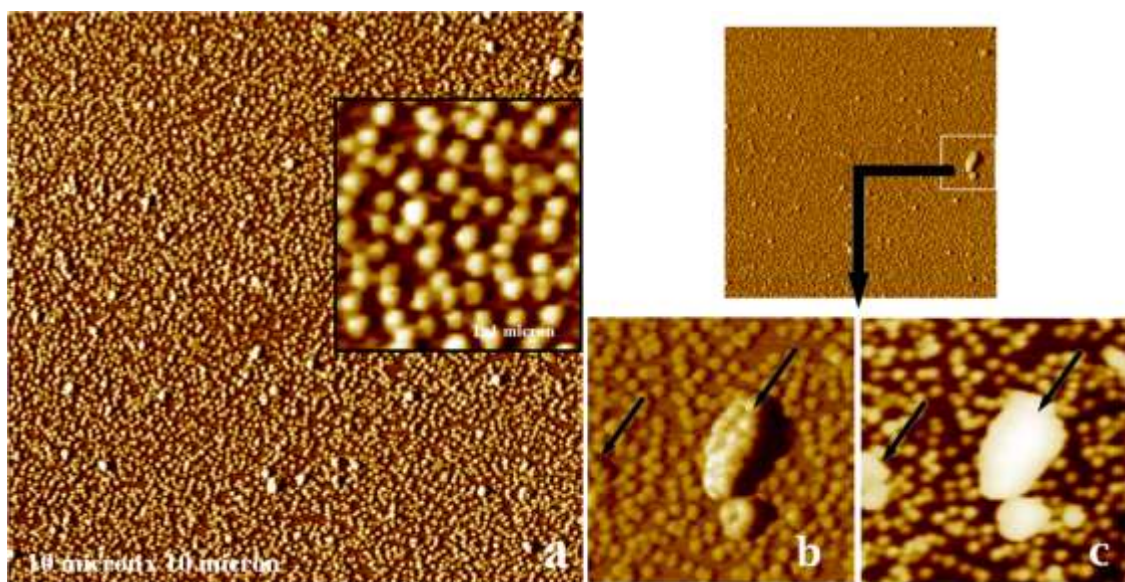


**Fig. 4.4**  $10\ \mu\text{m} \times 10\ \mu\text{m}$  AFM phase image of porphyrin nanoparticles on mica substrate. Inset shows the zoomed  $1\ \mu\text{m} \times 1\ \mu\text{m}$  part. Phase image is sharper than the topographic image

We have also performed FTIR spectroscopy (Figure 4.5) to analyze the nanocomposite formed by mixing PANI and PTBA.

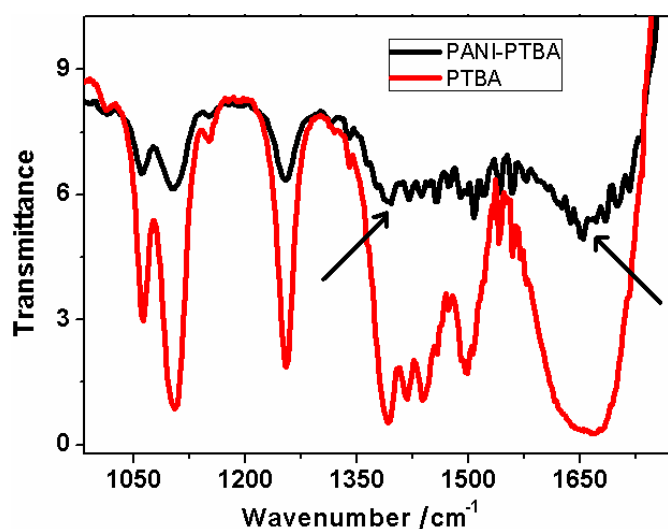


**Fig. 4.5** FTIR spectra of PANI and mixture of PANI and PTBA (nanoparticles) showing the multiple IR peaks in the case of nanoparticles (from  $1300$  to  $1700\ \text{cm}^{-1}$ )

In the case of porphyrin there is a broad peak of  $\text{-C=O}$  stretching at  $1670\text{ cm}^{-1}$ . In the case of nanocomposite the broad peak at  $1670\text{ cm}^{-1}$  splits into few more peaks as shown by arrows in Figure 4.5. The changes in the IR spectra in  $1600\text{ to }1800\text{ cm}^{-1}$  region indicate the structural changes surrounding the  $\text{-C=O}$  group. The appearance of the new peaks at  $1700$  and  $1716\text{ cm}^{-1}$  is indicative of the interaction between  $\text{-C=O}$  group and  $\text{-NH}$  groups. This information although not confirmatory yet furnishes us a clue that there might be aggregation among the PTBA particles in the PTBA-PANI nanocomposite sample.

The presence of water in the case of DMF/water system enhances the polarity of the solvent which induces the aggregation of porphyrin cores. This polarity driven aggregation may be helpful in controlling the size of the porphyrin nanoparticles. The driving forces behind the formation of the nanoparticles are  $\pi$ -stacking effect and hydrophobic interaction. Some of the PTBA molecules can also stack together to form J-aggregates due to the intermolecular association between the positively charged porphyrin rings and the negatively charged benzoic acid groups of the neighboring porphyrin molecules. The presence of four negatively charged groups attached on the periphery of the porphyrin may not cause repulsion since the negative charge of the attached groups is delocalized over the porphyrin ring [27,28]. The assembly of such J-aggregates driven by hydrophobic interaction and  $\pi$  stacking leads to the formation of the nanoparticles. This stacking of porphyrin has also been reported elsewhere [12,29]. *Meso*-tetra(4-sulfonatophenyl)porphine (TPPS<sub>4</sub>) [12] and *meso*-tetrakis(4-hydroxyphenyl)porphyrin (H<sub>2</sub>THPP) [29] have also been shown to form J-aggregates.

PTBA and PANI were also deposited separately on mica substrate and imaged using AFM. In the case of PANI on mica, the AFM image (Figure 4.6) shows a few lumps of polymer. In the case of PTBA (Figure 4.7) we observed clusters of aggregated mass (about 600 nm), which are possibly the bigger J-aggregates of PTBA stacked together. From the AFM images it is clear that the features we obtained in PTBA (Figure 4.7) are larger than the particles obtained in the case of PTBA-PANI mixture.

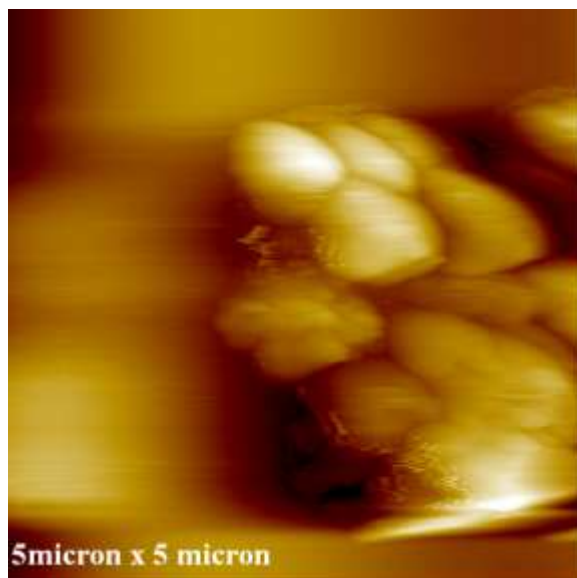


*Fig. 4.6 5  $\mu\text{m}$  x 5  $\mu\text{m}$  AFM image of PANI deposited on mica substrate*

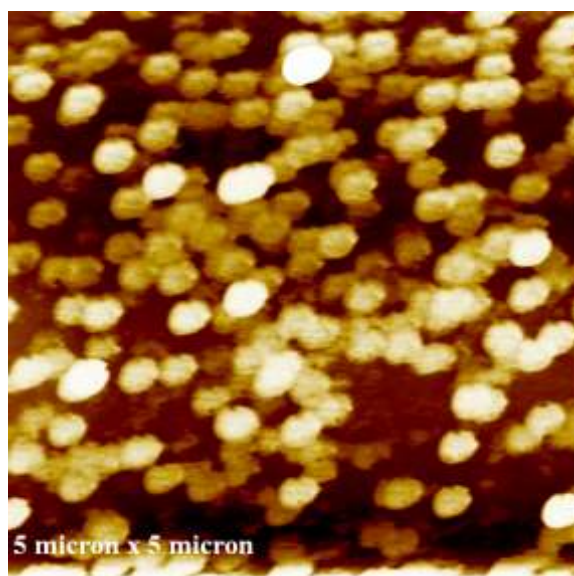
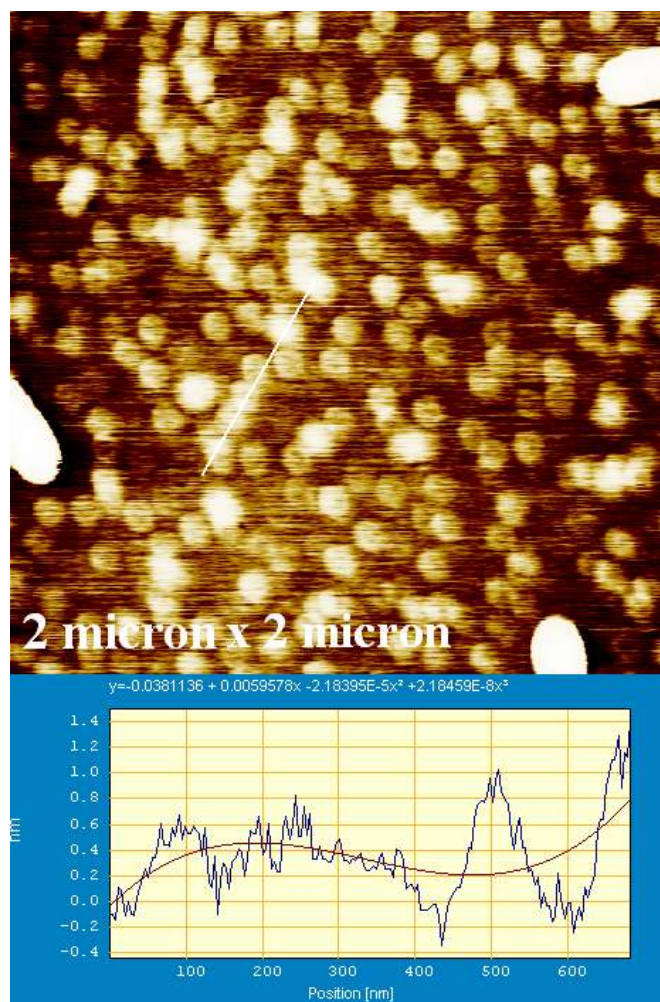


*Fig. 4.7 5  $\mu\text{m}$  x 5  $\mu\text{m}$  AFM image of PTBA deposited on mica substrate*

The nanoparticle synthesis was also carried out in the absence of water i.e. in DMF alone. Figure 4.8 shows the topographic image of the nanoparticles formed in the case of DMF as a solvent. In this case AFM image on mica shows less z-height. The height observed in DMF is around 0.5-0.8 nm while the x and y dimension are similar (80-100 nm) to the DMF/water case. Interestingly the thickness of single PTBA molecule is 0.5 nm [12] so the height observed in this case suggests the presence of nanostructures with the thickness of almost a single PTBA

molecule. This indicates that nanoparticles are less aggregated in DMF and mostly lie flat on mica sheet. The presence of water in the case of DMF/water system enhances the polarity of the solvent which induces the aggregation of porphyrin cores. This polarity driven aggregation may be helpful in controlling the size of the porphyrin nanoparticles.

Figure 4.9 shows the schematic diagram of the aggregation behavior of the PTBA molecules in DMF and DMF/water solutions.



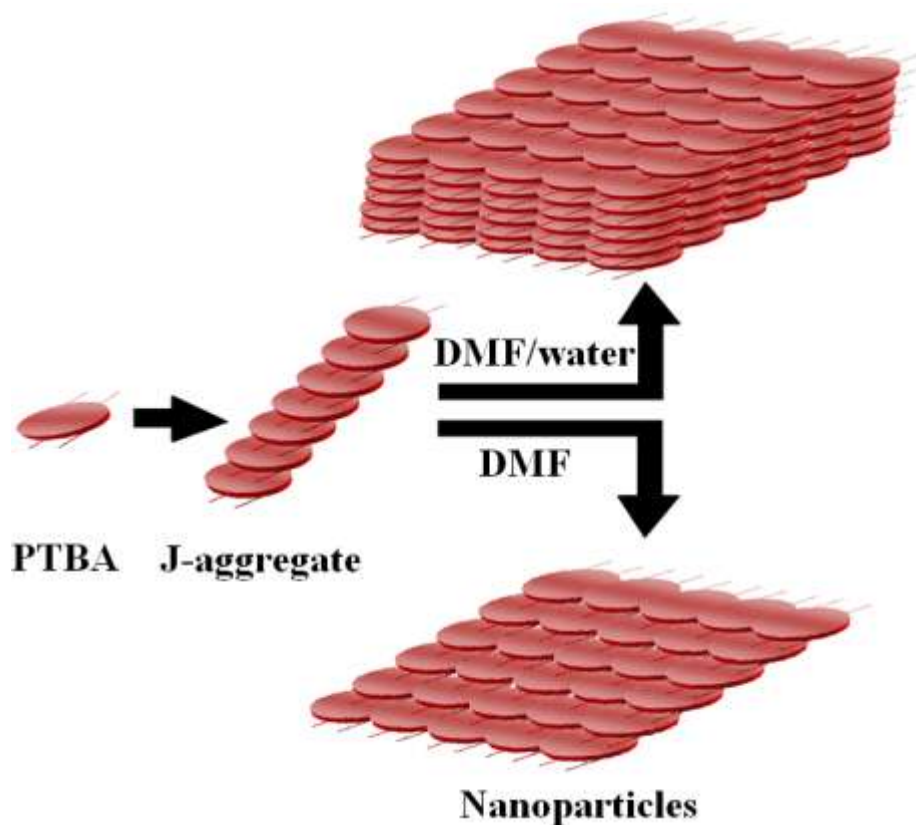
**Fig. 4.8**  $2\ \mu\text{m} \times 2\ \mu\text{m}$  AFM image of porphyrin nanoparticles on mica substrate formed in DMF and the height and size of nanoparticle

Table 4.1 summarizes the roughness parameters of the surface, the average roughness ( $S_a$ ), rms roughness ( $S_q$ ) and developed surfaces area ratio ( $S_{dr}$ ), which were measured using SPIP software [30,31]. The mica surface which was modified with the nanoparticles (prepared in DMF/water system) shows a value of  $S_{dr}$ , 0.357 % whereas for a surface modified with

nanoparticles formed in DMF,  $S_{dr}$  value comes out to be 0.0266%. Bare mica substrate shows the least value of  $S_{dr}$ , 0.00671 %. All the roughness data are calculated for a 10  $\mu\text{m}$  region. The higher roughness values in the case of nanoparticles in DMF/water system clearly indicates the effect of water in the polarity driven aggregation as discussed earlier.

Substrate	Average roughness ( $S_a$ )	rms roughness ( $S_q$ )	Developed surface Area ratio ( $S_{dr}$ )
Bare mica	0.508	0.727	0.00554%
Nanoparticles (DMF/water) modified mica	1.96	2.99	0.357%
Nanoparticles (DMF) modified mica	0.56	1.23	0.0266%

**Table 4.1** The roughness parameters of the surface, the average roughness ( $S_a$ ), rms roughness ( $S_q$ ) and developed surfaces area ratio ( $S_{dr}$ )



**Fig. 4.9** Schematic diagram of the aggregation behavior of the PTBA

To check the optical nonlinearity of the PTBA-PANI sample when compared to the individual components, we have carried out Z-scan experiment in each case. Figure 4.10 shows the laser fluence vs. normalized transmittance curve for the samples, it shows the significant enhancement in the nonlinear transmission for the PTBA-PANI nanocomposite compared to either of the constituents alone.

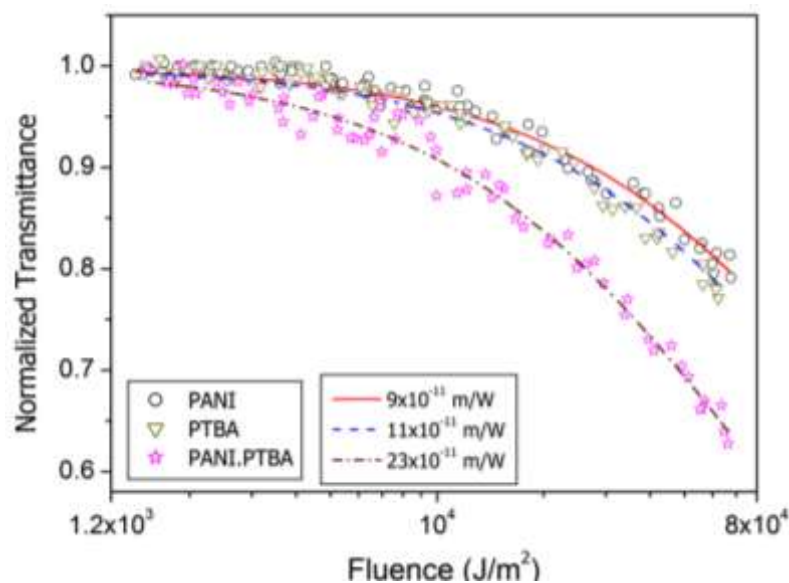


*Fig. 4.10* Laser fluence vs. Normalized transmittance curve for the samples.

#### 4.2.1.2 Photoluminescence spectroscopy analysis

There are a few reports on the enhancement of the nonlinear optical property in the case of charge transfer complex formed by porphyrins and phthalocyanines [15,32-35]. We have carried out photoluminescence measurements in the PTBA-PANI nanocomposite in order to get information about possible charge-transfer interaction between PTBA and PANI. However, no quenching was observed in the PTBA photoluminescence upon 420 nm excitation (position of the Soret band), implying the absence of a charge-transfer interaction. The photoluminescence spectrum of the nanocomposite shows the two-band red shifted luminescence similar to the spectra obtained by Serpone *et al.* for J and H- aggregates in the case of meso-tetraphenylporphyrin (H<sub>2</sub>TPP) [27]. Figure 4.11 shows the emission and excitation spectra of the nanocomposite sample. The excitation spectrum was taken at the fixed emission wavelength

of 650 nm (maximum emission wavelength), and it is almost identical to the absorption spectrum of the sample.

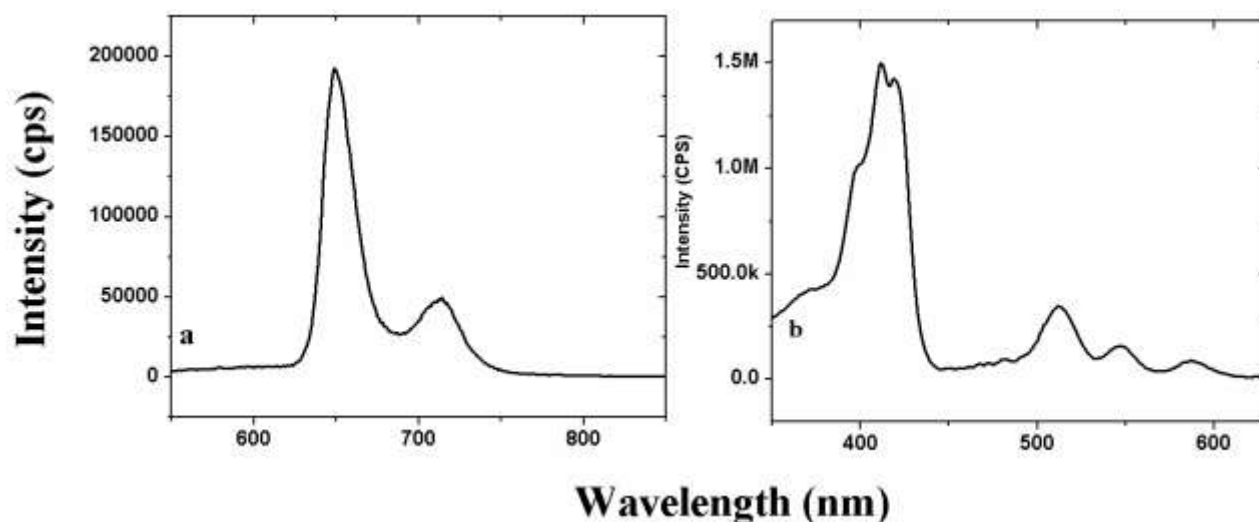


*Fig. 4.11 (a) Emission spectra and (b) excitation spectra of the PTBA-PANI mixture*

## 4.2.2 Formation of porphyrin/polyaniline nanostructures by layer-by-layer assembly and their application in ppb level lead sensing

### 4.2.2.1 Structural analysis

Figure 4.12a is the AFM surface topography image of the 4 layers of PTBA-PANI. It shows the presence of several nanoparticles of equal dimension. Figure 4.12b shows the z-height and x-y dimension of these nanoparticles. All the nanoparticles are of same size with x and y dimension around 150 nm and z-height of 13-15 nm.

In the first part of this chapter we have shown that the simple mixing of PTBA and PANI produces nanoparticles of dimension around 80-100 nm and z-height of 3-4 nm [36]. The formation of nanostructures during layer-by-layer assembly shows that interaction between PTBA and PANI is possible not only in bulk solution but also during the process of alternate layers formation. We have repeated the experiment to see the reproducibility of the AFM images. We observed that the images are reproducible and the dimensions of the nanostructures are comparable in all the images.

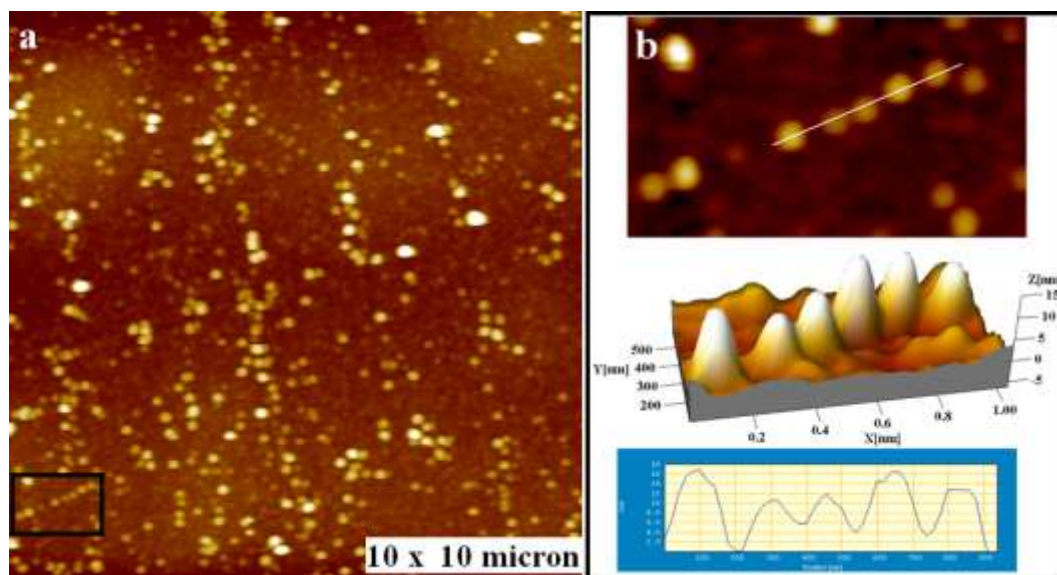


**Fig. 4.12** (a)  $10 \times 10 \mu\text{m}$  AFM image of 4 layers of PTBA-PANI showing the nanoparticles. (b) Zoomed portion from (a) showing the z-height and size of individual nanoparticles and 3d image of the zoomed area

The origin for the formation of these nanostructures is stacking of the PTBA J-aggregates [36]. These J-aggregates form due to the intermolecular association between the positively charged porphyrin rings and the negatively charged benzoic acid groups of neighboring porphyrins. Once we keep the 4-MPS modified substrate in PANI solution PANI deposits on the negatively charged surface and subsequently keeping this in PTBA solution, J-aggregates of PTBA assemble on the substrate. We repeat this process to build up alternate layers of PTBA and PANI. The driving force behind the formation of the nanostructures is  $\pi$ -stacking effect.

To confirm our hypothesis regarding the structure of nanocomposite we have conducted another experiment where we have deposited 8 layers of PTBA-PANI on 4-MPS modified gold substrate. The substrate was then imaged with an AFM in AC mode. Figure 4.13a is the AFM image of 8 layers of PTBA and PANI. We observed particles of x and y dimension around 200-300 nm and z-height of 30-40 nm. Figure 4.13b is the 3d image of 8 cycles of deposition of PTBA and PANI. The z-height observed in this case is almost twice the height of the nanoparticles observed in the case of 4 bilayers. This increase in size clearly reveals that the particles are growing in all the direction. Further layer deposition on gold shows the aggregation of the nanoparticles where we observed clusters of aggregated mass.

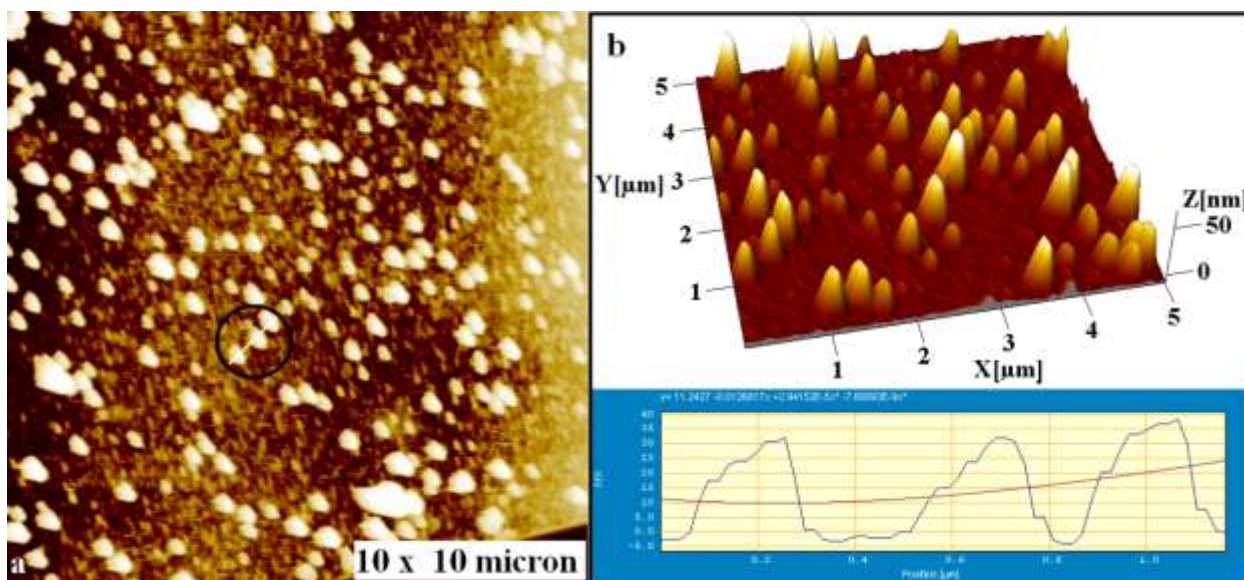


**Fig. 4.13** (a)  $10 \times 10 \mu\text{m}$  AFM image of 8 cycles deposited PANI and PTBA showing the nanoparticles. (b).  $5 \times 5 \mu\text{m}$  3d image of 8 cycles deposited PANI and PTBA and z- height and size of the nanoparticles

Different roughness parameters for the nanostructures modified gold substrate are shown in Table 4.2 [30]. The  $S_{dr}$  value calculated for 4-MPS modified gold substrate is 0.118% whereas for 4 layers PTBA-PANI and 8 layers PTBA-PANI,  $S_{dr}$  values are 0.713% and 1.19% respectively. The higher  $S_{dr}$  values are the indication of the surface having features of bigger size.

Substrate	Average roughness ( $S_a$ )	rms roughness ( $S_q$ )	Developed surface area ratio ( $S_{dr}$ )
4MPS SAM on gold	0.708	0.959	0.118 %
4 cycles deposited PTBA-PANI	3.90	6.02	0.713 %
8 cycles deposited PTBA-PANI	7.6	12.70	1.19 %

**Table 4.2** The roughness parameters of the surface the average roughness ( $S_a$ ), rms roughness ( $S_q$ ) and developed surfaces area ratio ( $S_{dr}$ )

### 4.2.2.2 Lead detection

The property of PTBA to chelate with heavy metal ions has been used to study the lead sensing response of the LbL film modified gold electrodes. The method used is the anodic stripping voltammetry (ASV) which is essentially a linear sweep voltammetry (LSV) with a preconcentration step [37-45]. At preconcentration step, lead deposits on the electrode surface on the application of the negative potential which subsequently stripped off during the positive potential scan. A very low concentration of lead down to 100 ppb was sensed with anodic stripping voltammetry (ASV). The film used here was 4-cycles deposited PTBA-PANI on gold.

Lead was deposited for an hour at a fixed potential of -1.0 V vs. SCE during the preconcentration step and it forms  $\text{Pb}^{2+}$  ion during the scan. During the preconcentration step lead deposits on the electrode surface and as the potential is scanned it oxidizes to  $\text{Pb}^{2+}$  which forms a chelate complex with the porphyrin present on the electrode surface in the nanoparticles. The chelate complex formation was confirmed by carrying out a simple LSV study in pure NaF, which shows the presence of the lead peak. This is also in accordance with the earlier work on the formation of chelate complex between PTBA and lead [16]. Figure 4.14A shows the potential scan during the ASV experiment. Figure 4.14B shows the ASV response for 100 ppb, 200 ppb, 300 ppb and 1000 ppb lead concentration. There is a clear stripping peak of lead observed at around -450 mV with linearly varying current in each case. The inset in Figure 4.14B shows the linear current vs. concentration curve.

For comparison the 8 layers PTBA-PANI was also studied. In this case the sensing was limited down to 1000 ppb only. This may be due to the more aggregation of the particles (see the AFM image Figure 4.13 in the case of 8 layers deposition) which may not be sterically preferable for the chelation to takes place. Since PTBA-PANI was shown to form nanoparticles just by simple mixing of the two components [36]. PTBA-PANI deposition on gold substrate was also carried out to check its sensitivity towards lead. In this case we did not observe any lead peak for 1000 ppb lead in our ASV experiment. The above experiment confirms that layer-by-layer assembly is crucial in the determination of lead.

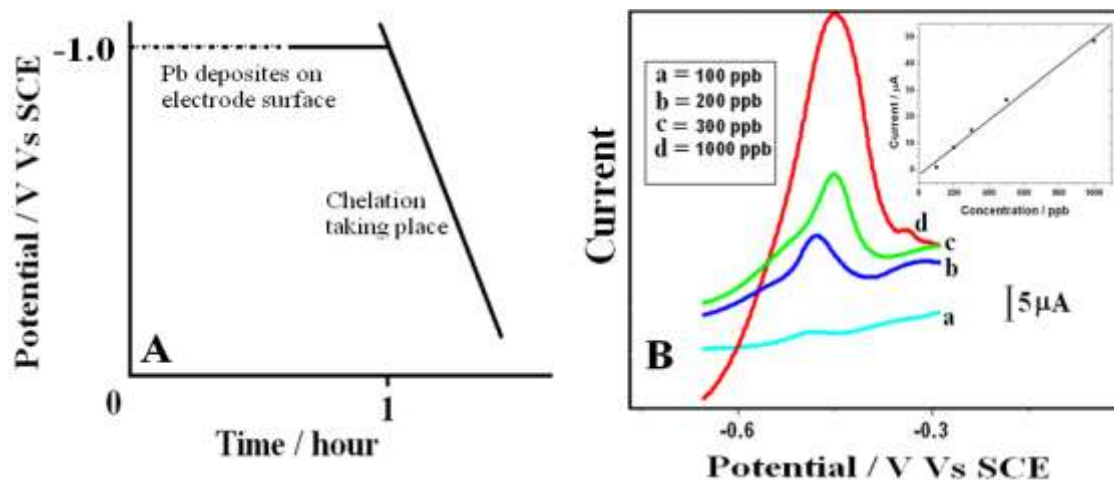


**Fig. 4.14** (A) Potential vs. time curve of anodic stripping voltammetry (ASV) for lead detection. (B) Anodic stripping voltammogram for lead concentration (a) 100 ppb, (b) 200 ppb, (c) 300 ppb and (d) 1000 ppb. Inset shows the current vs. concentration curve

A controlled deposition by layer-by-layer assembly provides us ample concentration of PTBA-PANI composite which is necessary for the lead sensing. Table 4.3 shows the standard deviation data for 1000 ppb lead concentration at different preconcentration time for 5 different electrodes.

Time / s	SD
480	0.608
720	0.687
900	2.48
1800	5.48
3600	10.88

**Table 4.3** The standard deviation data for 1000 ppb lead concentration at different preconcentration time for 5 different electrodes

### 4.2.3 Formation of porphyrin nanofibers (J-aggregates) and their optical property

The self association of dyes in solution or at the solid-liquid interface is a frequently encountered phenomenon in dye chemistry due to strong intermolecular van der Waals forces. As mentioned earlier in the chapter the porphyrin aggregates fall into the two categories *viz.* H-type and J-type

aggregates. The bathochromically shifted J-bands of the aggregates has been explained in terms of molecular exciton coupling theory, i.e., coupling of transition moments of the constituent dye molecules.

#### 4.2.3.1 Synthesis and characterization of porphyrin nanofibers

A 0.25 M PTBA solution was prepared in 1:1 DMF/water solvent as mentioned in the beginning of the chapter. The solution was made acidic by the addition of dilute  $\text{H}_2\text{SO}_4$  into the solution until a pH of 4.5 was achieved. This process is accompanied with the change in the color of the solution (from wine red to light yellow). The acidic PTBA solution was kept at  $50^\circ\text{C}$  using a water bath for 150 seconds. A drop of the above solution was casted on the freshly cleaved mica surface and allowed to evaporate in order to perform AFM imaging on the modified surface. Figure 4.15 shows the AFM image of the porphyrin nanofibers. The image shows an entangled network of the PTBA nanofibers of width about 50-100 nm. To check the reproducibility, the AFM imaging was carried out with different set of samples at different regions and we observed similar features everywhere. AFM imaging was also carried out for unheated sample and we did not observe any fibrous structures on the surface, which suggests that the significant activation energy is required for the formation of the aggregates in the form of the fibers.

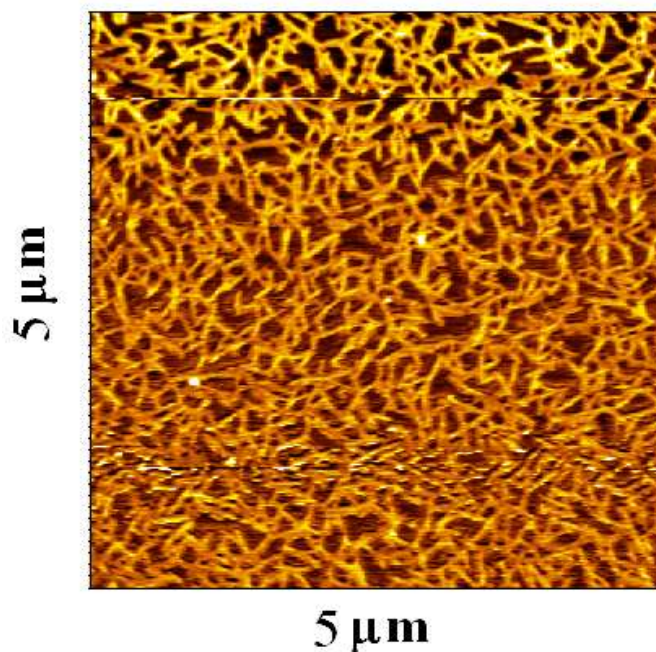
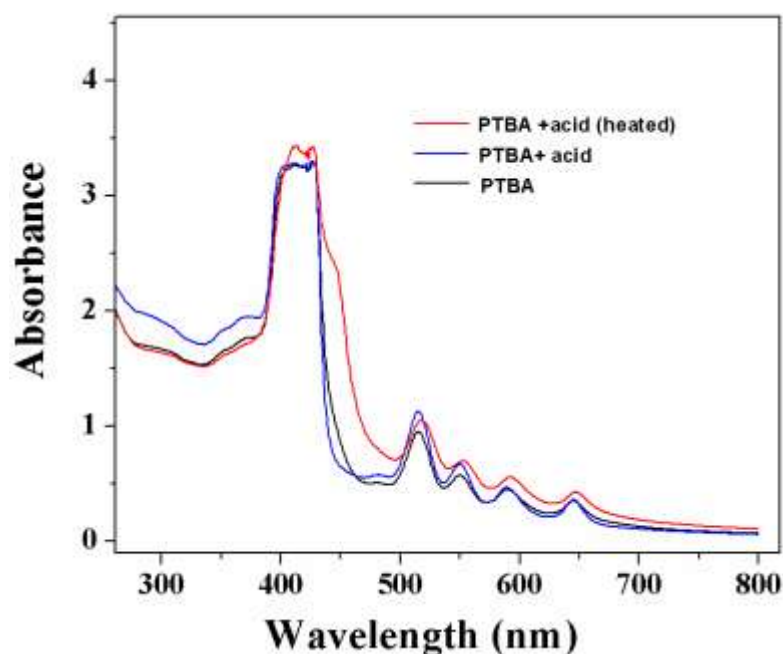


**Fig. 4.15**  $5\ \mu\text{m} \times 5\ \mu\text{m}$  AFM image of porphyrin nanofibers formed in DMF/water

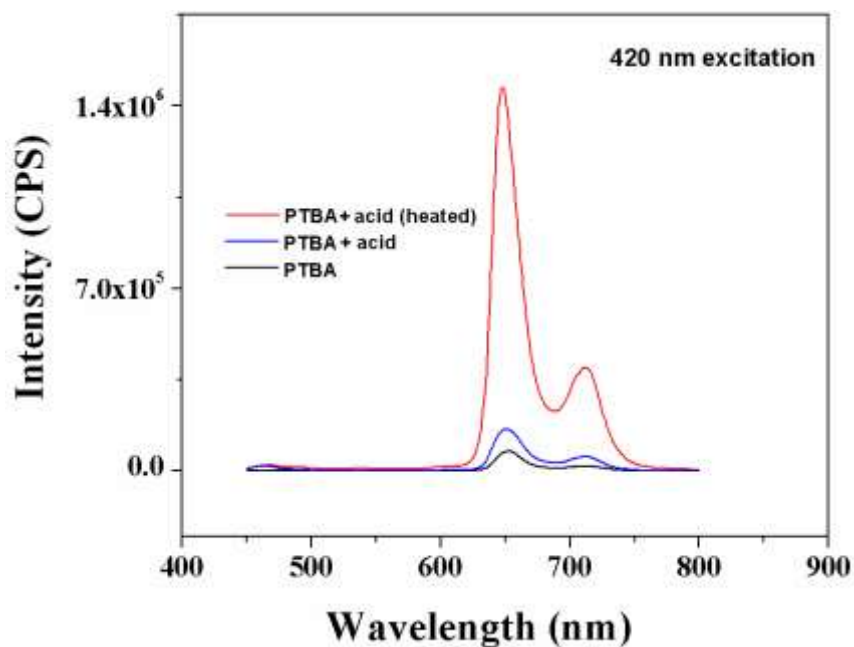
### 4.2.3.2 Optical properties of the PTBA nanofibers (UV-vis and photoluminescence spectroscopy)

Figure 4.16 shows the UV-vis spectroscopy results for PTBA solution (black) in the absence of acid, (blue) PTBA solution after acid addition and PTBA solution after the addition of acid and heating at 50 °C (red). All the three samples show a Soret band at 420 nm followed by a series of Q bands at higher wavelengths. In addition, the heated sample (red) shows a shoulder band in the Soret band and slightly red shifted Q bands. These features are attributed to the formation of J-aggregates in the solution [7,21-26,36].

Figure 4.17 shows the photoluminescence (PL) spectra of the PTBA solution at 420 nm excitation (without acid) in black, PTBA solution (after acid addition) in blue and PTBA solution (after addition of acid and heating) in red. The spectra are typical of the porphyrin PL spectra [38]. One can clearly see the huge enhancement, of about 20 times in the emission in the case of heated sample of PTBA. In fact the addition of acid also increases the emission (of about 2 times) as can be seen from the Figure 4.17.



**Fig. 4.16** UV-vis spectra of PTBA solution (black), PTBA after acid addition (blue) and PTBA after acid addition and heating (red)



**Fig. 4.17** PL spectra of PTBA solution (black), PTBA after acid addition (blue) and PTBA after acid addition and heating (red)

There are many reports on the quenching of the emission in case of aggregation but the enhancement in the emission phenomenon in the case of aggregates is a rare phenomenon [46-48].

The excited state of the aggregates often decays via non-radiative pathways, which is known as aggregation-caused quenching (ACQ) of light emission in the condensed phase. For example the formation of the aggregates solely due to the  $\pi$ - $\pi$  interaction tends to be non-emissive. In the aggregation induced emission (AIE) system, intramolecular motions (rotation and vibration) serve as relaxation pathways to deactivate the excited state in solutions. The excitonic energy can be transferred to the solvent during collisions of the excited molecule with the surrounding solvent molecules in the form of heat and therefore the restriction of these motions will decrease the nonradiative recombination rate of the excited state and enhance the emission efficiency, thus showing an AIE feature. In the present case also the formation of J-aggregates (spread deck of card kind of structures) leads to the blockage of the intramolecular motions and resulting in highly emissive aggregates.

### 4.3 Conclusions

We have shown that the porphyrin derivative 4,4',4'',4'''-(porphine-5,10,15,20- tetrayl) tetrakis (benzoic acid) (PTBA) forms nanoparticles when mixed with the conducting polymer PANI in a DMF/water mixture. The UV-vis absorption spectrum of the mixture shows the formation of the J-aggregates. Nonlinear optical absorption measurements at 532 nm show that the nanocomposite has an enhanced optical limiting property compared to the precursor compounds PTBA and PANI. This enhancement in the nonlinear absorption is due to the formation of aggregates of PTBA within the PTBA-PANI nanocomposite, which is also confirmed from AFM studies. The present studies is a clear demonstration of the fact that under favorable conditions for nanoparticle formation, even a simple procedure like mixing of two components can lead to a substantial modification of the net nonlinear optical property of a given chemical system.

We have also presented a simple technique to form nanostructured thin film by layer-by-layer assembly. The structural analysis was carried out using an AFM in AC mode. 4 and 8 layers of deposition was carried out on gold coated mica. Prior to the deposition, gold substrate was modified with self-assembled monolayer of 4-MPS to yield a negative charged layer. The modified electrode was used for lead detection and it was observed that the electrode is capable of detecting lead down to 100 ppb with the help of anodic stripping voltammetry.

We have also synthesized porphyrin nanofibers which are essentially the J-aggregates of porphyrin and studied their structure with the help of AFM. The optical properties (UV-vis and PL spectra) of the nanofibers were studied and it was observed that the nanofibers are highly emissive, contrary to the behavior of usual dye aggregates.

## Bibliography

- [1] R. Takahashi, Y. Kobuke, *J. Am. Chem. Soc.*, 125 (2003) 2372.
- [2] V. Lin, S. DiMugno, M. Therien, *Science*, 264 (1994) 1105.
- [3] Q. Zhou, C.M. Li, J. Li, X. Cui, D. Gervasio, *J. Phys. Chem. C*, 111 (2007) 11216.
- [4] A.D.F. Dunbar, T.H. Richardson, A.J. McNaughton, J. Hutchinson, C.A. Hunter, *J. Phys. Chem. B*, 110 (2006) 16646.
- [5] S. Anderson, H.L. Anderson A. Bashall, M. McPartlin, K.M. Sanders, *Angew. Chem. Int. Ed.*, 34 (2003) 1096.
- [6] D. Sun, F.S. Tham, C.A. Reed, P.D.W. Boyd, *Proc. Natl. Acad. Sci. USA*, 99 (2002) 5088.
- [7] X. Gong, T. Milic, C. Xu, J.D. Batteas, M.C.J. Drain, *J. Am. Chem. Soc.*, 124 (2002) 14290.
- [8] C.S. Doan, S. Shanmugham, D.E. Aston, J.L. McHale, *J. Am. Chem. Soc.*, 127 (2005) 5885.
- [9] E. Collini, C. Ferrante, R. Bozio, *J. Phys. Chem. B*, 109 (2005) 2.
- [10] Z.-B. Liu, Y.-Z. Zhu, Y. Zhu, S.-Q. Chen, J.-Y. Zheng, J.-G. Tian, *J. Phys. Chem. B*, 110 (2006) 15140.
- [11] M. Calvete, G.Y. Yang, M. Hanack, *Synth. Met.*, 141 (2004) 231.
- [12] R. Rotomskis, R. Augulis, V. Snitka, R. Valiokas, B. Liedberg, *J. Phys. Chem. B*, 108 (2004) 2833.
- [13] E.M. Ni Mhuirheartaigh, S. Giordani, W.J. Blau, *J. Phys. Chem. B*, 110 (2006) 23136.
- [14] S. Mo, M. Fazekas, E.G.A. Notras, W.J. Blau, M. Zawadzka, O.B. Locos, E.M. Ni Mhuirheartaigh, *Adv. Mater.*, 19 (2007) 2737.
- [15] L. Shen, X.M. Wang, B. Li, W.L. Jiang, P. Yang, S.X. Qian, X.T. Tao, M.H. Jiang, *J. Porphyrins. Phthalocyanines*, 10 (2006) 160.
- [16] K. Kilian, K. Pyrzynska, *Talanta*, 60 (2003) 669.
- [17] W. Yantasee, Y. Lin, K. Hongsirikarn, G.E. Fryxell, R. Addleman, C. Timchalk, *Environmental Health Perspectives*, 115 (2007) 1683.
- [18] Y. Xiao, A.A. Rowe, K.W. Plaxco, *J. Am. Chem. Soc.*, 129 (2007) 262.
- [19] S. Bhadra, N.K. Singha, D. Khastgir, *J. Appl. Poly. Sci.*, 104 (2007) 1900.
- [20] M.S. Bahae, A.A. Said, T.H. Wei, D.J. Hagan, E.W. Van Stryland, *IEEE J. Quantum Electron.*, 26 (1998) 760.
- [21] W. Xu, H. Guo, D.L. Akins, *J. Phys. Chem. B*, 105 (2001) 1543.
- [22] M.Y. Choi, J.A. Pollard, M.A. Webb, J.L. McHale, *J. Phys. Chem. B*, 125 (2003) 810.

- [23] Z.-Min Ou, H. Yao, K. Kimura, *J. Photochem. Photobiol A: Chemistry*, 189 (2007) 7.
- [24] Z. Wang, C.J. Medforth, J.A. Shelnett, *J. Am. Chem. Soc.*, 126 (2004) 15954.
- [25] T. Kobayashi, *J-Aggregates*; World Scientific: Singapore, New Jersey, London, Hong Kong, 1996.
- [26] H. Yao, K. Domoto, T. Isohashi, K. Kimura, *Langmuir*, 21 (2005) 1067.
- [27] R.F. Khairutdinov, N. Serpone, *J. Phys. Chem. B*, 103 (1999) 761.
- [28] T.G. Dewey, D.A. Raymond, D.H. Turner, *J. Am. Chem. Soc.*, 101 (1979) 5822.
- [29] Y.H. Zhang, Y. Wu, *Chinese Chemical Letters*, 16 (2005) 534.
- [30]  $S_{dr}$  expresses the ratio between the surface area while taking the z height into account and the area of the flat xy plane. For a totally flat surface the surface area and the area of the xy plane are the same and  $S_{dr} = 0\%$ .
- [31] J.F. Jorgensen, C.P. Jensen, J. Garnaes, *App. Phys. A: Materials Science & Processing*, 66 (1998) 847.
- [32] Y. Zhang, M. Ma, X.Wang, D. Fu, N. Gu, J. Liu, Z. Lu, Y. Ma, L. Xu, K. Chen, *J. Phys. Chem. Solids*, 63 (2002) 2115.
- [33] Z. Tian, C. He, C. Liu, W. Yang, J. Yao, Y. Nie, Q. Gong, Y. Liu, *Materials Chemistry and Physics*, 94 (2005) 444.
- [34] T. Zhang, F. Wang, H. Yang, Q. Gong, X. An, H. Chen, D. Qiang, *Chem. Phys. Lett.*, 301 (1999) 343.
- [35] W. Huang, S. Wang, R. Liang, Q. Gong, W. Qiu, Y. Liu, D. Zhu, *Chem. Phys. Lett.*, 324 (2000) 354.
- [36] R.K. Pandey, C. S. Suchand Sandeep, R. Philip, V. Lakshminarayanan, *J. Phys. Chem. C*, 113 (2009) 8630.
- [37] A. Zeng, E. Liu, S.N. Tan. S. Zhang, J. Gao, *Electroanalysis*, 14 (2002) 1294.
- [38] W. Zhao, Pei-Yu Ge, Jing-Jahn Xu, Hong-Yuan Chen, *Langmuir*, 23 (2007) 8597.
- [39] A.M. Zimer, R. Bertholdo, M.T. Grassi, A.J.G. Zarbin, L.H. Mascaro, *Electrochem Commun.*, 5 (2003) 983.
- [40] J.M. Zen, A.S. Kumar, D.M. Tsai, *Electroanalysis*, 15 (2003) 1073.
- [41] W. Kangbing, H. Shengshui, F. Junjie, B. Wen, *Anal. Chim. Acta*, 489 (2003) 215.
- [42] Y. Geng, J. Li, Z. Sun, X. Jing, F. Wang, *Synth. Met.*, 96 (1998) 1.
- [43] G. Abate, J.C. Masini, *Org. Geochem.*, 33 (2002) 1171.

- [44] K.D. Arabinda, M. Guardia, M.L. Cervera, *Talanta*, 55 (2001) 1.
- [45] W. Kangbing, H. Shengshui, F. Junjie, B. Wen, *Anal. Chim. Acta*, 447 (2001) 11.
- [46] Y. Hong, J. W. Y. Lam, B. Z. Tang, *Chem. Commun.*, (2009) 4332.
- [47] R. Deans, J. Kim, M. R. Machacek, T. M. Swager, *J. Am. Chem. Soc.*, 122 (2000) 8565.
- [48] B.-K. An, S.-K. Kwon, S.-D. Jung, S. Y. Park, *J. Am. Chem. Soc.*, 124 (2002) 14410.

## Chapter 5

# Electrochemical Synthesis of Palladium and Conducting Polymer Nanocomposite films for Applications in Electrocatalysis

*Platinum is the most extensively used noble metal for the electro-oxidation of small organic molecules such as methanol, ethanol and formic acid in direct fuel cells (DFCs), and in spite of the remarkable progress in minimizing the Pt loading to achieve optimum performance, the high price of Pt is a major constraint on its utility as an electrocatalyst. Therefore there is a clear need for a realistic, less expensive substitute of Pt, without compromising on catalytic activity. Owing to its lower cost, higher abundance and proven electrocatalytic effect on small organic molecules, Pd has the potential to emerge as a substitute for Pt. Instead of using conventional non-conducting carbon based supports, conjugated polymers provide the opportunity to have an encapsulating support matrix. This chapter deals with the synthesis, characterization and electrocatalytic studies on palladium and conducting polymer based nanocomposites.*

## 5.1 Introduction

Nanoparticles of noble metals in combinations with other low cost materials have the potential to emerge as unique catalysts materials for fuel cells. This approach of the formation of nanocomposites, would eventually lead towards the synthesis of low cost alternatives to Pt. The major challenge in effectively exploiting the high surface activity of the nanoparticles is to immobilize them on appropriate matrix without loss of catalytic activity. Carbon based supports are generally used for dispersing the nanoparticles and to achieve very high catalytic activity. In this respect conducting polymers are effective substitutes to the carbon supports due to their lower ohmic drop across the electrode and the ease with which they can be functionalized with biomolecules for different applications.

Among different metal nanostructures the palladium and its nanocomposites are drawing increasing attention in recent times due to their importance as catalytic material [1-4], hydrogen storage material [5-8], and sensors [9,10]. It is however essential to prepare porous Pd nanostructures containing nanosized particles on suitable substrates to exploit the high surface area to volume ratio and enhanced catalytic activity. Therefore, the preparation of Pd nanostructures that are either solution based or coated on suitable substrates is of considerable interest among various research groups [11-28].

Most of the methods for the preparation of Pd nanostructures reported in the literature are solution based and typically yield the nanoparticles that can be spread on the electrode surface or mixed with an electrode material such as carbon for immobilization and study of the catalytic reactions such as electro-oxidation of methanol, ethanol [12-14], or formic acid [15-24]. A strong potential dependent particle size effect was found by studying the particle effect in the Pd catalyzed electro-oxidation of formic acid [23]. Wieckowski *et al.* have studied the size effect of the unsupported palladium nanoparticles as the catalyst for the formic acid electro-oxidation [17] and concluded that the smaller particles having less 'd' band characteristics bind -COOH intermediate weakly, leaving the surface free for the oxidation reaction. There have been some reports on the formation of Pd-PANI composite in solution phase as well as on surfaces [29,30]. The studies show that there is a strong interaction between PANI and Pd nanoparticles in the composite. However most of the methods available in the literature for metal and conducting polymer nanocomposite synthesis are multistep.

In addition to PANI, PEDOT is another most studied conducting polymer. The very stable and highly conductive cationic-doped state and the low HOMO–LUMO bandgap of

conductive PEDOT makes it a useful component of many commercial devices such as antistatic films, transparent conductor, organic light emitting diodes, thin film transistors and electrochromic windows [32-40]. PEDOT can be prepared either by chemical or electrochemical polymerization. It is known that protic acids and a variety of Lewis acids can be used to catalyze an equilibrium reaction of EDOT to yield dimeric and trimeric compounds [41]. However mineral acids such as sulphuric acid, hydrochloric acid and other strong acids are commonly used for the electrochemical synthesis of PEDOT [41].

The present chapter is divided into two parts. The first part deals with the synthesis and characterization of Pd-PEDOT nanocomposite film and the electrocatalytic response of the resulting film towards ethanol oxidation in alkaline medium and hydrogen evolution reaction in acidic medium. The method consists of *in-situ* electrochemical generation of Pd ions in the solution from Pd wire anode which is immediately followed by reduction with EDOT present in the solution which in turn undergoes oxidative polymerization.

Second part deals with the synthesis and characterization of Pd-PANI nanofiber film and electrocatalytic response towards formic acid oxidation in acidic medium and alcohols (methanol and ethanol) oxidation in alkaline medium. The nanocomposite film was formed on gold substrate and later characterized using SEM, EDAX, ICP-MS and AFM.

## 5.2 Methods and materials

We have carried out the electrochemical characterization studies by coating Pd-PEDOT and Pd-PANI films on a gold disc working electrode of geometric area about  $0.002 \text{ cm}^2$ . We have used Pd-PEDOT and Pd-PANI films deposited on larger area gold substrate (deposited on glass by vacuum evaporation with chromium underlayer) for SEM, EDAX and AFM studies. For galvanostatic deposition of nanocomposite film, a 0.5 mm thick Pd wire of 99.9% purity (Advent, UK) was used as an anode and a gold electrode as the cathode.

The chronoamperometry measurements were carried out by the application of a potential pulse of 10 s duration with a step size of 10 mV. Prior to the application of each potential step, the electrode surface was subjected to a potential program of 5s each at 0.8 V and  $-0.65 \text{ V}$  vs. SCE. Application of the positive potential ensures the removal of surface poisons and the subsequent negative potential reduces the surface oxides formed during the application of the positive potential. This applied potential program acts as a pre-treatment for the surface exposing a fresh surface for chronoamperometry studies. This method is an adaptation of the pre-treatment technique reported by Herrero *et al.* [42]. The current data

obtained at the end of 10s of the potential pulse are used for the polarization plots and measurement of the Tafel slopes. More detailed discussion on Tafel slopes and their significance in the context of alcohols oxidation reaction is presented later in the chapter. Galvanostatic deposition was carried out using an EG&G potentiostat (model 263A) in constant current mode and interfaced to a PC through a GPIB card (National Instruments). The electrolyte temperature was varied using a temperature controller (JULABO- Model F25).

### **5.2.1 Enhanced electrocatalytic activity of Pd dispersed PEDOT film in hydrogen evolution and ethanol electro-oxidation reactions**

In the present chapter very high electrocatalytic activity of Pd nanoparticles dispersed PEDOT film on gold surface for ethanol electro-oxidation reaction in alkaline medium and H<sub>2</sub> evolution reaction in acidic medium has been demonstrated. The mechanism of the formation of the film in this case is similar to that of Li *et al.* of electrophoretic depositing PANI colloids on solid surfaces [43]. In their method the presence of -NH<sup>+</sup> groups on PANI helps in the electrophoretic deposition of PANI. While the reported methods in the literature generally involve multisteps, the present method has the benefit of having just a single step to simultaneously deposit Pd nanoparticles and PEDOT to form a stable nanocomposite thin film.

There are a few reports in the literature of metal and PEDOT composites where the nanocomposites of PEDOT were formed with gold, platinum and palladium [45-47]. Reetz *et al.* have described a method of producing size-selective Pd and Ni nanoclusters by using the respective metals as sacrificial anodes [48a,b]. In this method, for example, the dissolving Pd ions migrate towards the cathode which are then electrochemically reduced on the surface as Pd atom clusters and subsequently stabilized in the solution by tetraalkylammonium cations.

#### **5.2.1.1 Synthesis of the Pd-PEDOT nanocomposite on gold substrate**

The electrolyte was prepared by dissolving 5 mg of EDOT and 0.01 M SDS in 5 ml of 0.1 M HCl. Sodium dodecyl sulfate (SDS) was added in the electrolyte solution to increase the solubility of EDOT monomer in the electrolyte. The electrostatic interaction between SDS anion and EDOT radical cation yields strongly bonded complex between these ions [49,50]. In addition, an ordered film of PEDOT on gold can be formed at lower potentials in the presence of SDS in aqueous medium.

The present method consists of *in-situ* electrochemical generation of Pd ions from a Pd wire anode at high current densities. The dissolved Pd ions immediately form chloropalladate complex with chloride ions present in the solution. [51,52]. The chloropalladate being an oxidizing agent can initiate the polymerization of EDOT, chloropalladate in turn gets reduced to Pd nanoparticles. These Pd nanoparticles adhere on the PEDOT and form Pd-PEDOT nanocomposite. A similar process was reported earlier for the preparation of PANI coated Au nanostructures by using chloroauric acid, a powerful oxidizing agent [53]. The Pd-PEDOT nanocomposite owing to the positively charged thiophene moieties in it [41], electrophoretically deposit on the gold substrate as a thin film, a process similar to that of the electrophoretic deposition of PANI colloids on gold [43].

The electrolyte was continuously stirred using magnetic stirrer during the experiment. A Pd wire of 5 mm length and 0.5 mm diameter with an area of 0.1 cm<sup>2</sup> dipped in the electrolyte served as the anode and working electrode while a gold disc electrode of 0.002 cm<sup>2</sup> geometric area acted as the cathode and counter electrode. We have carried out the deposition in the galvanostatic mode with different current values for an hour to study the effect of current on the nature of coating. During the electrolysis there was an intense evolution of gases at both the electrodes due to water electrolysis. (*Caution! the cell should have gas outlets near both the electrodes!*) The solution, which was colorless in the beginning, turned light blue initially and to brown at the end. Simultaneously, a dark colored thin film is formed on the cathode surface. At higher currents (60 and 70 mA) the gas evolution was rapid and the dissolution of the metal was not uniform. Hence for all the characterization studies of the film, the specimen was deposited at a controlled anodic current of 50 mA. Figure 5.1 shows a photograph of the Pd-PEDOT nanocomposite coated on 0.15 cm<sup>2</sup> area electrode.

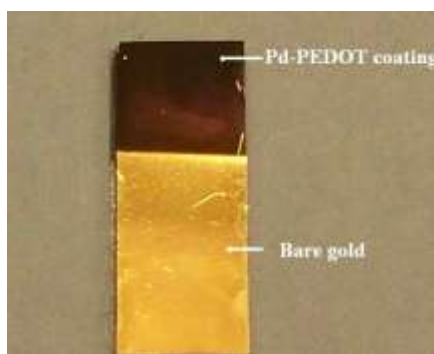


*Fig.5.1 A photograph of the Pd-PEDOT nanocomposite film deposited on evaporated gold on glass substrate*

The Pd content of the nanocomposite was evaluated using inductively coupled plasma-mass spectroscopy (ICP-MS) by dissolving the nanocomposite film in aquaregia (1:3 conc.  $\text{HNO}_3$ :conc.  $\text{HCl}$ ). The film was found to have a Pd content of  $0.31 \mu\text{g mm}^{-2}$  in the nanocomposite.

### 5.2.1.2 Characterization of the Pd-PEDOT coated surface

#### *SEM and EDAX analysis*

Figure 5.2 shows the SEM image of the Pd-PEDOT coated gold surface containing large clusters of about 200 nm in size, spread throughout the surface. There are also smaller particles on those clusters of size around 10-15 nm.

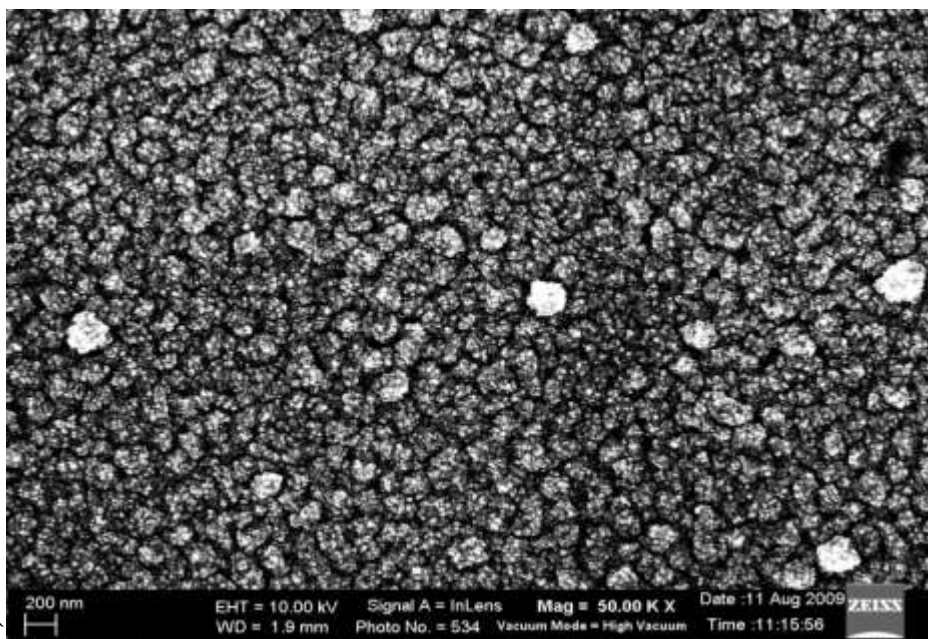


**Fig. 5.2** FE-SEM image of Pd-PEDOT nanocomposite showing the Pd nanoparticles (smaller particles) dispersed in PEDOT (Pd-PEDOT nanocomposite)

Table 5.1 presents the results of the elemental analysis obtained from the EDAX on the Pd-PEDOT modified surface. The weight % of Pd is 2.68, which is quite low compared to a much larger amount of carbon (13.38%) arising from the PEDOT film. Besides, the analysis reveals the presence of S, Na and O on the surface. The very large amount of gold (82.20 weight %) is contributed by the gold substrate, indicating the porous nature of the film. From the EDAX data, the amount of Pd present in the nanocomposite film (excluding the concentration of Au from the substrate) is calculated to be about 15%.

Element	Weight%	Atomic%
C	13.40	67.71
O	0.92	3.50
Na	0.50	1.27
S	0.34	0.64
Pd	2.68	1.53
Au	82.20	25.36

*Table 5.1 EDAX elemental analysis results for Pd-PEDOT nanocomposite film*

### ***AFM analysis***

We have carried out AFM imaging on the nanocomposite thin film to look into the 3-dimensional profile of the film. Figure 5.3 shows a 5  $\mu\text{m}$  x 5  $\mu\text{m}$  AFM image of the Pd-PEDOT coated surface. The corresponding line scan is also shown in the inset of the figure.

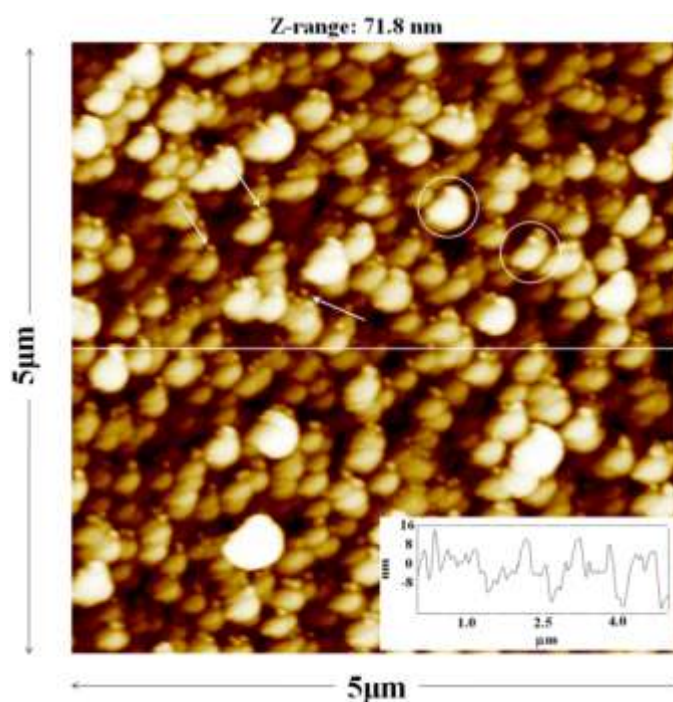


*Fig. 5.3 5  $\mu\text{m}$  x 5  $\mu\text{m}$  AFM image of Pd-PEDOT nanocomposite showing the Pd nanoparticles dispersed PEDOT film with the corresponding line scan in the inset*

The features observed in the AFM image show good similarity with those seen in the SEM image. As shown in the figure, there are disc like clusters on the surface (indicated as circles) and attached to them are smaller clusters (shown by arrows). We have carried out AFM imaging at several different regions on the surface and observed similar features. The

average height of the features observed in AFM image is 16 nm with an rms roughness of 9 nm. The rms roughness of the unmodified gold surface was 4.5 nm indicating that the surface roughness of the coated film is not significantly higher than that of bare substrate.

### **5.2.1.3 Voltammetric response of the Pd-PEDOT coated electrode in acid medium, catalytic activity towards hydrogen evolution reaction (HER)**

Palladium is well known to absorb massive quantities of hydrogen in bulk to form hydrides and therefore has a good technological potential as a hydrogen storage material [54]. We have carried out CV studies in acidic medium in order to study the hydrogen evolution reaction (HER) on Pd nanostructure enclosed in PEDOT matrix.

Figure 5.4 shows the voltammetric behavior of the Pd-PEDOT coated electrode in 0.5 M H<sub>2</sub>SO<sub>4</sub> at a scan range of -0.3 V to 1.2 V and at a scan rate of 100 mV s<sup>-1</sup>. The inset shows the voltammetric behavior of the Pd disc electrode in the same electrolyte. The CV for the Pd disc electrode in 0.5 M H<sub>2</sub>SO<sub>4</sub> shows a single broad anodic peak around 0.00 V. This broad hump is due to the oxidation of both the adsorbed and absorbed hydrogen on the Pd disc electrode, as reported earlier for bulk Pd electrodes [5,12]. On the other hand, the CV for the Pd-PEDOT coated disc electrode shows two peaks, one of which is a small shoulder peak in the negative potential region during the anodic sweep. The first peak at -0.13 V corresponds to the oxidation of the adsorbed hydrogen (H<sub>ads</sub>) while the subsequent peak at 0.0 V is due to the oxidation of the absorbed hydrogen (H<sub>abs</sub>) on Pd surface [5]. It is known from the literature that two well resolved peaks for the oxidation of adsorbed and absorbed hydrogen in Pd are manifested exclusively in the case of Pd nanoparticles [5,12]. This behavior is attributed to the larger number of surface sites available for adsorption on nanoparticles surface. The CV results support the above observation by exhibiting the characteristic behavior of the Pd nanoparticles on the electrode surface.

#### ***Effective catalytic surface area (ECSA) determination***

Since in the case of Pd, the absorption of hydrogen takes place along with its adsorption, the area calculated by measuring the charge under the H<sub>ads</sub> peak does not reflect the true surface area of the Pd in the nanocomposite [26]. However the electroactive surface area or the effective catalytic surface area (ECSA) of Pd can be measured from the palladium oxide stripping analysis [12,26]. The charge value under the stripping peak is measured to be 0.7 μC and with the conversion factor of 424 μC cm<sup>-2</sup> for Pd oxides stripping current [12], the ECSA for the Pd-PEDOT film is measured to be 1.65 x 10<sup>-3</sup> cm<sup>2</sup>.

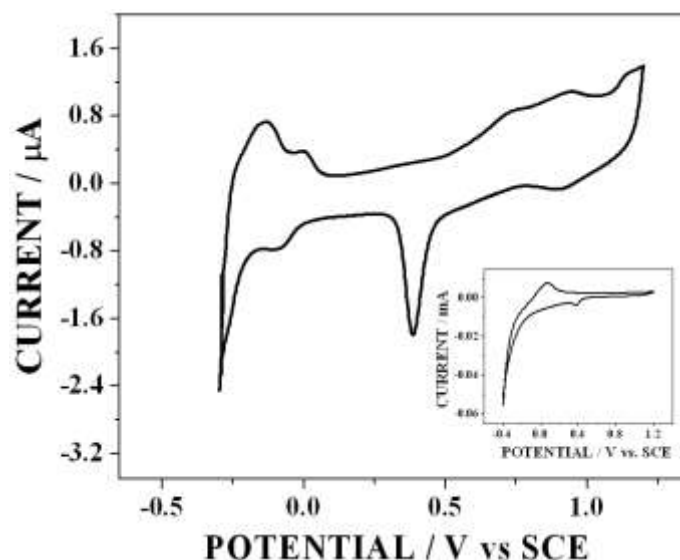


**Fig. 5.4** Voltammetric behaviour of the Pd-PEDOT coated disc electrode in 0.5 M  $H_2SO_4$  (scan rate =  $100 \text{ mV s}^{-1}$ ) showing the presence of two well separated peaks for the oxidation of adsorbed hydrogen and absorbed hydrogen. Inset shows the voltammogram for Pd disc electrode in 0.5 M  $H_2SO_4$

Even though the effective surface area value is relatively low for the electrode, it nonetheless exhibits a very high hydrogen evolution activity. This observation also confirms the very low Pd content measured using EDAX and ICP-MS, which show a value of 15 wt % and  $0.31 \mu\text{g mm}^{-2}$  Pd content in the nanocomposite film respectively.

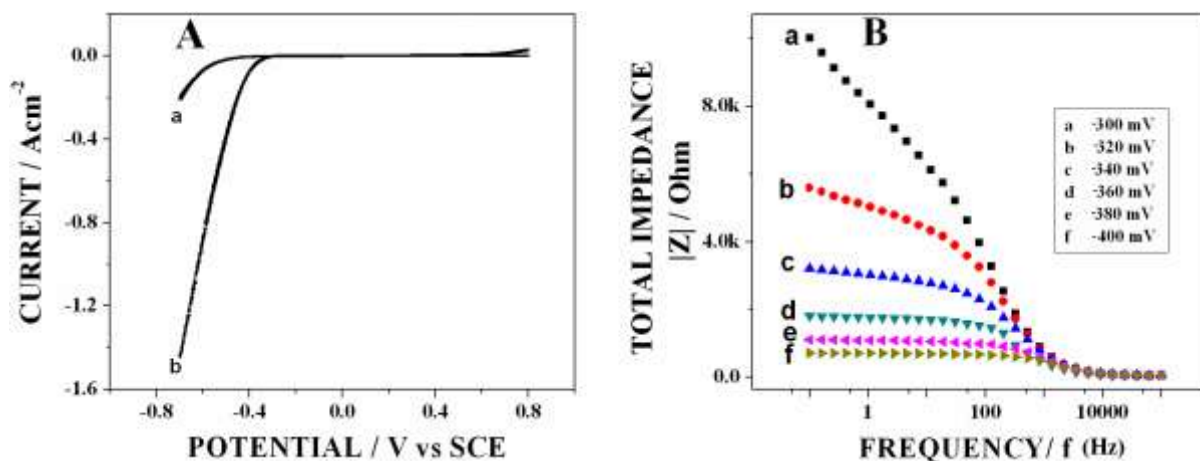
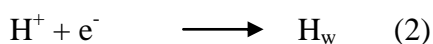
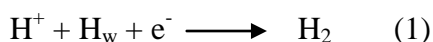


**Fig. 5.5** (A) (a) The voltammetric behavior of the Pd disc electrode in 0.5 M  $H_2SO_4$  at a scan rate of  $100 \text{ mV s}^{-1}$  and (b) the CV for Pd-PEDOT nanocomposite coated gold disc electrode in 0.5 M  $H_2SO_4$  at same scan rate. (B) The total impedance plot in 0.5 M  $H_2SO_4$  at different potentials (from a = -300 mV to f = -400 mV) for the Pd-PEDOT nanocomposite film

Figure 5.5A (a) and (b) show respectively the voltammetric behavior of the Pd disc electrode and Pd-PEDOT coated Au disc electrode in 0.5 M H<sub>2</sub>SO<sub>4</sub> at a scan rate of 100 mV s<sup>-1</sup>. It is clear from the figures that there is a huge increase in the hydrogen evolution current for Pd-PEDOT nanocomposite film. The measured onset potential (-0.28 V) is also significantly lower than -0.50 V, observed for Pd disc electrode. The large hydrogen evolution current is truly catalytic and not just due to the increase in surface area of the Pd nanoparticles. This aspect is clear when the hydrogen evolution currents are compared for unit area of the respective surfaces. For example, at a potential of -0.45 V, the currents per unit area in the case of Pd electrode and Pd-PEDOT modified electrodes are 7.0 and 230 mA cm<sup>-2</sup> respectively, an enhancement by a factor of about 33. In all the cases the currents are normalized with respective true surface area or effective catalytic surface area (ECSA), which was calculated by measuring the charge under the palladium oxides reduction peak as described earlier in this section.

According to the Heyrovsky-Volmer mechanism the HER follows the following reaction scheme for the Pt group metals [55].



In the above reactions H<sub>w</sub> denotes the weakly absorbed hydrogen into the bulk of the metal. In the case of Pd, as it absorbs hydrogen, a penetration reaction operates as follows:



In the above reaction Pd<sub>s</sub>, Pd<sub>b</sub> and H<sub>s</sub>, H<sub>b</sub> represent the surface and bulk state of Pd and hydrogen respectively. The absorbed hydrogen atoms later diffuse to the electrode surface where electro-oxidation reaction occurs according to the reaction 1 and 2 [56,57].

We have carried out EIS at different potentials between -300 mV to -400 mV in 0.5 M H<sub>2</sub>SO<sub>4</sub> for the Pd-PEDOT nanocomposite film. Figure 5.5B shows the plots of total impedance vs. frequency at different potentials (a) -300 mV, (b) -320 mV, (c) -340 mV, (d) -360 mV, (e) -380 mV and (f) -400 mV. The corresponding values of total impedance measured at the lowest frequency of 0.1 Hz are 10 kΩ, 5.6 kΩ, 3.2 kΩ, 1.8 kΩ, 1.1 kΩ and 0.7 kΩ respectively. This shows that the total impedance decreases systematically with the applied cathodic potential, thereby confirming the facile nature of the electron transfer process. The results of the EIS studies carried out in 0.5 M H<sub>2</sub>SO<sub>4</sub> for Pd disc electrode in the same conditions are shown in Figure 5.6. We have fitted the EIS data to an equivalent circuit

that is appropriate for porous films formed by layer-by-layer assembly [58]. The results obtained are presented in the Table 5.2 and the fitted curves are shown in Figure 5.7. Table 5.2 lists the impedance values obtained at 0.1 Hz for the Pd-PEDOT electrode. It can be seen that the impedance values are very much less in the case of Pd-PEDOT electrode towards HER.

Potential   mV	$R_s$   Ohm	$R_f$   Ohm	$R_{ct}$   Ohm	$C_f$   F ( $n = 0.9$ )	$C_{dl}$   F ( $n = 0.8$ )	Warburg ( $Y_o$ )   $S s^{1/2}$
-300	58.74	4852	3116	$3.9 \times 10^{-7}$	$1.17 \times 10^{-5}$	$5.5 \times 10^{-4}$
-320	58.59	3564	1339	$4.2 \times 10^{-7}$	$1.74 \times 10^{-5}$	$1.78 \times 10^{-3}$
-340	56.09	2108	784	$7.0 \times 10^{-7}$	$1.0 \times 10^{-5}$	$4.8 \times 10^{-3}$
-360	58.93	1387	301.5	$4.6 \times 10^{-7}$	$2.3 \times 10^{-5}$	$1.95 \times 10^{-2}$
-380	57.27	805	209	$7 \times 10^{-7}$	$1.0 \times 10^{-5}$	0.038
-400	58.98	517.2	126.7	$5.8 \times 10^{-7}$	$1.0 \times 10^{-5}$	0.08

**Table 5.2** The values obtained after fitting the data are shown in the table. The admittance ( $Y_o$ ) is shown for the Warburg part

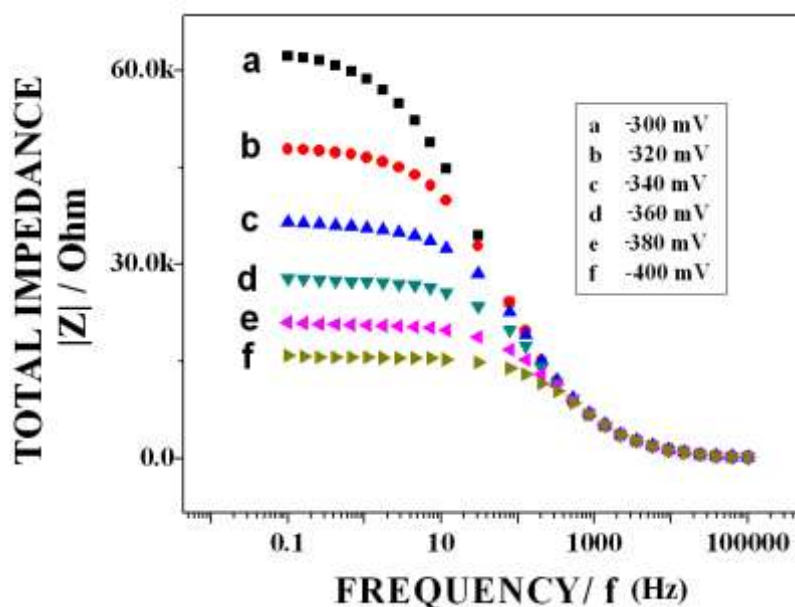


**Fig. 5.6** The total impedance plot at different potentials (from a = -300 mV to f = -400 mV) for the Pd disc electrode in 0.5 M  $H_2SO_4$

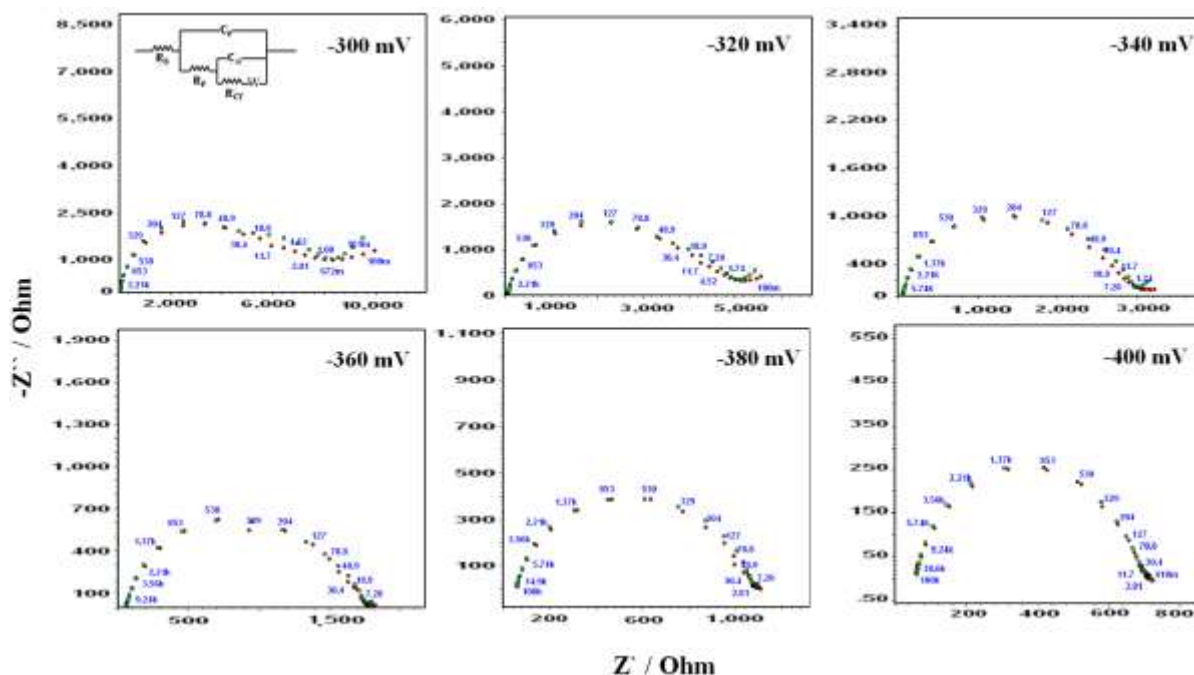


**Fig. 5.7** Fitting of the Nyquist plots obtained for HER reaction on Pd-PEDOT nanocomposite film at different potentials in 0.5 M  $H_2SO_4$ . Inset in the first figure shows the equivalent circuit used for the fitting of the data

In addition to the charge transfer resistance ( $R_{ct}$ ) and double layer capacitance ( $C_{dl}$ ), the contributions from film capacitance ( $C_f$ ), film resistance ( $R_f$ ) and Warburg impedance ( $Z_w$ ) are also considered. The diffusion of  $H^+$  ions to the Pd nanoclusters embedded in the polymer matrix results in the Warburg impedance in the equivalent circuit. The value of  $R_{ct}$  and  $R_f$  decreases with decreasing potential *i.e.* from -300 mV to -400 mV, which shows the increasingly facile nature of the reaction at higher cathodic potentials. The Warburg admittance (inverse of the Warburg impedance), increases with the potential which shows the enhanced diffusion of the reactants (hydrogen ions) at more negative potentials. The constant phase elements (CPEs) obtained by equivalent circuit fitting is analogous to the film capacitance ( $C_f$ ) and double layer capacitance ( $C_{dl}$ ) with  $n$  values 0.9 and 0.8 respectively. The variation in capacitance values with potential, however, is not very significant.

### 5.2.1.4 Catalytic activity of Pd-PEDOT coated electrode towards electro-oxidation of ethanol

#### *Cyclic voltammetry in alkaline medium*

The electrocatalytic oxidation of small alcohols has been intensively studied as it is the anodic reaction in direct alcohol fuel cells (DAFCs). Among other small chain alcohols

ethanol is being increasingly viewed as a better and safer alternative to methanol, in direct fuel cells, due its lower toxicity, higher energy density and easy availability through renewable and green chemical sources. Since the Pd nanoparticles are not directly deposited on the electrode surface and embedded within the polymeric matrix, the available effective active centers are higher which makes it an ideal electrocatalytic material.

A great amount of research work is focused on the alcohol oxidation in acidic media, for direct fuel cells with the use of proton exchange membranes especially Nafion. However due to the excessive reliance on Pt and with its loading reaching its lowest limit, there is an increasing interest in other noble and non-noble metal alternatives. Since many of the non-noble metals are stable in alkaline medium, a significant interest in the development of the hydroxyl ion conducting membranes, such as polysulphones is taking place worldwide [59].

In this work we have explored the Pd-PEDOT as a potential catalyst material in alkaline medium for electro-oxidation of ethanol. We have evaluated the electrocatalytic activity of Pd-PEDOT nanocomposite coated electrode by studying ethanol electro-oxidation as a model system in 0.5 M NaOH.

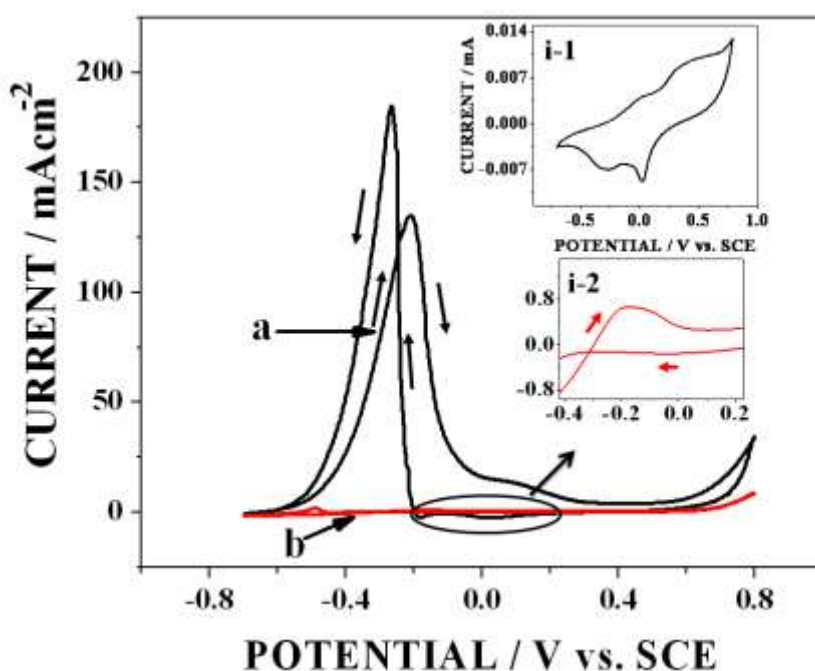


**Fig. 5.8** CVs for the electro-oxidation of 1 M ethanol in 0.5 M NaOH for (a) Pd-PEDOT nanocomposite and (b) Pd disc electrode. (insets) (i-1) CV for ethanol oxidation on PEDOT film surface without Pd. (i-2) zoom portion of the CV for ethanol oxidation on Pd disc electrode (scan rate :  $100 \text{ mV s}^{-1}$ )

Figure 5.8 (a) shows the ethanol electro-oxidation voltammogram for the Pd-PEDOT modified electrode in 1 M ethanol in 0.5 M NaOH. The onset potential for the ethanol electro-oxidation, at about 3% of the peak current was found to be around -0.56 V and the maximum current at -0.21 V of  $137 \text{ mA cm}^{-2}$ . The onset potential for the electro-oxidation and peak current observed in this work is comparable to the values reported in the literature [60-64]. For example Ksar *et al.* have reported a value of  $1.9 \text{ A cm}^{-2} \text{ mg}^{-1}$  at  $50 \text{ mVs}^{-1}$  for Pd nanowires, Nie *et al.* have observed a comparable value of  $150 \text{ mAcm}^{-2}$  for Au-Pd alloy catalyst.

During the reverse scan there is a secondary peak which starts at -0.18 V and the current reaching the peak at -0.27 V. The anodic current during the reverse potential scan arises due to the fact that the reduction of palladium oxides formed during the forward scan, creates a partially oxide free surface and the electro-oxidation of ethanol takes place on the freshly created Pd atoms sites. This reverse anodic peak behavior can be explained as due to the fact that the Pd atoms are not in equilibrium with the metallic lattice after the reduction of blocking oxide film and therefore the high energy sites possess excellent catalytic activity [15a,22]. The inset i-1 in Figure 5.8 shows the CV for ethanol electro-oxidation on PEDOT film without Pd. It can be seen that there is no peak corresponding to the electro-oxidation of ethanol. The voltammogram for ethanol electro-oxidation conducted in 1 M ethanol in 0.5 M NaOH using a Pd disc electrode is also shown in Figure 5.8(b). The peak potential in this case is -0.2 V and the corresponding peak current density is  $0.65 \text{ mA cm}^{-2}$  (inset i-2). This is much lower than a current of about  $137 \text{ mA cm}^{-2}$  in the case of the Pd-PEDOT electrode. The observed current values are quite large for a very low Pd loading of  $0.31 \text{ } \mu\text{g mm}^{-2}$ . This translates into a mass current density of about  $4.8 \text{ A mg}^{-1}$ .

### ***Mechanism of ethanol electro-oxidation***

The established mechanism for the electro-oxidation of ethanol in alkaline medium involves the oxidation of ethanol to acetate ions at the anode. The reaction can be summarized as following [61,62].



The third reaction, which is the removal of the adsorbed acyl groups by the adsorbed hydroxyl groups is the rate determining step (rds) [61,62]. This shows that an appropriate

amount of the adsorbed hydroxyl groups is required to achieve a high electro-oxidation current.

### ***Role of gold in the electrocatalysis reaction***

The synergistic effect of Au in Pd catalytic activity is very well known in literature. It is also known from the literature that Au and Pd alloy is a good catalytic material for ethanol electro-oxidation [63,64]. The effect of gold ad-atoms on Pd electrocatalysis in methanol oxidation reaction was studied by Watanabe *et al.* [65a]. Pd-Au alloy is also considered as good electrocatalyst [65b]. Gold as nanoparticles is also known to be a good catalyst for CO oxidation [65c].

To understand the role of underlying Au substrate on the electro-oxidation, we carried out an independent experiment on Pd-PEDOT nanocomposite film on Pd disc electrode (in the absence of Au), prepared in a similar way. This Pd-PEDOT electrode on Pd electrode does not show the significant catalytic activity towards ethanol electro-oxidation reaction. This indicates the role of gold surface in the catalysis. Since the nanocomposite film is thin and porous, we can not ignore the effect of substrate (Au) on the catalytic activity. Therefore we attribute this very high catalytic activity to the underlying gold substrate. This possibility arises from the adsorption of OH<sup>-</sup> ions on gold which can help in removing the poisonous CO in the form of CO<sub>2</sub> [63,64].

### ***Long term Stability test***

To check the long term stability of the Pd-PEDOT electrode towards the electro-oxidation of ethanol, we have conducted the CV for 200 cycles. We observed a very little decline (from 137 mA cm<sup>-2</sup> to 132 mA cm<sup>-2</sup>) in the electro-oxidation current of ethanol as can be seen in Figure 5.9. This shows that there is negligible poisoning of the catalytic surface due to any of the reaction products of ethanol oxidation. This is an important advantage of Pd-PEDOT nanocomposite electrode as the electrode poisoning is a major problem in electro-oxidation reactions of alcohols.

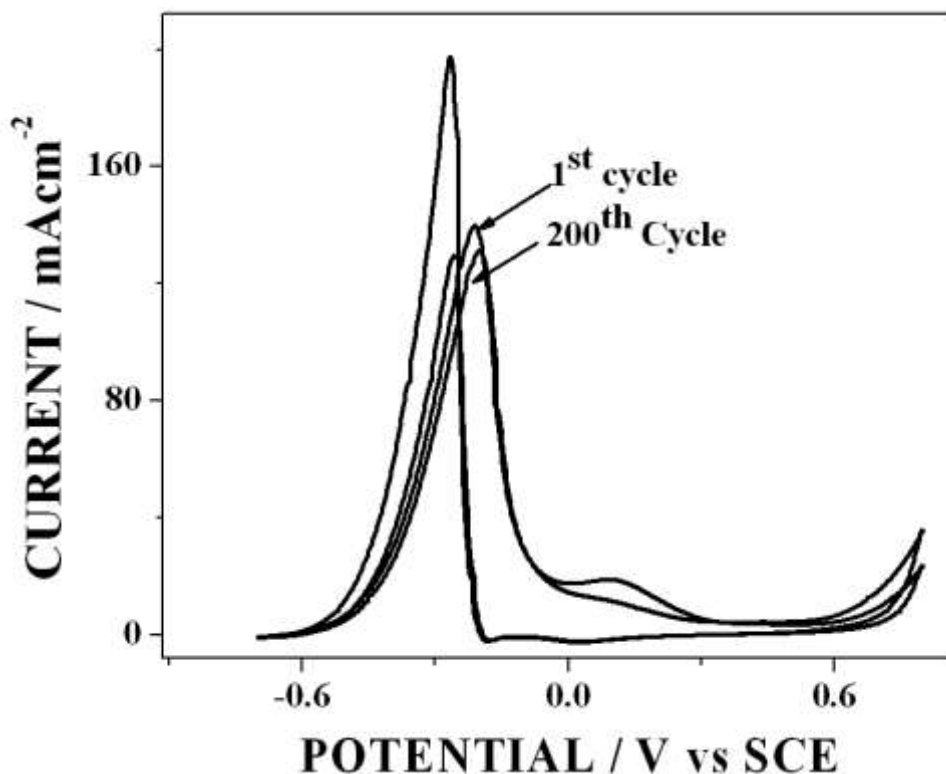


**Fig. 5.9** The 1<sup>st</sup> and 200<sup>th</sup> CVs for Pd-PEDOT nanocomposite coated Au disc electrode in 1 M ethanol in 0.5 M NaOH (scan rate: 100 mV s<sup>-1</sup>)

### 5.2.1.5 Kinetics of ethanol electro-oxidation

#### *Activation energy ( $E_a$ ) determination*

The Arrhenius plots (log I vs. 1/T) for ethanol oxidation on Pd-PEDOT electrode at different potentials, measured at potentials corresponding to the foot of the CV (-500 mV to -300 mV) are shown in Figure 5.10. A good linear relationship can be seen from these plots. This indicates that the essential mechanism of ethanol electro-oxidation remains the same at all the temperatures.

The apparent activation energies were calculated from the slope of the curves (slope =  $-E_a/2.3R$ ), R being the gas constant. The activation energy values have been labeled adjacent to their respective plots. The average  $E_a$  value for the potential range studied is 36.7 KJ mol<sup>-1</sup>. The  $E_a$  values obtained are comparable to the values observed for Pt, Au and Pd [60,65c,66] based catalytic materials. This indicates the facile nature of the ethanol electro-oxidation on Pd-PEDOT nanocomposite film.

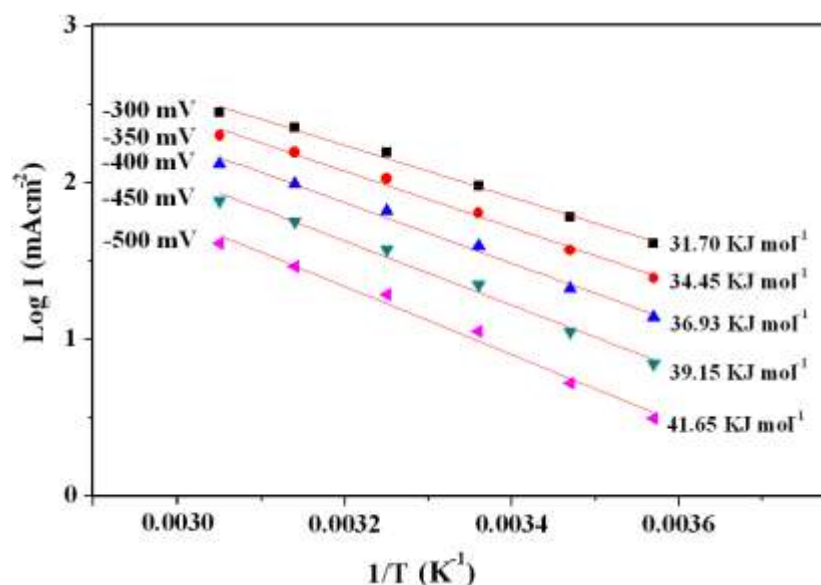


**Fig. 5.10** The Arrhenius plots ( $\log I$  vs.  $1/T$ ) for ethanol oxidation on Pd-PEDOT electrode at different potentials, near the foot of the CV (-500 mV to -300 mV). The potentials and corresponding activation energies, associated with each potential are labeled in the figure

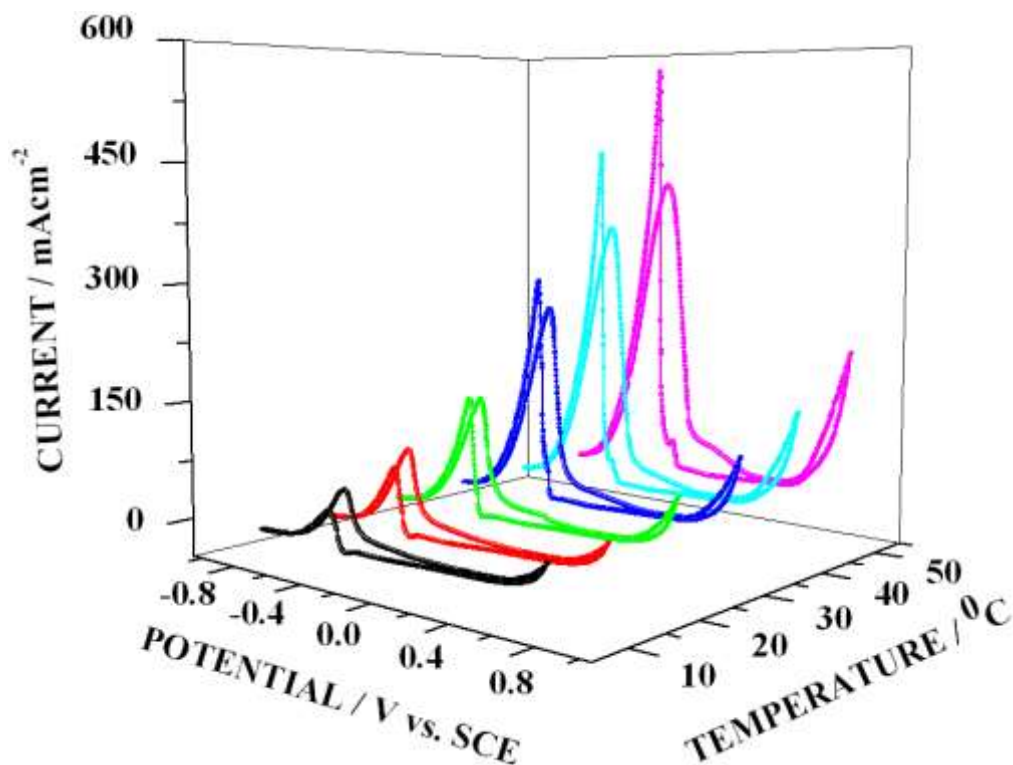
There may be several reasons for the effective electrocatalytic activity of the Pd nanoparticles, such as the presence of porous conducting polymer network, the role of underlying gold substrate and effective removal of poisoning intermediates [62]. This experiment also reveals that conducting polymers can be a potential alternative to carbon supports in electrocatalysis.

Figure 5.11 shows the CVs for ethanol oxidation at different temperatures. It is clear from the figure that the ethanol electrocatalysis currents have increased with the temperature and also the onset potentials have shifted to more negative values. This phenomenon can be attributed to the lower activation energy required at higher temperatures. The data is presented in Table 5.3.

Temperature / °C	Onset potential / V	Peak current / mAcm <sup>-2</sup>
7	-0.47	70
15	-0.50	101
25	-0.56	147
35	-0.58	253
45	-0.60	355
55	-0.64	413

**Table 5.3** Onset potential and peak current values for ethanol electro-oxidation at different temperatures

The high currents may be explained due to the fact that the increase in the temperature accelerates the adsorption of  $\text{OH}^-$  ions to form  $\text{OH}_{\text{ads}}$ . In the presence of  $\text{OH}_{\text{ads}}$  the electro-oxidation current is higher which minimizes the formation of poisoning species on the electrode [62,67-71]. As a consequence the electro-oxidation currents increase at higher temperatures. We find that the anodic current of reverse potential scan also increases with temperature. This current eventually attains a value higher than the anodic current of the forward potential scan.



**Fig. 5.11** CVs for electro-oxidation of 1 M ethanol on Pd-PEDOT electrode in 0.5 M NaOH at different temperatures (scan rate =  $100 \text{ mV s}^{-1}$ )

### **Tafel plot analysis**

The Tafel plots are known to provide valuable information on the nature and mechanisms of electrochemical kinetics. However in the case of electro-oxidation of organic molecules on the noble metal catalysts, the overpotential-current plots have totally different connotation. The surface poisoning by the intermediates during the reaction is a major problem in these reactions. Therefore the current–potential plots do not follow usual linear plots and the measured slopes are not the Tafel slopes referred in the exact sense of the term arising from the Butler-Volmer equation [70,71]. The values thus obtained are unusually large and do not reflect the mechanistic process. However, in keeping with the general literature terminology,

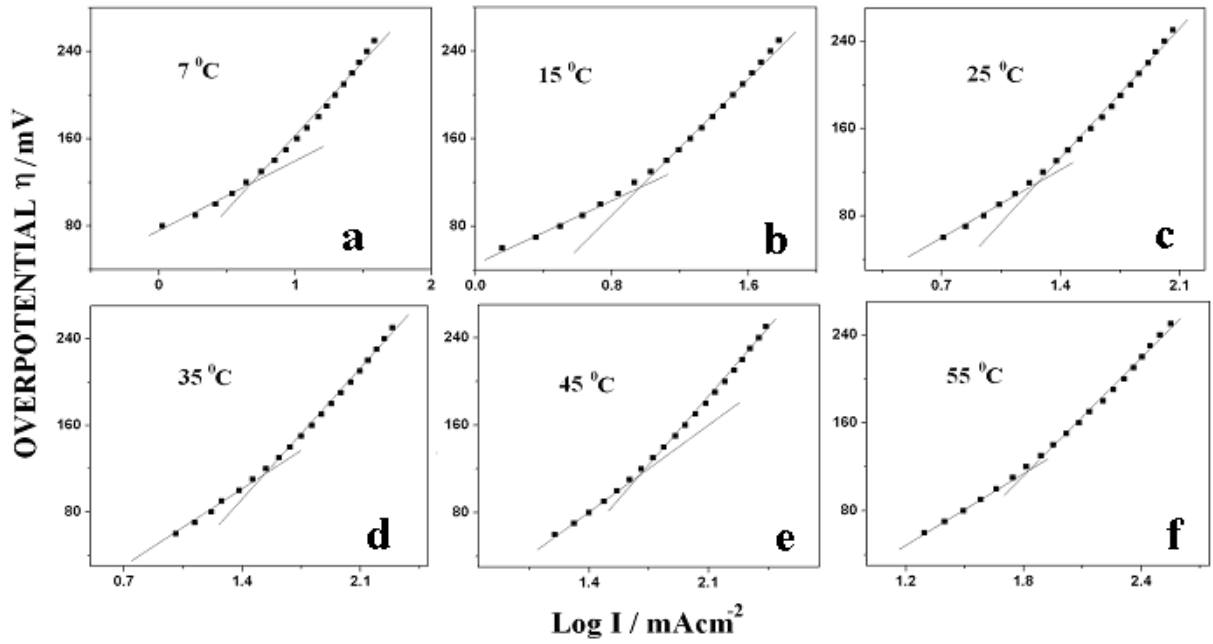
the slopes obtained here will be called the ‘Tafel slopes’. The information obtained with the Tafel slopes are quite valuable in understanding the effect of impurities on the surface sites, since the overpotential to be applied is larger for surface with the ‘blocked’ sites, which also changes with potential. The straight line between overpotential and  $\log I$  is not generally obtained [71] in the case of alcohols oxidation reaction.

Figure 5.12a-f shows the current-potential polarization plots for the ethanol oxidation observed at different temperatures (a (7°C), b (15°C), c (25°C), d (35°C), e (45°C) and f (55°C)). The plots were obtained by carrying out chronoamperometry experiment at the foot of the CV, a region of interest for any realistic application of a fuel cell.

The chronoamperometry measurements were carried out for Tafel plot by the application of a potential pulse of 10 s duration with a step size of 10 mV. Prior to the application of each potential step, the electrode surface was subjected to a potential program of 5s each at 0.8 V and -0.65 V vs. SCE as shown in Figure 5.13. The measured slope values as a function of temperature are given in Table 5.4. One can see from the plots that there are two slopes for all the temperatures studied. The values of the first slope (at lower overpotentials) are lower when compared to those of the second slopes (at higher overpotentials). This shows that as the reaction progresses more impurities get adsorbed on the surface, which can only be removed at very high anodic overpotentials.

The high values of Tafel slopes ( $d\eta/d\log I$ ) where  $\eta$  is the overpotential and  $I$  is the current density shows that when a larger overpotential is applied for a given value of current to flow, the slope becomes high. On a contaminated surface, the active surface sites are depleted due to which more overpotential is needed to maintain the defined current. The first slope value is low at lower temperatures and increases initially with the temperature and reaches a steady value at elevated temperatures. The value of the second slope, on the other hand, is smaller at lower temperatures but increases steadily with the temperature. The higher value of slopes at higher temperatures indicates that the large amounts of carbonaceous species generated during the oxidation of the ethanol adsorb at higher temperatures.

The Tafel slopes can act as reliable indicators for understanding the reaction process and its temperature dependence. In the present case, the value of the first Tafel slope (obtained at low overpotentials) increases initially with the temperature and then reaches a constant value of about 120 at higher temperatures. The values measured in this work are similar to those reported by Liang *et al.* [70].



*Fig. 5.12 Tafel plots (Overpotential ( $\eta$  vs.  $\log I$ ) at different temperatures and the linear fittings showing two slopes for ethanol electro-oxidation on Pd-PEDOT nanocomposite film*

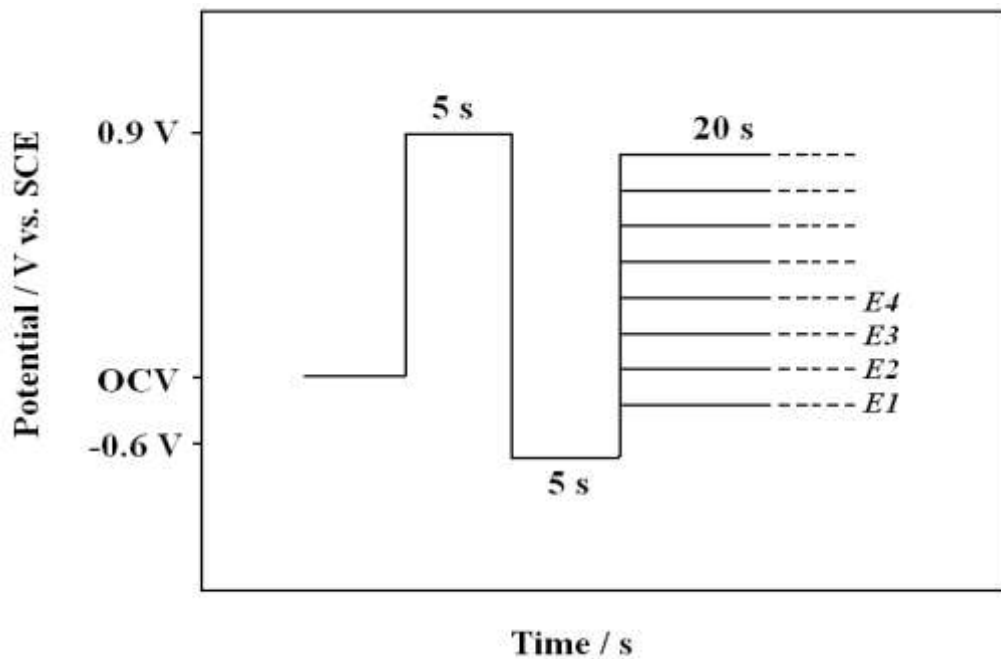


*Fig. 5.13 Potential program for chronoamperometry with delay at negative and positive potentials*

Temperature (°C)	1 <sup>st</sup> slope	2 <sup>nd</sup> slope
7	64.5	139.5
15	82.9	150.0
25	106.2	167.5
35	117.2	170.2
45	122.0	173.6
55	115.7	174.5

**Table 5.4** Tafel slope values for ethanol electro-oxidation at different temperatures near the foot of the voltammogram for Pd-PEDOT nanocomposite film

### Reaction order calculation

The effect of ethanol concentration on the reaction rate was also studied in order to know the reaction kinetics. This was carried out by calculating the reaction order by plotting the log I vs. log (ethanol concentration) as shown in Figure 5.14. The order was calculated by using the following equations [60]:

$$I = nFkc^m$$

Therefore,

$$\log I = \log nFk + m \log c$$

where F is the Faraday's constant, k is the reaction constant, c is the ethanol concentration and m is the reaction order with respect to ethanol.

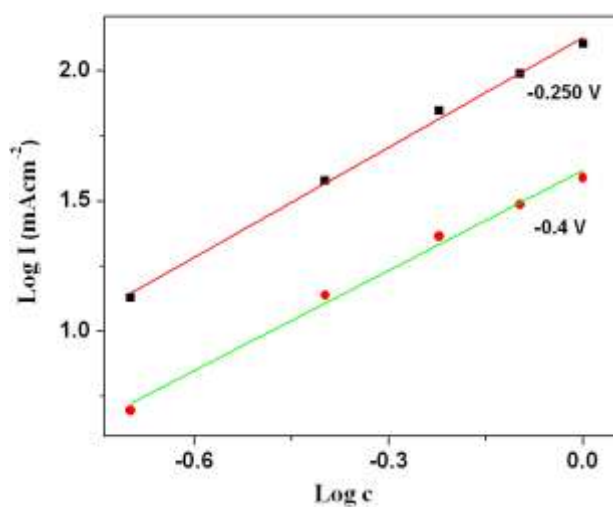


**Fig. 5.14** Linear fitting of the plots of log I vs. log c (ethanol concentration) at different potentials for calculating the reaction order

The slope of the plot at constant temperature and a given potential gives the apparent reaction order ( $m$ ) of ethanol electro-oxidation reaction with respect to the ethanol concentration [60]. We have calculated the order at two different potentials -0.4 V and -0.25 V. The values of the measured reaction orders are 1.28 and 1.4 at -0.4 V and -0.25 V respectively, which shows that there is no significant change in the reaction order with potentials and the reaction mechanism for ethanol oxidation essentially remains same at different potentials.

## **5.2.2 Electro-oxidation of formic acid, methanol and ethanol on electrodeposited Pd–PANI nanofiber film in acidic and alkaline Media**

In this part of the chapter a simple and direct electrochemical method of depositing a porous Pd-PANI nanofiber film on conducting surfaces is presented. The one step method consists of the *in-situ* polymerization of aniline in the solution and simultaneous formation of a film of Pd-PANI. The electrocatalytic property of the Pd-PANI nanostructured film towards electro-oxidation of formic acid and alcohols was studied in acidic and alkaline media respectively. It is worth pointing out here that formic acid is being increasingly viewed as a better and safer alternative to methanol in direct fuel cells, due to its lower toxicity, ability to function in acidic media and easy availability through renewable energy sources.

### **5.2.2.1 Synthesis of the Pd-PANI nanofiber film on gold substrate**

The electrolyte was prepared by dissolving 5 mg aniline in 5 ml of 0.1 M HCl. This was continuously stirred using a magnetic stirrer during the experiment. A Pd wire of 5 mm length and 0.5 mm diameter with an area of 0.1 cm<sup>2</sup> dipped in the electrolyte served as the anode and working electrode while an evaporated gold film electrode of 0.15 cm<sup>2</sup> geometric area acted as the cathode and counter electrode. We have carried out the deposition in the galvanostatic mode with different current values (10, 20, 30, 40 and 50 mA) for an hour. At these currents there was an evolution of gases at both the electrodes due to water electrolysis. (*Caution! the cell should have gas outlets near both the electrodes to allow the evolving gases to escape*) The solution which was colorless in the beginning turned light yellowish and finally to pink. Simultaneously, a dark colored film is formed on the cathode surface. At higher currents the gas evolution was rapid and the dissolution of the metal is not uniform. The deposition was also carried out at 60 and 70 mA currents and it was observed that the film was brittle and disintegrates gradually during the gas evolution. Hence the current value of 50 mA was observed to be the optimum, based on the studies of formic acid oxidation on

surfaces prepared at different galvanostatic currents. For all the characterization studies of the film, the specimen was deposited at the current of 50 mA unless otherwise stated.

The anodic dissolution of palladium produces  $\text{Pd}^{2+}$  ions in the solution which form complex with the chloride ions from the supporting electrolyte to form chloropalladate ions. The chloropalladate, being an oxidizing agent initiates the oxidative polymerization of aniline to form PANI in the solution while in the process being reduced to nanoparticles of Pd [51,52]. The process is similar to the bulk chemical preparation of Au-PANI nanostructures using chloroauric acid, a powerful oxidizing agent and aniline [53].

### ***Mechanism of the nanocomposite film formation***

The oxidative polymerization of aniline can be considered as a typical redox process which is dependent on the reduction potentials of the species involved [72]. The PANI binds and stabilizes the reduced Pd clusters within its matrix by forming the Pd-PANI nanocomposite in the solution [30]. In a strong acid medium, the Pd-PANI is positively charged with the amine and imine groups being protonated to  $(-\text{NH}_2^+-)$  and  $(-\text{NH}^+=)$  respectively [73]. In our system the positively charged protonated Pd-PANI composite can be deposited electrophoretically on the cathode surface in the form of nanofibers. The potential measured at the applied current of 50 mA is -4.5 V, a relatively low potential for the electrophoretic deposition. Li *et al.* [43] have recently reported similar process of electrophoretic method of depositing positively charged protonated PANI colloidal suspension in acetonitrile.

### **5.2.2.2 SEM, EDAX, AFM and XRD studies on Pd-PANI nanofiber film**

Figure 5.15a and b show the SEM images of the Pd-PANI nanocomposite deposited surface. The images show a highly porous nanocomposite film with a dendritic growth of the fibers that are about 50-100 nm diameter and a few  $\mu\text{m}$  in length. The SEM images at different locations on the modified substrate exhibit similar features.

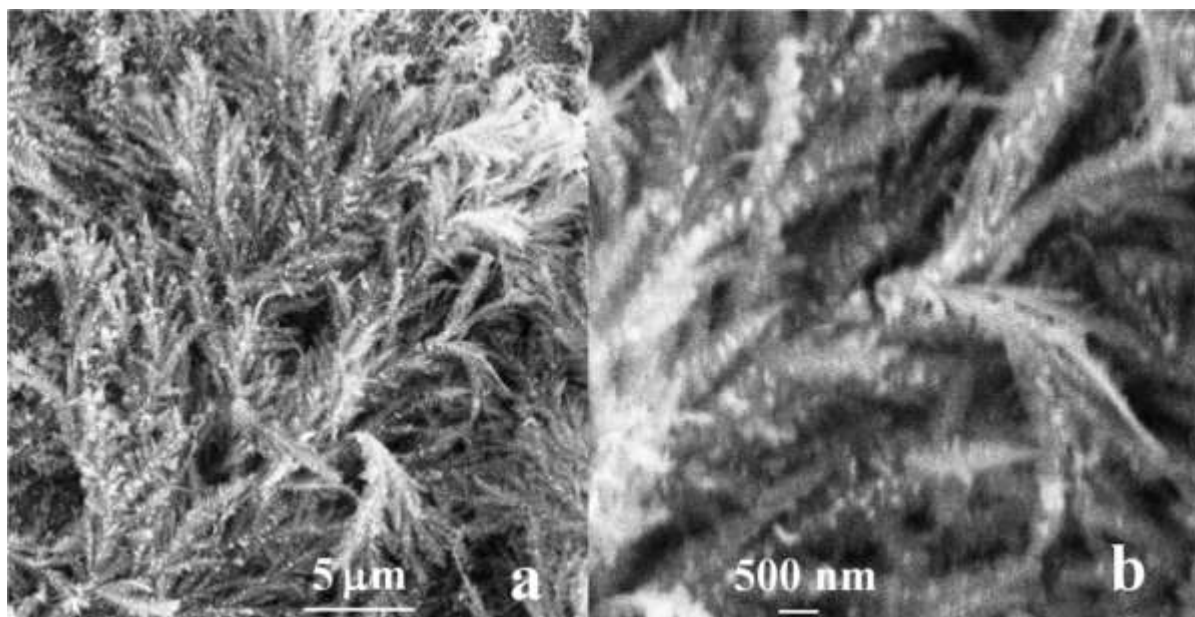


**Fig. 5.15** (a) Low resolution (scale bar-5  $\mu\text{m}$ ) and (b) high resolution (scale bar-500 nm) SEM images of the Pd-PANI film showing dendritic growth of the deposited film

In the high-resolution image (Figure 5.15b), several white spots of about 50 –100 nm are seen on the structures, which are Pd clusters adhering on the surface of PANI exhibiting fibrous structure. At very high current density beyond the limiting current density regime, the deposition takes place by fresh nucleation at different sites. The process creates new grains unlike the layer type growth preferred at low current densities. This leads to a dendritic growth of the Pd-PANI film as observed by SEM. EDAX of the Pd-PANI modified surface is shown in Figure 5.16a. The spectrum shows a clear peak for Pd and a peak for gold which is due to the underlying gold substrate [25,27].

Figure 5.16b shows the XRD pattern of coated Pd-PANI nanofiber film. The XRD pattern exhibits the diffraction lines corresponding to (111), (200), (220), (311) and (222) planes of Pd with the most dominant crystal plane being (111). [25-27]

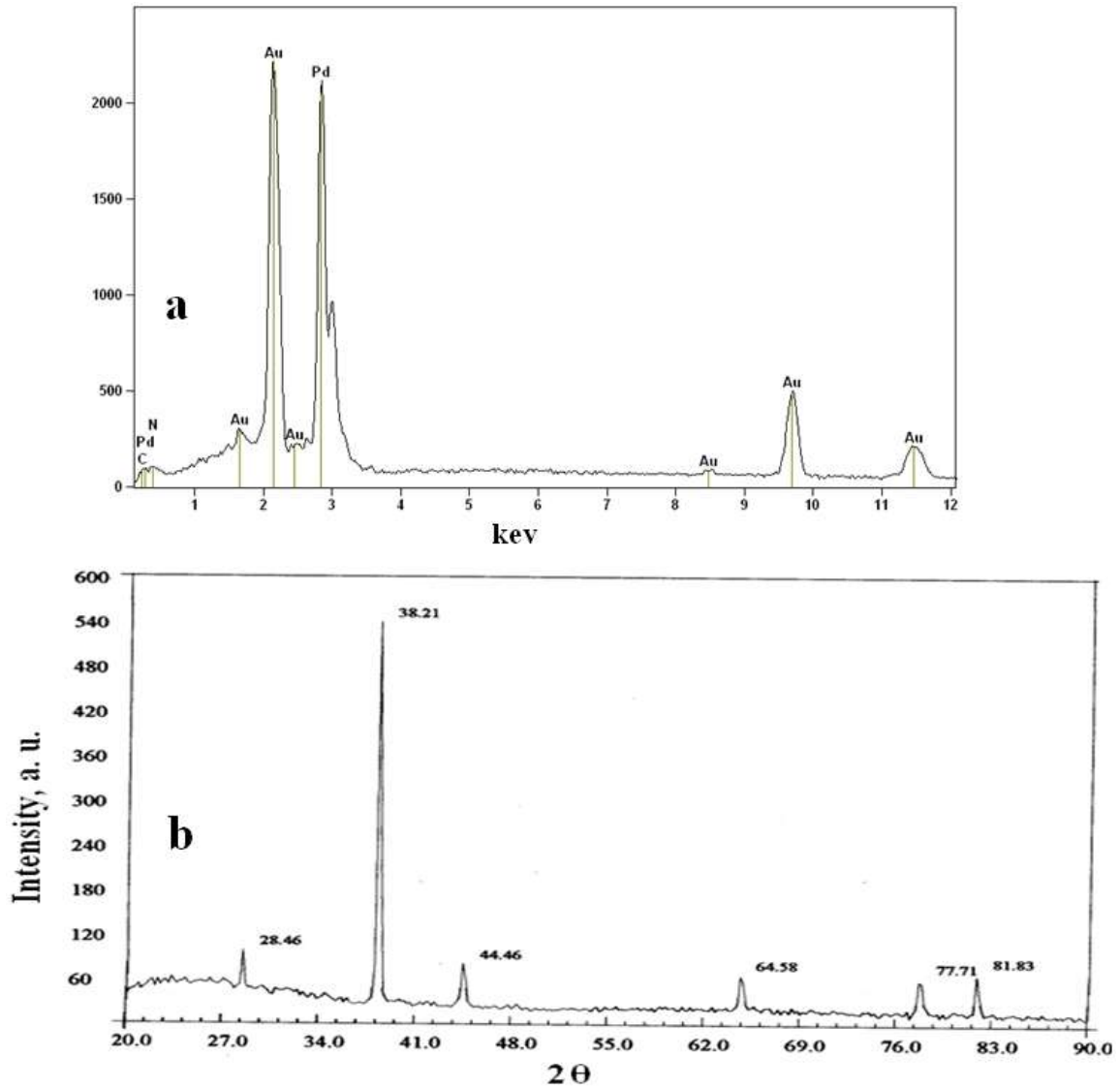


*Fig. 5.16 (a) Energy dispersive X-ray analysis (EDAX) spectra showing the peak for the metallic Pd and (b) XRD pattern of Pd-PANI nanocomposite showing the different crystal planes of the Pd. The most predominant plane is (111) plane at 38.21*

Atomic force microscope (AFM) was used to examine the surface of nanocomposite film and to study the 3-dimensional structure of Pd-PANI film. Figure 5.17 shows the 1500 nm x 1500 nm AFM images of the Pd-PANI nanocomposite film. The long rod like features present on the surface are uneven and inhomogeneously distributed Pd-PANI fibers.

The surface of the Pd-PANI nanocomposite shows high roughness and most of the features are more than 200 nm in height.

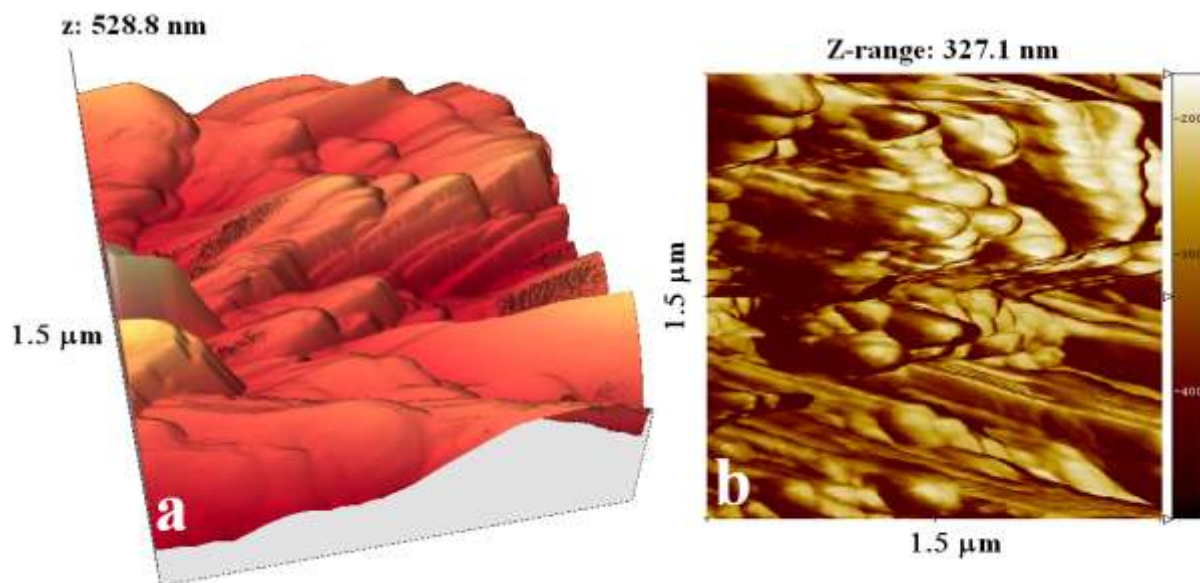


**Fig. 5.17**  $1.5 \mu\text{m} \times 1.5 \mu\text{m}$  AFM topographical 3d image (a) and phase image (b) of the Pd-PANI nanodendrites film

### 5.2.2.3 FTIR spectroscopy analysis

Figure 5.18 shows the FTIR spectrum of the coated material, which was scrapped out from the surface. The coated material (Pd-PANI nanocomposite) shows distinctive infra-red peaks for the conjugated polymer PANI [27]. The position of the peaks is shown in Table 5.5. The peak at group frequency region ( $2926 \text{ cm}^{-1}$ ) is for aromatic C-H stretching.

PANI shows characteristic infra-red peaks at the fingerprint region (between  $800 \text{ cm}^{-1}$  to  $1700 \text{ cm}^{-1}$ ). The peak at  $1266 \text{ cm}^{-1}$  is for the C-N stretch, which is the usual characteristic infrared peak for the aromatic amines. PANI infra-red spectra also show the characteristic peaks of benzenoid and quinoid form of the aromatic phenyl ring system. The two peaks at  $1509 \text{ cm}^{-1}$  and  $1642 \text{ cm}^{-1}$  are for the benzenoid and quinoid forms of the PANI respectively [73]. Both the peaks have almost similar intensity. The presence of the above mentioned infrared peaks confirms the presence of the polymer form of aniline in the coated material. Benzenoid and quinoid infrared peaks are slightly shifted towards the longer wavelength when compared to that in the case of hydrochloric acid doped PANI [73]. The shift in the infrared peaks can be rationalized as due to the change in the electron density near the benzenoid and quinoid units of PANI due to the presence of the Pd clusters surrounding them.

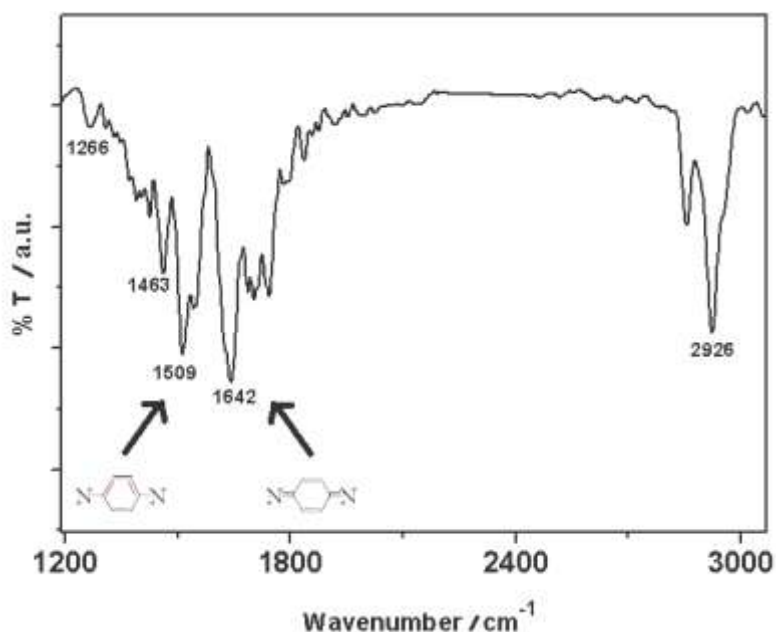


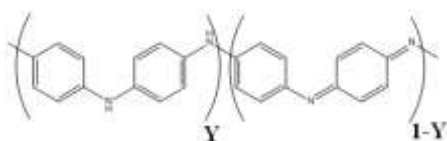
**Fig. 5.18** FTIR spectrum of Pd-PANI nanocomposite showing the characteristic benzenoid and quinoid peaks for the PANI in the composite

Peak position (cm <sup>-1</sup> )	Peak
1266	C-N stretching
1509	Benzenoid phenyl ring
1642	Quinoid phenyl ring
2926	Aromatic C-H stretching

**Table 5.5** The observed FTIR peaks for Pd-PANI nanofibers

The integrated intensity of IR peaks at 1642 cm<sup>-1</sup> (quinoid peak) and 1509 cm<sup>-1</sup> (benzenoid peak) can be used to calculate the “R” value which is the ratio of the area under the IR peaks at 1642 cm<sup>-1</sup> and 1509 cm<sup>-1</sup>. The R value for Pd-PANI nanocomposite was calculated to be 1.01. This shows that there is almost equal amount of both the forms in coated material [73-77]. From the R value which is often related to the oxidation state of the PANI, we define the following structure of PANI in the coated material.

For the following structure, with the R value:



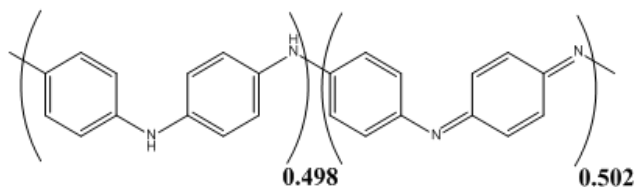
where,

$$R = 1-Y/Y$$

$$1.01 = 1-Y/Y$$

$$Y = 0.498 \text{ and } 1-Y = 0.502$$

We get the following structure:

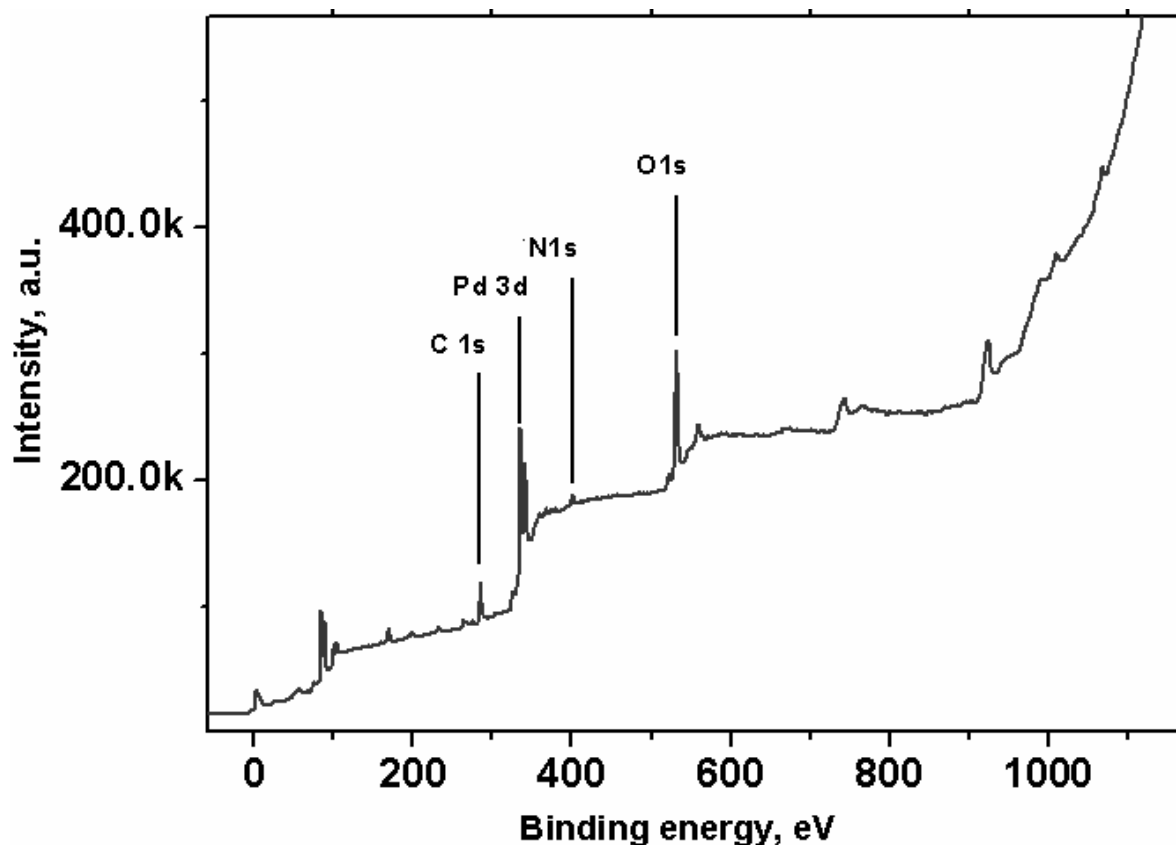


The above structure of PANI shows that no significant change has occurred in the structure of PANI and it is in conducting form.

#### 5.2.2.4 X-ray photoelectron spectroscopy (XPS) analysis

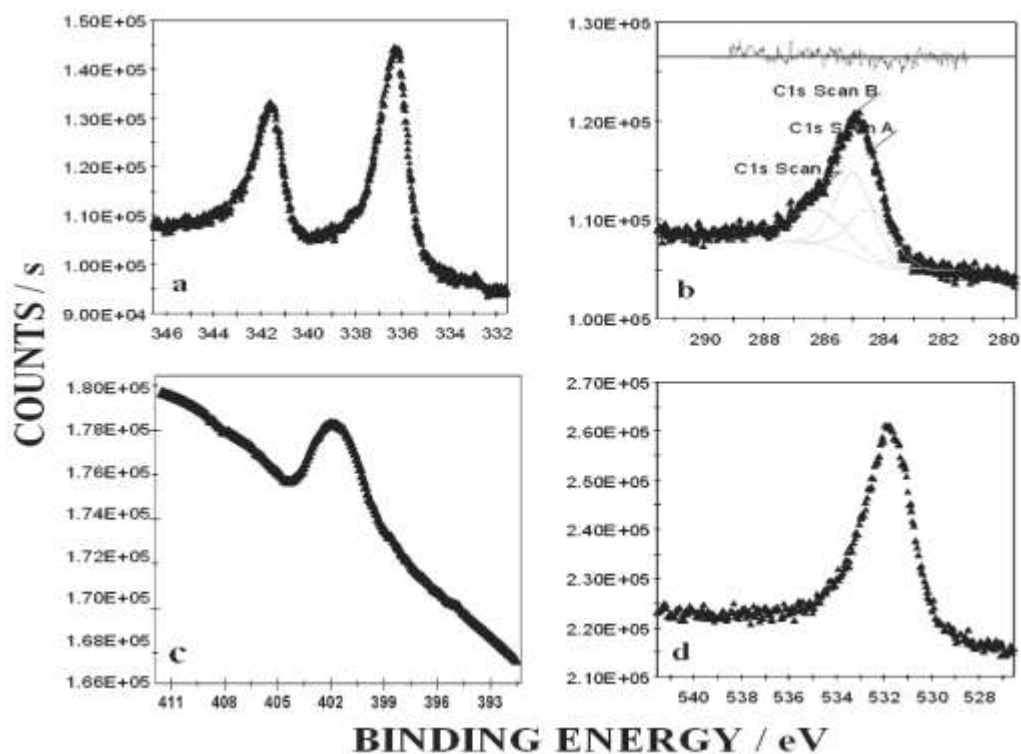
XPS provides valuable information on the density of occupied electronic states for a surface. The X-ray beam penetrates the material and ejects electrons from the valence or core levels yielding information about the atomic composition and the oxidation states of the atom in the material [78]. Figure 5.19 shows the XPS survey spectrum for the Pd-PANI nanofiber film where typical peaks for the Pd, carbon and nitrogen can be clearly identified. In addition, a peak for oxygen is also present in the survey spectrum, which is probably either due to the partial surface oxidation of material or simple chemisorption of oxygen on the surface. The binding energy values for Pd are in good agreement with the values reported in the literature for Pd nanoparticles. These peaks are the indication of the presence of metallic Pd in the Pd-PANI nanocomposite.

Figure 5.20a is the Pd 3d XPS spectrum which splits into two components, one at lower binding energy 336.2 eV (Pd 3d<sub>5/2</sub>) and another at 341.5 eV (Pd 3d<sub>3/2</sub>). The binding energy values are lower than that reported in the literature for Pd (II) salts (338 eV for Pd3d<sub>5/2</sub> and 343.5 eV for Pd3d<sub>3/2</sub>) [27,79]. However they are quite close to that of the oxide form of the Pd, PdO (336.1 eV for Pd3d<sub>5/2</sub> and 341.8 eV Pd3d<sub>3/2</sub>) [73]. The O<sub>1s</sub> peak present in the XPS spectra may point to partial surface oxidation of the material due to the formation of PdO on the surface or chemisorption of oxygen on the surface [27,80-82].



*Fig. 5.19 XPS survey spectrum for the Pd-PANI nanocomposite showing the characteristic peaks for Pd, C, N and O*

Figure 5.20b shows the  $C_{1s}$  XPS spectrum of the material, which can decompose into three peaks by a simple standard line shape analysis with binding energies 284.5 eV, 285 eV and 286.3 eV. The maximum intensity peaks are at 284.5 and 285 eV which can be attributed to the C-C, C-H and C-N species according to the literature [83,84]. The peak at higher binding energy can be assigned to the oxidized carbon species such as C-O. Figure 5.20c shows the XPS spectrum for the  $N_{1s}$  with the binding energy peak at 401.5 eV. This peak may be assigned to the  $N^+$  species in Pd-PANI composite. Figure 5.20d is XPS spectrum of the  $O_{1s}$  with the peak at 531.7 eV, and as discussed above this peak may be due to the partial surface oxidation of the nanocomposite.



**Fig. 5.20** (a) Pd 3d XPS spectrum, (b) C<sub>1s</sub> XPS spectrum, (c) XPS spectrum for the N<sub>1s</sub> and (d) O<sub>1s</sub> XPS spectrum of the nanocomposite showing the characteristic binding energy peaks

### 5.2.2.5 Cyclic voltammetry analysis and electrocatalytic activity of the Pd-PANI coated electrode

#### *Voltammetric response of the Pd-PANI coated electrode in acid medium*

Palladium is well known to absorb massive quantities of hydrogen in bulk to form hydrides and therefore has a great technological potential as a hydrogen storage material [85]. We have carried out CV studies in acidic medium to examine the affinity of hydrogen towards Pd-PANI nanofibers. Figure 5.21 shows the voltammetric behavior of the Pd-PANI coated electrode in 0.5 M H<sub>2</sub>SO<sub>4</sub> at a scan rate of 100 mVs<sup>-1</sup>. The inset shows the voltammetric behavior of the Pd wire electrode in the same electrolyte. The CV for the Pd wire in 0.5 M H<sub>2</sub>SO<sub>4</sub> shows a single broad anodic peak around 0.00 V. This broad hump is due to the oxidation of both the absorbed and adsorbed hydrogen on the Pd wire and has been earlier reported for bulk Pd electrodes [12]. On the other hand, the CV for the Pd-PANI coated disc electrode shows two distinct peaks, one of which is a small shoulder peak in the negative potential region during the anodic sweep [5,12,54,86]. The first peak at -0.18 V corresponds to the oxidation of the adsorbed hydrogen (H<sub>ad</sub>) while the subsequent peak at -0.04 V is due

to the oxidation of the absorbed hydrogen ( $H_{ab}$ ) on Pd surface [5]. The cathodic peak during the reverse scan at -0.15 V is due to both absorption and adsorption of hydrogen. It is known from the literature that two well resolved peaks for the oxidation of adsorbed and absorbed hydrogen in Pd are manifested exclusively in the case of Pd nanoparticles [5,12,54,86]. This behaviour is attributed to the larger number of surface sites available for adsorption on nanoparticles surface.

### ***Effective catalytic surface area (ECSA) determination***

The electroactive surface area of Pd has been measured from the palladium oxide stripping analysis [12,26]. The Pd oxide stripping appears during the reverse potential scan at 0.2 V and the charge under the peak is measured to be 850.0  $\mu\text{C}$ . With the value of the conversion factor of 424  $\mu\text{C cm}^{-2}$  for Pd oxide stripping current [12,26], the effective catalytic surface area (ECSA) for the Pd-PANI film is measured to be 2.0  $\text{cm}^2$ . This is a very large real surface area for the gold disc electrode with an initial geometric area of 0.002  $\text{cm}^2$ . This large surface area arises due to highly porous PANI film in which the Pd nanoparticles are dispersed making a *dot-on-fibers* type of structure. Since the Pd nanoparticles are not directly deposited on the electrode surface, the available effective active centers are higher which makes it an ideal electrocatalytic material.

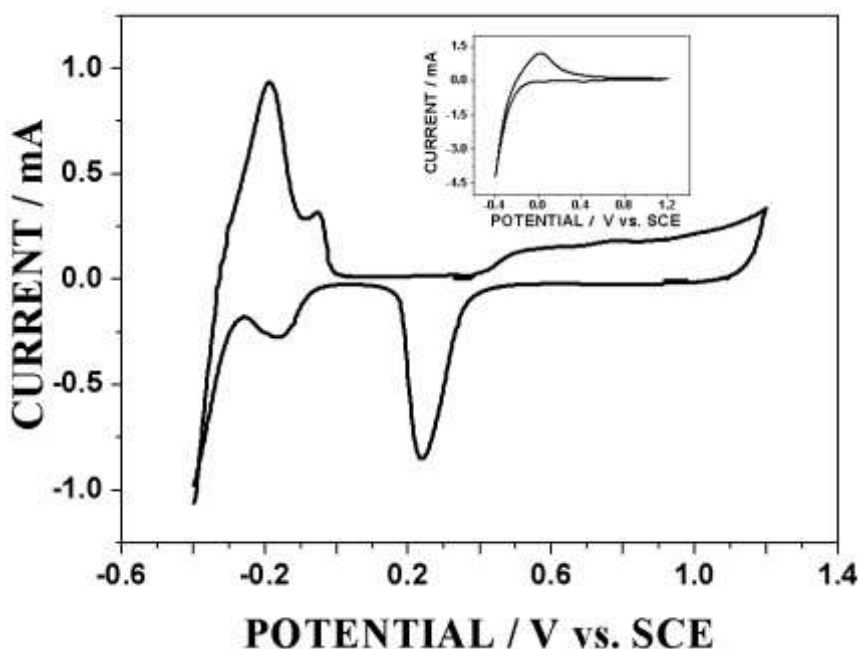


**Fig. 5.21** Voltammetric behaviour of the Pd-PANI coated disc electrode in 0.5 M  $\text{H}_2\text{SO}_4$ . (Geometric area of the gold substrate before forming the film = 0.002  $\text{cm}^2$ ). Inset shows the behaviour of Pd wire electrode in 0.5 M  $\text{H}_2\text{SO}_4$

### ***Catalytic activity towards electro-oxidation of formic acid***

The electrocatalytic oxidation of formic acid has been intensively studied as it is the anodic reaction in direct formic acid fuel cells (DFAFCs) [15-19]. This is especially important from the point of view of the development of micro fuel cells [17]. Formic acid is also an environment friendly alternative to methanol. There have been several catalytic materials such as Pt, Pt-Au, Pt-Ru, Pt-Sn and other alloys of Pt in acid media which have been explored as formic acid oxidation catalyst. Some of the early studies of formic acid electro-oxidation was carried out by Baldauf and Kolb on electrodeposited and epitaxially grown Pd thin film formed on low index planes of gold and Pt [14]. The advantage of Pd over Pt in catalyst materials for formic acid fuel cell is said to arise due to its resistant to CO poisoning [15a,b].

The catalytic current response is found to be sensitive to the crystallographic orientation of Pd [15a,17]. Wieckowski and co-workers have shown that Pd nanoparticles have excellent catalytic properties towards formic acid oxidation [17]. They have concluded that for unsupported Pd catalyst, the smaller sized nanoparticles of 9-11 nm possess better electrocatalytic properties than the larger (>40 nm) ones.

It is also observed by many of the researchers that the poisoning of the surface due to the carbon monoxide (CO) is not very significant in Pd nanoparticles modified electrodes [15a,b,18,24].

The formic acid electro-oxidation reaction can be considered to follow the following equation [15a]:

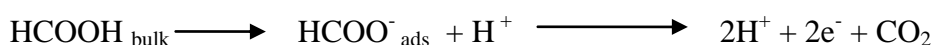
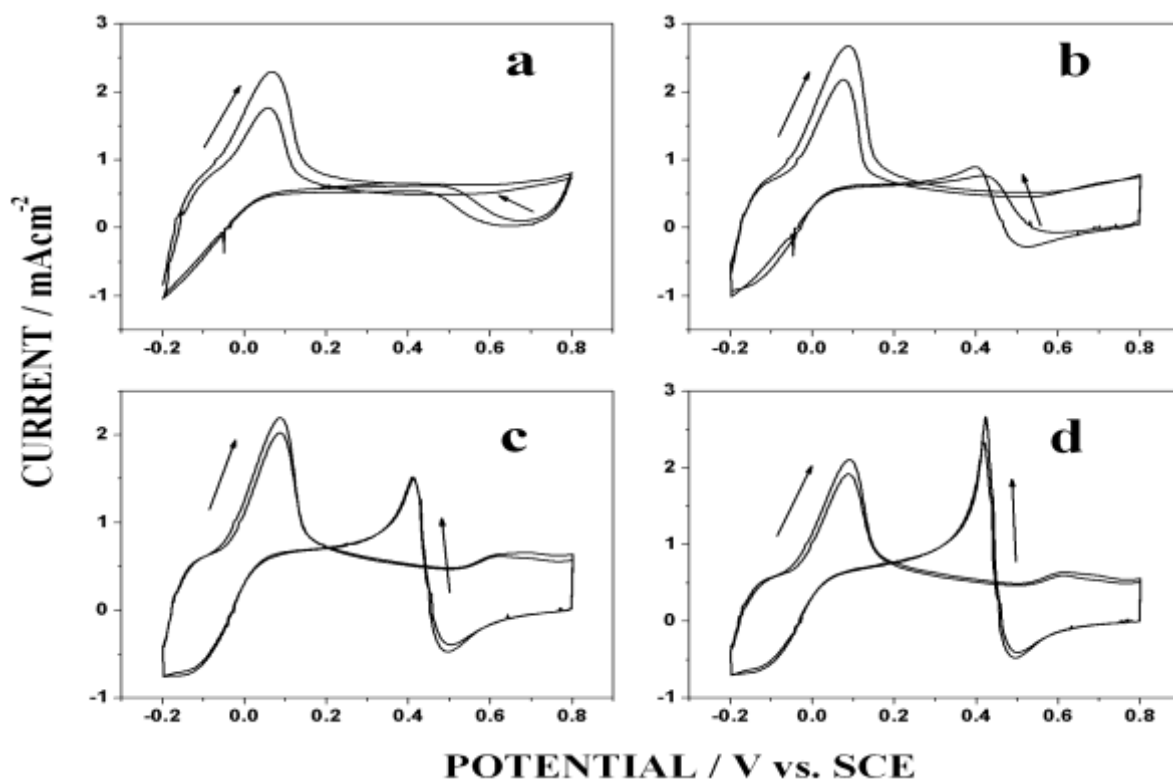


Figure 5.22a shows the 1<sup>st</sup> and 10<sup>th</sup> cycles of CVs for the electro-oxidation of 0.2 M formic acid on Pd-PANI film electrode in 0.5 M H<sub>2</sub>SO<sub>4</sub> solution. All the currents are reported for unit effective catalytic surface area (ECSA). It can be seen that the formic acid oxidation starts at about -0.11 V and maximum occurs at 0.07 V, where the peak current is measured to be 2.30 mA cm<sup>-2</sup>.

### ***Effect of oxides removal***

During the negative scan the oxidation current starts at +0.6 V, a feature observed by other workers also. The anodic current during the reverse potential scan arises due to the fact that the reduction of palladium oxides formed during the forward scan is followed by the electro-oxidation of formic acid on the freshly created Pd atoms sites.



**Fig. 5.22** (a) The CV for the electro-oxidation of 0.2 M formic acid in 0.5 M  $H_2SO_4$  (a) without any time delay, (b) with 5 s time delay at 0.8 V, (c) 10 s time delay, (d) 20 s time delay. Current values are reported for per unit effective catalytic surface area (ECSA) (Scan rate:  $100\text{ mV sec}^{-1}$  Geometric area of the gold substrate before forming the film =  $0.002\text{ cm}^2$  and effective catalytic surface area (ECSA) =  $2.0\text{ cm}^2$ )

Such a behaviour has been explained as due to the fact that Pd atoms are not in equilibrium with the metallic lattice after the reduction of oxide film and they possess good catalytic activity [15a,22]. The formic acid electro-oxidation current obtained for Pd-PANI nanofiber film are comparable to the currents observed by other researchers [17,21]. The onset potential and peak potential values for the electro-oxidation are also towards more negative potentials [17,21].

To further study the effect of oxide reduction on the response of formic acid electrocatalysis we have performed an interesting experiment in which we have given different time delays at the positive potential (0.8 V) to accumulate more Pd oxides in the form of monolayer and multilayer oxide films on the surface as observed in the literature [20a-d]. Figure 5.22b, c and d shows the CV experiments performed with time delays of 5, 10 and 20 seconds respectively at the positive potential. Table 5.6 shows the values of current obtained during reverse potential scan at different time delay. We observed an increase in the reverse anodic current with the time and the peak becomes sharper, which clearly

demonstrate the effect of oxide film removal on the electrocatalytic property of the Pd-PANI nanofiber film.

Time delay / s	Peak current / mA cm <sup>-2</sup>
0	0.62
5	0.91
10	1.52
20	2.67

**Table 5.6** The observed formic acid electro-oxidation peak currents during reverse potential scan at different time delays

The above experiment shows that Pd-PANI nanofibers can be easily tuned to achieve high electrocatalytic activity towards the formic acid electro-oxidation.

The presence of PANI in the material provides an extensive network of conductive paths which facilitate the electro-oxidation of formic acid on the Pd-PANI nanofiber film. To find whether PANI coated surface by itself can catalyze the electro-oxidation of formic acid, we have carried out CV studies on Pd free PANI film on gold in the same electrolyte containing formic acid and 0.5 M H<sub>2</sub>SO<sub>4</sub>. The PANI film on gold was prepared by electropolymerization of aniline in 0.5 M H<sub>2</sub>SO<sub>4</sub>. Figure 5.23 shows that there is no formic acid oxidation reaction on the PANI film on gold confirming that the electro-oxidation is due to Pd nanoparticles present in the nanocomposite. The only peak present during the forward scan in the CV at 0.2 V is due to the oxidation of emeraldine form of PANI.

Table 5.7 shows the maximum current measured at 0.07 V for the formic acid electro-oxidation on the Pd-PANI nanocomposite film electrodes, which are prepared under different deposition currents.

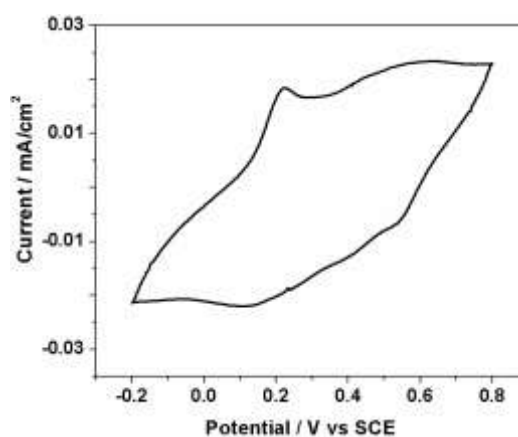


**Fig. 5.23** The CV for PANI film (without Pd) in 0.2 M formic acid in 0.5 M H<sub>2</sub>SO<sub>4</sub>

Deposition current / mA	Formic acid oxidation peak current / mA cm <sup>-2</sup>
10	0.49
20	0.40
30	0.63
40	1.83
50	2.30

**Table 5.7** The observed formic acid electro-oxidation peak currents measured at 0.07 V for different electrodes coated at different deposition currents

There is almost systematic increase in the values of the measured peak currents for formic acid oxidation with the increasing deposition current during the preparation of the Pd-PANI. We have also deposited Pd-PANI nanocomposite film on a large area (0.15 cm<sup>2</sup>) electrode in order to calculate the mass current density. The mass of the Pd-PANI nanocomposite film deposited on this electrode was 0.04 mg and the corresponding mass current density for formic acid electro-oxidation was calculated to be about 0.822 A mg<sup>-1</sup> of Pd. This large current value is very much comparable to that obtained by Ge *et al.* on hollow Pd nanospheres and nanoparticles supported on carbon [87].

### 5.2.2.6 Kinetics of the formic acid oxidation

#### *Activation energy calculation*

To understand the kinetic behaviour of formic acid catalysis on Pd-PANI electrode, we have carried out the electro-oxidation studies at different temperatures. The Pd-PANI system was found to be quite stable till 25°C beyond which there is an instability in the acid medium. Therefore the upper temperature limit of the experiment was kept at 25°C. The experiment was carried out at five temperatures *i.e.* 0, 3, 7, 15 and 25°C. Figure 5.24 shows the log I vs. 1/T plot (Arrhenius plot) for formic acid electro-oxidation on Pd-PANI electrode. The activation energy values calculated at different potentials are also shown in the figure. The average activation energy was calculated to be 45 KJ M<sup>-1</sup>. Figure 5.25 shows the formic acid electro-oxidation voltammograms taken at different temperatures. The data obtained from CVs is shown in Table 5.8. It is clear from the figure and table that the currents of formic acid oxidation have increased and the onset potential values have shifted to more negative potentials.

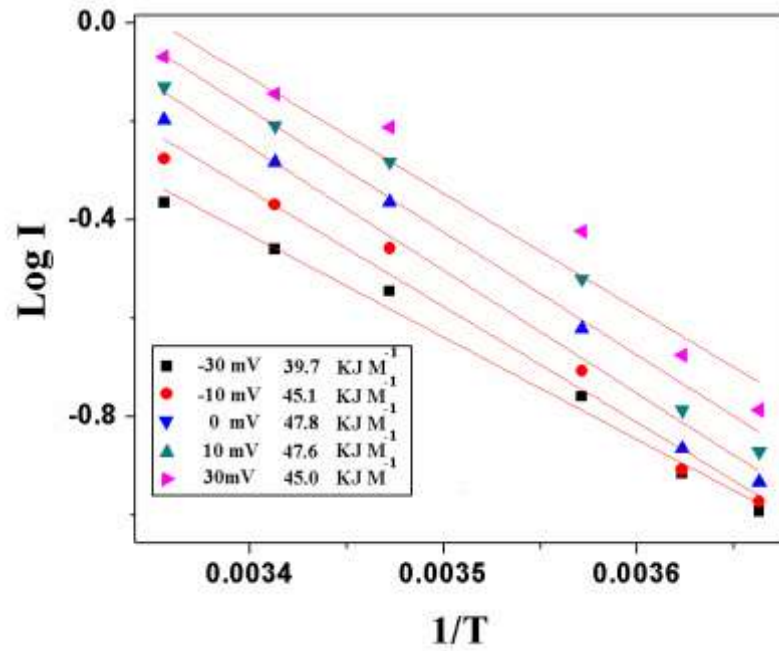


**Fig. 5.24** The Arrhenius plots ( $\log I$  vs.  $1/T$ ) for formic acid oxidation on Pd-PANI electrode at different potentials, near the foot of the CV (-30 mV to 30 mV). The potentials and corresponding activation energies, associated with each potential are shown in the figure

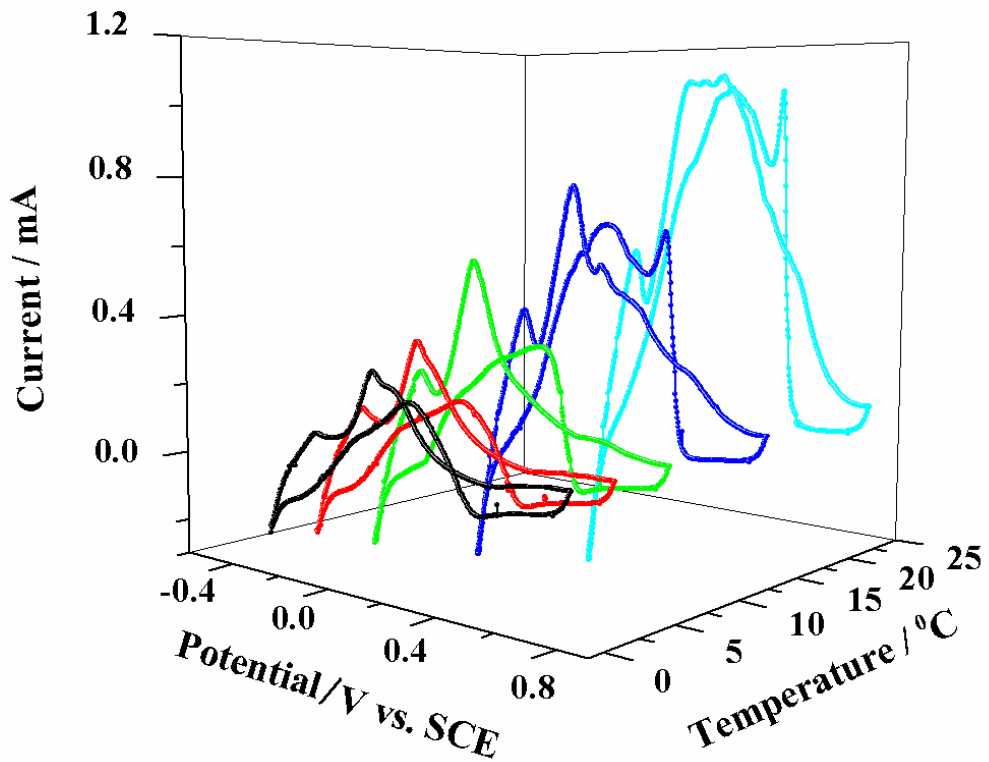


**Fig. 5.25** CVs for electro-oxidation of 0.5 M formic acid on Pd-PANI electrode in 0.5 M  $H_2SO_4$  at different temperature (scan rate =  $100 \text{ mV s}^{-1}$ )

Temperature / °C	Onset potential / mV	Peak current / mA
0	0.20	0.30
3	0.12	0.36
7	0.01	0.56
15	-0.03	0.76
25	-0.04	1.09

**Table 5.8** Onset potential and peak current values for ethanol electro-oxidation at different temperatures

### ***Reaction order calculation***

The variation in the electro-oxidation current with varying formic acid concentration was analyzed at two different potentials. This yields the reaction order for the formic acid electro-oxidation reaction with respect to formic acid concentration as discussed in the first part of the chapter. The plot of  $\log I$  vs.  $\log c$  is shown in Figure 5.26. The reaction order at -0.1 V was observed to be 0.33 while at 0 V the reaction order could not be calculated from the plot due to the nonlinear curve especially at higher concentration of formic acid, where the curve tends to become a plateau. There is a significant difference in the nature of the plots at 0.0 V and -0.1 V.

The apparent reason of this anomalous behaviour may be due to the fact that at -0.1 V there is another reaction taking place along with the formic acid oxidation reaction, which is the oxidation of adsorbed and absorbed hydrogen in the acid medium. The overall effect of these two reactions may influence the reaction rate calculation. The plot at 0.0 V shows that at higher concentration of formic acid the reaction does not entirely depend on formic acid concentration and essentially becomes zero order reaction with respect to formic acid concentration.

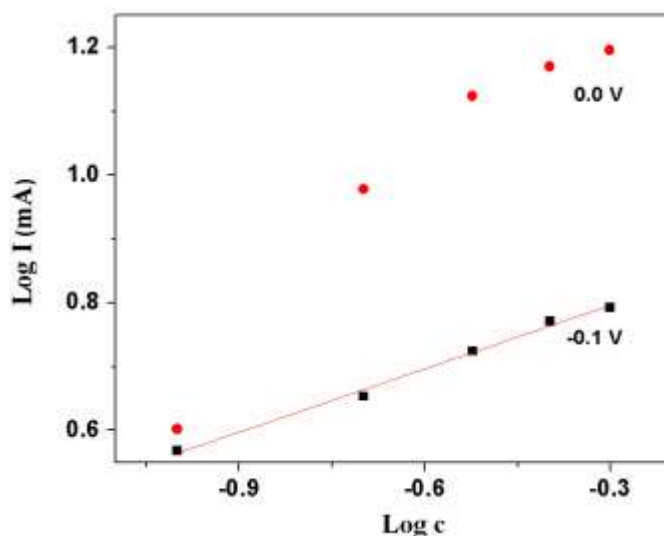


**Fig. 5.26** Plots of  $\log I$  vs.  $\log c$  (formic acid concentration) at two different potentials for calculating the reaction order

### 5.2.2.7 Catalytic activity of Pd-PANI surface towards electro-oxidation of ethanol and methanol

To examine the electrocatalytic activity of the Pd-PANI film in alkaline medium, we have studied the ethanol and methanol electro-oxidation reactions. The electrocatalytic oxidation reactions of these alcohols have been intensively studied as the anodic reaction in direct alcohols fuel cells (DAFCs). In this work we have evaluated the electrocatalytic activity of Pd-PANI nanocomposite coated electrode by studying electro-oxidation in 0.5 M NaOH. Figure 5.27a shows the CV for the electro-oxidation of 1 M ethanol in alkaline media. The figure in the inset shows the voltammogram in the absence of ethanol.

The ethanol oxidation starts at -0.70 V and peak current appears at -0.17 V. During the reverse scan there is a secondary peak at -0.40 V. This peak arises due to the reduction of Pd oxides formed during the forward scan which exposes a fresh Pd surface for electro-oxidation of alcohols.

We have carried out 200 cycles potential scans to check the reproducibility of the voltammogram. In Figure 5.27a the 1<sup>st</sup> and 200<sup>th</sup> cycles are indicated by arrows. We observed no decline in the electro-oxidation current even after 200 cycles potential scans as can be seen by comparing the currents of 1<sup>st</sup> and 200<sup>th</sup> cycles from Figure 5.27a. This shows that there is no adsorption of intermediates which can poison the catalytic surface. This is an important advantage of Pd-PANI nanocomposite electrode.

The mass current density for ethanol electro-oxidation is measured to be about  $1.3 \text{ A mg}^{-1}$  of Pd. This value, though substantial, is comparatively less than  $2.0 \text{ A mg}^{-1}$  peak current for Pd nanowires synthesized in hexagonal mesophase [61].

Figure 5.27b shows the CV for the electro-oxidation of 1 M methanol in alkaline media. The methanol oxidation current starts at about  $-0.62 \text{ V}$  and reaches the maximum current at  $-0.20 \text{ V}$ . The maximum current observed was  $0.82 \text{ mA cm}^{-2}$ . During the reverse scan there is a secondary oxidation peak at  $-0.40 \text{ V}$ . In this case also we did not observe any decline in the electro-oxidation current even after 200 potential scans as can be seen from Figure 5.27b ( $1^{\text{st}}$  and  $200^{\text{th}}$  cycles are shown by arrows). From the Figure 5.27b, the peak mass current density for methanol oxidation is calculated to be about  $1.03 \text{ A mg}^{-1}$ . This value is more than 10 times the value reported for Pd nanoflowers supported by carbon-PTFE matrix reported by Yin *et al.* [11].

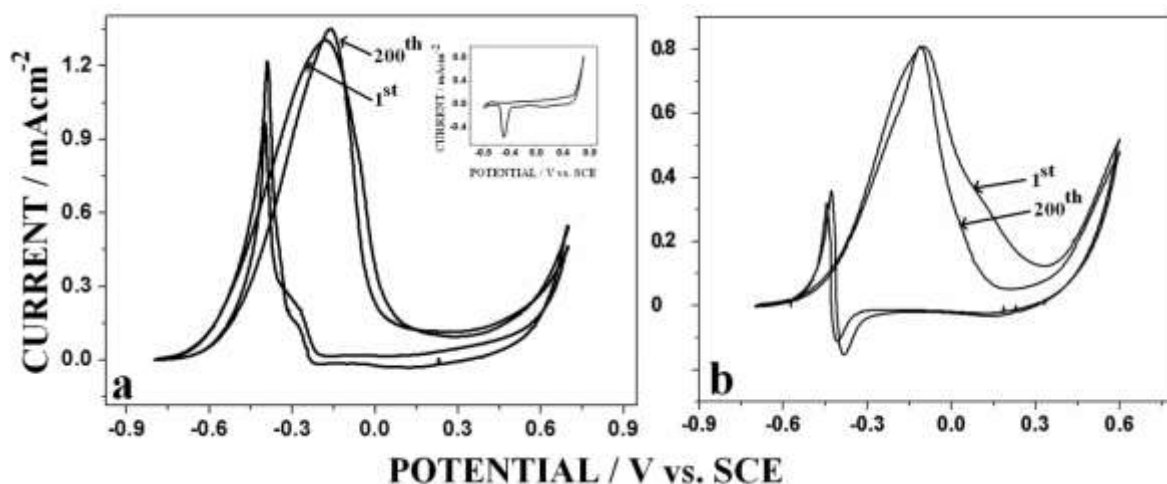
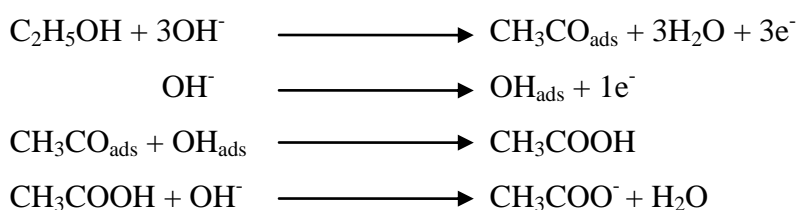


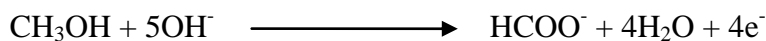
**Fig. 5.27** (a) 200 cycles CV for the electro-oxidation of 1 M ethanol in 0.5 M NaOH, (b) The 200 cycles CV for the electro-oxidation of 1 M methanol in 0.5 M NaOH, inset shows the CV in the absence of alcohols (scan rate =  $100 \text{ mV s}^{-1}$ )

### ***Mechanism of electro-oxidation***

The generally accepted mechanism for the electro-oxidation of ethanol in alkaline medium, which involves the oxidation of ethanol to acetate ions at the anode, can be summarized as follows [61].



It is known from the literature that the methanol oxidation reaction follows the following reaction of generation of formate ions similar to the acetate ions, observed in the case of ethanol [88,89].



### Activation energy calculation

Figure 5.28 a,b shows the  $\log I$  vs.  $1/T$  plots (Arrhenius plot) for a (ethanol) and b (methanol) electro-oxidation. The activation energy values calculated at different potentials are also shown in the figure. The average activation energy for ethanol electro-oxidation was calculated to be  $20.0 \text{ KJ M}^{-1}$  whereas average  $E_a$  for methanol electro-oxidation was calculated to be  $23.0 \text{ KJ M}^{-1}$ . The  $E_a$  values are quite low, which indicates the facile nature of catalytic oxidation of these alcohols on Pd-PANI nanofiber electrode. Figure 5.29 a,b shows the ethanol and methanol electro-oxidation voltammograms respectively taken at different temperatures. It is clear from the figure that the currents of alcohols oxidation have increased and the onset potential values have shifted to more negative potentials with temperature. The results obtained from CV for the ethanol and methanol electro-oxidation on Pd-PANI electrode are shown in Table 5.9 and 5.10 respectively.

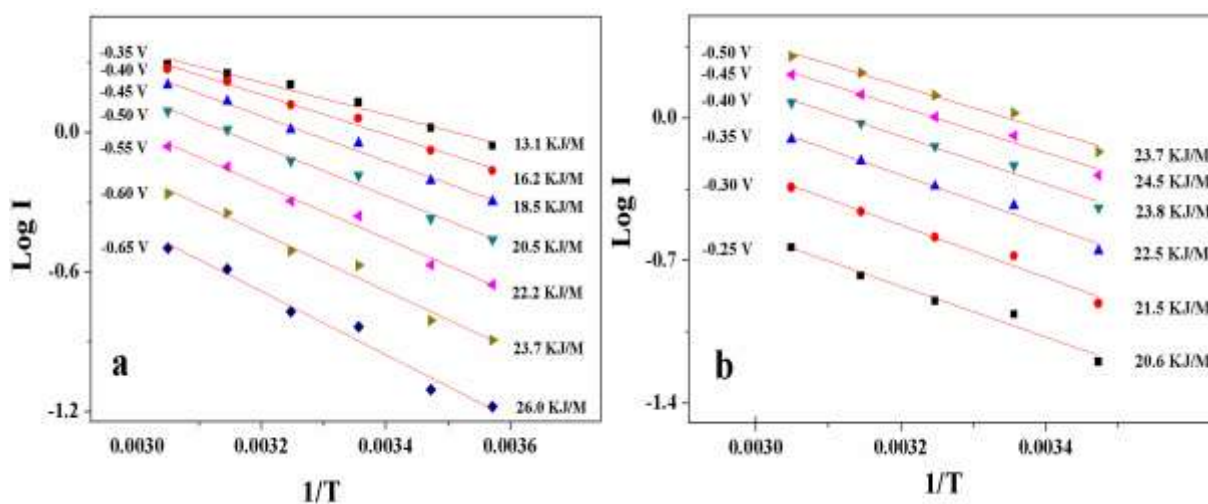


**Fig. 5.28** The Arrhenius plots ( $\log I$  vs.  $1/T$ ) for alcohols oxidation on Pd-PANI electrode at different potentials, near the foot of the CV (a) ethanol electro-oxidation (-0.65 V to -0.35 V) and (b) methanol electro-oxidation (-0.25 V to -0.5 V). The potentials and corresponding activation energies, associated with each potential are shown in the figure

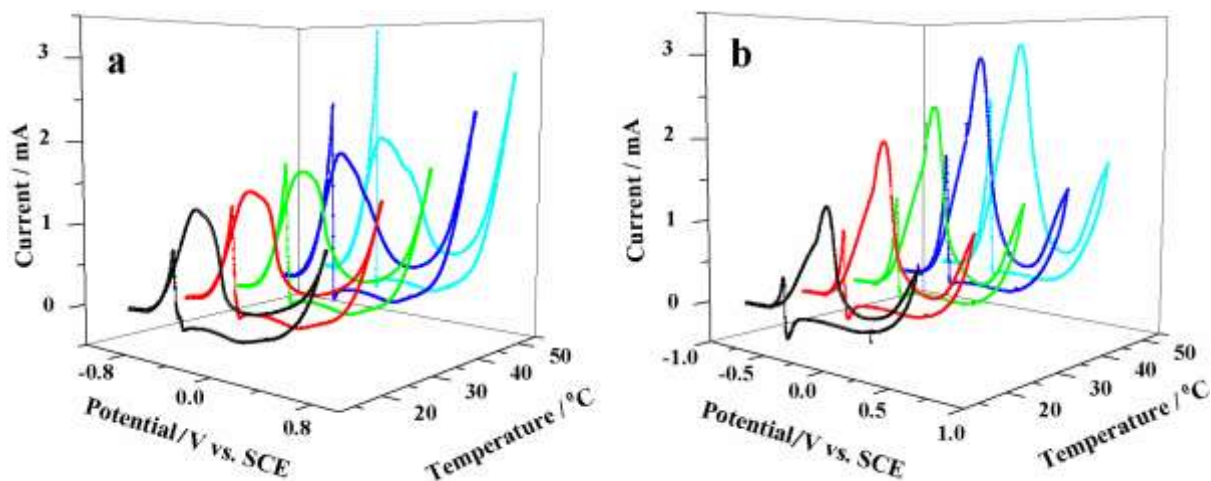


**Fig. 5.29** CVs for electro-oxidation of (a) 1.0 M ethanol and (b) 1 M methanol on Pd-PANI electrode in 0.5 M NaOH at different temperatures (scan rate = 100 mV s<sup>-1</sup>)

Temperature / °C	Onset potential / V	Peak current / mA
15	-0.62	1.29
25	-0.65	1.41
35	-0.67	1.60
45	-0.69	1.77
55	-0.71	1.93

**Table 5.9** Onset potential and peak current values for ethanol electro-oxidation on Pd-PANI modified electrode at different temperatures

Temperature / °C	Onset potential / V	Peak current / mA
15	-0.51	1.30
25	-0.54	1.98
35	-0.56	2.37
45	-0.58	3.00
55	-0.59	3.17

**Table 5.10** Onset potential and peak current values for methanol electro-oxidation on Pd-PANI modified electrode at different temperatures

### Tafel slope analysis

The Tafel slope analysis of alcohol electro-oxidation was carried out on Pd-PANI nanofiber film electrode at different temperatures, the overpotential range was chosen sufficiently negative which is also practically useful in fuel cells. The chronoamperometry measurements

were carried out for Tafel plot analysis by the application of a potential pulse of 20 s duration with a step size of 10 mV. Prior to the application of each potential step, the electrode surface was subjected to a potential program of 5s each at 0.8 V and -0.65 V vs. SCE similar to Figure 5.13.

These slopes, as we have discussed earlier can provide significant information about the reaction mechanism. Figure 5.30 shows the Tafel plots taken at 5 different temperatures (15, 25, 35, 45 and 55 °C) for ethanol electro-oxidation. The plots were fitted for 2 slopes at all the temperatures. Table 5.11 shows the values of 1<sup>st</sup> and 2<sup>nd</sup> slopes.

Figure 5.31 and Table 5.12 shows the Tafel plot characteristics of the methanol electro-oxidation on Pd-PANI nanofiber electrode. All of these Tafel plots fit well for a curve with two slopes except for temperature 45 °C. The first slope does not vary much with temperature while the second slope shows slight variation with temperature. It was earlier pointed out that the Tafel slopes in the case of adsorbed intermediate species on the electrode surface indicate the extent of blocking of the surface by the reaction intermediates. Since both the Tafel slopes are high, it indicates significant electrode contamination. The second slope is significantly higher than the first one at all temperatures. The first Tafel slope increases with temperature till 45 °C while there is no clear pattern in the second Tafel Slope variation with temperature.

In both the cases the first slope value is always lower than the second one, which indicates the adsorption of the impurities on the surface as the reaction progresses, these impurities can only be removed at very high anodic overpotentials. We have also observed that the slope values increase with temperature. The higher value of slopes at higher temperatures indicates that the large amounts of carbonaceous species generated during the oxidation of the ethanol get adsorb at higher temperatures. The Tafel slopes ( $d\eta/d\log I$ ) values are higher since a larger overpotential needs to be applied for a given value of current to flow. On a contaminated surface since the active sites are blocked, there is lack of available surface sites for adsorption of the reactants (alcohol) which demands for more overpotential to maintain the current.

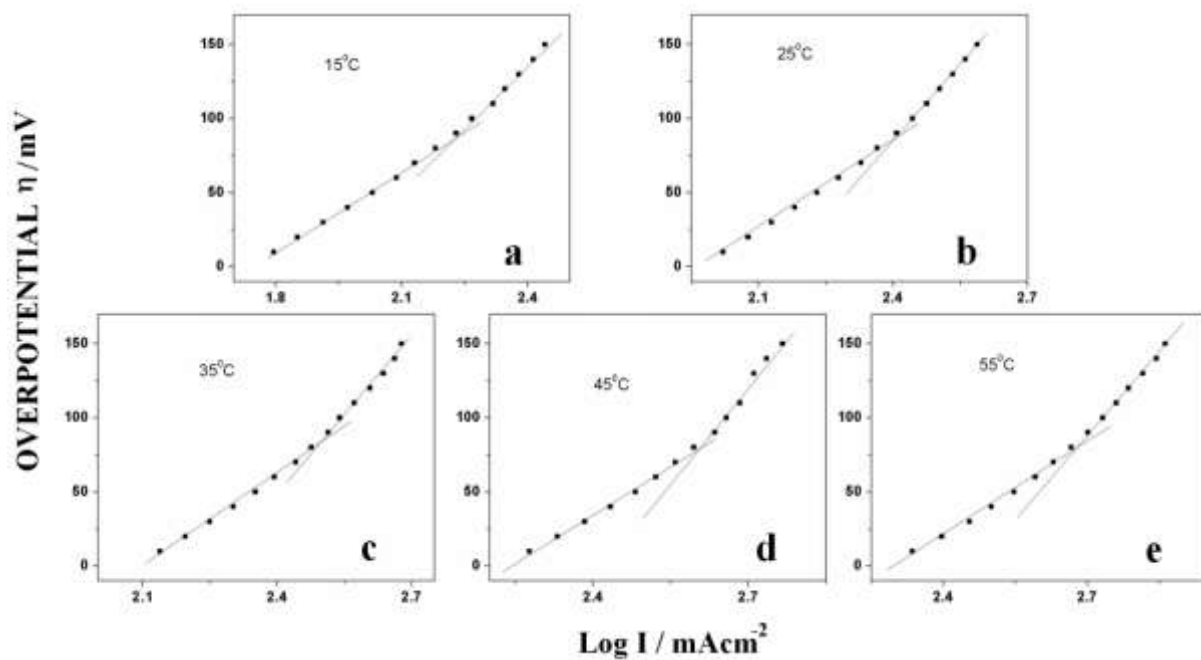


**Fig. 5.30** Linear fittings for Tafel slopes for ethanol electro-oxidation at different temperatures (near the foot of the voltammogram)

Temperature (°C)	1 <sup>st</sup> slope	2 <sup>nd</sup> slope
15	187.7	318.5
25	205.7	347.2
35	151.6	346.9
45	241.5	361.1
55	204.1	355.4

**Table 5.11** Tafel slope values for ethanol electro-oxidation at different temperatures (near the foot of the voltammogram) for Pd-PANI nanocomposite film

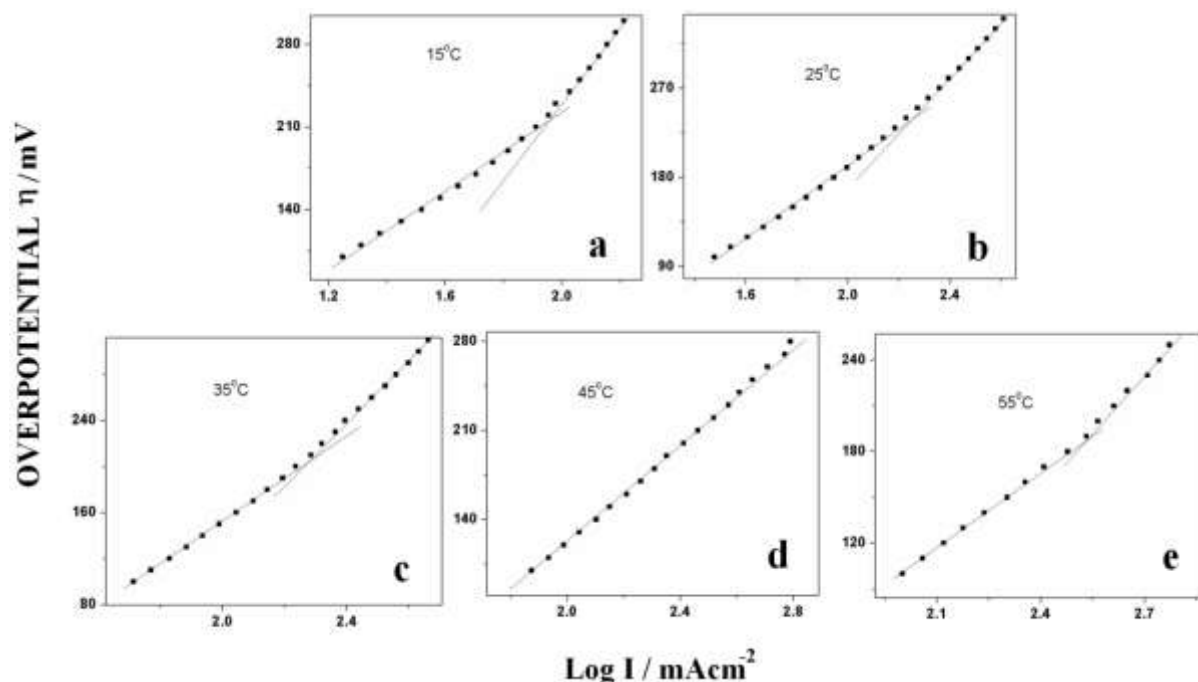


**Fig. 5.31** Linear fittings for Tafel slopes for methanol electro-oxidation at different temperatures (near the foot of the voltammogram)

Temperature (°C)	1 <sup>st</sup> slope	2 <sup>nd</sup> slope
15	166.2	334.2
25	186.6	283.0
35	192.0	291.0
45	223.0	-
55	169.0	341.6

**Table 5.12** Tafel slope values for methanol electro-oxidation at different temperatures (near the foot of the voltammogram) for Pd-PANI nanocomposite film

### **Reaction order calculation**

In addition to the Tafel slope calculation the reaction order calculation at two different potentials (near the foot of the voltammogram) with respect to the ethanol and methanol concentrations was also carried out as shown in Figure 5.32. The reaction orders for ethanol electro-oxidation reaction calculated at -0.6 V and -0.45 V are 0.23 and 0.26 respectively (Figure 5.32 a). For methanol the reaction orders calculated at -0.4 V and -0.2 V are 0.30 and 0.22 respectively (Figure 5.32 b). The reaction order values are lower compared to the values we obtained in the case of ethanol electro-oxidation on Pd-PEDOT nanocomposite film which signifies the less dependency of the reaction rate on reactant concentration in the case

of Pd-PANI nanocomposite. The values of reaction orders at these potentials are almost same, which indicates that no change in the reaction kinetics at different potentials.

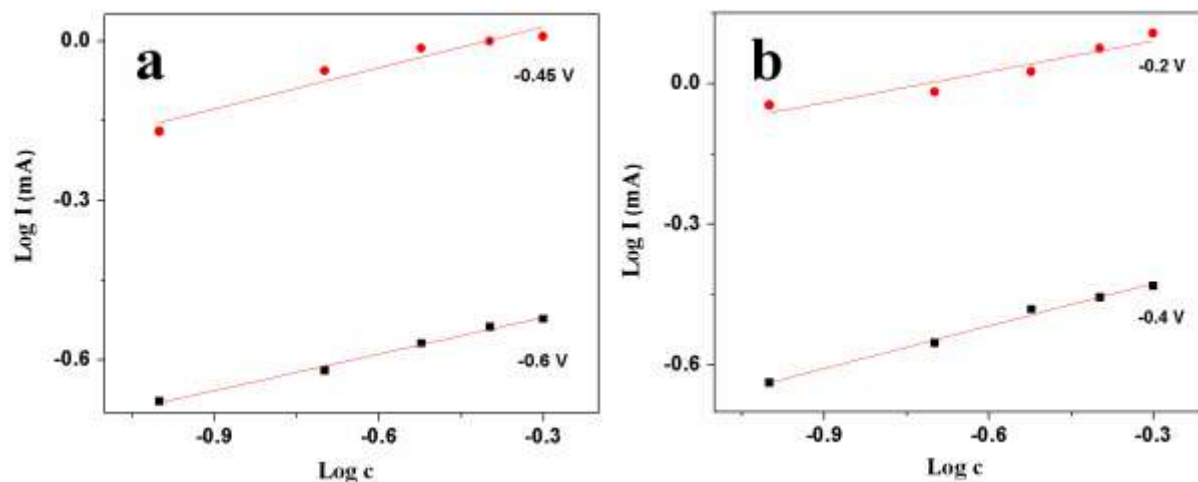


**Fig. 5.32** Plots of  $\log I$  vs.  $\log c$ , (a) (ethanol concentration) and (b) (methanol concentration) at different potentials for calculating the reaction order

### 5.3 Conclusions

In the present work we have proposed a single step electrochemical method of synthesizing Pd-PEDOT and Pd-PANI nanocomposite films on gold surface by the galvanostatic dissolution of Pd wire in the chloride containing acidic EDOT or aniline solution. A thin film of nanocomposite containing Pd nanoparticles embedded in the polymer matrix was formed on the surface. The Pd-PEDOT nanocomposite film exhibits very good stability and turns out to be an effective electrocatalyst for the hydrogen evolution and the ethanol electro-oxidation. The activation energy calculations and Tafel plot analysis at different temperatures further confirm the excellent catalytic activity of the nanocomposite film on gold surface. We have also described a novel electrochemical route to deposit Pd-PANI nanofiber film on an electrode surface. We have demonstrated that the galvanostatic dissolution of Pd wire in the acidic aniline solution yields Pd-PANI nanofibers on the cathode surface. The SEM images of the surface show the fibers of Pd-PANI nanocomposite with Pd nanoparticles adhering on the PANI surface. The film was characterized using SEM, EDAX, AFM, XRD and XPS. The Pd-PANI nanofiber film on the electrode shows voltammetric behaviour quite different from that of the pure Pd wire electrode for hydrogen adsorption and absorption in acidic medium. The excellent electrocatalytic activity of the nanofiber film electrode was confirmed from the electro-oxidation of formic acid in acidic media and ethanol and methanol in alkaline media.

Our studies show that the nanocomposite films of Pd with conjugated polymers are effective substitute of Pt in direct fuel cells (DFCs).

**Bibliography**

- [1] B.J. Gallon, R.W. Kojima, R.B. Kaner, P.L. Diaconescu, *Angew. Chem. Int. Ed.*, 46 (2007) 7251.
- [2] Y.F. Han, Z. Zhong, K. Ramesh, F. Chen, L. Chen, T. White, Q. Tay, S.N. Yaakub, Z. Wang, *J. Phys. Chem. C*, 111 (2007) 8410.
- [3] J. Hu, Y. Liu, *Langmuir*, 21(2005) 2121.
- [4] K. Mukhopadhyay, B.R. Sarkar, R.V. Chaudhari, *J. Am. Chem. Soc.*, 124 (2002) 9692.
- [5] H.P. Liang, N.S. Lawrence, T.G.J. Jones, C.E. Banks, C. Ducati, *J. Am. Chem. Soc.*, 129 (2007) 6068.
- [6] H.P. Liang, N.S. Lawrence, L.J. Wan, L. Jiang, W.G. Song, T.G.J. Jones, *J. Phys. Chem. C*, 112 (2008) 338.
- [7] H. Kobayashi, M. Yamauchi, H. Kitagawa, Y. Kubota, K. Kato, M. Takata, *J. Am. Chem. Soc.*, 130 (2008) 1828.
- [8] S. Horinouchi, Y. Yamanoi, T. Yonezawa, T. Mouri, H. Nishihara, *Langmuir*, 22 (2006) 1880.
- [9] F.J. Ibañez, F.P. Zamborini, *J. Am. Chem. Soc.*, 130 (2008) 622.
- [10] P. Zhou, Z. Dai, M. Fang, X. Huang, J. Bao, J. Gong, *J. Phys. Chem. C*, 111 (2007) 12609.
- [11] Z. Yin, H. Zheng, D. Ma, X. Bao, *J. Phys. Chem. C*, 113 (2009) 1001.
- [12] W. Pan, X. Zhang, H. Ma, Z. Zhang, *J. Phys. Chem. C*, 112 (2008) 2456.
- [13] B. Keita, G. Zhang, A. Dolbecq, P. Mialane, F. Sécheresse, F. Miserque, L. Nadjo L. *J. Phys. Chem. C*, 111 (2007) 8145.
- [14] M. Baldauf, D.M. Kolb, *J. Phys. Chem.*, 100 (1996) 11375.
- [15] (a) N. Hoshi, K. Kida, M. Nakamura, M. Nakada, K. Osada, *J. Phys. Chem. B*, 110 (2006) 12480. (b) C. Liao, Z.D. Wei, S.G. Chen, L. Li. M.B. Ji, Y. Tan, M.J. Liao *J. Phys. Chem. C*, 113 (2009) 5705. (c) V.N. Andreev, *Russian. J. Electrochem.*, 42 (2006) 1936.
- [16] F. Cheng, S.M. Kelly, N.A. Young, C.N. Hope, K. Beverley, M.G. Francesconi, S. Clark, J.S. Bradley, F. Lefebvre, *Chem. Mater.*, 18 (2006) 5996.
- [17] W.P. Zhou, A. Lewera, R. Larsen, R.I. Masel, P.S. Bagus, A. Wieckowski, *J. Phys. Chem. B*, 110 (2006) 13393.
- [18] K. Nishimura, K. Kunitatsu, K. Machida, M. Enyo, *J. Electroanal. Chem.*, 260 (1989) 181.

- [19] H. Meng, S. Sun, J.P. Masse, J.P. Dodelet, *Chem. Mat.*, 20 (2008) 6998.
- [20] a. M.I. Manzanares, A.G. Pavese, V.M. Solis, *J. Electroanal. Chem.*, 310 (1991) 159. (b) K.S. Kim, A.F. Gossmann, N. Winograd, *Anal. Chem.*, 46 (1974) 197. (c) V. Chausse, P. Regull, L. Victori, *J. Electroanal. Chem.*, 238 (1987) 115. (d) L.D. Burke, M.B.C. Roche, *J. Electroanal. Chem.*, 186 (1985) 139.
- [21] H. Lee, S.E. Habas, G.A. Somorjai, P. Yang, *J. Am. Chem. Soc.*, 130 (2008) 5406.
- [22] V. Mazumder, S. Sun, *J. Am. Chem. Soc.*, 131 (2009) 4588.
- [23] W. Zhou, J.Y. Lee, *J. Phys. Chem. C*, 112 (2008) 3789.
- [24] J. Zhang, C. Qiu, H. Ma, X. Liu, *J. Phys. Chem. C*, 112 (2008) 13970.
- [25] Y. Li, G. Lu, X. Wu, G. Shi, *J. Phys. Chem. B*, 110 (2006) 24585.
- [26] L. Xiao, L. Zhuang, Y. Liu, J. Lu, H.D. Abruna, *J. Am. Chem. Soc.*, 131 (2009) 602.
- [27] S.V. Vasilyeva, M.A. Vorotyntsev, I. Bezverkhyy, E. Lesniewska, O. Heintz, R. Chassagnon, *J. Phys. Chem. C*, 112 (2008) 19878.
- [28] Y. Zhou, H. Itoh, T. Uemura, K. Naka, Y. Chujo, *Langmuir*, 18 (2002) 277.
- [29] J. Wang, K.G. Neoh, E.T. Kang, K.L. Tan, *J. Mater. Chem.*, 10 (2000) 1933.
- [30] J.E. Park, S.G. Park, A. Koukuni, O. Hatozaki, N. Oyama, *Synth. Met.*, 141 (2004) 265.
- [31] Hong-Shi, M. Josowicz, D.R. Baer, M.H. Englehard, J. Janata, *J. Electrochem. Soc.*, 142 (1995) 798.
- [32] Q. Pei, G. Zuccarello, M. Ahlskog, O. Inganas, *Polymer*, 35 (1994) 1347.
- [33] P. Andersson, D. Nilsson, P.O. Svensson, M. Chen, A. Malmstrom, T. Remonen, T. Kugler, M. Berggren, *Adv. Mater.*, 14 (2002) 1460.
- [34] A.J. Epstein, F.C. Hsu, N.R. Chiou, V.N. Prigodin, *Synth. Met.*, 137 (2003) 859.
- [35] S.K.M. Jonsson, J. Birgeron, X. Crispin, G. Greczynski, W. Osikowicz, A.W. Denier van der Gon, W.R. Salaneck, M. Fahlman, *Synth. Met.*, 139 (2003) 1.
- [36] J. Ouyang, Q. Xu, C.W. Chu, Y. Yang, G. Li, J. Shinar, *Polymer*, 45 (2004) 8443.
- [37] T. Aemouts, P. Vanlaeke, W. Geens, J. Poortmans, P. Heremans, S. Borghs, R. Mertens, R. Andriessen, L. Leenders *Thin Solid Films*, 451 (2004) 22.
- [38] M.H. Halik, H. Klauk, U. Zschieschang, T. Kriem, G. Schmid, W. Radlik, K. Wussow, *Appl. Phys. Lett.*, 81 (2002) 289.
- [39] F. Jonas, G. Heywang, *Electrochim. Acta*, 39 (1994) 1345.
- [40] H.W. Heuer, R. Wehrmann, S. Kirchmeyer, *Adv. Funct. Mater.*, 12 (2002) 89.
- [41] S. Kirchmeyer, K. Reuter, J.C. Simpson, in: T.A. Skotheim and J.R. Reynolds, (Eds) *Conjugated Polymers-Theory Synthesis Properties and Characterization* CRC Press Taylor & Francis Group Boca Raton, FL. 2007, 3rd Edition.

- [42] E. Herrero, K. Franaszczuk, A. Wieckowski, *J. Phys. Chem.*, 98 (1994) 5074.
- [43] G. Li, C. Martinez, S. Semancik, *J. Am. Chem. Soc.*, 127 (2005) 4903.
- [44] H. Mao, X. Lu, X. Liu, J. Tang, C. Wang, W. Zhang, *J. Phys. Chem. C*, 113 (2009) 9465.
- [45] S.S. Kumar, C.S. Kumar, J. Mathiyarasu, K.L. Phani, *Langmuir*, 23 (2007) 3401.
- [46] B. Vercelli, G. Zotti, A. Berlin, *J. Phys. Chem. C*, 113 (2009) 3525.
- [47] S. Harish, J. Mathiyarasu, K.L.N. Phani, V. Yegnaraman, *J. Appl. Electrochem.*, 38 (2008) 1583.
- [48] (a) M.T. Reetz, W. Helbig, *J. Am. Chem. Soc.*, 116 (1994) 7401, (b) M.T. Reetz, W. Helbig, S.A. Quaiser, U. Stimming, N. Breuer, R. Vogel, *Science*, 267 (1995) 367.
- [49] S.H. Cho, S.M. Park, *J. Phys. Chem. B*, 110 (2006) 25656.
- [50] N. Sakmeche, E.A. Bazzaoui, M. Fall, S. Aeiyaach, M. Jouini, J.C. Lacroix, J.J. Aaron, P.C. Lacaze, *Synth. Met.*, 84 (1997) 191.
- [51] R.K. Pandey, V. Lakshminarayanan, *J. Phys. Chem. C*, 113 (2009) 21596.
- [52] K.H. Lubert, M. Guttmann, L. Beyer, K. Kalcher, *Electrochem Commun.*, 3 (2001) 102.
- [53] K. Mallick, M.J. Witcomb, A. Dinsmore, M.S. Scurrel, *Macromolec. Rapid Comm.*, 26 (2005) 232.
- [54] Y. Gimeno, A. Hernandez Creus, S. Gonzalas, R.C. Salvarezza, A.J. Arvia, *Chem. Mater.*, 13 (2001) 1857.
- [55] M. Wu, P.K. Shen, Z. Wei, S. Song, M. Nie, *J. Power Source*, 166 (2007) 310.
- [56] W.S. Zhang, X.W. Zhang, H.Q. Li, *J. Electroanal Chem.*, 481 (1997) 13.
- [57] A.C.D. Angelo, in : Jerkiewicz, G.; Feliu, J. M.; Popov, B. N. (Eds) Hydrogen at surface and interfaces: proceedings of the international symposium, Electrochemical Society Meeting, Pennington, NJ, Electrochemical Society, Inc., 2000.
- [58] T.H. Silva, V. Garcia-Morales, C. Moura, J.A. Manzanares, F. Silva *Langmuir*, 21 (2005) 7461.
- [59] S. Lu, J. Pan, A. Huang, L. Zhuang, J. Lu, *Proc. Nat. Ac. Sci.*, 105 (2008) 20611.
- [60] D. Chu, S. Gilman, *J. Electrochem. Soc.*, 143 (1996) 1685.
- [61] F. Ksar, G. Surendran, L. Ramos, B. Keita, L. Nadjjo, E. Prouzet, P. Beaunier, A. Hagege, F. Audonnet, H. Remita, *Chem. Mater.*, 21 (2009) 1612.
- [62] C. Bianchini, P.K. Shen, *Chem. Rev.*, 109 (2009) 4183.
- [63] F. Cheng, X. Dai, H. Wang, S.P. Jiang, M. Zhang, C. Xu, *Electrochim. Acta*, 55 (2010) 2295
- [64] M. Nie, H. Tang, Z. Wei, S.P. Jiang, P.K. Shen, *Electrochem. Commun.*, 9 (2007) 2375.

- [65] (a) M. Watanabe, S. Motoo, *J. Electroanal. Chem.*, 60 (1975) 259. (b) R. W.J. Scott, O.M. Wilson, S.-K. Oh, E.A. Kenik, R.M. Crooks, *J. Am Chem. Soc.*, 126 (2004) 15583, (c) M. Haruta, *Gold Bulletin*, 37 (2004) 27.
- [66] Y. Su, C. Xu, J. Liu, Z. Liu, *J. Power Sources*, 194 (2009) 295.
- [67] M. Beltowska-Brzezinska, J. Heitbaum, *J. Electroanal Chem.*, 183 (1985) 167.
- [68] R. Parsons, T. VanderNoot, *J. Electroanal. Chem.*, 257 (1988) 9.
- [69] Z. Borkowska, A. Tyomsiak-Zielinska, R. Nowakowski, *Electrochim. Acta*, 49 (2004) 2613.
- [70] (a) Z.X. Liang, T.S. Zhao, J.B. Xu, L.D. Zhu, *Electrochim. Acta*, 54 (2009) 2203, (b) W. Chrzanowski, A. Wieckowski, *Langmuir*, 14 (1998) 1967.
- [71] S.L. Gojkovic, T.R. Vidakovic, D.R. Durovic, *Electrochim. Acta*, 48 (2003) 3607.
- [72] N. Gospodinova, L. Terlemezyan, *Prog. Poly. Sci.*, 23 (1998) 1443.
- [73] D.W. Hatchett, M. Josowicz, J. Janata, *J. Phys. Chem. B*, 103 (1999) 10992.
- [74] D.W. Hatchett, M. Josowicz, J. Janata, *J. Electrochem. Soc.*, 146 (1999) 4535.
- [75] Y.W. Wei, K.F. Hsueh, G.W. Jang, *Macromolecules*, 27 (1994) 518.
- [76] S. Quillard, G. Louarn, S. Lefrant, A.G. MacDiarmid, *Phys. Rev. B*, 50 (1994) 12496.
- [77] X.R. Zeng, T.M. Do, *J. Polym. Phys.*, 35 (1997) 1993.
- [78] J. Chastain, *Handbook of XPS*, Perkin Elmer: Minneapolis, MN, 1992.
- [79] S.W. Huang, K.G. Neoh, C.W. Shih, D.S. Lim, E.T. Kang, H.S. Han, K.L. Tan, *Synth. Met.*, 96 (1998) 117.
- [80] M. Borasio, O. Rodríguez de la Fuente, G. Rupprechter, H.J. Freund, *J. Phys. Chem. B*, 109 (2005) 17791.
- [81] E.H. Voogt, A.J.M. Mens, O.L.J. Gijzeman, J.W. Geus, *Surf. Sci.*, 373 (1997) 210-220.
- [82] R. Imbihl, J.E. Demuth, *Surf. Sci.*, 173 (1986) 395.
- [83] W. Liang, J. Lei, C.R. Martin, *Synth. Met.*, 52 (1992) 227.
- [84] G.B. Street, In *Handbook of Conductive Polymers*; Skotheim T. A., Ed., Marcel Dekker: New York, 1986; Vol. 1.
- [85] J.C. Barton, J.A.S. Green, F.A. Lewis, *Nature*, 197 (1963) 1293.
- [86] C. Batchelor-McAuley, C.E. Banks, A.O. Simm, T.G.J. Jones, R.G. Compton, *ChemPhysChem*, 7 (2006) 1081.
- [87] J. Ge, W. Xing, X. Xue, C. Liu, T. Lu, J. Liao, *J. Phys. Chem. C*, 111 (2007) 17305.
- [88] Z. Borkowska, A. Tyomsiak-Zielinska, G. Shul, *Electrochim. Acta*, 49 (2004) 1209.
- [89] K.A. Assiongbon, D. Roy, *Surf. Sci.*, 594 (2005) 99.

## Chapter 6

# Electrochemical Synthesis of Nanocomposite Films of Gold with Different Conducting Polymers and Their Applications in Electrocatalysis

*Polyaniline (PANI), polypyrrole (PPY), polythiophene (PTP) and poly(3,4-ethylenedioxythiophene) (PEDOT) are four most studied conducting polymers (CPs) for device applications and in preparation of different polymeric nanostructures. These polymers are very stable under ambient conditions, and also quite stable in contact with strong acidic and alkaline electrolytes, including nafion film, KOH and NaOH. This makes them as potential medium for the dispersion of electrocatalyst materials. The present chapter is focused on the electrocatalytic studies carried out with gold and different conducting polymers nanocomposites.*

## 6.1 Introduction

Gold is generally considered inert in bulk form. Interestingly it is a potent catalyst when used as nanoparticles [1]. Incorporating gold nanoparticles in CP matrix is an appropriate method of tapping the potential of gold nanoparticles as catalyst material. Among many advantages of using conducting polymers (CPs) as a matrix, the important one is its use as an alternative to the carbon powder normally used as a support in fuel-cell electrodes [2-10]. CPs possess the advantage of being able to accommodate large quantities catalytic of particles. The high porosity and extended structure of CPs allow electrocatalytic materials to properly disperse in a 3-dimensional structure. This makes maximum number of catalytic centers available for the reacting species and thus significantly improves the electrocatalytic performance.

There are two main methods of preparation of the CPs *viz.* chemical method and electrochemical method. For the chemical synthesis of polymer, ammonium peroxydisulfate, hydrogen peroxide etc., are among the most common oxidizing agents for monomer oxidation. Whereas acids such as sulfuric acid, hydrochloric acid and other strong acids are commonly used electrolytes for the electrochemical synthesis of the polymers. There are reports available on the use of gold tetrachloride as an oxidizing agent for the aniline oxidation [9,10]. Wang *et al.* have in their recent work prepared PANI nanofibers and gold nanoparticles simultaneously by using chloroaurate ( $\text{AuCl}_4^-$ ) as the oxidant [10,11]. But most of the methods available in the literature are solution based and multistep. In literature there is no report on single step electrochemical preparation of the Au-CP nanocomposites.

This chapter is essentially an extension of the last chapter except the main focus of study will be gold nanoparticles dispersed conducting polymers namely; polyaniline (PANI), polypyrrole (PPY), polythiophene (PTP) and polyethylenedioxythiophene (PEDOT). We present the electrochemical method similar to one described for Pd nanocomposite [12], to produce gold and CP nanocomposite films on the conducting surfaces. The unique method involves the *in-situ* polymerization of the monomer to yield the polymer nanocomposite with gold and subsequent deposition on cathode. PANI, PPY, PTP, and PEDOT were the polymers studied in this work.

The polymer and gold nanocomposites were formed *in-situ* during the galvanostatic deposition process in the presence of their respective monomers in HCl with Au wire as anode and another gold electrode as cathode. The conjugated polymer based metal nanocomposites are very useful electrocatalyst for the oxidation of small organic molecules

as shown by the studies on the electro-oxidation of methanol on Pt-PANI and Pt nanoparticles dispersed PEDOT electrodes [13,14].

The present method is of particular significance due to the fact that it is a single step electrochemical method which avoids the extra steps of the preparation of CPs separately and subsequent mixing of polymer and gold. The prepared nanocomposite film can be directly used for further studying its properties such as electrocatalytic activity. The surface of the film was examined with SEM, EDAX, AFM and FTIR spectroscopy. The nanocomposite of Au and CPs modified surface was found to be exceptionally porous.

A high rate of electro-oxidation of ethanol in alkali media was observed for nanocomposite modified electrode. The electrocatalytic activity of all the nanocomposite films towards ethanol electro-oxidation was studied in alkaline medium and their electrocatalytic responses were compared. The high electrocatalytic activity of the nanocomposite films is attributed to the presence of additional active centers on gold nanoparticles dispersed in the conducting matrix of CP.

The studies presented here will be useful in understanding the formation of interesting nanocomposite structures from gold and also as an efficient substitute of Pt in direct ethanol fuel cells (DEFC). Ethanol can be obtained in large amount through a fermentation process from sources such as sugar cane, wheat, corn, etc. This kind of supply chain is already available for ethanol worldwide without the worry of fuel getting over. This is in sharp contrast to the use of fossil fuels. The use of ethanol would also help in overcoming both the storage and developing infrastructure challenge of hydrogen for fuel cell applications.

Although fuel cells based on acidic electrolytes (mainly Nafion) have received more attention in the literature than alkaline electrolytes based fuel cells yet there is plenty of room for alkaline electrolytes based fuel cells because fuel cells based on acidic electrolytes function mainly with Pt based catalysts. This dependency makes them more expensive [15,16]. However the alkaline fuel cells can function with cheaper metals such as Au, Ag and Ni too.

## **6.2 Methods and materials**

Galvanostatic deposition was carried out using an EG&G potentiostat (model 263A) in chronopotentiometry mode and interfaced to a PC through a GPIB card (National Instruments). For Tafel slope calculations for ethanol electro-oxidation on different Au-CPs

systems, we have carried out chronoamperometry with a potential program similar to the one used in chapter 5 (Figure 5.13) with delay at negative and positive potentials.

### **6.2.1 Synthesis of the Au-CP nanocomposites on gold substrate**

The method is similar to the synthesis of Pd-PEDOT and Pd-PANI nanocomposite films as described in previous chapter [17-20]. The nanocomposite preparation method can be summarized as following. A 10 ml beaker was used as an electrochemical cell for galvanostatic deposition, 5 mg of monomer (aniline for PANI, pyrrole, for PPY thiophene, for PTP and 3,4-ethylenedioxythiophene for PEDOT) solutions were prepared in 5 ml 0.1 M HCl, a current of 50 mA was used during the process of deposition. Au wire of 5 mm length and 0.5 mm diameter working as anode and an evaporated gold film electrode of 0.15 cm<sup>2</sup> area working as cathode were used. The deposition was also carried out at different currents, and it was observed that at lower currents (<50 mA) the electrocatalytic response of the film of coated material was comparatively low. At higher currents (>50 mA) the Au-CP nanocomposite was not adhering enough on the cathode surface during the gas evolution. However we found that the deposition at a current of 50 mA provides very good electrocatalytic activity and better adhesion. Therefore we have optimized the current value to 50 mA based on shorter time of deposition, improved electrocatalytic response and robust surface film. Therefore, for all the characterization studies of the film, all the specimens were deposited at a current of 50 mA unless otherwise stated.

The synthetic approach for all the Au-CP nanocomposite films are similar as described earlier for Pd dispersed PANI and PEDOT. We present below only the observation during the formation of the film.

#### ***Au-PANI nanocomposite***

In the beginning of the experiment the aniline solution turned to light bluish color from the colorless solution which finally, at the end of experiment turned to reddish-pink. Simultaneously, a dark brown colored film was formed on the cathode surface.

#### ***Au-PPY nanocomposite***

The pyrrole solution which was colorless in the beginning turned to black color soon after the start of the experiment, indicating of the formation of PPY in the solution. The electrode was coated with the film of black color, simultaneously during the experiment.

### *Au-PTP nanocomposite*

The colorless thiophene solution turned to light yellow color in the beginning of the experiment which remained the same after the completion of the experiment. Simultaneously a light yellow-brown film was formed on the electrode surface.

### *Au-PEDOT nanocomposite*

The 3,4-ethylenedioxythiophene solution turned blue in the beginning and finally into a dark blue colored solution at the end of the experiment. Simultaneously a black film was formed on the electrode surface.

## **6.2.2 Characterization of Au-CP nanocomposites with SEM, EDAX, AFM and FTIR spectroscopy**

### **6.2.2.1 SEM analysis**

Figure 6.1-6.4 show the SEM image of the Au-CPs nanocomposite deposited on the gold substrate. Figures 6.1a,b shows the SEM images of Au-PANI nanocomposite film. Figure 6.1a shows the spherical disc like features of diameter around 100-400 nm. In addition there are smaller features present on the surface of diameter around 50-100 nm. We observed similar kind of features at different locations on the modified substrate.

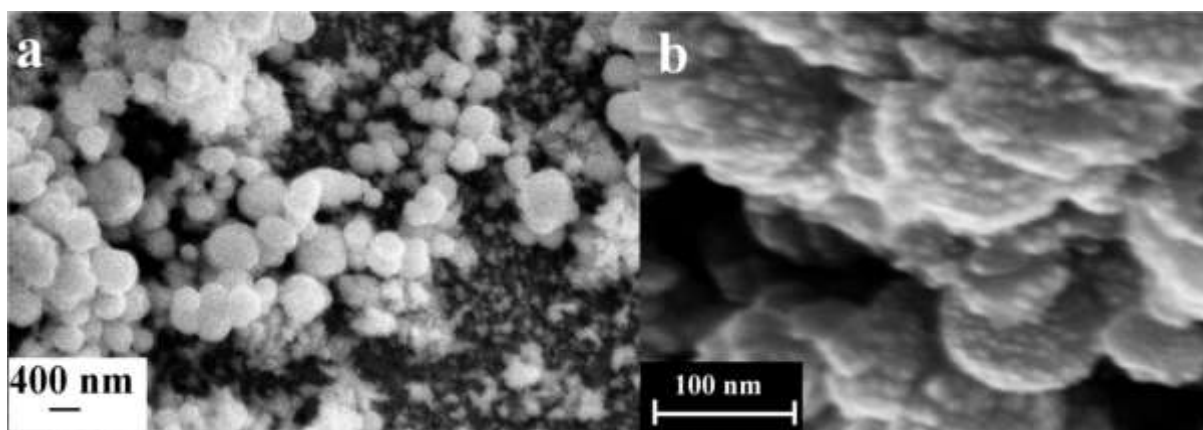


**Fig. 6.1** (a) FESEM image of Au-PANI nanocomposite film (scale bar = 400 nm) and (b) high resolution FESEM image of Au-PANI nanocomposite showing the gold nanoparticles adhering on the surface (scale bar = 100 nm)

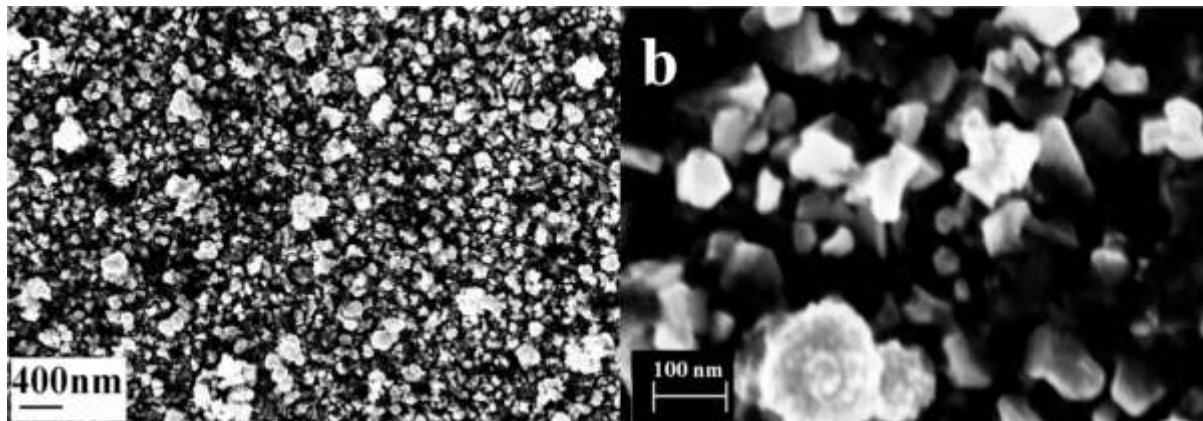


**Fig. 6.2** (a) FESEM image of Au-PPY nanocomposite film scale bar = 400 nm and (b) high resolution FESEM image of Au-PPY nanocomposite showing the features in detail (scale bar = 100 nm)

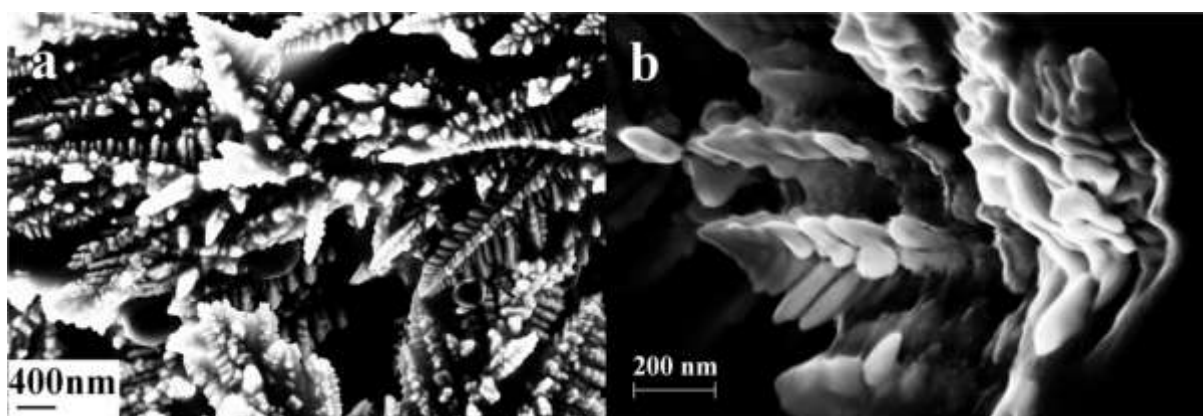


**Fig. 6.3** (a) FESEM image of Au-PTP nanocomposite film showing the dendritic growth of the nanostructures (scale bar = 400 nm) and (b) high resolution FESEM image of Au-PTP nanocomposite clearly shows the dendritic structures (scale bar = 200 nm)

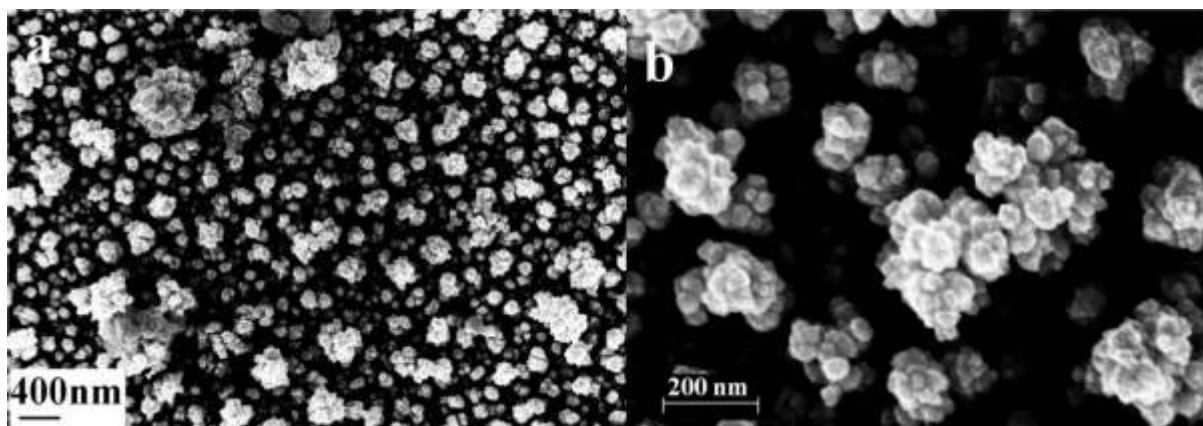


**Fig. 6.4** (a) FESEM image of Au-PEDOT nanocomposite film shows the cauliflowers like fractal growth of the nanostructures (scale bar = 400 nm) and (b) high resolution FESEM image of Au-PEDOT nanocomposite showing the flower like structures in detail (scale bar = 200 nm)

Figure 6.1 b is high resolution SEM image of the Au-PANI nanocomposite film. It shows clearly that the disc like features observed in Figure 6.1a are actually composed of smaller particles of 5-10 nm size embedded in it, which appear to be the gold nanoparticles embedded in the PANI matrix.

Figure 6.2a, b shows the SEM images of the Au-PPY coated surface. The images show features of irregular shapes with sharp edges. These features are 20-100 nm in size and spread throughout the surface. In addition to these features there are few cauliflower like structures present on the surface showing the fractal morphology of the Au-PPY nanocomposite in those regions. Figure 6.2b shows the high resolution SEM image of the Au-PPY nanocomposite film showing the nanostructured features with size of about 10-20 nm.

Figure 6.3a, b is the SEM images of the Au-PTP nanocomposite coated surface. Unlike the other Au-CPs nanocomposite the images show the presence of dendritic structure of the Au-PTP nanocomposite. These dendritic structures are more than a  $\mu\text{m}$  in length and from the high resolution SEM image (Figure 6.3b) of a single dendrite structure in much better resolution, we observe that the side branches of the dendritic structure have diameters of about 10-20 nm.

Figure 6.4a, b is the SEM images of the Au-PEDOT nanocomposite coated surface. The image shows the presence of cauliflower like nanostructures throughout the surface with sharp edges. These features resemble to the flower like structure with fractal growth. The size of these structures varies from 20 nm to 100 nm, which can grow as large as 500 nm as seen

in the figure. In high resolution Figure 6.4b, the fractal nature of growth is clearly visible and it shows that the flower like structures are composed of small 10-30 nm features.

The above SEM imaging analysis shows that the structure of the Au-CP nanocomposite coated surface varies for different CPs. This is an important observation as we can form varieties of nanostructures for various applications by this simple one step preparation method. However one common feature among these nanocomposite films is the fractal like growth, which indicates diffusion limited aggregation at high current densities employed for the film formation [21].

### 6.2.2.2 EDAX analysis

EDAX studies were also carried out on all Au-CPs coated surfaces. Tables 6.1-6.4 show the EDAX elemental analysis results for Au-PANI, Au-PPY, Au-PTP and Au-PEDOT nanocomposite films respectively. EDAX results show the presence of metallic Au and carbon in all the Au-CPs nanocomposite films along with nitrogen (Au-PANI and Au-PPY) and sulfur (in Au-PTP and Au-PEDOT). The Au-PEDOT nanocomposite film also shows the presence of O and Na (from SDS). The EDAX analysis confirms the presence of Au and respective CPs in all Au-CPs nanocomposite films.

Element	Weight %	Atom %
C	7.66	46.45
N	4.02	20.88
Au	88.33	32.67

*Table 6.1 EDAX elemental analysis results for Au-PANI nanocomposite film*

Element	Weight %	Atom %
C	5.18	44.12
S	2.49	7.93
Au	92.33	47.95

*Table 6.2 EDAX elemental analysis results for Au-PPY nanocomposite film*

Element	Weight %	Atom %
C	5.18	44.12
S	2.49	7.93
Au	92.33	47.95

*Table 6.3 EDAX elemental analysis results for Au-PTP nanocomposite film*

Element	Weight %	Atom %
C	3.93	26.15
S	2.00	4.98
Au	85.3	34.6
O	2.5	12.49
Na	6.27	21.78

*Table 6.4 EDAX elemental analysis results for Au-PEDOT nanocomposite film*

### 6.2.2.3 AFM analysis

The 3-dimensional nature and the roughness parameters of the Au-CP nanocomposite films were studied using an AFM, operating in tapping mode. Figure 6.5a-d shows the 5  $\mu\text{m}$  x 5  $\mu\text{m}$  AFM topographic images of Au-PANI, Au-PPY, Au-PTP and Au-PEDOT nanocomposite films respectively. Au-PANI and Au-PTP nanocomposite films were found to be very rough while the roughness of Au-PPY and Au-PEDOT nanocomposite films was considerably less.

The roughness parameters, i.e. the average and rms roughness calculated from the respective 5  $\mu\text{m}$  x 5  $\mu\text{m}$  AFM images are presented in Table 6.5. The average and rms roughness are maximum for Au-PTP surface followed by Au-PANI, Au-PEDOT and Au-PPY surface.

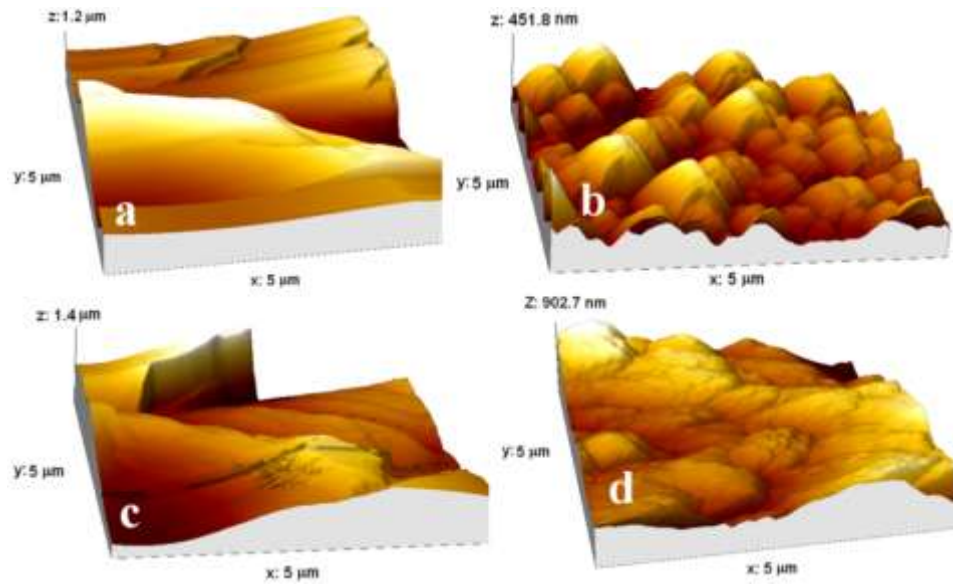


**Fig. 6.5** AFM image of Au-CP nanocomposites (a) Au-PANI nanocomposite, (b) Au-PPY nanocomposite, (c) Au-PTP nanocomposite and (d) Au-PEDOT nanocomposite

Nanocomposite	Average roughness / nm	rms roughness / nm
Au-PANI	187.0	229.0
Au-PPY	57.0	70.0
Au-PTP	185.0	225.0
Au-PEDOT	106.0	137.0

**Table 6.5** Roughness parameters calculated from the AFM images

#### 6.2.2.4 FTIR spectroscopy analysis

Infra-red spectroscopy was performed to check the chemical composition of the material in the film. Figure 6.6 shows the FTIR spectrum of the coated material in all the Au-CPs nanocomposite films.

Figure 6.6a shows FTIR spectra of Au-PANI nanocomposite, the distinctive infra-red peaks for the PANI are clear in the spectra. The peak at  $1266\text{ cm}^{-1}$  is for the C-N stretch which is the characteristic infrared peak for the aromatic amines. The infra-red spectra of PANI show the characteristic peaks of benzenoid and quinoid form of the aromatic phenyl ring system. The two peaks at  $1513\text{ cm}^{-1}$  and  $1637\text{ cm}^{-1}$  are for the benzenoid and quinoid forms of the PANI respectively. The presence of the above mentioned infrared peaks confirms the presence of the polymer form of aniline in the coated material [12,22-26].

The integrated intensity of IR peaks at  $1637\text{ cm}^{-1}$  (quinoid peak) and  $1513\text{ cm}^{-1}$  (benzenoid peak) can be used to calculate the R value, which is the ratio of the area under the IR peaks at  $1637\text{ cm}^{-1}$  and  $1513\text{ cm}^{-1}$  [12,22].

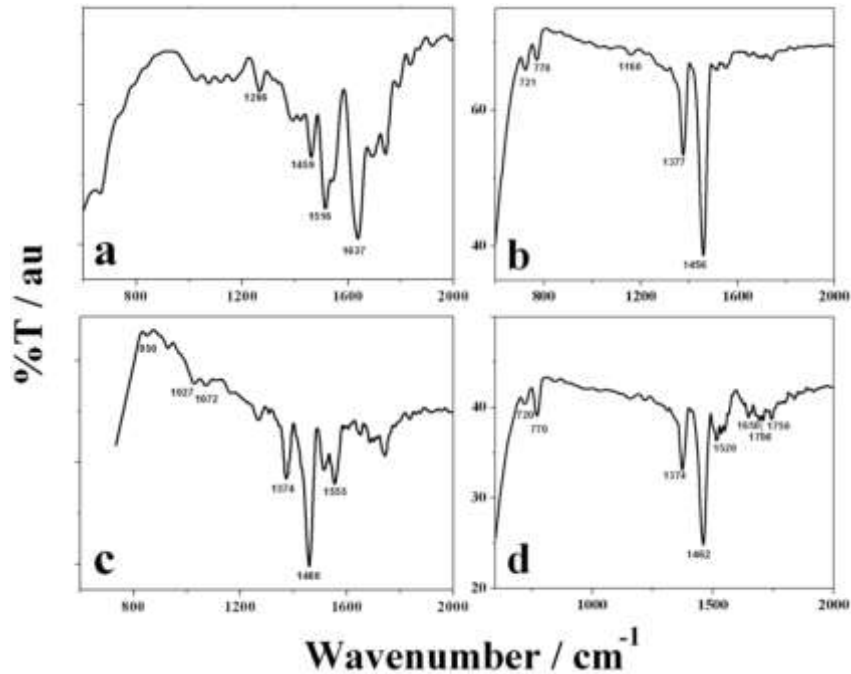


**Fig. 6.6** FTIR spectra of Au-CP nanocomposites (a) Au-PANI nanocomposite showing the characteristic benzenoid and quinoid peaks for the PANI in the composite, (b) Au-PPY nanocomposite, (c) Au-PTP nanocomposite and (d) Au-PEDOT nanocomposite

In Au-PANI nanocomposite the R value was calculated to be 0.91. This shows that there are more benzenoid rings than quinoid rings in the PANI. With the help of R value which is often related with the oxidation state of the PANI, we have defined the following structure of PANI in the coated material.

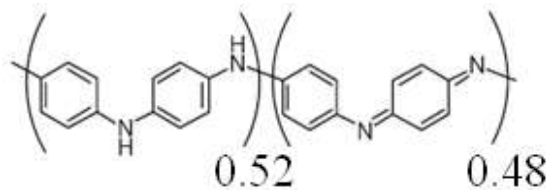
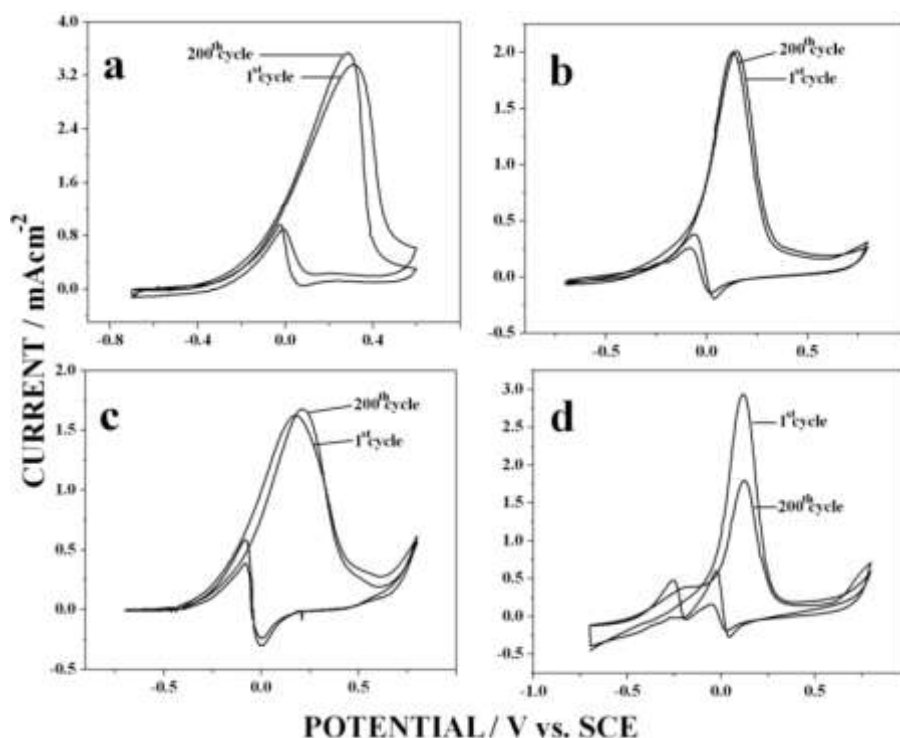


Figure 6.6b shows the FTIR spectra of Au-PPY scraped out from the coated surface. The peaks at  $1456$  and  $1377\text{ cm}^{-1}$  may be assigned to typical PPY ring vibrations. The peaks at  $721$ ,  $770$  and  $1160\text{ cm}^{-1}$  is assigned due to the  $=\text{C-H}$  out of plane vibrations and C-N stretching vibrations respectively [27-29]. Figure 6.6c shows the FTIR spectra of the Au-PTP scraped out from the coated surface. It shows a C=C aromatic ring stretch at  $1555$ ,  $1460$  and

1374  $\text{cm}^{-1}$  and in-plane C–H deformation at 1027 and 1072  $\text{cm}^{-1}$ . The spectra also show the C–S bending band at 850  $\text{cm}^{-1}$  [28,30]. Figure 6.6d is the FTIR spectra of the Au-PEDOT nanocomposite. The spectra show the infrared peaks at 1374, 1462, 1520  $\text{cm}^{-1}$  for stretching mode of C–C and C=C in the thiophene ring. The peaks at 770 and 720  $\text{cm}^{-1}$  are associated with the C–S bending vibration. The peaks at 1650, 1700 and 1750  $\text{cm}^{-1}$  may be assigned to the doped state of the polymer [31]. In all the above mentioned cases the slight shift in the peak positions is due to the presence of gold atoms which are attached to the polymer and cause the change in the electron density.

### 6.2.3 Electrocatalytic activity of Au-CP nanocomposite films for ethanol oxidation

The electrocatalytic oxidation of small chain alcohols has been intensively studied as it is the anodic reaction in direct alcohol fuel cells (DAFCs). The CP nanocomposites with gold have the potential to emerge as a very good catalytic material due to the high porosity, conducting nature and easy access of reacting species to the electrocatalytic centers.



**Fig. 6.7** 200 cycles, voltammogram for the electro-oxidation of 1.0 M ethanol in 0.5 M NaOH at different Au-CP nanocomposite film (a) Au-PANI nanocomposite film, (b) Au-PPY nanocomposite film, (c) Au-PTP nanocomposite film and (d) Au-PEDOT nanocomposite film

We have evaluated the electrocatalytic activity of different Au-CP nanocomposite coated electrodes by studying ethanol electro-oxidation as a model system in alkaline medium of 0.5 M NaOH.

Figure 6.7a-d shows the ethanol electro-oxidation voltammogram for the different Au-CP modified electrodes (a-Au-PANI, b-Au-PPY, c-Au-PTP and d-Au-PEDOT) in 1 M ethanol in 0.5 M NaOH. In all the cases we have carried out 200 potential cycles experiment in order to determine the reproducibility of the electrocatalysis results and stability of the nanocomposite modified electrode. All the current values are corrected to the respective effective catalytic surface area (ECSA). ECSA of all Au-CP nanocomposite films was measured from the gold oxide stripping analysis carried out in 0.5 M sulfuric acid solution [32].

Table 6.6 shows the CV results obtained for different Au-CP nanocomposites in terms of onset potential, peak potential and peak current. Among the four systems we have studied, the Au-PTP system was found to be the best in terms of onset potential for ethanol oxidation. The Au-PTP modified electrode shows the lowest onset potential of -0.40 V followed by Au-PEDOT (-0.36 V), Au-PPY (-0.35 V) and Au-PANI (-0.34 V) modified electrodes. The onset potential was constant in all the four systems even after the 200 potential cycles.

Nanocomposite	Onset Potential / V		Peak Potential / V		Peak Current / mAcm <sup>-2</sup>	
	1 <sup>st</sup> cycle	200 <sup>th</sup> cycle	1 <sup>st</sup> cycle	200 <sup>th</sup> cycle	1 <sup>st</sup> cycle	200 <sup>th</sup> cycle
<b>Au-PANI</b>	-0.34	-0.34	0.314	0.286	3.36	3.5
<b>Au-PPY</b>	-0.35	-0.4	0.144	0.128	2.02	2.0
<b>Au-PTP</b>	-0.40	-0.4	0.17	0.20	1.63	1.68
<b>Au-PEDOT</b>	-0.36	-0.36	0.118	0.124	2.93	1.8

**Table 6.6** The ethanol electrocatalysis results obtained for different Au-CP nanocomposites in terms of onset potential, peak potential and peak current

The Au-PANI nanocomposite modified electrode was found to be the best in terms of peak current. The peak current, 3.36 mAcm<sup>-2</sup> of Au-PANI electrode was found to be the maximum among the four systems studied, which was closely followed by Au-PEDOT (2.93 mAcm<sup>-2</sup>), Au-PPY (2.02 mAcm<sup>-2</sup>) and Au-PTP (1.68 mAcm<sup>-2</sup>). The peak currents of Au-PANI, Au-PPY and Au-PTP modified electrodes were unchanged after 200 potential cycles. The decline in the peak current was observed in Au-PEDOT modified electrode from 2.93 mAcm<sup>-2</sup> to 1.80 mAcm<sup>-2</sup>.

During the reverse potential scan there is a secondary peak in all the Au-CP nanocomposite systems. This reverse anodic peak behavior can be explained as follows. The oxide film forms during the forward scan and it gets removed from the surface during the reverse scan, this process exposes fresh gold surface and the exposed Au atoms are not in equilibrium with the metallic lattice and therefore these high energy sites possess excellent catalytic activity [33].

### 6.2.3.1 Mechanism of electro-oxidation

The established mechanism for the electro-oxidation of ethanol in alkaline medium involves the oxidation of ethanol to acetate ions at the anode. The reaction can be summarized as following [34-37].



In the above mentioned reaction scheme reaction 3 is the rate limiting step. An *in-situ* FTIR spectroscopy studies by de Lima *et al.* shows that the acetate ions are the primary product of ethanol electro-oxidation on gold in alkaline medium [36].

In all the nanocomposite systems the onset potential is more negative and the current is more than the previous reported values for ethanol electro-oxidation on porous gold nanoparticles film [36,37]. This shows that the combination of CP and gold in the form of nanocomposite serves as a better electrocatalyst for ethanol oxidation than gold nanoparticles alone. Except in Au-PEDOT system which shows a 38% decline in the catalytic current, 200 cycles, voltammetry experiment in Au-CP nanocomposite films shows no decline in the electro-oxidation current of ethanol. This shows that there is negligible poisoning of the catalytic surface due to any of the reaction products of ethanol oxidation and a high CO tolerance. This is an important advantage of Au-CP nanocomposite electrodes as the electrode poisoning is a major problem in electro-oxidation reactions of alcohols.

## 6.2.4 Kinetics of ethanol electro-oxidation

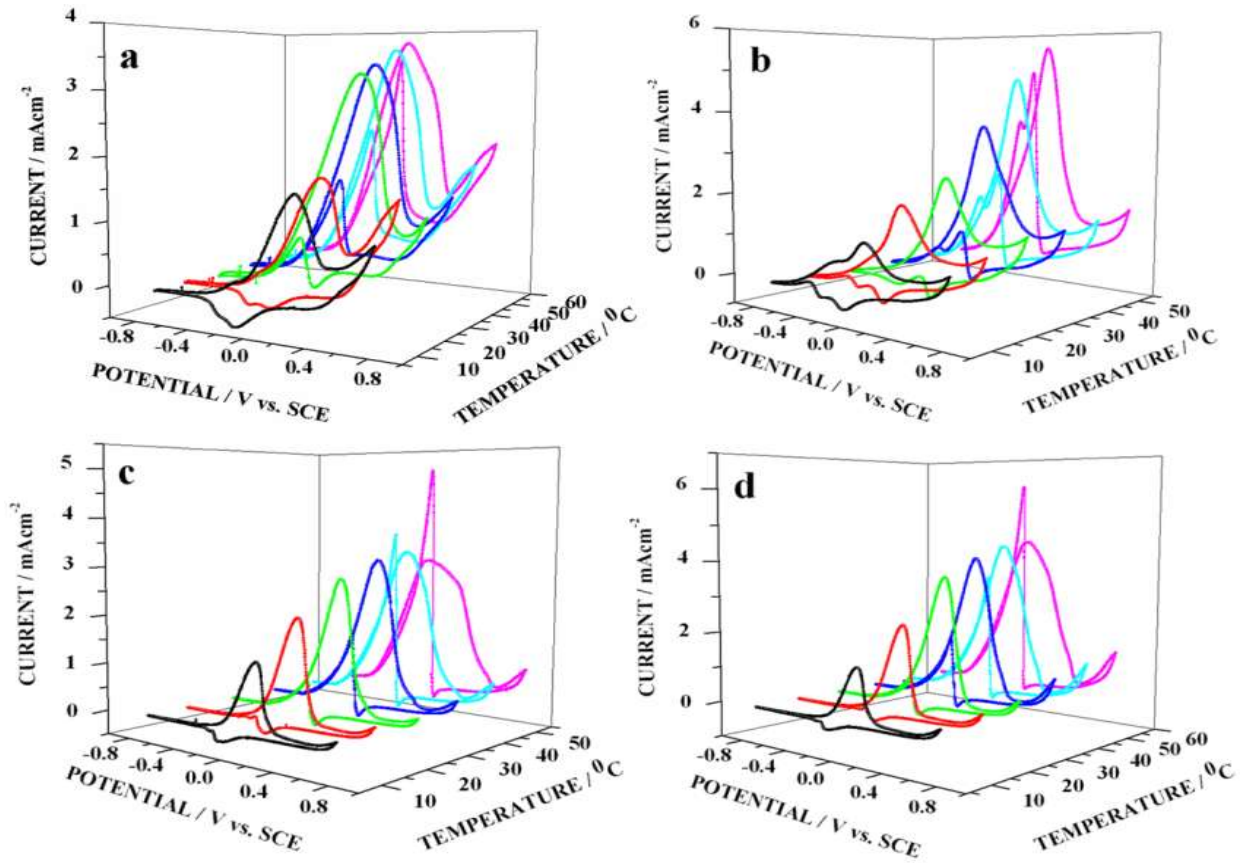
### 6.2.4.1 Activation energy ( $E_a$ ) determination

Figure 6.8 shows the CVs for ethanol oxidation at different temperatures for all Au-CP nanocomposite films. In all the Au-CP nanocomposite films it is clear from the figure that the ethanol electrocatalysis currents have increased with the temperature and also the onset potentials have become more negative.

The change in the onset potential at higher temperature is attributed to the low activation energy requirement at higher temperatures. This can be due to the fact that the increase in the temperature accelerates the adsorption of  $\text{OH}^-$  ions to form  $\text{OH}_{\text{ads}}$  and the presence of  $\text{OH}_{\text{ads}}$  is in fact helpful in achieving higher electro-oxidation current. It also helps in suppressing the formation of poisoning species, like CO which is converted to  $\text{CO}_2$  rapidly at higher temperatures [38-41]. The adsorption of hydroxyl ions on gold has been a well established fact in the literature [42-44]. The adsorption plays a key role in determining the catalytic properties of gold electrode for electro-oxidation of small organic molecules [45].

At high temperatures we also observe an increase in the anodic current of reverse potential scan. This current eventually becomes higher than the anodic current of the forward potential scan.

The plots between  $\log I$  vs.  $1/T$  (Arrhenius plot) for ethanol oxidation on all Au-CP electrodes at different potentials, near the foot of the CV (-500 mV to -100 mV) are shown in Figure 6.9. A very good linear relationship can be seen from these plots. This shows that the essential mechanism of ethanol electro-oxidation remains the same at all the temperatures. The apparent activation energies were calculated from the slope of those curves (slope =  $-E_a/2.3R$ ),  $R$  being the gas constant. The activation energy values are labeled adjacent to their respective plots. The average  $E_a$  values for different Au-CPs films in the potential range studied are  $37.5 \text{ kJ mole}^{-1}$ ,  $56.7 \text{ kJ mole}^{-1}$ ,  $54.1 \text{ kJ mole}^{-1}$  and  $56.9 \text{ kJ mole}^{-1}$  for Au-PANI, Au-PPY, Au-PTP and Au-PEDOT nanocomposite films respectively. It is clear that the  $E_a$  required for the Au-PANI system is the lowest among all the Au-CPs, this is followed by Au-PTP system. While for Au-PPY and Au-PEDOT the activation energies required are almost the same. The lower  $E_a$  value in the case of Au-PANI system than other Au-CPs systems can be accounted due to the small size particles present on the surface as seen in the SEM image (Figure 6.1b). The values obtained of  $E_a$  are comparable to the values observed for Pt, Pd and Au [46-48], based catalytic materials.



**Fig. 6.8** Cycle voltammograms for the electro-oxidation of 1.0 M ethanol in 0.5 M NaOH at different Au-CP nanocomposite film at different temperatures (a) Au-PANI nanocomposite film, (b) Au-PPY nanocomposite film, (c) Au-PTP nanocomposite film and (d) Au-PEDOT nanocomposite film

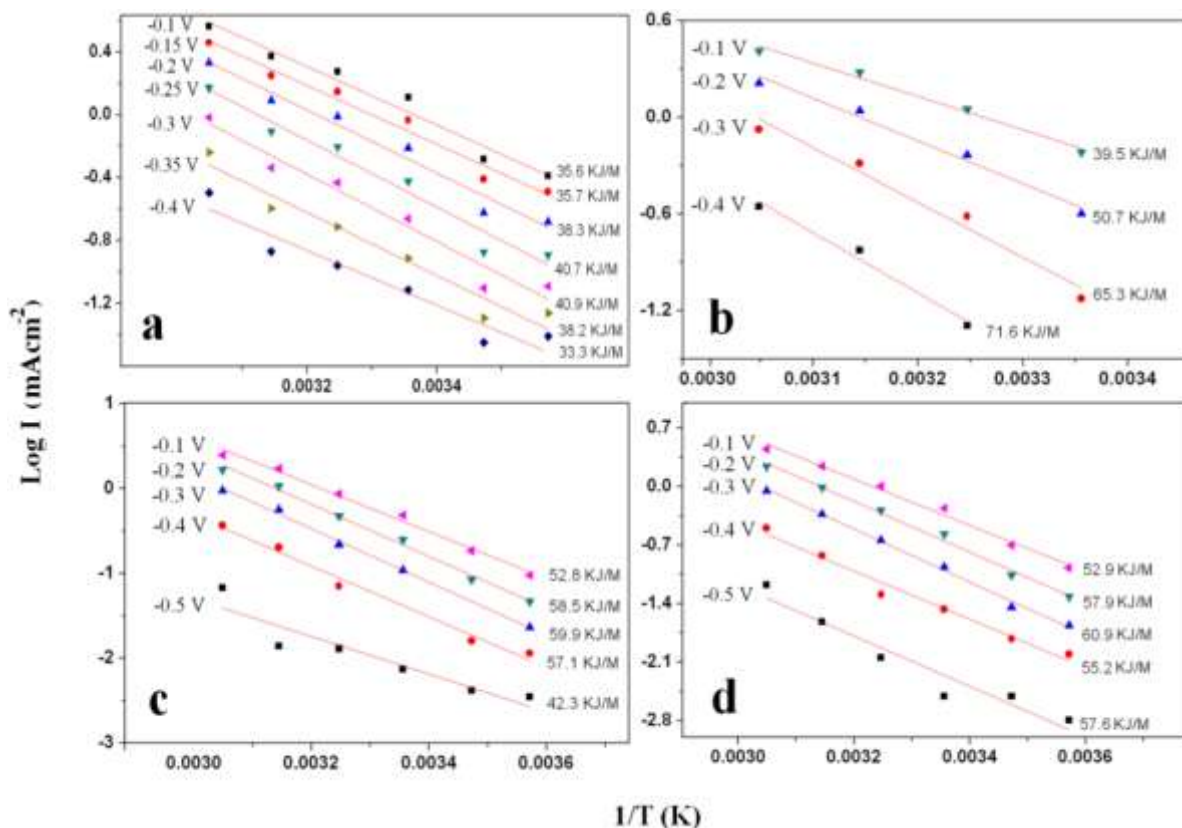


**Fig. 6.9** *Log I vs. 1/T (Arrhenius plots) for different Au-CP nanocomposite film at different potentials, corresponding activation energy values are labeled adjacent to the curves. (a) Au-PANI nanocomposite film, (b) Au-PPY nanocomposite film, (c) Au-PTP nanocomposite film and (d) Au-PEDOT nanocomposite film*

#### 6.2.4.2 Tafel plot analysis for ethanol electro-oxidation

As pointed out in the previous chapter the current–potential plots and the Tafel slopes derived from them have different connotation in the case of alcohol oxidation reaction in which the surface active sites are blocked by adsorbed intermediates. However the values of Tafel slopes provide meaningful information on the surface blocking by adsorbed intermediates.

Figures 6.10 to 6.13 show the Tafel plots for the different Au-CP systems Au-PANI (Figure 6.10), Au-PPY (Figure 6.11), Au-PTP (Figure 6.12) and Au-PEDOT (Figure 6.13). The values of the slopes for all the Au-CP systems are given in Table 6.7.

Nanocomposite → Temperature ↓	Slopes							
	Au-PANI		Au-PPY		Au-PTP		Au-PEDOT	
	1 <sup>st</sup>	2 <sup>nd</sup>						
7 °C	65.8	144.7	247.0	-	137.2	248.0	222.0	-
15 °C	73.6	146.2	173.0	-	191.2	269.7	243.0	-
25 °C	63.1	129.0	98.6	308.0	202.9	308.0	313.0	-
35 °C	106.3	160.1	192.0	449.0	223.0	360.0	381.0	-
45 °C	118.1	184.8	447.0	-	269.0	445.0	469.0	-
55 °C	132	211.8	479.0	-	319.3	650.0	668.0	-

*Table 6.7 The Tafel slopes for ethanol electrocatalysis obtained at different temperatures for different Au-CP nanocomposites*

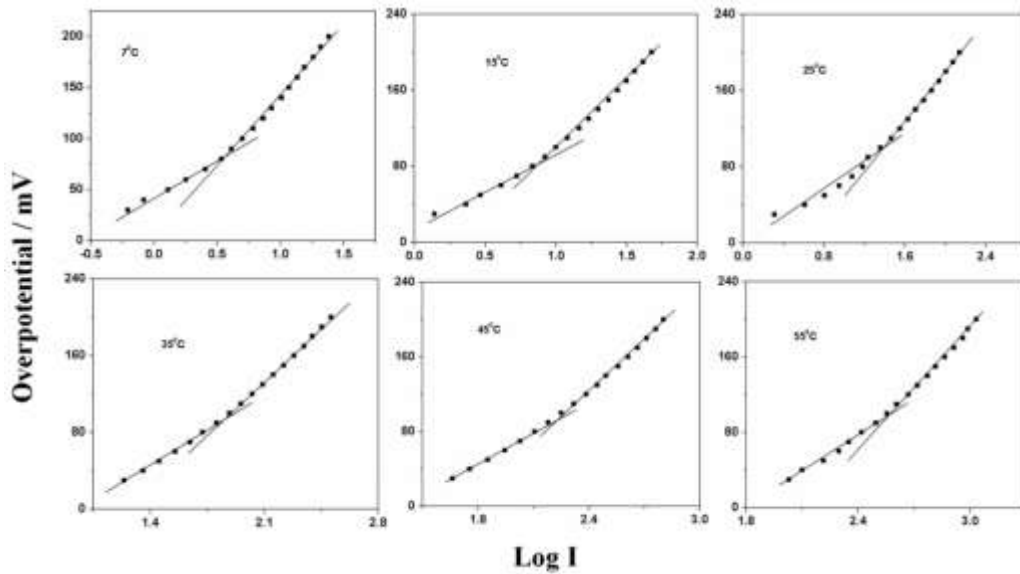


*Fig. 6.10 Tafel plots (Overpotential ( $\eta$ ) vs.  $\log I$  ( $\text{mAcm}^{-2}$ )) for Au-PANI nanocomposite at different temperatures and the fitting for two slopes*

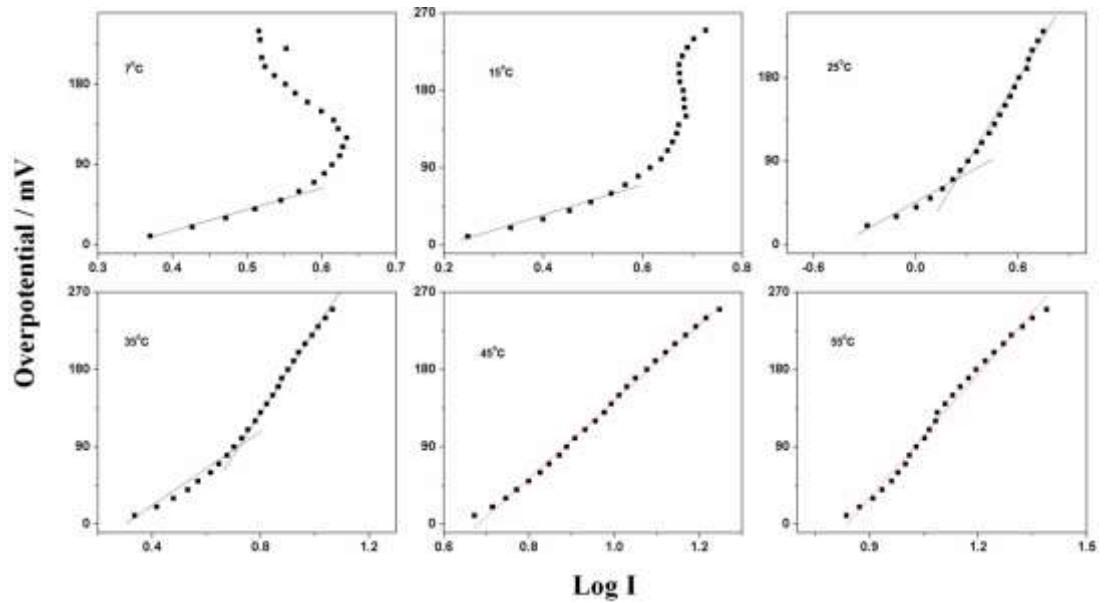


**Fig. 6.11** Tafel plots (Overpotential ( $\eta$ ) vs.  $\log I$  ( $\text{mAcm}^{-2}$ )) for Au-PPY nanocomposite at different temperatures and the fitting for first slope at  $7^\circ\text{C}$ ,  $15^\circ\text{C}$  two slopes at  $25^\circ\text{C}$  and  $35^\circ\text{C}$  and linear curve at  $45^\circ\text{C}$  and  $55^\circ\text{C}$

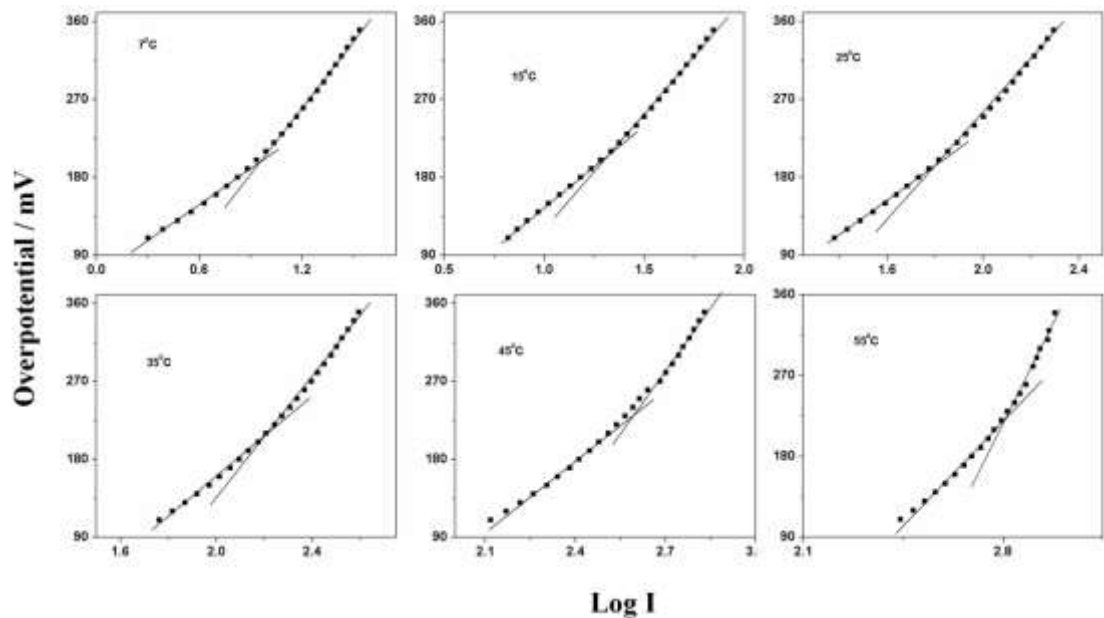


**Fig. 6.12** Tafel plots (Overpotential ( $\eta$ ) vs.  $\log I$  ( $\text{mAcm}^{-2}$ )) for Au-PTP nanocomposite at different temperatures and the fitting for two slopes

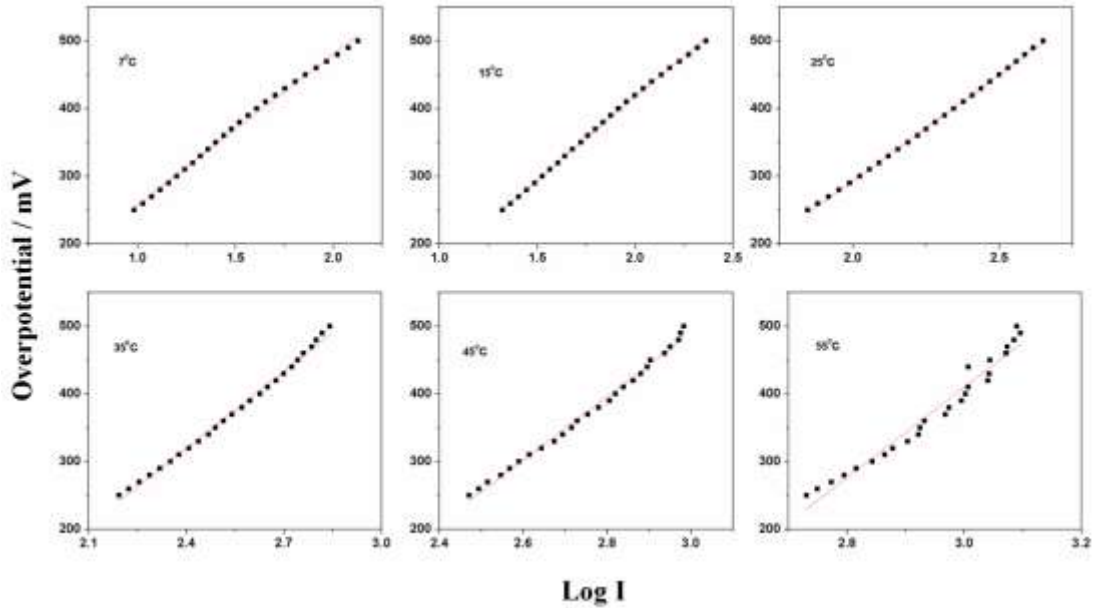


**Fig. 6.13** Tafel plots (Overpotential ( $\eta$ ) vs.  $\log I$  ( $\text{mAcm}^{-2}$ )) for Au-PEDOT nanocomposite at different temperatures and the fitting for a straight line

It can be seen that the Tafel slopes are unusually large for all systems except Au-PANI electrode. This shows that the extent of contamination and surface blocking by adsorbed intermediates are minimum in the case Au-PANI compared to other polymers. The plots of Au-PANI and Au-PTP systems fit for the two slopes at lower and higher overpotentials, having the first slope value lower than the second slope as can be seen from the Figure 6.10 and 6.12. The values of both first and second slopes increase steadily with the temperature. The higher slope values at higher temperatures indicate the enhanced adsorption of carbonaceous species, formed after the ethanol electro-oxidation reaction, on the electrode surface at elevated temperatures. These adsorbed species may block the available active sites and can only be oxidized at very high overpotentials. The values of the first slope (at lower overpotentials) can be compared to those of the second slopes (at higher overpotentials). It can be seen that second slope values are always higher than the first slope, which again shows that as the reaction progresses the impurities get adsorbed on the surface, which can only be removed at very high anodic overpotentials. The higher slope values of both the slopes (first and second) in Au-PTP system than that of Au-PANI system indicate that the reaction is more favored in the case of Au-PANI system than Au-PTP system.

Tafel plot analysis of Au-PPY system (Figure 6.11) shows completely different behavior with temperature. At lower temperatures (7 and 15°C) the Tafel plot which is linear in the beginning (lower overpotentials) deviates to become nonlinear at higher overpotentials.

The plots fit well for two slopes at intermediate temperatures (25 and 35 °C) and again deviate at elevated temperatures (45 and 55 °C).

Unlike Au-PANI and Au-PTP systems the Tafel plots of Au-PEDOT system can be fitted for the straight line at all the temperatures as can be seen from Figure 6.13. Au-PEDOT system also shows the trend of higher slope values with increasing temperature. The slope values are much higher than those of Au-PANI system. The presence of a linear curve and higher slopes values perhaps indicate the significant electrode poisoning and the adverse effect of impurities adsorption, which does not vary much as the reaction progress.

Au-PANI system shows the lowest slope values among all the Au-CP systems studied in this work. The smaller slope values even at elevated temperatures in the case of Au-PANI indicate that the adverse effect of the carbonaceous species is the lowest in this case. All these observations suggest that Au-PANI has the potential to emerge as the best catalyst for the ethanol oxidation research. This is also in conformity with the low activation energy values measured for ethanol electro-oxidation in Au-PANI system.

### 6.2.4.3 Reaction order calculation

The reaction order with respect to ethanol was also calculated by plotting the  $\log I$  vs.  $\log c$  (ethanol concentration) for all Au-CP nanocomposite films as shown in Figure 6.14. The order was calculated by using the following equations:

$$I = nFkc^m \text{ and}$$

$\log I = \log nFk + m \log c$ , where,  $F$  is the Faraday's constant,  $k$  is the reaction rate constant,  $c$  is the ethanol concentration and  $m$  is the apparent reaction order with respect to ethanol.

The slope of the  $\log I$  vs.  $\log c$  plot, at any constant temperature gives the apparent reaction order ( $m$ ) of ethanol electro-oxidation reaction with respect to the ethanol concentration [46,49,50]. We have calculated the reaction order at two different potentials - 0.2 V and 0.0 V. The values of reaction order are shown in Table 6.8. In all the Au-CP systems except the Au-PANI system there is a change in the reaction order at different potentials. Reaction order of Au-PANI remains the same at both the potentials with a value of 0.57. This shows that the reaction mechanism for ethanol oxidation essentially remains same at different potentials.

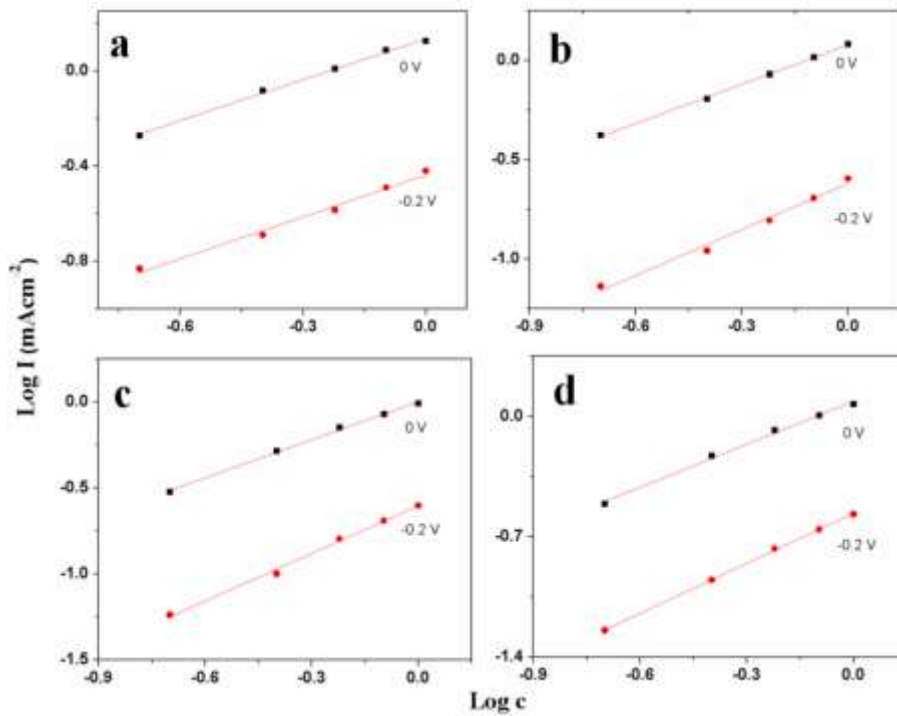


**Fig. 6.14** *Log I vs. log c plots for different Au-CP nanocomposite films at two different potentials (a) Au-PANI nanocomposite film, (b) Au-PPY nanocomposite film, (c) Au-PTP nanocomposite film and (d) Au-PEDOT nanocomposite film*

The slight change in the reaction order in Au-PPY, Au-PTP and Au-PEDOT systems can be seen from the Table 6.8, the reaction order is more at lower overpotentials (-0.2 V) and less at higher overpotentials (0 V).

Nanocomposite	Reaction order	
	-0.2 V	0.0 V
Au-PANI	0.57	0.57
Au-PPY	0.77	0.66
Au-PTP	0.92	0.74
Au-PEDOT	0.97	0.83

**Table 6.8** *The calculated reaction order with respect to ethanol concentration for different Au-CP nanocomposites*

### 6.3 Conclusions

In conclusion a novel one step electrochemical method to prepare gold and different CP namely PANI, PPY, PTP, PEDOT nanocomposites in ambient conditions is proposed. The nanocomposites were then subjected to ethanol electrocatalysis experiment and found to be

very efficient catalysts for ethanol electro-oxidation reaction. Based on the electrocatalysis experimental results we can conclude that Au-PANI nanocomposite is the best electrocatalyst material among all the nanocomposites studied in this work in terms of the activation energy required, electro-oxidation current and lower Tafel slopes. The other Au-CP nanocomposites although show a low onset potential value for ethanol electro-oxidation yet require relatively higher activation energy. We believe that the analysis of Au and CP nanocomposites towards ethanol electro-oxidation carried out in this work, may have useful implication in the development of anode catalyst in direct alkaline alcohol fuel cells.

## Bibliography

- [1] M. Haruta, *Gold Bulletin*, 37 (2004) 27.
- [2] L. Coche, J.-C. Moutet, *J. Am. Chem. Soc.*, 109 (1987) 6887.
- [3] S. Holdcroft, B.L. Funt, *Synth. Met.*, 28 (1989) C121.
- [4] M.F.G. Lyons, D.E. McCormack, P.N. Bartlett, *J. Electroanal. Chem.*, 261 (1989) 51.
- [5] T.N.S. Kumar, A.Q. Contractor, *Bull. Electrochem.*, 6 (1990) 333.
- [6] C.T. Hable, M.S. Wrighton, *Langmuir*, 7 (1991) 1305.
- [7] C.S.C. Bose, K. Rajeshwar, *J. Electroanal. Chem.*, 333 (1992) 235.
- [8] H. Laborde, J.M. Leger, C. Lamy, *J. Appl. Electrochem.*, 24 (1994) 219.
- [9] Z. Peng, L. Guo, Z. Zhang, B. Tesche, T. Wilke, D. Ogermann, S. Hu, K. Kleinermanns *Langmuir*, 22 (2006) 10915.
- [10] J. Wang, K.G. Neoh, E.T. Kang, K.L. Tan, *J. Mater. Chem.*, 10 (2000) 1933.
- [11] P.R. Sajanalal, T.S. Sreeprasad, A.S. Nair, T. Pradeep, *Langmuir*, 24 (2008) 4607.
- [12] R.K. Pandey, V. Lakshminarayanan, *J. Phys. Chem. C*, 113, 2009, 21596.
- [13] S. Patra, N. Munichandraiah, *Langmuir* 25 (2009) 1732
- [14] K.R. Prasad, N. Munichandraiah, *J. Power Sources*, 103 (2002) 300
- [15] S. Lu<sup>1</sup>, J. Pan, A. Huang, L. Zhuang, J. Lu, *Proc. Nat. Ac. Sci.*, 105 (2008) 20611.
- [16] N.J. Robertson, H.A. Kostalik, T.J. Clark, Paul F. Mutolo, H.D. Abruna, G.W. Coates *J. Am. Chem. Soc.* 132 (2010) 3400
- [17] M.T. Reetz, W. Helbig, *J. Am. Chem. Soc.*, 116 (1994) 7401.
- [18] M.T. Reetz, W. Helbig, S.A. Quaiser, U. Stimming, N. Breuer, R. Vogel, *Science*, 267 (1995) 367.
- [19] G. Li, C. Martinez, S. Semancik, *J. Am. Chem. Soc.*, 127 (2005) 4903.
- [20] S. Kirchmeyer, K. Reuter, J.C. Simpson, in: T.A. Skotheim and J.R. Reynolds, (Eds) *Conjugated Polymers-Theory Synthesis Properties and Characterization* CRC Press Taylor & Francis Group Boca Raton, FL. 2007, 3rd Edition.
- [21] J.O.M. Bockris, S.U.M. Khan, *Surface Electrochemistry, A molecular Level Approach*; Plenum Press: New York, 1993.
- [22] D.W. Hatchett, M. Josowicz, J. Janata, *J. Phys. Chem. B*, 103 (1999) 10992.
- [23] D.W. Hatchett, M. Josowicz, J. Janata, *J. Electrochem. Soc.*, 146 (1999) 4535.
- [24] Y.W. Wei, K.F. Hsueh, G.-W. Jang, *Macromolecules*, 27 (1994) 518.
- [25] S. Quillard, G. Louarn, S. Lefrant, A.G. MacDiarmid, *Phys. Rev. B*, 50 (1994) 12496.
- [26] X.-R. Zeng, T.-M. Do, *J. Polym. Phys.*, 35 (1997) 1993.

- [27] S. Richard, P. Gnanakan, M. Rajasekhar, A. Subramania, *Int. J. Electrochem. Sci.*, 4 (2009) 1289.
- [28] F. Mohammad, *J. Phys. D: Appl. Phys.*, 31 (1998) 951.
- [29] S.V. Vasilyeva, M.A. Vorotyntsev, I. Bezverkhyy, E. Lesniewska, O. Heintz, R. Chassagnon, *J. Phys. Chem. C*, 112 (2008) 19878.
- [30] L.M.H. Groenewoud, G.H.M. Engbers, J.G.A. Terlingen, H. Wormeester, J. Feijen, *Langmuir*, 16 (2000) 6278.
- [31] S.V. Selvaganesh, J. Mathiyarasu, K. L. N. Phani, V. Yegnaraman, *Nanoscale Res. Lett.*, 2 (2007) 546.
- [32] S. Trasatti, O. A. Petrii, *Pure Appl. Chem.*, 63 (1991) 711.
- [33] N. Hoshi, K. Kida, M. Nakamura, M. Nakada, K. Osada, *J. Phys. Chem. B*, 110 (2006) 12480.
- [34] Z. Yin, H. Zheng, D. Ma, X. Bao, *J. Phys. Chem. C*, 113 (2009) 1001.
- [35] F. Ksar, G. Surendran, L. Ramos, B. Keita, L. Nadjjo, E. Prouzet, P. Beaunier, A. Hagege, F. Audonnet, H. Remita, *Chem. Mater.*, 21 (2009) 1612.
- [36] R. B. de Lima, H. Varela, *Gold Bull.*, 41 (2008) 15.
- [37] D. H. Nagaraju, V. Lakshminarayanan, *J. Phys. Chem. C*, 113 (2009) 14922.
- [38] C. Bianchini, P.K. Shen, *Chem. Rev.*, 109 (2009) 4183.
- [39] M. Beltowska-Brzezinska, J. Heitbaum, *J. Electroanal Chem.*, 183 (1985) 167.
- [40] R. Parsons, T. VanderNoot, *J. Electroanal. Chem.*, 257 (1988) 9.
- [41] Z. Borkowska, A. Tyomsiak-Zielinska, R. Nowakowski, *Electrochim. Acta*, 49 (2004) 2613.
- [42] H. Angerstein-Kozłowska, B.E. Conway, B. Barnett, J. Mozota, *J. Electroanal. Chem.*, 100 (1979) 417.
- [43] H. Angerstein-Kozłowska, B.E. Conway, A. Hamelin, *J. Electroanal. Chem.*, 277 (1990) 233.
- [44] A. Chen, J. Lipkowski, *J. Phys. Chem. B*, 103 (1999) 682.
- [45] S.-G. Sun, A. Chen, *Electrochim. Acta*, 39 (1994) 969.
- [46] D. Chu, S. Gilman, *J. Electrochem. Soc.*, 143 (1996) 1685.
- [47] Y. Su, C. Xu, J. Liu, Z. Liu, *J. Power Sources*, 194 (2009) 295.
- [48] C. Jia, H. Yin, H. Ma, R. Wang, X. Ge, A. Zhou, X. Xu, Y. Ding, *J. Phys. Chem. C*, 113 (2009) 16138.
- [49] A. Aramata, M. Masuda, *J. Electrochem. Soc.*, 138 (1991) 1949.
- [50] S. L. Gojkovic, T.R. Vidakovic, D.R. Durovic, *Electrochim. Acta.*, 48 (2003) 3607.

## Chapter 7

### Summary and Prospects for Future Works

In this chapter we summarize the work presented in the thesis, highlight the significant results and also indicate the importance and possible future prospects. In broad terms the work presented in the thesis can be classified as follows:

- 1.** Formation and characterization of different types of ultrathin films on gold substrate for example, Langmuir-Blodgett (LB) film, self-assembled monolayer (SAM) and polyelectrolytes layer-by-layer assembly (LbL).
- 2.** Formation and characterization of diverse range of nanostructures in bulk and in the form of a thin film, from a porphyrin derivative and polyaniline (PANI): Optical properties and electrochemical lead sensing.
- 3.** A simple route for electrochemically synthesizing the nanocomposite film of palladium and polyethylenedioxythiophene (PEDOT). The electrocatalytic studies on the nanocomposite film towards ethanol oxidation in alkaline medium and hydrogen evolution reaction (HER) in acidic medium.
- 4.** Electrochemical synthesis and characterization of the nanocomposite film of palladium and polyaniline (PANI). The electrocatalytic studies on the nanocomposite film towards the oxidation of small chain alcohols (ethanol and methanol) in alkaline medium and formic acid oxidation in acidic medium.
- 5.** Electrochemical synthesis and characterization of nanocomposite films of gold with different conducting polymers namely; polyaniline (PANI), polypyrrole (PPY), polythiophene (PTP) and polyethylenedioxythiophene (PEDOT). The electrocatalytic studies on nanocomposite films towards ethanol oxidation in alkaline medium.

## **(1) Formation and characterization of different types of ultrathin films on gold electrode: Langmuir-Blodgett (LB) film, self-assembled monolayer (SAM) and polyelectrolyte layer-by-layer assembly (LbL)**

In this work, we have prepared and characterized different types of ultrathin molecular films on gold substrate. We have also studied the electrochemical properties of these films in aqueous and nonaqueous systems. The electron transfer and ion permeation studies were carried out through the cholesterol monolayers and multilayer films formed on self-assembled monolayers of thiophenol (TP) and 2-naphthalenethiol (2NT) on Au substrate. The molecular films of cholesterol have also been characterized using STM, AFM and grazing angle FTIR studies. We observed that the charge transfer resistance and interfacial capacitance values depend upon the structure of the monolayer. A model is proposed for the structure of the cholesterol molecules on 2NT SAM modified surface.

In the second part of the work, the electrochemical barrier properties of the LB films of a discotic liquid crystal (hexaalkoxytriphenylene with bromide counterion (PyTp) and its complex with DNA were studied with two different redox probes namely, potassium ferrocyanide/ferricyanide and ferrocene. The study shows that in the case of ferrocene redox system the bridge-mediated electron transfer process is responsible for the very low charge transfer resistance values. However, the high charge transfer resistance values obtained in the case of potassium ferrocyanide system is due to the fact that the LB film of DNA-discogen is impermeable to the ferrocyanide ions.

In the third part, we have analyzed the self-assembly of the inclusion complexes formed between  $\beta$ -cyclodextrin and thiocholesterol. Electrochemical and AFM studies were carried out for the characterization of the SAM. The self-assembled monolayer was imaged by using lateral force microscopy (LFM) and the force-distance measurements between the hydrophilic AFM tip and the sample were also carried out. Two distinct regions were found in each of the cases having hydrophilic and hydrophobic nature. Friction images were analyzed to understand the dissimilar chemical nature of both the regions. Hydrophilic region was made up of cyclodextrin inclusion complex whereas the hydrophobic region was composed of only thiocholesterol molecules. Force-distance spectroscopy reveals the greater tip-surface interaction in hydrophilic regions than the hydrophobic regions. Electrochemical studies such as cyclic voltammetry and

electrochemical impedance spectroscopy were also carried out in aqueous medium to obtain the further insight to the inclusion complex SAM.

The final part of the chapter deals with the layer-by-layer (LbL) films of oppositely charged polyelectrolytes namely, polystyrenesulfonate (PSS) and polyallylamine hydrochloride (PAH). We have analyzed the polyelectrolyte films with the help of AFM and cyclic voltammetry. The studies show an increase in the roughness and electron transfer barrier properties (in potassium ferrocyanide/ferricyanide system) with the increasing thickness of the film.

## **(2) Formation and characterization of nanostructures of a porphyrin derivative and polyaniline (PANI): Optical properties and electrochemical lead sensing**

We have studied the nanoparticles formed by a porphyrin derivative 4,4',4'',4'''-(porphine-5,10,15,20-tetrayl)tetrakis(benzoic acid) (PTBA) and polyaniline (PANI) in a DMF/water mixture. The nanostructures were characterized with the help of AFM by drop casting them onto a freshly cleaved mica sheet. Nonlinear optical absorption measurements were carried out at 532 nm, which show that the nanocomposite has an enhanced optical limiting property compared to the precursor compounds PTBA and PANI.

We have also presented a simple technique to form nanostructures by layer-by-layer assembly. These nanostructures are composed of alternate PTBA-PANI layers and grow perpendicular to the surface. The morphological analysis of the LbL films was carried out using an AFM in tapping mode. Multilayer films of 4 and 8 layers were formed on gold-coated mica. The modified electrode was used for lead detection and it was observed that it is capable of detecting lead down to 100 ppb with the help of anodic stripping voltammetry.

We have also prepared PTBA nanofibers, which are essentially the J-aggregates of porphyrin. The nanofibers were characterized with the help of AFM, UV-vis spectroscopy and PL spectra. It was observed that the nanofibers are highly emissive, contrary to the behavior of usual dye aggregates.

### **(3) A novel electrochemical synthesis of nanocomposite film of palladium and polyethylenedioxythiophene (PEDOT) and its electrocatalytic studies**

We have proposed a novel single step electrochemical method of synthesizing Pd-PEDOT nanocomposite film on gold surface by the galvanostatic dissolution of Pd wires in the acidic EDOT solution. A thin film of nanocomposite containing Pd nanoparticles embedded in the polymer matrix was formed on the surface. The nanocomposite film surface was characterized by using SEM, EDAX, ICP-MS, AFM and electrochemical experiments. The ICP-MS and Pd oxides stripping peak in cyclic voltammetry show that the Pd loading in the nanocomposite is quite low. Nevertheless, the nanocomposite film exhibited good stability over time and proved to be an effective electrocatalyst for hydrogen evolution and ethanol electro-oxidation reactions in these experiments. The activation energy calculations and Tafel plot analysis at different temperatures further confirm the excellent catalytic activity of the nanocomposite film on gold surface.

### **(4) Electrochemical synthesis and characterization of the nanocomposite film of palladium and polyaniline (PANI) and its electrocatalytic studies**

In this work, we have described a novel electrochemical route to deposit Pd-PANI nanofiber film on electrode surface. We have demonstrated that the galvanostatic dissolution of Pd wire in the acidic aniline solution yields Pd-PANI nanofiber film on the cathode surface. The film was characterized using SEM, EDAX, AFM, XRD and XPS. The SEM images of the surface show the nanofibers of Pd-PANI nanocomposite with Pd nanoparticles adhering on the PANI surface.

The Pd-PANI nanofiber film on the electrode shows a different voltammetric behavior from that of the pure Pd wire electrode for hydrogen adsorption and absorption in acidic medium. The excellent electrocatalytic activity of the nanofiber film electrode was confirmed from the electro-oxidation of formic acid in acidic medium and alcohols (ethanol and methanol) in alkaline medium. The activation energy calculations and Tafel plot analysis at different temperatures were also carried out to understand the kinetics of the electrocatalysis on Pd-PANI modified surface. These studies show that the nanofiber film of Pd-PANI is a potential substitute of Pt in direct fuel cells (DFCs). The mass current densities observed in all the experiments were either superior or comparable to the best available electro-oxidation currents in the literature.

## **(5) Electrochemical synthesis and characterization of nanocomposite films of gold with different conducting polymers and their electrocatalytic studies**

In this work a single step electrochemical method to prepare nanocomposite films of gold and different conducting polymers namely; polyaniline (PANI), polypyrrole (PPY), polythiophene (PTP) and polyethylenedioxythiophene (PEDOT) in ambient conditions is proposed. The nanocomposite films were characterized using SEM, EDAX, FTIR spectroscopy and AFM.

The nanocomposite films were found to be very efficient catalysts for ethanol electro-oxidation reaction. The activation energy calculations and Tafel plot analysis at different temperatures were carried out in order to study the kinetics of the electro-oxidation. Based on the electrocatalysis experimental results, we conclude that Au-PANI nanocomposite is the best electrocatalytic material among all the Au-CP nanocomposites studied in this work in terms of the low activation energy, high electro-oxidation current and low onset potential required for the ethanol electro-oxidation reaction.

### **Prospects for future works**

The work presented in the thesis can be broadly divided into two parts with the first part dealing with the formation of thin films of different materials and their applications. The second part deals with the electrocatalysis studies with metal and conducting polymers nanocomposites. We summarize below the importance of these studies and the prospects and scope for future work.

(1) In chapter 3 and 4 we have given an account of different types of ultrathin films that can be formed on different substrates *i.e.* the Langmuir-Blodgett (LB), self-assembled monolayer (SAM) and layer-by-layer (LbL) films. Among them, the layer-by-layer assembly has several potential applications in biosensor devices due to its ability to accommodate bio-molecules in its soft surroundings.

(2) We have carried out the immobilization of cholesterol on different self-assembled monolayers modified surfaces, which is important from the point of view of biological systems. For example the immobilization of certain phospholipids along with cholesterol on gold surface can mimic the bilayer membrane on solid surfaces. The electron transfer and ionic mobility studies through these model membranes can have considerable significance in biology.

(3) Nanoscale films produced with the above techniques find applications in the fabrication of nanomaterials and molecular electronics. Fundamental processes such as charge transfer mechanisms involving biomolecules can also be investigated at the molecular level. For example, the study of the DNA complex films will be helpful in understanding the nature of electrical and ion conduction mechanism of these biomolecular films and in designing the anisotropic ion conducting materials for different applications.

(4) Our studies with cyclodextrins and thiocholesterol inclusion complex SAMs are the examples of how patterned hydrophilic and hydrophobic surfaces can be prepared. The mixed hydrophilic and hydrophobic surfaces of this type will be useful in molecular recognition, pathogen detection and bio-sensing applications in general.

(5) In fourth chapter we have discussed the synthesis of nanostructures from a porphyrin derivative and polyaniline and their LbL film. The present study is a clear demonstration of the fact that under favorable conditions for nanoparticle formation, even a simple procedure like mixing of two media can lead to a substantial modification of the net nonlinear optical property of a given chemical system. Different conducting polymers can also be used for the preparation of the nanostructures, which have interesting optical properties. In addition, the electrochemical method of sensing lead shows the potential of the nanostructured thin film in metal ion sensing.

(6) The nanofibers, which are essentially the J-aggregates of porphyrin show enhanced emission property. The interesting results obtained from the optical and electrochemical studies signify the importance of these nanostructures in various optical and sensing devices.

(7) Our studies with Pd-PEDOT and Pd-PANI nanocomposite films have shown that these films can find potential applications in direct fuel cells (DFCs). Most of the electrocatalytic materials utilized for fuel cells are either metals or more specifically the noble metals. Some of the main catalytic materials include platinum, iridium, ruthenium, palladium, gold and silver. As of now the most common electrocatalytic material is platinum metal because of its ability to function close to the thermodynamic potential. However the high price of Pt has led researchers to work on developing alternative catalytic materials. A few of the non-noble metals have also demonstrated catalytic activity, often in combination with the noble elements, and they include nickel, iron, cobalt, chromium, vanadium, molybdenum, tin, tungsten. The study shows that a

similar method when adopted for non-noble metals in combinations with conducting polymers will lead to interesting possibilities in electrocatalysis.

**(8)** We believe that further studies will reveal that the mesoporous Pd-PEDOT nanocomposite and Pd-PANI nanofiber films prepared by the method described in this work may find wide applications as materials for catalysts, sensors and hydrogen storage.

**(9)** We have formed gold and conducting polymers nanocomposites, which may find useful applications in electrocatalysis. A detailed study, which includes the study of the electrocatalysis kinetics, Tafel slope analysis and activation energy calculation, carried out by us reveals the importance of these nanocomposite films in ethanol electrocatalysis in alkaline medium. Further studies will throw more light on the practical applications of these materials in alkaline fuel cells.

**(10)** The work presented here on metal-conducting polymer nanocomposites primarily focuses on the method of preparation and nature of these films. The possible potential applications have been explored and discussed. However, to confirm their utility in practical device applications, for example in fuel cells, a more detailed study of the material stability at higher temperatures, integrity in strong acidic and alkaline environments and the effect of surface contaminations by adsorbed impurities on the catalytic activity etc., are required.

## Appendix

This section contains the list of the essential chemicals used during the thesis work. All the chemicals used in this study were AR grade reagents and most of them were used without further purification. Millipore water having a resistivity of 18.2 M $\Omega$  cm was used to prepare the aqueous solutions throughout the work. The table below shows the most common chemicals used during the thesis work.

<b>Chemical</b>	<b>Manufacturer</b>
2-naphthalenethiol (2NT)	Aldrich
Thiophenol (TP)	Spectrochem
5-cholest-3 $\beta$ -ol (cholesterol)	Aldrich
HPLC grade ethanol	Merck
HPLC grade chloroform (Merck).	Merck
$\beta$ -cyclodextrin	Fluka
Methyl $\beta$ -cyclodextrin	Fluka
Thiocholesterol	Aldrich
Isopropanol	Merck
Polystyrene sulfonate (PSS)	Aldrich
Polyallylamine hydrochloride	Aldrich
4,4',4'',4'''-(Porphine-5,10,15,20-tetrayl)tetrakis(benzoic acid) (PTBA)	Aldrich
HPLC grade DMF	Merck
3,4-ethylenedioxythiophene (EDOT)	Aldrich
Sulfuric acid	Merck
Hydrochloric acid	Nice Chemicals
Sodium dodecyl sulfate (SDS)	S D Fine Chemicals
Aniline	Merck
Pyrrole	Spectrochem
Thiophene	Spectrochem